Optical Excitation and Electron Relaxation Dynamics at Semiconductor Surfaces

A combined Approach of Density Functional and Density Matrix Theory
applied to the Silicon (001) Surface

vorgelegt von
Diplom-Physiker Norbert Bücking
aus Filderstadt

der Fakultät II – Mathematik und Naturwissenschaften
der Technischen Universität Berlin zur Erlangung des akademischen Grades

Doktor der Naturwissenschaften
– Dr. rer. nat. –

genehmigte Dissertation

Promotionsausschuss:

Vorsitzender: Prof. Dr. Mario Dähne
1. Gutachter: Prof. Dr. Andreas Knorr
2. Gutachter: Prof. Dr. Matthias Scheffler

Tag der wissenschaftlichen Aussprache: 5. November 2007

Berlin 2007
D 83

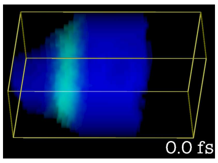

Zusammenfassung

In dieser Arbeit wird ein neuer theoretischer Formalismus eingeführt mit dem Ziel, die phononinduzierte Relaxation einer Nicht-Gleichgewichts-Verteilung zu einer Gleichgewichtsverteilung an einer Halbleiteroberfläche numerisch zu simulieren. Die Nichtgleichgewichts-Verteilung wird dabei durch eine optische Anregung erzeugt. Der Ansatz dieser Arbeit besteht in der Kombination zweier bewährter, herkömmlicher Verfahren zu einem neuen, umfassenderenden Zugang: während Halbleiteroberflächenstrukturen mittels der Dichtefunktionaltheorie präzise beschrieben werden können, kommt für dynamische Prozesse in Heterostrukturen die Dichtematrixtheorie zum Einsatz. In dieser Arbeit werden die Parameter für die Dichtematrixtheorie aus den Ergebnissen von Dichtefunktionalrechnungen bestimmt.

Die Arbeit gliedert sich in zwei Teile. In Teil I werden allgemeine theoretische Grundlagen erörtert, von den Grundlagen der kanonischen Quantisierung bis zur Diskussion von Dichtefunktional- und Dichtematrixtheorie in zweiter Bornscher Näherung. Während der Dichtefunktionalformalismus zur Strukturbestimmung lange etabliert ist und fertige Programme existieren, gehen die Erfordernisse an den Dichtematrixformalismus bezüglich der zugrundeliegenden Geometrie und der Anzahl der einbezogenen Bänder über das gewöhnlich in diesem Gebiet erforderliche Maß hinaus. Ein besonderes Augenmerk wird beim Dichtematrixformalismus daher auf Erweiterungen bestehender Formulierungen unter Ausnutzung geometrischer Symmetrien der Halbleiterstruktur und der Gleichungen gelegt.

In Teil II wird der Einsatz des entwickelten Formalismus am Beispiel einer Silizium (001) Oberfläche in 2×1-Rekonstruktion diskutiert. Zunächst werden dazu Bandstruktur-Rechnungen mit Dichtefunktionaltheorie und dem LDA-Funktional durchgeführt, wovon dann die *Kohn-Sham*-Wellenfunktionen und Eigenwerte zum Einsatz bei der Berechnung von Wechselwirkungsmatrixelementen für die Elektron-Phonon-Kopplung und die optische Anregung kommen. Diese Matrixelemente werden für optische Übergange von den Valenzbändern in die Leitungsbänder und für die Elektron-Phonon-Prozesse innerhalb der Leitungsbänder bestimmt, wobei die Kopplung an Phononen mittels Deformationspotentialen realisiert wird. Von besonderem Interesse ist dabei das Zusammenspiel von den Volumenbändern und spezieller Oberflächenbänder, die von der Rekonstruktion an der Oberfläche herrühren und teilweise die Bandlücke ausfüllen. Im Anschluß an die Bestimmung der Matrixelemente wird die dynamische Entwicklung mit den oben abgeleiteten Gleichungen simuliert.

Den Abschluß der Arbeit bildet ein Vergleich mit experimentellen Daten. Hierbei wird eine gute Übereinstimmung erzielt, sowohl was die zeitliche Abfolge des Relaxationsprozesses betrifft, als auch in Hinblick auf die entsprechenden Relaxations-Zeitskalen.

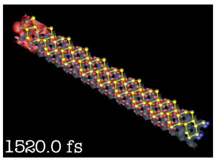

Abstract

In this work a new theoretical formalism is introduced in order to simulate the phonon-induced relaxation of a non-equilibrium distribution to equilibrium at a semiconductor surface numerically. The non-equilibrium distribution is effected by an optical excitation. The approach in this thesis is to link two conventional, but approved methods to a new, more global description: while semiconductor surfaces can be investigated accurately by density-functional theory, the dynamical processes in semiconductor heterostructures are successfully described by density matrix theory. In this work, the parameters for density-matrix theory are determined from the results of density-functional calculations.

This work is organized in two parts. In Part I, the general fundamentals of the theory are elaborated, covering the fundamentals of canonical quantizations as well as the theory of density-functional and density-matrix theory in 2^{nd} order Born approximation. While the formalism of density functional theory for structure investigation has been established for a long time and many different codes exist, the requirements for density matrix formalism concerning the geometry and the number of implemented bands exceed the usual possibilities of the existing code in this field. A special attention is therefore attributed to the development of extensions to existing formulations of this theory, where geometrical and fundamental symmetries of the structure and the equations are used.

In Part II, the newly developed formalism is applied to a silicon (001) surface in a 2×1 reconstruction. As first step, density-functional calculations using the LDA functional are completed, from which the *Kohn-Sham*-wave functions and eigenvalues are used to calculate interaction matrix elements for the electron-phonon-coupling an the optical excitation. These matrix elements are determined for the optical transitions from valence to conduction bands and for electron-phonon processes inside the conduction bands, where the coupling to phonons is realized by a deformation potential approach. A special interest is attributed to the interplay of bulk and surface bands originating from the surface reconstruction, which partly reach into the band gap. From these matrix elements, the dynamical evolution of the initial electron distribution is calculated using the derived equations.

The thesis is completed by a comparison to experimental data. Here, a good agreement is found, both for the temporal evolution of the electron population, and for the relaxation timescales that can be extracted from the simulated data.

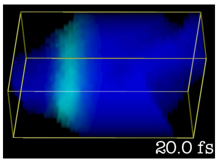

Contents

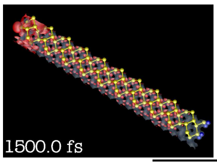
1500.0 fs

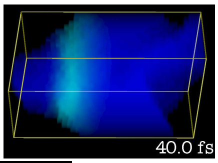
40.0 fs

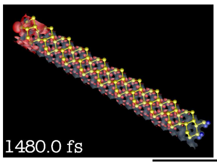

1480.0 fs

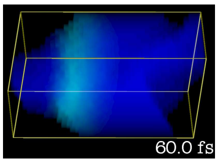

Chapter 1

Introduction

The material properties of semiconductors have been of a leading technological importance, as the they are the basis of modern electronics and therefore essential for *telecommunications*, *computer technics*, *optoelectronics* and many other applications. While the technical development of the past decades was mostly based on macroscopically structured material, the evolution has proceeded over the microstructured (integrated circuits in microcomputers) to the nano-scaled materials (quantum dots, nano wires, quantum wells, negative index materials). This miniaturization is a great challenge to the design and fabrication of new devices, but it also requires new theoretical approaches for the description of the physical properties, as both the electronic and the optical properties enter a new regime of description: While for the electrons, nanostructures can lead to a confinement and thus modification of the quantum wave function, the interaction of the nano-structured material to the light can be controlled to a so far unreachable level, such that completely new effects can be designed ([Sch06]).

Besides these technological developments, nano-structures have been in the focus of a wide academic interest for the past years. This is not only caused by the technological impact of the new techniques, but also by the fact that new investigation techniques have become available is the recent years. For experimental investigation, the availability of pulsed coherent laser light with a fs-period, and a high intensity at a so far unreachable frequency range (THz) has opened new avenues of analysis, while improved scanning-tunnel and force-field microscopy on the one hand and miniaturization in material conditioning (like lithography) on the other hand allow a better manufacturing of the samples. On the theoretical side, a great improvement is achieved due to the still increasing computer power, which allows the calculation of increasingly complex systems with more and more parameters, but also an important effort in developing dedicated formalisms both by combining and adapting known approaches and deriving completely new algorithms is ventured.

As a side effect to this miniaturization challenge, also notice is attracted to some aspects of long established fundamental research, which can be reinvestigated by improved modern techniques, or which have an effect on nanostructures. In this context, some aspects of the study of surfaces are very important for various reasons: on the one side, surfaces or at least interfaces are a basic ingredient of nanostructures, as these are obtained by assembling layers of different materials. The ratio of interfaces to volume increases in favour of the interface by decreasing the structure – it is likely that surface effects are of growing importance by miniaturization. As an extreme example, some nanomaterials are build up by combining functional molecules to a surface. On the other side, relaxation phenomena on semiconductors, e.g. as a consequence of

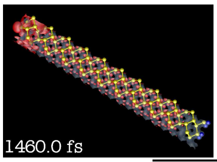

phonon scattering, have come into the focus, as fs-resolved spectroscopy allows a resolution of these phenomena on the genuine timescale [Sha99], which are long known to have effects on the line shape in the spectra of nano structures (e.g. quantum wells). For ordinary spectroscopy, the effect of such scattering is out of reach, and the hitherto research was only able to consider this only on a phenomenological level. For surfaces, the specific electronic structure (which has a great influence on the the optical properties) can effect very particular coupling mechanisms to phonons, forming specific modes at the surface.

Among the semiconductors, silicon has always had an outstanding position due to its physical properties and also its practically unlimited availability. Although it has been widely used for various kinds of electronic devices, an accurate theoretical investigation of the band structure is quite difficult due to the non-parabolic character of the bandstructure, which prevents the application of a simple, low order $\mathbf{k}\cdot\mathbf{p}$ approach [Kit91]. Another consequence of the bandstructure is the theoretical description of the optical excitation. Here, the *indirect transitions*, which assure the transitions at a low level of energy, are difficult to handle, as they are a second-order process involving multi-particle scattering with phonons. In addition, a feature of the electronic band structure of silicon which has attracted interest for a long time are the various surface reconstructions, in particular the reconstructions of the (001) surface. By these reconstructions, specific surface bands emerge in the band structure, partly inside the semiconductor-bandgap, and thus influence the optical absorption [GP94, Hai95, HGL$^+$97] and also the phonon scattering [JB99, TT03, WKFR04].

1.1 Aim of this work

In this thesis, two focuses are discussed. As first subject, in part I, the development of a new approach is in the center. This new approach is based on the combination of two long established methods, which have, however, developed independently, this is comprehensible from the fact that they focus on different fields of semiconductor physics. As a consequence of the difficulties modelling phonon relaxation in a semiconductor surface environment mentioned above, it is obvious that enhancements have to be made to existing theoretical descriptions. The dynamics in bulk semiconductors (as in Gallium-Arsenide [SMH$^+$96, LFL$^+$96, HGB00a, HGB00b, HGB01, HGB03]) and nano-structured systems of various dimensionalities (as for quantum dots [FWDK03, FSKK06] or quantum wells [WFK03, WFL$^+$04, But07]) has been very successfully investigated by using the *density-matrix formalism* [KHSK96, AM98, KSM$^+$99]. While the density-matrix formalism is a general framework leading to differential equations to describe the dynamics of a quantum system, the dimensionality, energetical properties and transition rates figure inside these equations as quasi external parameters, in the form of an electronic band structure and transition matrix elements for the interactions. Here, usually, as a good approximation for many applications, simple assumptions for the electronic band structure (parabolic bands) and for the matrix elements (resulting from slowly varying envelope wave functions (SVEA) with constant microscopical matrix elements) are used, which allow, due to further internal symmetries, often an analytical simplification of the scatter equations [FWDK03, WFK03, WFL$^+$04].

For surface structures, however, a description within these these assumptions is at least in principle dubious – from the fact, that such a system can not be reasonably interpreted as a bulk-structure or a confined two-dimensional structure [JRM01], no obvious characterization of envelope functions or confined parameter restrictions exists [BKSK07b]. As a matter of fact, re-

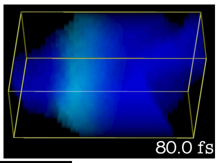

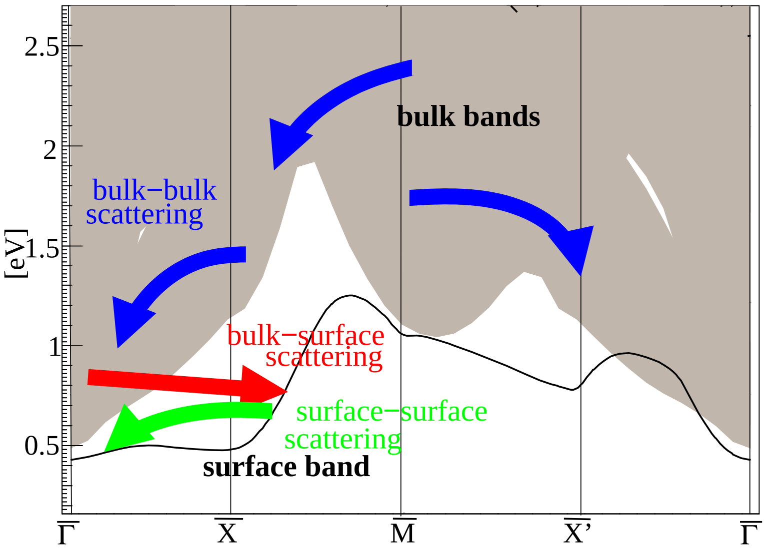

Figure 1.1: *Schematical Overview of the expected relaxation processes at a silicon (001) surface. In the background, the bulk bandstructure (grey) and the D^{down} surface band (black) are shown. While the bulk-bulk scattering (blue) yet occurs in a bulk system, the bulk-surface (red) and surface surface processes (green) are directly related to the surface reconstruction.*

cent investigations with an Indium-Phosphide model system have shown that the application of such approximations in this context can lead to a qualitatively good description of the dynamical evolution of a system (cmp. Sec. 1.3) [RWK04b, RWK04a, TGH$^+$04, ZBG$^+$04, ZBFK05], while a quantitative agreement fails in the first instance. Thus, a more realistic description using a density-matrix formalism can only be expected by employing more realistic parameters for the relaxation equation [BKSK07b, BKSK07a]. The first intent of this thesis is to provide a method to implement structure calculations for surfaces by *density-functional theory* (DFT) into the density-matrix framework [RMKR03]. Density-functional theory is one of the leading methods for theoretical analysis of microscopic structures, ranging from clusters to periodical systems, and has proved its applicability in numerous contexts. The basic idea of our approach is to perform structure calculations to obtain an accurate electronic bandstructure, which is based on the corresponding *Kohn-Sham* wavefunctions and the self-energy correction by the *GW-formalism*, and using the resulting wavefunctions to calculate transition matrix elements for several interactions (in this thesis, the interactions in the dynamics are however restricted to optical excitation and phonon-induced relaxation). As an extension, one should also think of additional calculations for phonon modes [FP95], this, however, is not elaborated in this work.

The second part of this thesis consists of an application of the newly derived formalism. To this end, phonon-induced relaxation processes are discussed as a consequence of optical excitation for a silicon (001) surface. An overview over the possible processes, which are related to the D^{down} surface band in such a structure (cmp. Sec. 5.2), are shown in Fig. 1.1. While ordinary density-functional calculations for the silicon (001) 2×1 surface are discussed in Chapter 5 for several parameters, the calculations of the matrix elements and electronic band structure for use in the density-matrix calculation are presented in Chapter 6. The dynamical calculation is finally done in Chapter 7, where the effects of the relaxation processes are widely

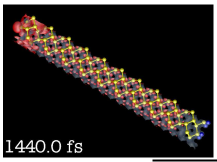

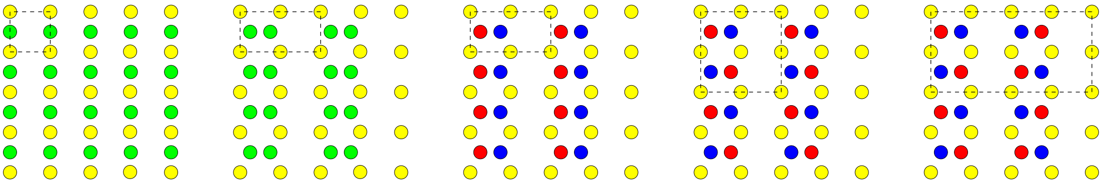
(1×1) $(2 \times 1)_{\text{symmetric}}$ $(2 \times 1)_{\text{asymmetric}}$ (2×2) (4×2)

Figure 1.2: *The various surface reconstructions of silicon (001). In the Figures, the two topmost layers of the surface are shown. The top-level atoms are depicted in green where they are all at the same height or in red (higher level atom) and blue (lower level atom) where they form a tilted dimer, the second level atoms are shown in yellow. The surface unit cells for the structure are symbolized by a black rectangle.*

discussed for various initial conditions. A comparison to the few experimental findings in this field is also discussed.

1.2 Physical aspects of the silicon (001) surface

Besides the known crystallization behaviour in the bulk, where, due to its 4-valence, silicon condenses in a diamond structure, the silicon (001) surface has led to controversial arguments for a long time. The usual surface reconstruction geometries are shown if Fig. 1.2 [DM00, DS92, FP95, RBK95]: The 1×1 surface is the basic unit cell of the (001) surface without reconstruction. More realistic configurations for the clean surface are 2×1 reconstructions, where the bulk lattice has been dissolved at the surface in favor of the formation of a dimer. This dimer formation is a characteristic of the diamond-like structures and has been experimentally confirmed since a long time. The symmetric and asymmetric 2×1 reconstructions differ in the tilting of the dimer, in the symmetric case, the dimer is flat on the surface, while in the asymmetric case, an angle to the surface is found. Energetically more favorable than the 2×1 case are the 2×2 and 4×2 reconstructions. These differ from the 2×1 case by the orientation of the dimers: the asymmetrical 2×1-reconstruction consists of rows of parallelly oriented dimers, while at the 2×2 reconstruction, the dimers are alternating, but the neighboring rows are equally oriented. At the 4×2 reconstruction, finally, the dimers are alternating in the two directions.

At room temperature (300 K), the differences in the formation energy for the asymmetrical dimers are too low to allow a clear distinction of the predominant dimer phase at the surface [DM00]. At low temperature (below 90 K), however, a discrepancy was deduced from the experimental and theoretical findings concerning the tilting angle: while the most favorable reconstruction was theoretically found to be the 4×2 reconstruction and a definite result was that it is energetically unfavorable to have a flat dimer (the symmetric 2×1 case), at this surface, there was no experimental evidence for an asymmetric reconstruction. As this deviation could not be explained by thermodynamical reasons, it is today related to the interplay of the measurement device (often a STM-tip with a certain voltage to the surface) and the dimer tilting potential [SSB04, SS06]. As a consequence, it is the accepted position today that at low temperature the 4×2 dimer reconstructions prevails. Still the effects of the different reconstructions for the band structure is a topic of research [Egg05], which requires theoretical techniques beyond the density functional approach, and still, the results are not coherent. In

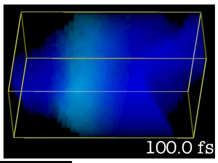

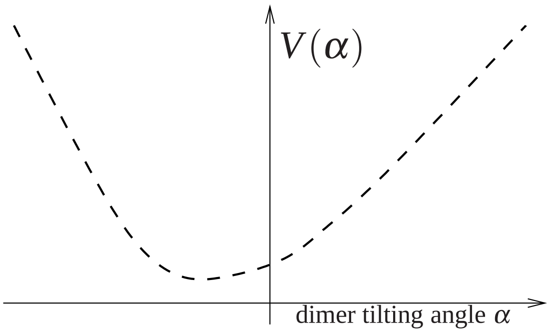

Figure 1.3: *Schematic illustration of the tilting potential of the dimer. The tilting towards one side is favored over the other side.*

this thesis, due to the example character of the discussion, the calculations are performed for an asymmetric 2×1 reconstruction.

The tilting of the dimer is dominated by a potential as illustrated in Fig. 1.3, where the minimum of the potential is shifted to a non-zero angle α. Such a potential gives rise to a surface-localized phonon mode[1] with a strong coupling to surface-related electronic bands, especially the states of the D^{up} and D^{down} bands (cmp. Chapter 5). It is likely that the strong coupling to the surface attributes an important role in a surface-related relaxation process to this phonon mode, especially in combination with an optical exposure of the surface. In the present work, however, the phonon spectrum is not calculated microscopically, but only schematically by an approximated phonon spectrum. Thus the dimer tilting effects are neglected in the phononic relaxation.

1.3 Optical excitation and phonon induced relaxation at the Indium-Phosphide (001) surface

One approach to describe the relaxation involving surface states has been formulated by adapting the specialized density-matrix theory used for the simulation of quantum-heterostructures to a generalized multiband system and using basically the same assumptions as in the former case. A surface structure whose electronic properties are approximatively described by a two-dimensional parabolic band structure has found to be the Indium-Phosphide (100) surface [HBS$^+$86, SB98, SBE$^+$98, FVV$^+$00, SEE$^+$00]. A model [ZBG$^+$04, ZBFK05] has been developed for a simulation of a Two Photon Photoemission experiment [HSK$^+$93, THE$^+$03, TGE$^+$05].

In the first step of [ZBFK05], the band structure is described by a model of four parabolic bands, which are interpreted as two-dimensional or three-dimensional according to their character (Fig. 1.4): A bulk valence band, a bulk conduction band, a surface band with a lower effective mass, intersecting the bulk conduction band and an additional vacuum band to model the emission process with quasi-free electrons. For every band, a set of wave functions is introduced, for the bulk bands, these are ordinary bulk wave functions based on three-dimensional Bloch waves (cmp. Eq. (2.25)), while for the two-dimensional bands (the surface and vacuum bands), a two-dimensional Bloch description in the surface-parallel direction is combined with an exponential decay in the z-direction (rhs of Fig. 1.4). To allow a simple analytic calculation

---

[1] The description in term of phonons (which are a linear approximation for small elongation in a parabolic potential, cmp. Sec. 2.3.3), might however break down for a highly non-parabolic potential.

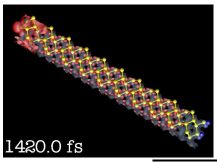

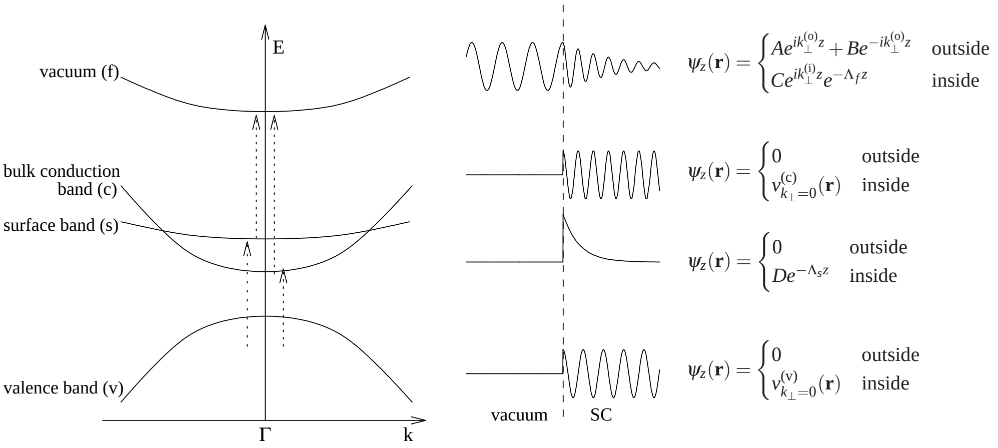

Figure 1.4: *Band structure and simplified z-component of the wave functions for the Indium-Phosphide (100) surface.*

of the matrix elements, the surface (at $z = 0$) is modelled by an abrupt decay at the surface for the bulk bands and the surface band (which means for the bulk bands that the effect of surface is neglected) and by coupling to an external plane wave via the formulation of transmission and reflection rates for the vacuum band. For a "realistic" choice of parameters, the exponential decay rates used in this model are introduced heuristically by extracting a decay factor from the presumed surface states in a corresponding density-functional theory calculation [ZBG$^+$04, ZBFK05] for the surface band or by a reasonable choice of the penetration depth of free-electron states into a solid for the vacuum band [ZBFK05]. For this direct semiconductor, all wave functions of the bands (with a two-dimensional dependency on $\mathbf{k}$ for the surface and vacuum bands and a three-dimensional dependency on $\mathbf{k}$ for the other bands) are approximated by the wave function at $\mathbf{k} = 0$, as it is a common choice in nanostructure physics of two-dimensional systems (as in quantum wells [But07]).

From these definitions, matrix elements for the optical excitation and for the relaxation (via LO-phonons and Fröhlich-coupling) can be derived. While the electron-phonon interaction between the two bulk bands evaluates to standard matrix elements $D^{\text{val/cond}}_{\mathbf{k},\mathbf{k}',\mathbf{q}}$ which are known from bulk parameters, the situation is more complicated for the two-dimensional bands. For the matrix elements from the surface band to the vacuum band (here, only the optical interaction is relevant, as phononic relaxation does not occur into and inside the vacuum states), also simple expressions are found. For the transitions from bulk to surface and to vacuum however, the formulation of a coherent expression is not possible based on the given assumptions, as the wave functions are defined for different dimensionalities. By interpreting the exponential decay shapes as an envelope to an underlying three-dimensional bulk wave, analytical expressions based on the bulk matrix elements and the decay rates can be deduced, e.g. the matrix element for a transition from the bulk conduction band to the surface band reads:

$$D^{\text{cond/surf}}_{\mathbf{k},\mathbb{k}',\mathbf{q}} = \sqrt{\frac{e^2\hbar\omega_{\text{LO}}}{2V\varepsilon_0\varepsilon_{\text{phon}}}}\,\delta_{\mathbb{k}',\mathbf{k}+\mathbf{q}}\frac{i\Lambda_s^{1/2}}{q_z - k_z + \frac{i\Lambda_S}{2}}D^{\text{cond/surf}} \tag{1.1}$$

Here, ω_{LO} is the optical phonon frequency, $\varepsilon_{\text{phon}}$ the effective permittivity due to the Fröhlich-

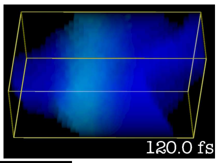

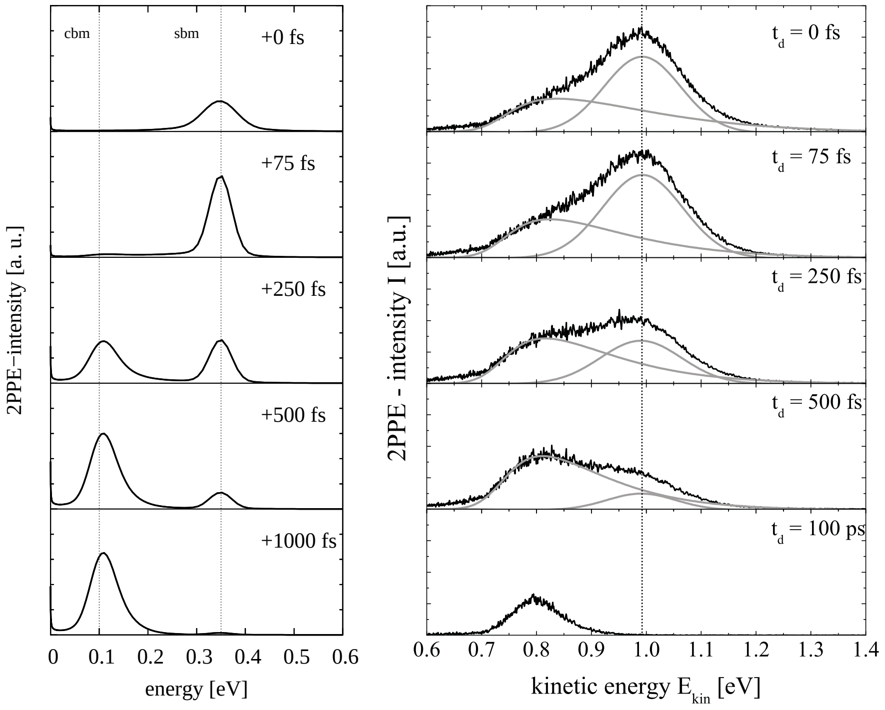

Figure 1.5: *Comparison of theoretical and experimental relaxation at the InP (100) surface. The theoretical data are simulated with the simplified four mode model (Fig. 1.4), the experiment is performed with a two-color-two-photon-photoemission setup. From [TGE$^+$05].*

coupling, V the unit cell volume and Λ_s the surface state decay rate towards the bulk[2]. Analogous to the models used in density-matrix theory [But07], the matrix element constant $D^{\text{cond/surf}}$ is given by the three dimensional overlap of the Bloch waves for the conduction bulk and surface bands:

$$D^{\text{cond/surf}} = \int_\Omega d^3r \bar{u}_0^{\text{cond}}(\mathbf{r}) u_0^{\text{surf}}(\mathbf{r}). \tag{1.2}$$

With respect to surface theory, this is a dubious assumption, as the decay of the states near the surface needs not necessarily extend to multiple bulk unit cells. It is also obvious that the suppression of surface effects in the bulk wave functions can lead to a strong deviation from the realistic values even if the exponential decay of the surface state is a good approximation.

As result, the theoretical photoemission spectrum can be calculated time resolved by drawing the population of the vacuum state on an energy axis. In Fig. 1.5, the relaxation simulated with the four-band model is compared to the experimental results from [TGE$^+$05]. It is obvious that the qualitative features of the relaxation are in a good agreement: the shape and position of the peaks and the temporal evolution are quite congruent. A discrepancy is found in this superficial comparison for the first timesteps (while in experiment, the peak at lower energy,

---

[2] The following material parameters are used for this calculation: valence band min. 0 eV, conduction band min. 1.339eV, surface band min. 1.589eV, vacuum band min. 7.7eV, effective masses: $m^v_{\text{eff}}=-0.45\ m_e$, $m^c_{\text{eff}}=0.078\ m_e$, $m^s_{\text{eff}}=0.2\ m_e$, $m^f_{\text{eff}}=1.0\ m_e$, surface band damping $\Lambda_s = 0.5\text{nm}^{-1}$, vacuum band penetration depth $\Lambda_f = 2.4\text{nm}^{-1}$, $\varepsilon_0=9.52$, $\varepsilon_\infty=12.35$, T=300K, Phonon energy 43meV, dipole matrix elements: val./cond. 0.3 e nm, val./surf. 1.2/0.0 e nm, cond./vac.=0.3 e nm, surf./vac.=0.09 e nm . Cmp. [ZBFK05].

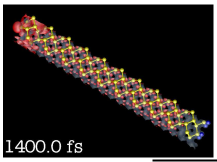

corresponding to the conduction bulk band minimum, is pronounced for every timestep, it appears only after 250 fs of relaxation in the simulation), and in the relation of the heights of the two peaks (here, in the experiment, the higher energy peak is more pronounced, while this holds for the lower energy peak in the simulation). The biggest handicap in this comparison is however the fact that the same timescale in the theoretical and experimental relaxation can only be found by artificially augmenting the size of the wave function overlap $D^{\mathrm{cond/surf}}$ (Eq. 1.1, which are theoretically limited by the *Cauchy-Schwartz-equation*, restricting the scalar product of two wave functions to one) to a value of 4. This is far from a physically reasonable choice, as the value of this matrix element is rather expected to be fairly below one.

As a conclusion, we can state that the "classical" modelling for quantum-heterostructures is insufficient for the description of surface structures. A reason for this is that while in a quantum well, the band structure is accurately defined by a few parameters (as the reduced bulk masses of the compound materials and the thickness of the layers) and a lot of information about an electron state can be extracted from the same parameters (like the envelope function in the confinement direction), nothing is known about the electronic structure at a surface from pure bulk data, and even if the bandstructure could be parametrized, no coherent information could be extracted from it for the electronic wave functions and without a time-consuming solution of the Hamiltonian. As a consequence, it appears favorable to persecute an approach of calculating the electronic band structure and the corresponding wave functions by an *ab-initio* method, as it was proposed in Sec. 1.1 and in the following parts of this thesis.

1.4 Other approaches for the investigation of optical excitation or phonon-induced relaxation

In this section, we will present two methods which have been used to model similar processes as presented in Sec. 1.1 and Sec. 1.3. Most methods are based on density-functional calculations. We can however state that none of the methods in this section provides a general framework open for the inclusion of additional interactions on a truly quantum-physical basis, or a coherent connection of the relaxation processes to macroscopical temperatures (which implies the unambiguousness of the final state after relaxation). This doesn't put the applicability of the presented methods for specific situations into question.

1.4.1 Quasi-particle corrections to the band structure

While formally higher order correlation effects are described within the theoretical formulation of density-functional theory, most practically used functionals (in particular the local-density approximation, cmp. Sec. 3.3) combined with the *Kohn-Sham-equations* lack an appropriate description of such effects. For semiconductors, where the valence and conduction bands are separated by the band gap, one effect of this somewhat reduced formulation manifests in an often underestimated *Kohn-Sham* bandgap energy as a result of the DFT calculation. This is mainly due to neglecting polarization effects, which can be introduced as energy corrections stemming from quasi-particles formed of an excited electron in the conduction bands and a missing electron (hole) in the valence bands having a high binding due to their complementary charges (it should be mentioned that basically all electrons can form quasi-particles with electron (or holes) in other states, however, they are not necessarily strongly bound).

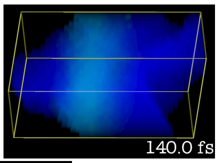

An alternative to the standard density-functional theory which is able to to introduce such quasi-particle corrections has been formulated in the GW-approach by [Hed65]. In their approach, which is based on a *Green's function formalism*, they introduce a variational principle to formulate equations for the microscopical permittivity and the self-energy of the electrons in a structure. For the resulting equations, a perturbation expansion using *Dyson's equation* is derived. As an input to the GW-formalism, *Kohn-Sham* eigenvalues and the corresponding eigenfunctions as a result of a density-functional calculation can be used. The result of a GW-calculation is an adjustment of the *Kohn-Sham eigenvalues*, in the the first order approximation this is usually denoted as G_0W_0, as the correction to the eigenvalues are directly computed from the *Green's functions* based on the initial *Kohn-Sham* eigenfunctions.

The GW-approach is one of the standard methods of structure analysis [ORR02], widely used for the calculation of optical spectra [DG93, ARSO98] and often very accurate [RQN$^+$05]. For surface structures the application of the formalism is not always possible, especially if they are metallic. The relatively high computational effort necessary for the GW-calculation makes it furthermore impossible to use the formalism in slab structures with too many layers (cmp. Sec. 5.2), so often, in such a context, it has to be decided whether it is more desirable to have a calculation with a small slab, but an accurate band structure for only a few bands (what can make the bandstructure too unprecise for the description of the surface) or a calculation with a big slab and an uncorrected band structure for many bands (cmp. Figs. 5.6-5.11).

A drawback of this statical form of quasi-particle correction is that the implicit dynamical properties of quasi-particles, especially of the energetically relevant excitons, are neglected in favor of the computation of aa final state after long-time "relaxation" of the quasi-particles. This is doubtlessly very useful for the derivation of the optical spectra, but in the context of this thesis, with the aim to discuss the phonon-induced relaxation on a picosecond timescale, a discussion of the electron-phonon interaction leading to dynamical processes is needed in the time domain. Additionally, the dynamics might depend on exciton formation. While exciton formation and dynamics can be discussed in the energy domain – similar to the GW-formalism – by employing the *Bethe-Salpeter-equation* [WRKP05], it is likely that it interacts with the phonon relaxation and thus must be discussed dynamically, e.g. within density-matrix theory by an appropriate Hamiltonian. On the other hand, no method has been found to implement a phononic relaxation beyond phenomenological theory into the combined DFT/GW/Bethe-Salpeter-approach, so an discussion of dynamics on another basis cannot be avoided in this context.

In silicon, calculations on the basis of the GW-formalism have been performed in various contexts, different works have been published about the (100) surface [KP95, FP95, RBK95, SSB04, Egg05, SS06] and its reconstructions. For silicon (amongst other semiconductors), it has been found that the corrections of the bandgap are quasily constant throughout the whole Brillouin zone, the GW-correction falls back to a simple augmentation of all conduction band energies about a certain constant value. As a consequence, also the corrections to the *Kohn-Sham-states* are usually $\mathbf{k}$-independent (or even vanish). This procedure is usually denoted as *scissors-shift* of the band structure. In the calculations described in Chapter 7, we apply such a scissors shift, as there is no known alternative method (besides a full implementation of dynamical quasi-particle interaction) to obtain a fairly realistic band structure from the demonstrably incorrect result of a density functional calculation within the *local-density* approximation[3].

---

[3] The local-density approximation cannot generally give correct results for the bandstructure calculation, as some features are unrealistic, e.g. the lack of self-interaction in the functional and the missing $\delta V/\delta n$-discontinuity.

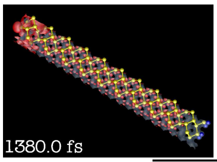

1.4.2 Time-dependent density-functional theory

A different extension to density-functional theory is the integration of dynamical evolution of the electron state into the formalism [RG94]. A time-development of the electron distribution can only expected in a non-equilibrium environment, thus, this approach requires the adaption the ground state formulation in DFT towards a non-equilibrium behaviour. While optical excitation can be considered by dipole coupling to a classical field, the strength of this approach lies in the consistent dynamical calculation of electronic and lattice properties: Through the electronic density distribution known at every timestep, also the system of ions can be dynamically evolved on the basis of the classical forces. By this, it is possible to trace the lattice vibrations without the need to apply a phonon formalism, such that the dynamics is not restricted to linear approximations. This formalism is used in various contexts, e.g. for molecular vibrations, and has also been applied to the time-evolution of the silicon (001) surface [vHLP05].

In comparison to the dynamical formalism in this thesis, the evidence of a time-dependent density-functional approach is based on a different level. While the dynamical evolution in the energy-space, based on the population of particular electron states based on a pure quantum-dynamical description, is in the foreground in the density-matrix formalism, the calculation of the dynamical development of an electron distribution and a more or less classical evolution of the lattice is performed in TDDFT. While the integration of quantum-coherence effects is one of the central points in DMT, this is not directly possible in TDDFT. On the other hand, TDDFT allows a much more detailed analysis of the nature of lattice vibrations, which can be of interest for the investigation of surface dimer vibrations not necessarily in a harmonic potential (cmp. Fig. 1.2). However, the dissipation process to finally cool the lattice vibrations into an equilibrium distribution is still unsatisfactory for TDDFT, while it is an intrinsic property of the density-matrix formalism through the bath hypothesis (cmp. Sec. 4.2.3).

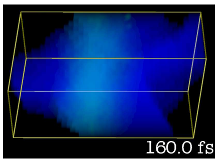

Part I

Theoretical Foundations

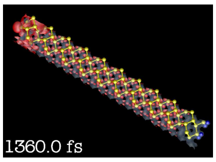
1360.0 fs

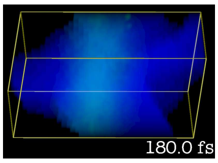

Chapter 2

Time dependent quantum theory

The electronic properties of a solid state material under non-equilibrium conditions have to be described in many-particle quantum theory due to the existence and interaction of many electrons and nuclei. In this chapter, the basic concepts of quantum theory incorporating non-equilibrium dynamics are presented. The basic idea of our approach is to use a two step approach by dividing the statical contributions of the Hamiltonian (which then can be calculated using an *ab-initio* approach, Chapter 3) from the dynamical non-equilibrium contributions (using density-matrix theory, Chapter 4).

2.1 Schrödinger picture vs. Heisenberg picture

A quantum system is described by a Hamiltonian H [Sch02, SW93, CTDL07]. The Hamiltonian incorporates a kinetic energy term T and a potential V:

$$H = T + V. \tag{2.1}$$

While T is generally time independent, V might explicitly depend on time. The state $\Phi_S(t)$ of the quantum system is found by solving the fundamental time-dependent *Schrödinger equation*:

$$i\hbar\frac{\partial}{\partial t}\Phi_S(t) = T\Phi_S(t) + V\Phi_S(t). \tag{2.2}$$

Contributions to V can usually be obtained by taking a classical potential a transcribing all contained observables (e.g. electron density or position) to quantum mechanical operators.

A physically identical formulation of a quantum system can be achieved by transforming the operators and wave functions with an unitarian operator $U(t,t_0)$. By applying the time-development operator

$$U(t,t_0) = e^{-i\hbar\int_{t_0}^{t} H(t')dt'}, \tag{2.3}$$

we obtain an alternative description, where the quantum state $\Phi_H = U(t,t_0)\Phi_S(t)$ is no longer time dependent. The temporal development of the quantum system is now uniquely determined by the operators. Corresponding to the *Schrödinger-equation* (2.2), the dynamical evolution of the operators is determined by the *Heisenberg-equation* of motion for an operator O:

$$i\hbar\frac{\mathrm{d}}{\mathrm{d}t}O = [\mathscr{H}, O] + i\hbar\frac{\partial}{\partial t}O. \tag{2.4}$$

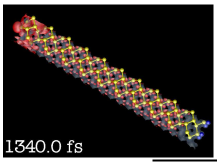

By now, no special assumptions about the many-particle quantum system have been used to develop the equations. The kinetic energy operator T of an n-particle quantum system is usually decomposed into a sum of single-particle kinetic energy operators:

$$T = \sum_i -\frac{\hbar^2}{2m_i}\Delta_{\mathbf{r}_i}. \tag{2.5}$$

The potential energy operator V, however, can generally not be treated in a similar way, as all inter-particle potentials are also described by this part of the Hamiltonian. Nevertheless, it can be split into a decomposable part (e.g. a static external or background potential) and an interaction part:

$$V = \sum_i v_i(\mathbf{r}_i) + V_{\text{int}}(\mathbf{r}_1, ..., \mathbf{r}_n), \tag{2.6}$$

where the $v_i(\mathbf{r}_i)$ now only depend on the coordinate of a single particle. Furthermore, the interaction potential V_{int} can be interpreted in terms of a statical part $V_{\text{int}}^{\text{stat}}$ and a dynamical part $V_{\text{int}}^{\text{dyn}}$. The idea of splitting-up the potential is to separate the parts that contribute to the equilibrium state of the system from those which only have an effect in the case of a non-equilibrium electron population. The latter can be either understood in terms of an excitation potential (e.g. coupling to an electromagnetic field) or a relaxation potential which tends to restore the equilibrium state. The Schrödinger equation of the statical part can then be solved by an adapted method (cmp. Chapter 3) using the statical Hamiltonian

$$H^{\text{stat}} = T + \sum_i v_i(\mathbf{r}_i) + V_{\text{int}}^{\text{stat}}, \tag{2.7}$$

whereas in the dynamical part, the remaining dynamical contributions to the Hamiltonian are treated as a perturbation to the statical part by an appropriate approach (cmp. Chapter 4):

$$H^{\text{dyn}} = H^{\text{stat}} + V_{\text{int}}^{\text{dyn}}. \tag{2.8}$$

In addition to those potential related assumptions, also simplifications are applied to the wave functions. Corresponding to the decomposition of the statical potential in (2.6), we approximate the many-particle wave function $\Phi(\mathbf{r}_1, ..\mathbf{r}_n)$ by a totally antisymmetric product function, where the wave functions $\phi_i(\mathbf{r})$ of the single-particle states of an effective single particle Hamiltonian occur. This can be expressed in terms of the *slater-determinant*:

$$\Phi(\mathbf{r}_1, ..., \mathbf{r}_n) = \frac{1}{\sqrt{n!}} \begin{vmatrix} \phi_1(\mathbf{r}_1) & \cdots & \phi_n(\mathbf{r}_1) \\ \vdots & \ddots & \vdots \\ \phi_1(\mathbf{r}_n) & \cdots & \phi_n(\mathbf{r}_n) \end{vmatrix} \tag{2.9}$$

It is obvious that this simplification is no constraint for a quantum system that only contains a potential which can be split into single contributions depending on a single coordinate without interaction terms. Within the interaction contribution of the potential, on the other hand, this approximation has to be justified for the particular system.

2.2 Quantum field theory – canonical quantization procedure

The formalism introduced in Sec. 2.1 suffices to describe a quantum system with a fixed particle number and a given set of quantum states. If, however, a quantum statistical discussion is

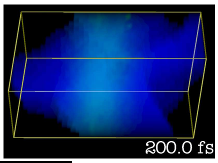

necessary or the number of particles varies, the formalism has to be extended. The canonical way to find a many particle description is to apply a canonical field quantization procedure to the quantum fields in the Hamiltonian, which also provides the possibility to treat quasi-particles (like excitons, phonons) or massless particles (like photons) quantum mechanically (usually this is referred to as *second quantization*). The canonical prescript to quantize a system is as follows:

1. From a known wave equation $W(\xi_i, \dot{\xi}_i, \nabla\xi_i, t) = 0$ (this can be for example a *Schrödinger equation*, an electromagnetic wave equation, a phonon dispersion), a *Lagrange*-density $\mathscr{L}$ [BD65, Büc04] is constructed to fulfill the variational equation

$$W(\xi_i, \dot{\xi}_i, \nabla\xi_i, t) = \partial_t \frac{\partial \mathscr{L}}{\partial(\partial_t \xi_i)} + \sum_{j=1}^{3} \partial_j \frac{\partial \mathscr{L}}{\partial(\partial_j \xi_i)} - \frac{\mathscr{L}}{\xi_i} = 0. \tag{2.10}$$

2. A canonical momentum for the field variable ξ_i is defined by

$$\pi_i = \frac{\mathscr{L}}{\partial(\partial_t \xi_i)}. \tag{2.11}$$

Using this momentum, we can formulate a Hamiltonian density

$$\mathscr{H} = \sum_i \pi_i \partial_t \xi_i - \mathscr{L} \tag{2.12}$$

and a Hamilton-Function

$$H = \int \mathrm{d}\mathbf{r}^3 \mathscr{H}. \tag{2.13}$$

The field variables ξ_i are now interpreted as field operators Ξ_i, which is achieved by introducing fundamental commutation relations for the field operators, which correspond to classical Poisson-braces**Poisson braces** for the field functions [BD65]. The character of the particle described by Ξ_i determines the choice of a commutator $[O, O']_- = OO' - O'O$ for bosons or an anticommutator $[O, O']_+ = OO' + O'O$ for fermions:

$$[\Xi_i, \Pi_j]_\pm = \delta_{ij} \tag{2.14a}$$

$$[\Xi_i, \Xi_j]_\pm = 0 \tag{2.14b}$$

$$[\Pi_i, \Pi_j]_\pm = 0 \tag{2.14c}$$

By this step, the Hamilton-function is transformed into a Hamilton-operator. The time-development of observables can then be evaluated using the *Heisenberg-equation* (2.4), as the field operators Ξ_i are now canonically in the *Heisenberg-picture* (Sec. 2.1).

A usually more convenient representation of the quantum fields can be obtained by performing a mode expansion. The field function $\xi_i(t, \mathbf{r})$ and the corresponding field operators Ξ depend on time and location. On the other hand, solving the field equation (2.10) for a field variable ξ into a complete set of complex modes, the mode operators $m_k^\dagger(t)$ and $m_k(t)$ can be defined

$$\Xi_i(\mathbf{r}, t) = \sum_k \left(f_r^1 \xi_i^k(\mathbf{r}) m_k + f_i^1 (\xi_i^k)^*(\mathbf{r}) m_k^\dagger \right) \tag{2.15a}$$

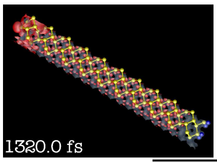

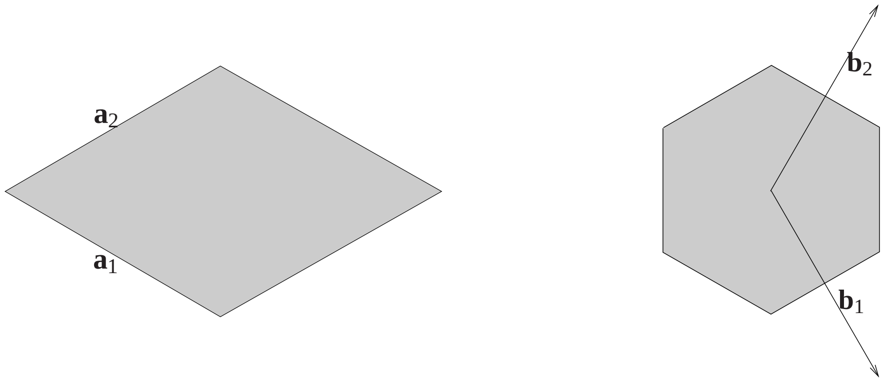

Figure 2.1: *Example of a two dimensional hexagonal unit cell (lhs) and the corresponding reciprocal lattice vectors and first Brillouin zone (rhs)*

$$\Pi_i(\mathbf{r},t) = \sum_k \left(f_r^2 \xi_i^k(\mathbf{r}) m_k + f_i^2 (\xi_i^k)^*(\mathbf{r}) m_k^\dagger \right) \tag{2.15b}$$

and the new commutation relations for the mode operators are then given by

$$[m_k, m_l^\dagger]_\pm = \delta_{kl}, \quad [m_k^\dagger, m_l^\dagger]_\pm = 0, \quad [m_k, m_l]_\pm = 0. \tag{2.16}$$

The choice of the factors f_r^1, f_i^1, f_r^2 and f_i^2 depends on the character of the fields ξ_i. For a classical real field for example, we have $f_r^1 = 1$, $f_i^1 = 1$, $f_r^2 = i$ and $f_i^2 = -i$. The correct commutator depends, as in Eqs. (2.14), on the nature of the particle, for fermions, the choice is the anticommutator, for bosons the commutator.

2.3 Quantum physical properties of a regular solid state material

The quantum mechanical properties of periodical systems can be described on a different level of abstraction with respect to a free system [AM81, Czy00]. Periodicity in a solid state material can be expressed through the lattice axes $\mathbf{a}_1$, $\mathbf{a}_2$ and $\mathbf{a}_3$. Inside the parallelepiped spanned by the axes $\mathbf{a}_1$, $\mathbf{a}_2$, $\mathbf{a}_3$, the unit cell of the structure is located, which is repeated in the specific directions with a period of the corresponding lattice vector. Consequently, a lattice vector

$$\mathbf{R}_i \in \{n_1\mathbf{a}_1 + n_2\mathbf{a}_2 + n_3\mathbf{a}_3\} \tag{2.17}$$

points to the identical origins of the lattice. The quantum description of the periodical system with the *Schrödinger equation* can be entirely derived from a single unit cell. Corresponding to this restriction in real space, the area in the according Fourier (or **k**-) space is limited by the reciprocal lattice $\{\mathbf{b}_1, \mathbf{b}_2, \mathbf{b}_3\}$, which is given by the definition

$$\mathbf{b}_1 = \frac{2\pi \mathbf{a}_2 \times \mathbf{a}_3}{\mathbf{a}_1 \times \mathbf{a}_2 \cdot \mathbf{a}_3}, \quad \mathbf{b}_2 = \frac{2\pi \mathbf{a}_3 \times \mathbf{a}_1}{\mathbf{a}_1 \times \mathbf{a}_2 \cdot \mathbf{a}_3}, \quad \mathbf{b}_3 = \frac{2\pi \mathbf{a}_1 \times \mathbf{a}_2}{\mathbf{a}_1 \times \mathbf{a}_2 \cdot \mathbf{a}_3}, \tag{2.18}$$

and the reciprocal lattice vectors are then – similarly to Eq. (2.17) – defined by

$$\mathbf{G}_i \in \{n_1\mathbf{b}_1 + n_2\mathbf{b}_2 + n_3\mathbf{b}_3\}. \tag{2.19}$$

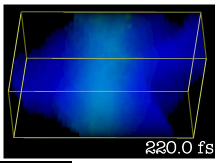

The *first Brillouin zone* can be constructed from the reciprocal lattice vectors as the space which is bound by the condition

$$2\mathbf{k}\cdot\mathbf{G}_i \leq \mathbf{G}_i^2 \tag{2.20}$$

for all $\mathbf{G}_i$. The relations between the real space and $\mathbf{k}$-space representations are illustrated in Fig. 2.1.

The periodicity of the structure implies a translational symmetry in space by the lattice vectors $\mathbf{a}_1$, $\mathbf{a}_2$ and $\mathbf{a}_3$ and their multiples. This property can be expressed by introducing a *translation operator* $\mathscr{T}_{\mathbf{R}}$

$$\mathscr{T}_{\mathbf{R}} f(\mathbf{r}) = f(\mathbf{r}+\mathbf{R}) \tag{2.21}$$

which can be defined by

$$\mathscr{T}_{\mathbf{R}} = e^{\mathbf{R}\cdot\nabla}, \tag{2.22}$$

such that periodicity is established when $\mathscr{T}_{\mathbf{R}_i}$ and H commute, and for normalization, all valid eigenfunctions of H must also be eigenfunctions of $\mathscr{T}_{\mathbf{R}_i}$ to an eigenvalue with a modulus of one.

2.3.1 Two dimensional systems

The three-dimensional definitions in Eq. (2.18) can in principle be formulated for a system where phase space of the electrons is of lower dimensionality [BE88, Lüt93, Bec03, DS96]. This can be either a restricted system (like a quantum well or a quantum dot) or a naturally low dimensional system (like a graphene-sheet). In this context, the surface structures have a special status, because although the symmetrical properties are those of a two-dimensional system, it is in fact three-dimensional, as the third dimension extends on a whole half-space. In numerical calculations, this situation is usually described by a *slab approach*: the surface structure is specified in three dimensions, where the directions parallel to the surface are given in their genuine surface symmetry and the periodicity is used for the corresponding coordinates. The direction perpendicular to surface is described to a certain depth by specifying a finite number of layers and a vacuum layer.

In this thesis, to make a clear distinction between the dimensionalities of differents systems, we introduce a two-dimensional vector

$$\mathbb{v} = \begin{pmatrix} v_1 \\ v_2 \\ 0 \end{pmatrix}. \tag{2.23}$$

In the surface structures, it is assumed that the three-dimensional lattice vector $\mathbf{a}_3$ is always parallel to the z-direction and oriented perpendicular to the surface. It determines the extension of the slab perpendicular to surface, while the other vectors $\mathbf{a}_1$ and $\mathbf{a}_2$ are given by the geometry of the surface elementary cell. Although a three-dimensional Brillouin zone can be defined by these three vectors (using Eq. (2.18)), the discussion of the physical properties is only based on the two reciprocal lattice vectors

$$\mathbb{b}_1 = \frac{2\pi\mathbf{a}_2\times\mathbf{e}_z}{\mathbf{a}_1\times\mathbf{a}_2\cdot\mathbf{e}_z} \quad \mathbb{b}_2 = \frac{2\pi\mathbf{e}_z\times\mathbf{a}_1}{\mathbf{a}_1\times\mathbf{a}_2\cdot\mathbf{e}_z} \tag{2.24}$$

where $\mathbf{e}_z$ is the unit vector in z-direction.

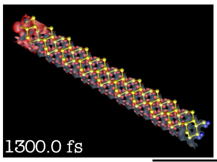

2.3.2 General considerations on electronic properties

A formulation of the statical *Schrödinger-equation* (2.2) with a periodic potential allows to restrict the possible solutions the unimodular eigenfunctions of the translational operator (Eq. (2.21)) [Czy00, AM81]. This is fulfilled by introducing the so-called Bloch-functions

$$\phi_{n\mathbf{k}}(\mathbf{r}) = e^{i\mathbf{k}\mathbf{r}} u_{n\mathbf{k}}(\mathbf{r}), \tag{2.25}$$

where $u_{n\mathbf{k}}(\mathbf{r}) = u_{n\mathbf{k}}(\mathbf{r}+\mathbf{R}_i)$ is a lattice-periodic function. The **k**-vector is an element of the first Brillouin zone Ω (Eq. (2.20)) and constitutes a continuous quantum number additionally to the band index n. It is convenient to describe the periodicity of $u_{n\mathbf{k}}(\mathbf{r})$ by a Fourier series, where the reciprocal lattice is exploited:

$$u_{n\mathbf{k}}(\mathbf{r}) = \sum_{\mathbf{G}} u_{n\mathbf{k}}(\mathbf{G}) e^{i\mathbf{G}\cdot\mathbf{r}}. \tag{2.26}$$

For obvious reasons, orthonormality of these wave functions is no longer constituted on the whole space $\mathbb{R}^3$, but can be defined on the volume of the unit cell $\Omega = |\mathbf{a}_1 \times \mathbf{a}_2 \cdot \mathbf{a}_3|$. The corresponding orthogonality relation is

$$\int_{\Omega} \overline{u}_{n\mathbf{k}} u_{n'\mathbf{k}} = \delta_{n,n'}, \tag{2.27}$$

or, in terms of the Fourier representation 2.26,

$$\sum_{\mathbf{G}} \overline{u}_{n\mathbf{k}}(\mathbf{G}) u_{n'\mathbf{k}}(\mathbf{G}) = \delta_{n,n'}. \tag{2.28}$$

Together with the representation of the electronic waves 2.25, it follows the orthogonality relation

$$\int_{\Omega} \overline{\phi}_{n\mathbf{k}} \phi_{n'\mathbf{k}} = \delta_{n,n'} \delta_{\mathbf{k},\mathbf{k}'}. \tag{2.29}$$

Also the corresponding energy eigenvalues of the *Schrödinger* equation are defined by the two quantum numbers n and **k**:

$$E_{n\mathbf{k}}, \quad \mathbf{k} \in \Omega. \tag{2.30}$$

2.3.3 Vibrations (Born-Oppenheimer approximation)

In principle, the dynamics of both electrons and nuclei are important for the quantum mechanical description of a solid. Nevertheless, the masses of the electrons m and the nuclei M_i and the corresponding kinetic energies are fairly different ($m \ll M_i$). The impact of the nuclear motion on the electrons is much bigger than vice-versa, and the wave functions of the nuclei are much more localized than those of the electrons. The dynamics of the nuclei can be described on a classical basis without restricting the quantum mechanical description of the electrons. This approach is called the *Born-Oppenheimer approximation* [Czy00, SW02]. On the other hand, the nuclear coordinates can be decomposed into

$$\mathbf{R}_i(t) = \mathbf{R}_i\Big|_0 + \mathbf{c}_i(t), \tag{2.31}$$

where the $\mathbf{c}_i(t)$ denote a small deviation from the minimum position of total energy $\mathbf{R}_i|_0$. A perturbation expansion of the *vibrations* $\mathbf{c}_i(t)$ is used to express the potential. Although they

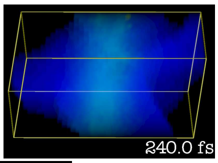

are in principle a discrete set of nuclear elongation coordinates, it is useful to interpret the vibrations as continuous fields $\mathbf{c}_i(\mathbf{r},t)$, where the index now counts the different atomic positions in the unit cell. With this declaration, a quantization procedure (Sec. 2.2) can be applied and they can be described as vibrational quanta *phonons*.

The potential which acts on a nucleus originates mostly from Coulomb interaction (cmp. Sec. 2.3.4). The core electrons are usually bound to the nuclei, such that it is better to refer to the ions as the oscillating particles, although the electrons have practically no effect on the mass. By a series expansion of the ion-ion potential by the vibrational fields at the ion positions, the first order of $\mathbf{c}_i(\mathbf{r},t)$ vanishes due to the placement of the ions near their equilibrium positions (where the total energy reaches is minimum value), such that the first non-vanishing order is the second. As a consequence, the forces on the ions are determined by a superposition of Hooke's law for the neighbouring ions, and the corresponding dynamical equations yield for the ion at position $\mathbf{R}_i$ with mass M_i:

$$M_i\ddot{\mathbf{c}}^i(\mathbf{r},t) = \sum_j D_{\mathbf{R}_i\mathbf{R}_j}\mathbf{c}^j(\mathbf{R}_j+\mathbf{r},t). \tag{2.32}$$

The dynamical matrix $D^{ij}_{\mathbf{R}_i\mathbf{R}_j}$ is given by the second derivatives of the potential between the ion at position $\mathbf{R}_i$ and the ion at position $\mathbf{R}_j$ in the elementary cell.

While the vibrational fields $\mathbf{c}_i(\mathbf{r},t)$ are useful for classical interpretation of the elongations, it is more convenient for quantization and calculus to introduce the normalized complex modes by

$$\mathbf{c}_i(\mathbf{r},t) = \frac{1}{2}\left(\sqrt{\frac{1}{\hbar M_i\omega_i}}\mathbf{s}_i(\mathbf{r},t) + \sqrt{\frac{1}{\hbar M_i\omega_i}}\bar{\mathbf{s}}_i(\mathbf{r},t)\right), \tag{2.33a}$$

$$\dot{\mathbf{c}}_i(\mathbf{r},t) = \frac{1}{2i}\left(\sqrt{\frac{\omega_i}{\hbar M_i}}\mathbf{s}_i(\mathbf{r},t) - \sqrt{\frac{\omega_i}{\hbar M_i}}\bar{\mathbf{s}}_i(\mathbf{r},t)\right). \tag{2.33b}$$

Due to the translational invariance of the periodical structure and the homogeneity of the differential equation (2.31) , the normalized modes have to fulfill the ansatz

$$\mathbf{s}_i(\mathbf{r},t) = e^{i\mathbf{q}\cdot\mathbf{r}-\omega_i t}\mathbf{e}_i, \tag{2.34}$$

where $\mathbf{e}^i$ is the polarization vector for mode i and $\mathbf{q}$ is a vector from the first Brillouin zone. By inserting this into the dynamical equations (2.31), the *secular equation* for the phonon dispersion can be obtained, and by choosing the $\mathbf{e}^i$ as eigenvectors of the dynamical matrix, the phonon dispersion can be calculated from the eigenvalues of $D(\mathbf{q})$:

$$-\omega_i^2 = \mathbf{e}_i\cdot D(\mathbf{q})\mathbf{e}_i. \tag{2.35}$$

The number of phonon modes can be calculated from the number of ions in the unit cell N as $3N$, where a degeneracy of some modes is usual, according to the symmetry of the structure. The first 3 modes, which have $\omega_i(0) = 0$, are called acoustical modes, while the other $3(N-1)$, with $\omega_i(0) \neq 0$, are the optical modes. For a small $\mathbf{q}$, the acoustical modes can be approximated by a linear dispersion with the sonic speed c_i as $\omega_{\text{acoust}} = c_i|\mathbf{q}|$, while optical phonons have a more or less flat dispersion and can often be approximated by a constant $\omega_{\text{opt}} = \omega_0$.

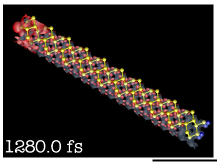

2.3.4 Coulomb interaction

Due to the nature of the electrons and ions in a solid state material as charged particles, the most important interaction is the Coulomb interaction. Inside a solid state material, the classical Coulomb energy for a classical charge distribution $\rho(\mathbf{r})$ is cast into several contributions which take into account the many-particle nature of a solid [SW02, SW93]:

$$
\begin{aligned}
V_{\text{Coul}} &= \frac{1}{2}\int \mathrm{d}^3r \int \mathrm{d}^3r' \frac{e^2}{4\pi\varepsilon_0}\frac{\rho(\mathbf{r})\rho(\mathbf{r}')}{|\mathbf{r}-\mathbf{r}'|}\\
&= \underbrace{\underbrace{\frac{1}{2}\sum_{ij}\frac{e^2}{4\pi\varepsilon_0}\frac{Z_iZ_j}{|\mathbf{R}_i-\mathbf{R}_j|}}_{\text{nucleus-nucleus potential}} + \underbrace{\frac{1}{2}\sum_{i}\int \mathrm{d}^3r\frac{e^2}{4\pi\varepsilon_0}\frac{Z_i\rho_{\text{Core}}(\mathbf{r})}{|\mathbf{R}_i-\mathbf{r}|}}_{\text{nucleus-core electron potential}} + \underbrace{\frac{1}{2}\int \mathrm{d}^3r\int \mathrm{d}^3r'\frac{e^2}{4\pi\varepsilon_0}\frac{\rho_{\text{Core}}(\mathbf{r})\rho_{\text{Core}}(\mathbf{r}')}{|\mathbf{r}-\mathbf{r}'|}}_{\text{Core electron-electron potential}}}_{\text{independent of shell electrons} \mathrel{\widehat{=}} \text{constant}}\\
&\quad + \underbrace{\underbrace{\frac{1}{2}\sum_{i}\int \mathrm{d}^3r\frac{e^2}{4\pi\varepsilon_0}\frac{Z_i\rho(\mathbf{r})}{|\mathbf{R}_i-\mathbf{r}|}}_{\text{nucleus-electron potential}} + \underbrace{\frac{1}{2}\int \mathrm{d}^3r\int \mathrm{d}^3r'\frac{e^2}{4\pi\varepsilon_0}\frac{\rho_{\text{Core}}(\mathbf{r})\rho(\mathbf{r}')}{|\mathbf{r}-\mathbf{r}'|}}_{\text{Core electron-electron potential}}}_{V_S} \qquad (2.36)\\
&\quad + \underbrace{\frac{1}{2}\int \mathrm{d}^3r\int \mathrm{d}^3r'\frac{e^2}{4\pi\varepsilon_0}\frac{\rho(\mathbf{r})\rho(\mathbf{r}')}{|\mathbf{r}-\mathbf{r}'|}}_{\text{electron-electron potential}}.
\end{aligned}
$$

The Z_i refer to the charges of the nuclei, which are assumed as point-like particles, due to their limited extension with respect to the valence electrons. $\rho(\mathbf{r})$ corresponds to the electron-related charges, which can be delocalized in a solid. Usually, a distinct description of core electrons and valence electrons is desirable, as the chemical lattice bonding is mainly related to the valence charges, while the core charges are strongly attached to the nuclei. To this end, a core charge $\rho_{\text{Core}}(\mathbf{r})$ is introduced for the non-valence electrons. The *Born-Oppenheimer approximation* (Eq. (2.31)) is used to separate nuclear and electronic motion by inserting Eq. (2.31). As a consequence, an interaction term of phonons and electrons can be derived by performing a series expansion of the phonon modes $c_i(\mathbf{r},t)$ using a functional derivative (cmp. Sec. B.2.2):

$$
V_S \approx V_S\Big|_{\mathbf{s}=0} + \int \mathrm{d}^3r \sum_i \mathbf{c}_i(\mathbf{r},t)\frac{\delta}{\delta \mathbf{c}_i(\mathbf{r},t)} V_S. \tag{2.37}
$$

The overall Coulomb energy is then given by

$$
\begin{aligned}
V_{\text{Coul}} = & \underbrace{E_0 + \int \mathrm{d}^3r V_{\text{Nucl}}\rho(\mathbf{r}) + \int \mathrm{d}^3r V_{\text{Core}}(\mathbf{r})\rho(\mathbf{r})}_{V_{\text{Lat}}} \qquad (2.38)\\
& + \underbrace{\int \mathrm{d}^3r \sum_i \mathbf{c}_i \frac{\delta}{\delta \mathbf{c}_i}\int \mathrm{d}^3r' V_{\text{Core}}\rho(\mathbf{r}')}_{\text{electron-phonon-coupling}} + \underbrace{\int \mathrm{d}^3r\int \mathrm{d}^3r'\frac{e^2}{4\pi\varepsilon_0}\frac{\rho(\mathbf{r})\rho(\mathbf{r}')}{|\mathbf{r}-\mathbf{r}'|}}_{\text{electron-electron-coupling}},
\end{aligned}
$$

where V_{Lat} is the effective lattice potential including core-electron interaction and nuclear interaction. Using Eq. (B.11), the electron-phonon coupling term can be expressed in terms of

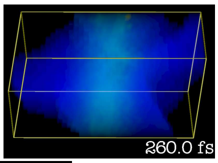

the following formula [SW02]:

$$V_{\text{El-Ph}} = \int \mathrm{d}^3 r \sum_i \Big(\mathbf{c}_i(\mathbf{r},t)\mathbf{D}_i^0(\mathbf{r}) + \frac{\partial \mathbf{c}_i(\mathbf{r},t)}{\partial \mathbf{r}} \mathbf{D}_i^1(\mathbf{r}) \Big) \rho(\mathbf{r}). \tag{2.39}$$

The electron-phonon potential $D_i(\mathbf{r})$ can in some cases be derived microscopically, but can also be treated as parameter.

The transcription of the interaction energy contributions to quantum mechanical quantities is achieved by replacing the electron density function $\rho(\mathbf{r})$ by the electron density operator for a many-particle system

$$\rho(\mathbf{r}) = e \sum_i \delta(\mathbf{r} - \mathbf{r}_i), \tag{2.40}$$

where the $\mathbf{r}_i$ are the coordinates for the N electrons. The energy expectation value is then obtained by calculating the expectation value with the N-particle wave functions (2.9):

$$E_{\text{Coul}} = \langle \Phi | V_{\text{Coul}} | \Phi \rangle. \tag{2.41}$$

The evaluation of this expression for the particular elements in Eq. (2.38) yields, by making use of the orthonormality of the one-particle wave functions $\phi_i(\mathbf{r})$:

$$E_{\text{Lat}} = E_0 + \sum_i \int \mathrm{d}^3 r V_{\text{Core}}(\mathbf{r}) \overline{\phi}_i(\mathbf{r}) \phi_i(\mathbf{r}), \tag{2.42a}$$

$$E_{\text{El-Ph}} = \sum_i \sum_j \int \mathrm{d}^3 r \Big(\mathbf{c}_i(\mathbf{r},t)\mathbf{D}_i^0(\mathbf{r}) + \frac{\partial \mathbf{c}_i(\mathbf{r},t)}{\partial \mathbf{r}} \mathbf{D}_i^1(\mathbf{r}) \Big) \overline{\phi}(\mathbf{r}) \phi(\mathbf{r}), \tag{2.42b}$$

$$E_{\text{El-El}} = \underbrace{\sum_i \sum_j \int \mathrm{d}^3 r \int \mathrm{d}^3 r' \frac{e^2}{4\pi\varepsilon_0} \frac{\overline{\phi}_i(\mathbf{r})\phi_i(\mathbf{r})\overline{\phi}_j(\mathbf{r}')\phi_j(\mathbf{r}')}{|\mathbf{r}-\mathbf{r}'|}}_{\text{Hartree-term}}, \tag{2.42c}$$

$$- \underbrace{\sum_i \sum_{j \neq i} \int \mathrm{d}^3 r \int \mathrm{d}^3 r' \frac{e^2}{4\pi\varepsilon_0} \frac{\overline{\phi}_i(\mathbf{r})\phi_i(\mathbf{r}')\overline{\phi}_j(\mathbf{r}')\phi_j(\mathbf{r})}{|\mathbf{r}-\mathbf{r}'|}}_{\text{exchange term}}.$$

While the existence of multiple electrons in the system has no significance for the E_{Lat} and $E_{\text{El-Ph}}$ contributions, it has an effect for the $E_{\text{El-El}}$ interaction. Here, the term consists of two parts: the *Hartree-term* refers to classical interaction of single electrons, whereas the *exchange term* is due to the fact that Pauli's principle requires a totally antisymmetric wavefunction (Eq. (2.9)). For a single-particle theory, all terms besides the exchange term can be described by a local (multiplicative) interaction term $V(\mathbf{r})$ in the Hamiltonian, while the latter is cast into a non-local (integrative) expression.

2.3.5 Electron-Light coupling

In contrast to the inherent statical Coulomb interaction of the charged particles, the coupling to an external electromagnetic field is included by a U(1)-invariance of the wave function into the Hamiltonian[1] [BD65, AE75, SW93]. The electromagnetic field is expressed by the vector

---

[1] An exact description of the particle-electromagnetic field interaction would require a coherent solution of electromagnetic field equations (Maxwell-equations) inside the material with the boundary conditions given by the external field. Keeping in mind that the light pulse should model a short, weak exposure, our approximations seem tolerable.

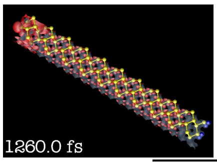

potential $\mathbf{A}(\mathbf{r},t)$, which is set into Coulomb gauge [Jac99]:

$$\nabla \cdot \mathbf{A} = 0, \tag{2.43}$$

and the electrostatic potential $V(\mathbf{r},t)$, which can be cast to zero without loss of generality. The vector potential enters the *Schrödinger* equation through the replacement of the momentum operator $\mathbf{p}$ by

$$\mathbf{p} = \frac{\hbar}{i}\nabla \longrightarrow \frac{\hbar}{i}\nabla - q\mathbf{A}(\mathbf{r},t), \tag{2.44}$$

effecting several contributions to the original equations:

$$i\hbar\frac{d}{dt}\phi(\mathbf{r},t) = -\frac{1}{2m}\left(\hbar^2\Delta - 2q\mathbf{A}(\mathbf{r},t)\frac{h}{i}\nabla + q^2|\mathbf{A}(\mathbf{r},t)|^2\right)\phi(\mathbf{r},t). \tag{2.45}$$

Two approximations are now used with regard to this equation. First, due to the long wavelength of the optical light compared to the typical size of microscopic structures, the spatial dependence of the vector potential can be neglected, so $\mathbf{A}(\mathbf{r},t)$ is expressed as $\mathbf{A}(t)$. This is usually called the *dipole approximation*. As a second approximation the $|\mathbf{A}(t)|^2$-contribution in Eq. (2.45) is neglected, as the fields used in our discussion are rather small and are therefore of minor influence due to the quadratic order.

The use of the vector potential $\mathbf{A}(t)$, which is only given indirectly by the physical observables electrical and magnetical field, is often inconvenient for the description of the optical interaction. An equivalent form of the coupling based on the electrical field can be obtained by applying a U(1)-phase transformation to the wave function in the Schrödinger equation[2] by

$$U(\mathbf{r},t) = e^{\frac{i}{\hbar}q\mathbf{r}\mathbf{A}(t)}. \tag{2.46}$$

The transformed Schrödinger equation then reads

$$i\hbar\frac{d}{dt}\phi(\mathbf{r},t) = -\frac{\hbar^2}{2m}\hbar^2\Delta\phi(\mathbf{r},t) + q\mathbf{r}\mathbf{E}(t)\phi(\mathbf{r},t). \tag{2.47}$$

The most significant difference to Eq. (2.45), besides the emergence of the electrical field $\mathbf{E}(t) = -d/dt\mathbf{A}(t)$, is the appearance of the *dipole operator* $\mathbf{d} = q\mathbf{r}$. It can be shown that under normal conditions, the two formulations (2.45) and (2.47) are quasi identic. To this end, if we look at a matrix element of two arbitrary states $|\phi_i\rangle$ and $|\phi_j\rangle$, which corresponds to an optical transition from state $|\phi_i\rangle$ to state $|\phi_j\rangle$, it can be seen that

$$\langle\phi_i|\mathbf{r}|\phi_j\rangle = \frac{\langle\phi_i|[\mathbf{r},H]|\phi_j\rangle}{E_j - E_i} = \frac{i\hbar}{m(E_j - E_i)}\langle\phi_i|\mathbf{p}|\phi_j\rangle. \tag{2.48}$$

While the pulse is now sufficiently long to ensure a sharp transition ($E_j - E_i \cong \hbar\omega$, where ω denotes the frequency of the light), the two formulations (neglecting the $|A|^2$-term in (2.45)) yield exactly the same expression, as the electrical field is related by derivative to the vector potential.

---

[2] This also implies a gauge transformation of the vector potential $A(t)$ such that $\tilde{A}(t) = 0$.

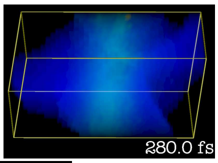

2.3.6 Statical and dynamical system Hamiltonian

By combining the interaction terms in sections 2.3.4 and 2.3.5 with the kinetic energy contribution, the overall Hamiltonian (2.1) can be obtained. As presented in Eq. (2.6), this Hamiltonian is then divided into a statical and a dynamical part. The complete expression for the Hamiltonian is given by

$$H = T + V_{\text{El}} + V_{\text{Phon}} + V_{\text{El-Opt}} + V_{\text{El-Phon}} + V_{\text{El-El}}. \tag{2.49}$$

In our approach, the static contribution to the Hamiltonian is equivalent to the ground state, as we will assume that the final state after relaxation does not differ significantly from the ground state. In the ground state discussion, we will assume that the system is neither perturbed through vibrations nor by optical excitations. The Coulomb-interaction between the electrons, on the other hand, is of course important, but only between the electrons in the ground states, while other electrons are not affected. Consequently, the ground-state Hamiltonian reads:

$$H_{\text{eq}} = T + V_{\text{El}} + V_{\text{eq,El-El}}. \tag{2.50}$$

The remaining terms in Eq. (2.49) are treated in a non-equilibrium approach by second quantization of the electron and vibrational (phonon) fields. The single-particle description of the ground-state theory enables us to interpret the entire ground state Hamiltonian (2.50) as a single-particle Hamiltonian usable for the quantization procedure (Sec. 2.2):

$$H_{\text{noneq}} = H_{\text{eq}} + V_{\text{Phon}} + V_{\text{El-Opt}} + V_{\text{El-Phon}} + V_{\text{noneq,El-El}}. \tag{2.51}$$

The quantization will be performed in Sec. (4.1). While the calculation of the ground state will be elaborated in Chapter 3, the dynamical theory incorporating the non-equilibrium contributions (Eq. 2.51) is discussed in Chapter 4.

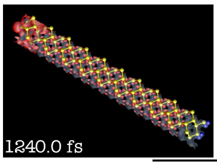
1240.0 fs

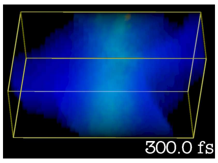

Chapter 3

Basic aspects of Density-Functional Theory

Although there are known numerical approaches to find the solutions of the single particle Hamiltonian (2.50) in an iterative and self-consistent way, the numerical effort is considerable and often too high. Based on the decomposition of the wave functions by a slater determinant (2.9), the electron-electron interaction $V_{\text{el-el}}$ in the Schrödinger equation, is given by two contributions (cmp. Eq. (2.42c)) [Czy00]:

$$V_{\text{el-el}}\phi_i(\mathbf{r}) = \underbrace{\frac{e^2}{4\pi\varepsilon_0}\sum_j \int \mathrm{d}^3r' \frac{\overline{\phi}_j(\mathbf{r}')\phi_j(\mathbf{r}')}{|\mathbf{r}-\mathbf{r}'|}\phi_i(\mathbf{r})}_{\text{Hartree-term}} + \underbrace{\frac{e^2}{4\pi\varepsilon_0}\sum_j \int \mathrm{d}^3r' \frac{\overline{\phi}_j(\mathbf{r}')\phi_i(\mathbf{r}')}{|\mathbf{r}-\mathbf{r}'|}\phi_j(\mathbf{r})}_{\text{exchange-term}}. \tag{3.1}$$

While the Hartree-term can be calculated with justifiable effort due to its dependency from the overall electron density

$$f(\mathbf{r}) = \langle\Phi|\rho(\mathbf{r})|\Phi\rangle = \sum_i |\phi_i(\mathbf{r})|^2, \tag{3.2}$$

the exchange term requires a numerical integration for every wave function $\phi_i(\mathbf{r})$. Apart from the high cost through this calculation step, the scaling in dependence of the size of the system (number of electronic states, discretization) is bad. In spite of the highly increased computational potential in comparison to the past, the systems that can be investigated by this *Hartree-Fock-approach* are still very limited in size.

In 1964, Hohenberg and Kohn [HK64] developed a different approach. Their basic idea was that the ground state of a quantum system is injectively related to the electron density $f(\mathbf{r})$. In the *Hohenberg-Kohn-Theorem*, they have shown that the ground state energy E_0 is an one-to-one mapping of the ground state electron density $f_0(\mathbf{r})$. The proof of this theorem is based on the facts that different ground state energies in a non-degenerate system require different Hamiltonians and that furthermore a difference in Hamiltonians of the form (2.50) with equal electron density can only affect the single-particle potential, because all other contributions rely on the density. The single particle potential, on the other hand, is not influenced by the electronic structure and is non-ambiguous for a system[1]. Hence, the task is to derive a set of

---

[1] It should however be noted that there exist a trivial exception to that statement. The minimum value of the energy has no physical relevance and can be chosen arbitrarily, therefore the ground state energy is only fixed up to a constant. This exception is mentioned in the original Hohenberg-Kohn theorem [HK64].

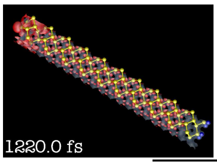

equations that no more rely on the exchange-term of single particle wave functions, but on the particle density $f(\mathbf{r})$.

3.1 Variational principle

From the fact that the ground state energy is un-ambiguous, it follows by the Hohenberg-Kohn theorem that this also holds for the electron density. On the other hand, as the density $f(\mathbf{r})$ can be chosen from a continuous configuration space, the minimum of the ground state functional $E_{\text{Ground}}[f(\mathbf{r})]$ can be found using a variational principle. The electron density at this minimum is then the ground state density. The density can however not be chosen fully independently, but it must reflect the fixed particle number N of the system through

$$\int \mathrm{d}^3r\, f(\mathbf{r}) = N. \tag{3.3}$$

The variation can now be performed by using the functional derivative (B.3) with the this constraint by introducing Lagrange multiplicators for the constraint conditions:

$$\frac{\delta}{\delta f(\mathbf{r})}\left(E_{\text{Ground}}[f(\mathbf{r})] - \mu \int \mathrm{d}^3r\, f(\mathbf{r})\right) \overset{!}{=} 0. \tag{3.4}$$

By now, no assumptions have been made with respect to the form of the ground state energy E_{Ground} and the electron density $f(\mathbf{r})$. In the spirit of a Hartree-Fock approach, it is now self-evident to propose a partition of the energy in the following way:

$$E_{\text{Ground}}[f(\mathbf{r})] = T_{\text{S}}[f(\mathbf{r})] + E_{\text{Lat}}[f(\mathbf{r})] + E_{\text{H}}[f(\mathbf{r})] + E_{\text{XC}}[f(\mathbf{r})]. \tag{3.5}$$

$T_{\text{S}}[f(\mathbf{r})]$ stands for the kinetic energy of the system of non-interacting electrons, E_{Lat} denotes the statical Lattice potential, and $E_{\text{H}}[f(\mathbf{r})]$ and $E_{\text{XC}}[f(\mathbf{r})]$ represent the Hartree and exchange-correlation energy terms (Eq. (2.42c)). The "correlation" denotes an extension to the pure "exchange" term based on the fact that the product wave function Eq. (2.9) is not exact and doesn't take many-particle effects into account. Such corrections to the one-particle description can be numerically calculated by a many-particle theory (e.g. Green's functions [Hed65]). The first two of those contributions can be expressed by

$$E_{\text{Lat}} = \int \mathrm{d}^3r V_{\text{Lat}} f(\mathbf{r}) \tag{3.6}$$

and

$$E_{\text{H}} = \int \mathrm{d}^3r V_{\text{H}} f(\mathbf{r}) = \int \mathrm{d}^3r \int \mathrm{d}^3r' \frac{e^2}{8\pi\varepsilon_0} \frac{f(\mathbf{r}')f(\mathbf{r})}{|\mathbf{r}-\mathbf{r}'|} \tag{3.7}$$

The electron density $f(\mathbf{r})$ can be interpreted corresponding to Eq. (3.2). By this step, we implicitly assume that the electronic states can be calculated by solving a statical single particle Schrödinger equation for the single particle states in $f(\mathbf{r})$, namely

$$E_i\phi_i(\mathbf{r}) = T\phi_i(\mathbf{r}) + V_{\text{S}}\phi_i(\mathbf{r}). \tag{3.8}$$

Following Eq. (2.5), the one-particle kinetic energy $T = -\hbar^2/2m_e\Delta$, where all statical contributions and contributions from other electrons are now combined in the single-particle potential V_{S}.

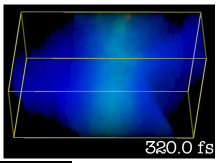

3.2 Kohn-Sham equations

By executing the variations of Eq. (3.5), a set of serviceable equations can be found. This derivation was first performed by W. Kohn and L. Sham in 1965 [KS65], who gave the name to the resulting equations. From Eqs. (3.5) and (3.4), we get the relation

$$0 = \frac{\delta E_{\mathrm{Ground}}}{\delta f(\mathbf{r})} - \mu = \frac{\delta T}{\delta f(\mathbf{r})} + V_{\mathrm{Lat}}(\mathbf{r}) + V_{\mathrm{H}}(\mathbf{r}) + \frac{\delta E_{\mathrm{XC}}}{\delta f(\mathbf{r})} - \mu. \tag{3.9}$$

While the conversion from E_{Lat} to V_{Lat} is a more or less trivial calculation following Eqs. (3.6) and (3.7), no explicit expression for the relation between T and $f(\mathbf{r})$ on the one hand and E_{XC} and $f(\mathbf{r})$ on the other hand is known in advance. Otherwise, by the variation of E_{S}, under the constraint $\int \mathrm{d}r\, f(\mathbf{r}) = 1$, we obtain

$$0 = \frac{\delta E_{\mathrm{S}}}{\delta f(\mathbf{r})} - \mu_{\mathrm{S}} = \frac{\delta T}{\delta f(\mathbf{r})} + V_{\mathrm{S}} - \mu_{\mathrm{S}}. \tag{3.10}$$

By subtracting Eqs. (3.9) and (3.10), the kinetic energy T can be eliminated and a definite expression for V_{S} is obtained:

$$V_{\mathrm{S}}(\mathbf{r}) = V_{\mathrm{Lat}} + V_{\mathrm{H}} + \frac{\delta E_{\mathrm{XS}}}{\delta f(\mathbf{r})} + \mu - \mu_{\mathrm{S}}. \tag{3.11}$$

The two constant Lagrange parameters μ and μ_{S} cannot influence a wave function calulated with V_{S} and are suppressed. By this equation, a direct connection between the single particle wave functions ϕ_i and the density-dependent Hartree potential V_{H} and exchange-correlation potential $\delta E_{\mathrm{XS}}/\delta f(\mathbf{r})$ is found. The electron density, however, is related to the wave functions by Eq. (3.2). On this basis it is now possible to express a self-consistent algorithm by a consecutive evaluation of the electron density and the single particle Schrödinger equations (3.8). The conception of such an algorithm is shown in Fig. 3.1.

The ground state energy from these calculations is finally found using Eq. (3.5). We find

$$E_{\mathrm{Ground}} = \sum_i E_i - \int \mathrm{d}^3 r V_{\mathrm{S}}(\mathbf{r}) f(\mathbf{r}) + \int \mathrm{d}^3 r V_{\mathrm{Lat}}(\mathbf{r}) f(\mathbf{r}) + E_{\mathrm{H}} + E_{\mathrm{XC}}. \tag{3.12}$$

By inserting Eq. (3.11), this finally results in

$$E_{\mathrm{Ground}} = \sum_i E_i - \frac{1}{2} E_{\mathrm{H}} - \int \mathrm{d}^3 r \frac{\delta E_{\mathrm{XC}}}{\delta f(\mathbf{r})} f(\mathbf{r}) + E_{\mathrm{XC}}. \tag{3.13}$$

The *Kohn-Sham* equations are generally only valid for the ground state density and the associated lowest single-particle electron states. It is however possible to calculate more states than needed for the ground state in the single particle Schrödinger equation (3.8), but as no Coulomb and exchange interaction is taken into account in Eq. (3.11) for these states (only the ground state density is incorporated), their values are only approximative. In this spirit, is also possible to use a thermal distribution function (*Fermi-function*) for the occupation of the electronic states, this can be important for the investigation of temperature related effects at the *Fermi-level*. For excited states, generally also many-particle-effects of higher order (beyond the exchange-correlation functional), namely quasiparticle interactions (for example *excitons*), are important for the determination of the energy structure.

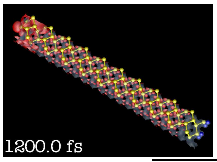

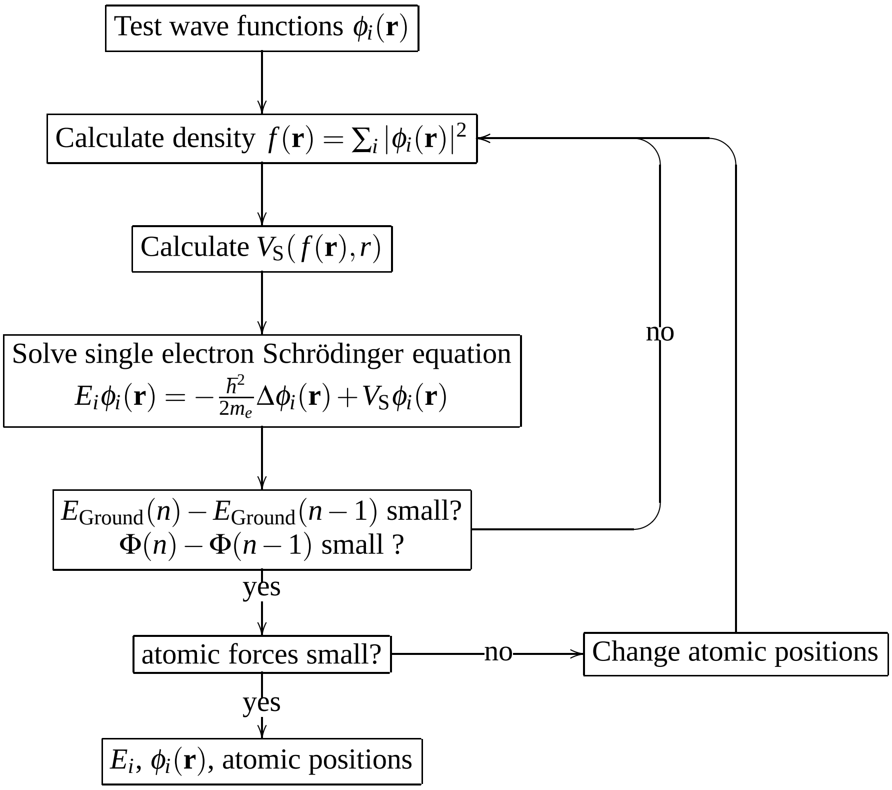

Figure 3.1: *Flow diagram for a typical density-functional calculation run. The initial test functions are usually chosen according to the specific geometrical requirements of the system [BKNS97].*

3.3 Exchange-Correlation functional

While all "classical" interactions for the electrons (V_{Lat}, V_{H}) are implemented exactly in the Kohn-Sham-equations, the crucial point of the theory is the formulation of the exchange-correlation functional E_{XC}. Although the *exchange* part of this functional is conceptionally based on the exchange part in Eq. (3.1), there is no direct analytical transcription of the dependency on the wave functions $\phi_i(\mathbf{r})$ to a dependency on the electron density $f(\mathbf{r})$.

By specific, simplifying assumptions on the electronic system, it is however possible to find approximated expressions for E_{XC}. In the so called *Jellium model*, where the positive charges are introduced as a constant homogenous background charge, it is possible to derive an analytic expression for the exchange term [Czy00]:

$$E_{\text{X}} = \int \mathrm{d}r \left(-\frac{e^2}{16\pi^2\varepsilon_0} (3\pi^2 f(\mathbf{r}))^{\frac{1}{3}} \right) f(\mathbf{r}). \tag{3.14}$$

The E_{C} contribution can only be solved analytically for the special cases $f \to 0$ and $f \to \infty$. Usually, interpolations of numerical simulations of the intermediate densities are used for the calculation. This approach is referred to as the *local-density approximation* (LDA).

We should mention that there are also more elaborated extensions to the local-density approximation. In the *generalized gradient approximation* (GGA), also the dependency on $\nabla f(\mathbf{r})$

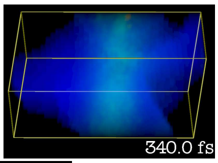

is parametrized in the simulation of the functional. For molecular physics, various functionals are used depending on the purpose.

3.4 Structure relaxation

Although in the derivation scheme of density-functional theory (sections 3.1 and 3.2) the lattice enters as an external statical potential, it is possible to calculate the classical forces on the ions induced by both ionic and electronic forces. If the Ground state energy (depending implicitly on the ionic coordinates through the lattice and core electron potential) is interpreted as a classical potential [Hel37, Fey39], the force on an ion i at position $\mathbf{R}_i$ is defined as

$$\mathbf{F}_i = -\nabla_{\mathbf{R}_i}\left(E_{\text{ionic}} + E_{\text{Ground}}\right). \tag{3.15}$$

The energy E_{ionic} is the classical potential energy of the ion-ion interaction (cmp. Eq. (2.36)). Apart from the discussion in terms of the density in Sec. 3.2, there is also a description in terms of a “Ground state Hamiltonian” as

$$E_{\text{Ground}} = \langle\Phi|H_{\text{Ground}}|\Phi\rangle, \tag{3.16}$$

which can be constructed using Eqs. (3.11) and (3.13). With this identity, we can express the gradient of the ground state energy as follows:

$$\begin{aligned}\nabla_{\mathbf{R}_i}E_{\text{Ground}} =& \nabla_{\mathbf{R}_i}\langle\Phi|H_{\text{Ground}}|\Phi\rangle \\ =& \langle\Phi|\left(\nabla_{\mathbf{R}_i}H_{\text{Ground}}\right)|\Phi\rangle + \left(\nabla_{\mathbf{R}_i}\langle\Phi|\right)H_{\text{Ground}}|\Phi\rangle + \langle\Phi|H_{\text{Ground}}\left(\nabla_{\mathbf{R}_i}|\Phi\rangle\right).\end{aligned} \tag{3.17}$$

After applying the Hamilton operator to $|\Phi\rangle$ and $\langle\Phi|$, the last two terms can be combined:

$$= \langle\Phi|\left(\nabla_{\mathbf{R}_i}H_{\text{Ground}}\right)|\Phi\rangle + E_{\text{Ground}}\nabla_{\mathbf{R}_i}\langle\Phi|\Phi\rangle.$$

By the normation of the electronic wave functions $|\Phi\rangle$, the second term vanishes. In H_{Ground}, only the V_{Lat}-contribution has an explicit dependency on R_i, so we finally conclude the following expression:

$$\mathbf{F}_i = -\nabla_{\mathbf{R}_i}E_{\text{ionic}} - \int \mathrm{d}^3r \nabla_{\mathbf{R}_i}V_{\text{Lat}}\, f(\mathbf{r}). \tag{3.18}$$

Note that the application of the Hamiltonian in Eq. (3.17) is only valid for an electronic system in an eigenstate. Therefore it is important at this point that the electron density entering Eq. (3.18) is well converged towards the ground state configuration. From the knowledge of the forces, ionic moves can be parametrized, leading to a relaxation of the structure towards the ground state equilibrium position. This is only reasonable as an outer loop to an ground state calculation (as in Fig. 3.1). Another application is the computation of a “frozen phonon” spectrum, where the ions are explicitly put into a non-equilibrium position to evaluate their force constants.

3.5 Pseudopotentials

As introduced in Eq. (2.38) the core and valence electrons can be described separately due to the properties of chemical bonding. Hence, it is a convenient way and a good approximation

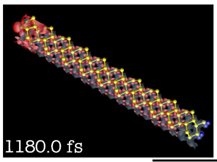

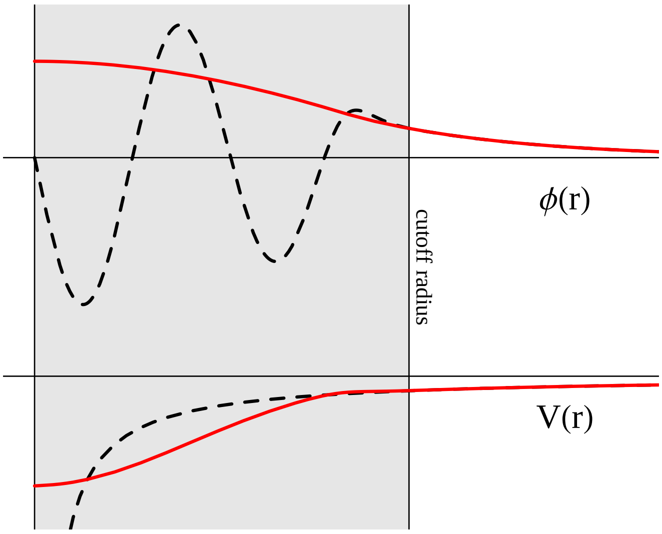

Figure 3.2: *Schematic description of the pseudopotential approximation. The nuclear potential (bottom, black, dashed) is replaced by an effective core potential (red), where the interaction of core electrons incorporated. Outside a cutoff radius, the potentials are equal. This procedure reduces the number of knots of a valence wave function (top; black, dashed: valence wave function for nuclear potential, red: valence wave function for core potential.*

[Ham89] to drastically reduce the computational effort to replace the potentials of the nuclei (which form the basic background lattice potential) by an effective *pseudopotential*, where also the effects of the core electrons are included (Fig. 3.2). An important feature of such a substitution is that the number of knots of a valence wave function is also reduced, as the core electrons are no more considered as solutions of the underlying Schrödinger equation (this, of course, induces an additional reduction of the numerical effort).

The derivation of such a *pseudo-potential*, however, is a non-trivial task, as some requirements are imposed on the type of such a potential function. Apart from the basic request that the potential and the valence wave functions should be identical to the preliminary nuclear solutions outside of a certain cutoff radius, it is also desirable that the charge contained inside the cutoff radius is conserved, or the integral of the valence wave functions over the cutoff radius should remain the same (referred to as "norm conserving pseudopotential").

For the use of a pseudopotential within a density-functional calculation, the interaction of the valence electrons can be subtracted. The transfer from the spherical symmetry of the ionic subsystems to a Cartesian symmetry of a lattice requires furthermore a non-local integration of the pseudopotential which can be treated in a combined local/non-local description [Ham89].

3.6 Calculational aspects of density-functional theory in periodical systems

While so far no assumptions about the nature of the underlying material system are included into the equations, another aspect of using a density-functional algorithm is the choice of the numerical description of the wave functions, densities and potentials. The most significant

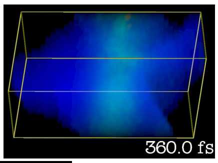

feature of a solid state system is its periodicity (cmp. Sec. 2.3), the wave functions can be expressed explicitly by a form as in Eq. (2.25). The natural choice for the basis of the wave functions in a periodical system is therefore to express the wave functions in terms of the lattice periodic Bloch-waves $u_{n\mathbf{k}}(\mathbf{G})$ (Eq. (2.26)), where

$$\phi_{n\mathbf{k}}(\mathbf{r}) = \sum_i u_{n\mathbf{k}}(\mathbf{G}) e^{i(\mathbf{G}+\mathbf{k})\mathbf{r}}. \tag{3.19}$$

The phase factor $e^{i\mathbf{kr}}$ is only relevant in the description of the wave functions, while all potentials and the electron density are truly lattice periodic and can, as the Bloch-waves (2.26), be described by a fourier series on $\mathbf{G}$. Consequently all equations besides the one-particle Schrödinger equation (3.8) can be entirely formulated with the Bloch-waves $u_{n\mathbf{k}}(\mathbf{G})$, while the latter can be transformed by explicit evaluation of the phase factors into

$$E_{n\mathbf{k}} u_{n\mathbf{k}}(\mathbf{r}) = -\frac{\hbar^2}{2m_e}\left(\mathbf{k}^2 + 2i\mathbf{k}\nabla + \Delta\right) u_{n\mathbf{k}}(\mathbf{r}) + V_S u_{n\mathbf{k}}(\mathbf{r}). \tag{3.20}$$

The two great advantages of the Fourier-series representation are now that some operators used in this Schrödinger equation comply very well with the k-space picture, as they can be expressed much simpler in Fourier space, e.g. the ∇ and Δ operators in Eq. (3.20) become multiplicative, and that the transformation from real space to $\mathbf{k}$ space can by implemented very efficiently by *Fast-Fourier-Transformation*. Hence it is possible to maintain the real space and the $\mathbf{k}$-space representations of the wave functions and the densities in parallel and use for all specific potential contributions the representation that is suitable. With it, the Schrödinger equation (3.20) is again transformed and finally yields

$$E_{n\mathbf{k}} u_{n\mathbf{k}}(\mathbf{G}) = -\frac{\hbar^2}{2m_e}\left(\mathbf{k}+\mathbf{G}\right)^2 + V_{\text{realspace}}(\mathbf{r}) u_{n\mathbf{k}}(\mathbf{r}) + \sum_{\mathbf{G}'} V_{k\text{-space}}(\mathbf{G}-\mathbf{G}') u_{n\mathbf{k}}(\mathbf{G}'). \tag{3.21}$$

The diagonalization of this equation can be performed by an appropriate algorithm, usually an iterative approach is used in this context.

For the use of the Fourier-series in a numerical computation, the choice of a cutoff condition, which limits the number of frequency contributions to the series, is crucial. The most coherent method is to define a cutoff energy E_{cutoff}, so that

$$\frac{\hbar^2}{2m_e}\left(\mathbf{G}+\mathbf{k}\right)^2 \leq E_{\text{cutoff}} \tag{3.22}$$

holds, e.g. only the $\mathbf{G}$-vectors satisfying the condition are considered in the series. By this setting, the shortest wavelength of the spatial oscillations for the wave functions in real space is limited homogeneously for all spatial directions to $\lambda = \sqrt{2m_e E_{\text{cutoff}}}/\hbar$. Another great advantage of the Fourier description is clarified by the following considerations: the number of $\mathbf{G}$-vectors inside the "energy sphere" ((3.22)) can be estimated by the relation

$$n_{\mathbf{G}} \leq \frac{4\pi}{3} \frac{\sqrt{2m_e E_{\text{cutoff}}}^3}{\hbar^3 |\mathbf{b}_1 \times \mathbf{b}_2 \cdot \mathbf{b}_3|}, \tag{3.23}$$

where the range n_1 of $\mathbf{G}$-vectors in the first lattice coordinate is within $\{-E_{\text{cutoff}}/|\mathbf{b}_1|, E_{\text{cutoff}}/|\mathbf{b}_1|\}$ and similarly for the other lattice coordinates (cmp. Eq. (2.19)). In the corresponding

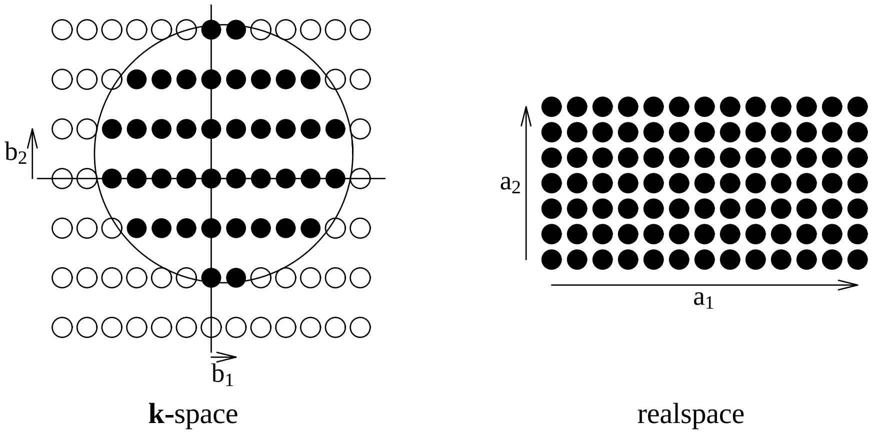

Figure 3.3: *Illustration of the relations between the k-space and real space representations. In k-space, only the points fulfilling the energy condition* (3.23) *(indicated by the black circle) are used for the expansion of the basis, while in real space, all points are required. The energy condition also ensures an equidistant mesh in all directions in real space, whereas in k-space, not the mesh, but the extension is equidistant.*

real space representation with a corresponding number of supporting points, the number of necessary **R**-vectors is given by

$$n_{\mathbf{r}} \geq 8\frac{E^3_{\text{cutoff}}}{|\mathbf{b}_1||\mathbf{b}_2||\mathbf{b}_3|}, \tag{3.24}$$

as basically all real-space points have to be used. The result shows that the description in **k**-space can help to save a considerable amount of memory.

3.7 Structure calculations for surfaces

The calculation of a surface structure according to the slab model (Sec. 2.3.1) affects a breaking of the periodicity in the surface-perpendicular direction. This is in contradiction to the Fourier-series representation of Eq. (3.19), where an explicit periodicity is implied also in that direction. This disaccord can be resolved by the *supercell approach*. The basic idea of this approach is to enlarge the slab unit cell artificially in the z-direction to create a vacuum layer of a certain depth above or below the structure. If the vacuum layer is chosen sufficiently thick, the bound states in the structure (which are the only ones of interest here) decline to zero inside the vacuum. Consequently, no coupling (tunneling) of the electron states can occur between several periodical slabs, and the wave functions are entirely located in z-direction inside a single slab. A direct consequence of this is that the dependency of the wave function on the **k**-vector vanishes in the z-direction: due to the vacuum, the electron problem for the potential $V_{\text{slab}}(z)$ in z-direction can be solved inside the slab without taking the periodicity into account. First, we consider the Hamiltonian in one isolated slab. As the wave functions $\phi_i(z)$ of this problem are bound, a discrete energy E_i spectrum, independent from a continuous wave vector variable k_z, is expected:

$$E_i\phi_i(z) = -\frac{\hbar^2}{2m_e}\Delta\phi_i(z) + V_{\text{slab}}(z)\phi_i(z). \tag{3.25}$$

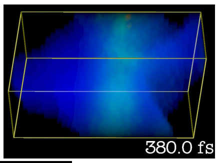

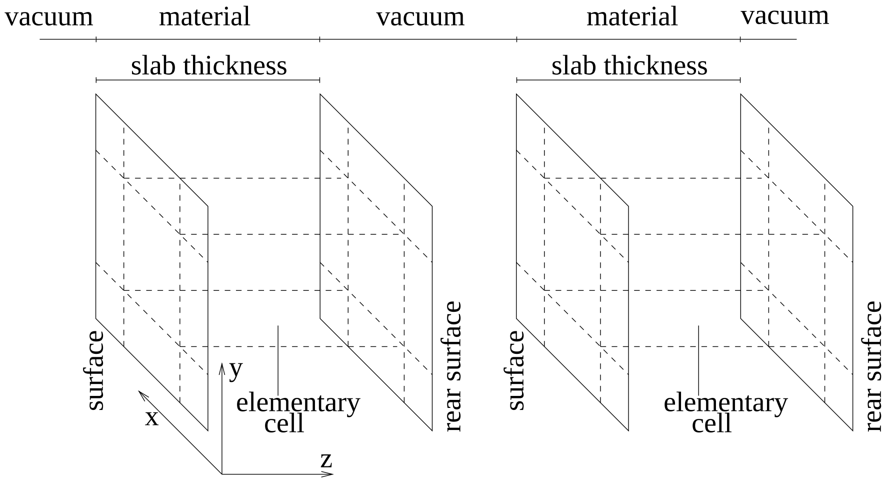

Figure 3.4: *Schema of the supercell model.*

On the other hand, for the repeated slabs, the description from Eq. (3.20) for a Bloch wave function $u_{nk_z}(z)$ must also be valid because of the imposed periodicity by the Fourier expansion:

$$E_{nk_z}u_{nk_z} = -\frac{\hbar^2}{2m_e}\left(k_z^2 + 2ik_z\frac{\partial}{\partial z} + \frac{\partial^2}{\partial z^2}\right)u_{nk_z} + \sum_{k=-\infty}^{\infty} V_{\text{slab}}(z - k|\mathbf{a}_3|)u_{nk_z}. \tag{3.26}$$

Now, as the wave functions are localized and bound to only one of the potentials in the sum in Eq. (3.26), the energy values in Eqs. (3.25) and (3.26) must be the same. This is only possible by choosing u_{nk_z} according to

$$u_{nk_z}(z) = e^{-ik_z\left((z-a_{\text{vac}}) \bmod |\mathbf{a}_3| + a_{\text{vac}}\right)}\,\phi_n(z), \tag{3.27}$$

where a_{vac} is a z-coordinate of a location in the vacuum where the wave function $\phi_n(z)$ vanishes – hence the discontinuity of the exponential does not matter. Consequently, the two representations (3.25) and (3.26) fall back to the same energy values and represent, up to a phase factor which is constant on one slab, the same wave functions. Furthermore, the k_z-dependency has been factored out. As a conclusion, it can be stated that the supercell approach is an extension to the standard density-functional approach for periodical systems. It does not require a change of the code.

The implications of the geometry of the slab, however, require some additional thoughts. Besides the choice of a certain surface orientation, there does not need to be any relation between the symmetries of the underlying bulk system and the slab. The symmetries of the slab mirror the symmetries at surface (in x and y direction), which is often reconstructed and therefore only matches the bulk lattice symmetry by specific integer factors in the lattice directions. This effect, of course, is irrelevant for the lower atom layers in the slab. In the z-direction, there is obviously no symmetry at all under normal conditions. At the “back end” of the slab (denoted as “rear surface” in Fig. 3.4), no surface with reconstruction should be modeled, but it is intended to simulate a preferably smooth transition to the bulk material (cmp. sec 2.3.1). To this end, chemical bondings (which arise from the cut of the structure at the back end) are not left open (as it is the case at the surface – this allows for the reconstruction), but passivated by

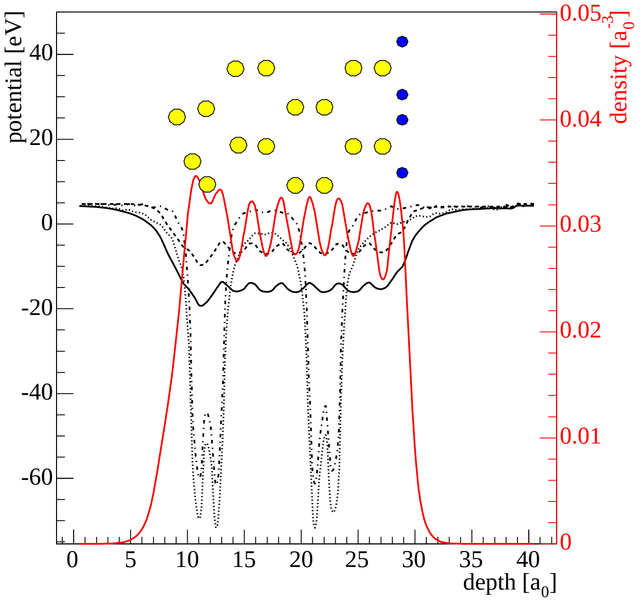

Figure 3.5: *Illustration of the link between atomic positions, electronic potential and particle density $f(\mathbf{r}$ in the supercell approach for a Silicon (100) 2×1 reconstruction. The atomic positions are indicated by the yellow circles (Silicon) and blue circles (passivating Hydrogen). The electronic potential for four different cuts along the z-axis is shown in black, the partially integrated electron density is depicted in red. At the surface (lhs), the tilted dimer reconstruction is clearly observable. In the vacuum zones left and right of the slab, the potential converges to the vaccum level, while the electron density approximates zero.*

geometrically placed protons (≙ Hydrogen ions), which counterbalance the electrical charges and effect a consistent fading out of the wave functions at the rear side. As an example the positions of the atoms, the potential in z-direction and the total electron distribution are shown for a silicon (001) 2×1 surface slab calculation of seven layers in Fig. 3.5.

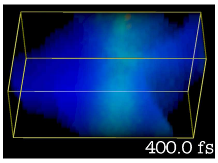

Chapter 4

Density-Matrix Theory

While the density-functional theory presented in Chapter 3 can be employed to investigate the equilibrium properties of a surface system, we will develop equations to examine the dynamical properties in this Chapter [RK02, HJ98]. The approach discussed within density-matrix formalism is based on a canonically quantized description (cmp. Sec. 2.2) of the expectation values of the microscopic population and polarizations. The non-equilibrium dynamics is driven by those parts of the total interaction potential (Eq. (2.49)) which are not contained in the ground state Hamiltonian (Eq. (2.51)). The solutions of the ground state are evaluated using density-functional theory, consequently, the second quantization here will be based on the DFT-solutions of the *Kohn-Sham* equations.

4.1 Canonical Quantization of the system variables

There are three fields occurring in the Hamiltonian which are candidates for a canonical field quantization procedure (Sec. 2.2, [BD65, Hak73, Mah81]): the electronic waves $\phi_{n\mathbb{k}}(\mathbf{r})$, the phonon field $\mathbf{c}^i(\mathbf{r},t)$ and the vector potential $\mathbf{A}(\mathbf{r},t)$. Nevertheless, only the first two of these will be treated in a quantum mechanical way, whereas the latter will be kept in the classical picture.

The global Lagrange-density $\mathscr{L}$ for an interacting single-particle system with electrons obeying the Schrödinger equation and phonons as classical vibrations coupled to electrons is given by

$$\begin{aligned}\mathscr{L} =& i\hbar\phi\frac{\partial}{\partial t}\overline{\phi}+i\hbar\overline{\phi}\frac{\partial}{\partial t}\phi-\frac{\hbar^2}{2m}\nabla\overline{\phi}\nabla\phi-V_{\text{eq}}\overline{\phi}\phi-V_{\text{el-el,noneq}}\overline{\phi}\phi-V_{\text{el-light}}\overline{\phi}\phi \\ &+\frac{M_i}{2}\sum_i\frac{\partial}{\partial t}\mathbf{s}^i\frac{\partial}{\partial t}\mathbf{s}^i-\sum_i\sum_j U^{ijkl}_{\mathbf{R}_j}\mathbf{s}^i_k\mathscr{T}_{\mathbf{R}_i}\mathbf{s}^j_l-\sum_i V_{\text{el-phon}}\mathbf{s}^i\overline{\phi}\phi,\end{aligned} \tag{4.1}$$

where the phonon potential $\sum_i\sum_j U^{ijkl}_{\mathbf{R}_j}\mathbf{s}^i_k\mathscr{T}_{\mathbf{R}_i}\mathbf{s}^j_l$ incorporates the translational operator Eq. (2.21). By applying the generalized Lagrange formalism (Sec. B.3), the Schrödinger equation for the electron fields ϕ, the adjoint Schrödinger equation for the fields $\overline{\phi}$ and the phonon motion equation Eq. (2.32) is obtained again.

The canonical momenta (Eq. (2.11)) for the fields are then given by

$$\pi_\phi = i\hbar\overline{\phi} \tag{4.2a}$$

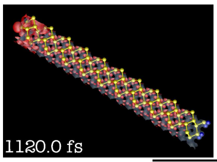

$$\pi_{\overline{\phi}} = i\hbar\phi \tag{4.2b}$$

$$\pi_{\mathbf{s}_i} = M_i \frac{\partial}{\partial t}\mathbf{s}^i \tag{4.2c}$$

and we can calculate the Hamilton density (Eq. (2.12)) as

$$\begin{aligned}\mathscr{H} =& \frac{\hbar^2}{2m}\nabla\overline{\phi}\nabla\phi + V_{\text{eq}}\overline{\phi}\phi + \frac{\hbar}{i}\mathbf{A}\overline{\phi}\nabla\phi + V_{\text{el-el,noneq}}\overline{\phi}\phi \\ &+ \frac{1}{2M_i}\sum_i \pi_{\mathbf{s}^i}\pi_{\mathbf{s}^i} + \sum_i\sum_j U^{ijkl}_{\mathbf{R}_j}\mathbf{s}^i_k \mathscr{T}_{\mathbf{R}_i}\mathbf{s}^j_l + \sum_i \mathbf{D}^i\mathbf{s}^i\overline{\phi}\phi .\end{aligned} \tag{4.3}$$

After transforming the fields to the field operators

$$\begin{aligned}\phi &\rightarrow \Phi & \pi_\phi = \overline{\phi} &\rightarrow \Phi^\dagger \\ \mathbf{s}^i &\rightarrow \mathbf{S}^i & \pi_{\mathbf{s}^i} &\rightarrow \Pi_{\mathbf{S}^i},\end{aligned} \tag{4.4}$$

the Hamiltonian in second quantization can be written down:

$$\begin{aligned}H =& -\frac{\hbar^2}{2m}\int d^3r\nabla\Phi^\dagger\nabla\Phi + \int d^3r V_{\text{eq}}\Phi^\dagger\Phi + \int d^3r\frac{\hbar}{i}\mathbf{A}\Phi^\dagger\nabla\Phi + \int d^3r V_{\text{el-el,noneq}}\Phi^\dagger\Phi \\ &+ \sum_i \frac{1}{2M_i}\int d^3r \Pi_{\mathbf{S}^i}\Pi_{\mathbf{S}^i} + \sum_i\sum_j \int d^3r U^{ijkl}_{\mathbf{R}_j}\mathbf{S}^i_k \mathscr{T}_{\mathbf{R}_i}\mathbf{S}^j_l + \sum_i\int d^3r \mathbf{D}^i\mathbf{S}^i\Phi^\dagger\Phi .\end{aligned} \tag{4.5}$$

Now, mode expansions are applied for the three fields. For the electrons, the mode expansion consists of the ground state wave functions that solve the Schrödinger equation for the ground state Hamiltonian (2.50) and can be obtained as discussed in Chapter 3:

$$\Phi(\mathbf{r},t) = \sum_{n\mathbf{k}} e^{i\omega_{n\mathbf{k}}t}\phi_{n\mathbf{k}}(\mathbf{r})a_{n\mathbf{k}} \tag{4.6a}$$

$$\Phi^\dagger(\mathbf{r},t) = \sum_{n\mathbf{k}} e^{-i\omega_{n\mathbf{k}}t}\overline{\phi}_{n\mathbf{k}}(\mathbf{r})a^\dagger_{n\mathbf{k}} \tag{4.6b}$$

so that the commutation relations for those fermionic *creation* and *annihilation* operators are then given corresponding to Eq. (2.16):

$$[a^\dagger_{n\mathbf{k}}, a_{n'\mathbf{k}'}]_+ = \delta_{nn'}\delta_{\mathbf{k},\mathbf{k}'} . \tag{4.7}$$

For the bosonic phonon modes, the expansion is slightly more elaborate. The complex modes are the same as in Eq. (2.33). The link between these modes and the real field operators is then:

$$\begin{aligned}\mathbf{S}^i =& \frac{1}{2}\sum_{\mathbf{q}}\left(\mathbf{s}^i_{\mathbf{q}}(\mathbf{r})e^{i\omega_{i\mathbf{q}}t}b^\dagger_{i\mathbf{q}} + \overline{\mathbf{s}}^i_{\mathbf{q}}(\mathbf{r})e^{-i\omega_{i\mathbf{q}}t}b_{i\mathbf{q}}\right) \\ \Pi_{\mathbf{S}^i} =& \frac{i}{2}\sum_{\mathbf{q}}\omega_{i\mathbf{q}}\left(\mathbf{s}^i_{\mathbf{q}}(\mathbf{r})e^{i\omega_{i\mathbf{q}}t}b^\dagger_{i\mathbf{q}} - \overline{\mathbf{s}}^i_{\mathbf{q}}(\mathbf{r})e^{-i\omega_{i\mathbf{q}}t}b_{i\mathbf{q}}\right)\end{aligned} \tag{4.8}$$

In this case, the commutators apply for the phonon creators $b^\dagger_{i\mathbf{q}}$ and annihilators $b_{i\mathbf{q}}$:

$$[b^\dagger_{i\mathbf{q}}, b_{i'\mathbf{q}'}]_- = \delta_{i,i'}\delta_{\mathbf{q},\mathbf{q}'} . \tag{4.9}$$

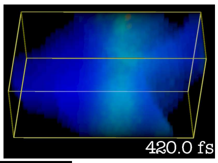

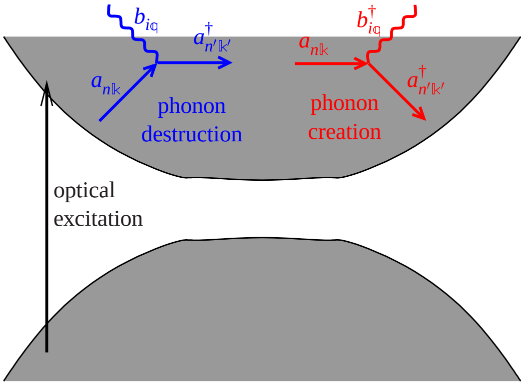

Figure 4.1: *Illustration of the processes treated by the Hamiltonian* (4.11)*. Besides optical excitation, electronic redistribution* $a_{n\mathbb{k}} \to a^\dagger_{n'\mathbb{k}'}$ *by phonon emission* $b_{i\mathbb{q}}$ *or absorption* $b^\dagger_{i,-\mathbb{q}}$ *is considered.*

The time-dependence of the modes can be released by switching to the Heisenberg picture and applying a unitary transformation (2.3) to the electronic and phononic modes and operators. As a result, the operators are now time dependent, while the modes are not. By inserting these complete mode expansions into the Hamiltonian (4.5), the field equations (the Schrödinger equation (2.2) for the equilibrium part and the vibrational wave equation (2.32)) and the completeness can be used and a commonly known simplified form of the Hamiltonian is derived:

$$\begin{aligned} H = & \underbrace{\sum_{n\mathbf{k}} E_{n\mathbf{k}} a^\dagger_{n\mathbf{k}} a_{n\mathbf{k}}}_{\text{Eq. electrons}} + \underbrace{\sum_{n\mathbf{k}} \sum_{n'\mathbf{k}'} \underbrace{\int \mathrm{d}^3 r \overline{\phi}_{n\mathbf{k}}(\mathbf{r}) \frac{\hbar}{i} \nabla \phi_{n'\mathbf{k}'}(\mathbf{r})}_{=\mathbf{p}^{n'\mathbf{k}'}_{n\mathbf{k}}} \mathbf{A}(t) a^\dagger_{n\mathbf{k}} a_{n'\mathbf{k}'}}_{\text{electron-light coupling}} + \underbrace{V_{\text{el-el,noneq}}}_{\text{neglected}} \\ & + \underbrace{\sum_{i\mathbf{q}} \hbar\omega_{i\mathbf{q}} \Big(b^\dagger_{i\mathbf{q}} b_{i\mathbf{q}} + \underbrace{\frac{1}{2}}_{\substack{\text{const. energy}\\ \text{neglected}}} \Big)}_{\text{Eq. phonons}} + \underbrace{\sum_{n\mathbf{k}} \sum_{n'\mathbf{k}'} \sum_{i\mathbf{q}} \underbrace{\int \mathrm{d}^3 r \mathbf{D}^i \mathbf{s}^i_{\mathbf{q}}(\mathbf{r}) \overline{\phi}(\mathbf{r}) \phi(\mathbf{r})}_{=D^{n'\mathbf{k}'}_{\substack{n\mathbf{k}\\ i\mathbf{q}}}} a^\dagger_{n\mathbf{k}} a_{n'\mathbf{k}'} b_{i\mathbf{q}}}_{\text{phonon destruction}} \\ & + \underbrace{\sum_{n\mathbf{k}} \sum_{n'\mathbf{k}'} \sum_{i\mathbf{q}} \underbrace{\int \mathrm{d}^3 r \mathbf{D}^i \overline{\mathbf{s}}^i_{-\mathbf{q}}(\mathbf{r}) \overline{\phi}(\mathbf{r}) \phi(\mathbf{r})}_{=D^{n'\mathbf{k}'}_{\substack{n\mathbf{k}\\ i,-\mathbf{q}}}} a^\dagger_{n\mathbf{k}} a_{n'\mathbf{k}'} b^\dagger_{i\mathbf{q}}}_{\text{phonon creation}} \, . \end{aligned} \tag{4.10}$$

Two contributions in this Hamiltonian are not discussed any further. First, the coulomb interaction between the electrons is neglected during the dynamical evolution of the non-equilibrium system. It is known from the physical properties of quantum heterostructures that the corresponding dynamical effects are rather slow, and furthermore, the deviation from the equilibrium is small, and for an relaxation well above the band edge, excitonic effects can be neglected [Bin92, SKS$^+$96, HKK03]. This behaviour can not be expected for a silicon surface structure, as excitonic effects are visible in the surface dynamics [WKFR04]. Nevertheless, in the current formulation of our theory, we do not consider the coulomb interaction at the surface. The second suppressed term in (4.10) is the $\hbar\omega_{i\mathbf{q}}$ contribution inside the phonon Hamiltonian. Although it supplies a constant contribution of $1/2\hbar\omega_{i\mathbb{q}}$ to total the energy and usually affects the lattice constant by a factor of about 0.05% due to anharmonicity effects of the phonon potential, it has no influence on the dynamics discussed in Sec. 4.2 and can therefore be neglected

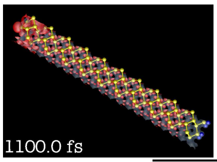

for this part of the discussion.

The interaction matrix elements $\mathbf{p}^{n'\mathbf{k}'}_{n\mathbf{k}}$ and $D^{n'\mathbf{k}'}_{n\mathbf{k};i,\mathbf{q}}$ are entirely determined by the one-particle wave functions. The final goal of this work is the description of a surface structure in the slab geometry (cmp. Sec. 2.3.1), consequently, the three-dimensional **k**-vectors occuring in Eq. (4.10)) can be replaced by two-dimensional ones ($\mathbb{k}$).

With these declarations and after regrouping the last two terms of Eq. (4.10) (where $\bar{\mathbf{s}}^i_{\mathbf{q}}(\mathbf{r}) = \mathbf{s}^i_{-\mathbf{q}}(\mathbf{r})$ due to an internal symmetry of Eq. (2.35)), the resulting Hamiltonian is finally

$$
\begin{aligned}
H = & \sum_{n\mathbb{k}} E_{n\mathbb{k}} a^{\dagger}_{n\mathbb{k}} a_{n\mathbb{k}} + \sum_{i\mathbb{q}} \hbar\omega_{i\mathbb{q}} b^{\dagger}_{i\mathbb{q}} b_{i\mathbb{q}} + \sum_{n\mathbb{k}} \sum_{n'\mathbb{k}'} \mathbf{p}^{n'\mathbb{k}'}_{n\mathbb{k}} \mathbf{A}(t) a^{\dagger}_{n\mathbb{k}} a_{n'\mathbb{k}'} \\
& + \sum_{n\mathbb{k}} \sum_{n'\mathbb{k}'} \sum_{i\mathbb{q}} D^{n'\mathbb{k}'}_{\substack{n\mathbb{k} \\ i\mathbb{q}}} a^{\dagger}_{n\mathbb{k}} a_{n'\mathbb{k}'} \left(b_{i\mathbb{q}} + b^{\dagger}_{i,-\mathbb{q}} \right)).
\end{aligned}
\tag{4.11}
$$

This Hamiltonian is furtheron used to derive the dynamical evolution of the system, which will be outlined in the next section.

4.2 Dynamical equations

In second quantization, all observables are expressed in terms of the creation and destruction operators of the involved quantized fields, notably the electronic operators $a^{\dagger}_{n\mathbb{k}}$ and $a_{n\mathbb{k}}$, and the phononic operators $b^{\dagger}_{i\mathbb{q}}$ and $b_{i\mathbb{q}}$. The observables that give an insight in the dynamical evolution of the system in our case are the electronic density (cmp Eq. (3.2))

$$
f(\mathbf{r}) = \sum_{n\mathbb{k}} \sum_{n'\mathbb{k}'} \bar{\phi}_{n\mathbb{k}}(\mathbf{r}) \phi_{n'\mathbb{k}'}(\mathbf{r}) a^{\dagger}_{n\mathbb{k}} a_{n'\mathbb{k}'}
\tag{4.12}
$$

and the macroscopic polarization, which can be related to electrodynamical Maxwell-material equations,

$$
\mathbf{P}(\mathbf{r}) = \sum_{n\mathbb{k}} \sum_{n'\mathbb{k}'} \bar{\phi}_{n\mathbb{k}}(\mathbf{r}) \phi_{n'\mathbb{k}'}(\mathbf{r}) \mathbf{d}^{n'\mathbb{k}'}_{n\mathbb{k}} a^{\dagger}_{n\mathbb{k}} a_{n'\mathbb{k}'}
\tag{4.13}
$$

with the dipole matrix element $\mathbf{d}^{n'\mathbb{k}'}_{n\mathbb{k}}$, which is bound to the momentum matrix element $\mathbf{p}^{n'\mathbb{k}'}_{n\mathbb{k}}$ by Eq. (2.48). Measurable quantities are given by the expectation values $\langle \psi | O | \psi \rangle$ of these operators. The quantum state $|\psi\rangle$ is not known, it can only be described statistically in terms of the density operator

$$
\rho = \sum_{n\mathbb{k}} p^{n'\mathbb{k}'}_{n\mathbb{k}} |\phi_{n\mathbb{k}}\rangle \langle \phi_{n'\mathbb{k}'}|.
\tag{4.14}
$$

Here, the population polarizations $p^{n'\mathbb{k}'}_{n\mathbb{k}}$ describe the probability to find an electron in the superposition of the two single particle states $|\phi_{n\mathbb{k}}\rangle$ and $|\phi_{n'\mathbb{k}'}\rangle$. For $n = n'$ and $\mathbb{k} = \mathbb{k}'$, this signifies the population probability of the state $|\phi_{n\mathbb{k}}\rangle$, so we make the additional definition

$$
f_{n\mathbb{k}} = p^{n\mathbb{k}}_{n\mathbb{k}}
\tag{4.15}
$$

In an unperturbed system, only these diagonal parts of the density matrix are non-vanishing (pure states). The expectation value of an operator O is then given by

$$
\langle O \rangle = \mathrm{tr}(\rho O)
\tag{4.16}
$$

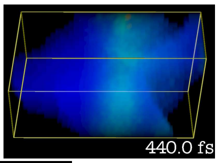

with the trace $\operatorname{tr} O = \sum_i \langle \phi_i | O | \phi_i \rangle$. For the operators $a^\dagger_{n\mathbb{k}} a_{n\mathbb{k}}$ and $a^\dagger_{n\mathbb{k}} a_{n'\mathbb{k}'}$, one obtains the expectation values

$$\langle a^\dagger_{n\mathbb{k}} a_{n\mathbb{k}} \rangle = f_{n\mathbb{k}} \quad \text{and} \quad \langle a^\dagger_{n\mathbb{k}} a_{n'\mathbb{k}'} \rangle = p^{n'\mathbb{k}'}_{n\mathbb{k}}. \tag{4.17}$$

As a consequence, the physically investigatable quantities can be totally expressed in terms of the statistical population densities $f_{n\mathbb{k}}$ and $p^{n\mathbb{k}}_{n\mathbb{k}}$.

4.2.1 General construction scheme and hierarchy problem

The actual dynamics of a second-quantized system in Heisenberg representation can be investigated by evaluating the Heisenberg equations of motion (2.4). By this, the dynamical evolution of operators can be calculated [HK90, Kuh98].

To find the temporal evolution of the electronic density (4.15), we apply Eq. (2.4) with the Hamiltonian (4.11) to the polarization operator $a^\dagger_{n\mathbb{k}} a_{n'\mathbb{k}'}$ and make use of the commutation relations (4.7):

$$\begin{aligned}
i\hbar \frac{d}{dt} (a^\dagger_{m\mathbb{l}} a_{m'\mathbb{l}'}) &= [a^\dagger_{m\mathbb{l}} a_{m'\mathbb{l}'}, H] \\
&= (E_{m\mathbb{l}} - E_{m'\mathbb{l}'}) a^\dagger_{m\mathbb{l}} a_{m'\mathbb{l}'} + \mathbf{A}(t) \sum_{n\mathbb{k}} \left(\mathbf{p}^{n\mathbb{k}}_{m\mathbb{l}} a^\dagger_{n\mathbb{k}} a_{m'\mathbb{l}'} - \mathbf{p}^{m'\mathbb{l}'}_{n\mathbb{k}} a^\dagger_{m\mathbb{l}} a_{n\mathbb{k}} \right) \\
&\quad + \sum_{n\mathbb{k}} \sum_{i\mathbb{q}} \left(D^{m\mathbb{l}}_{\substack{n\mathbb{k}\\ i\mathbb{q}}} a^\dagger_{m'\mathbb{l}'} a_{n\mathbb{k}} (b^\dagger_{i,-\mathbb{q}} + b_{i,\mathbb{q}}) - D^{m'\mathbb{l}'}_{\substack{n\mathbb{k}\\ i\mathbb{q}}} a^\dagger_{m\mathbb{l}} a_{n\mathbb{k}} (b^\dagger_{i,-\mathbb{q}} + b_{i,\mathbb{q}}) \right).
\end{aligned} \tag{4.18}$$

This set of equations is not closed, as these dynamical equations depend on the phonon-assisted density matrices $a^\dagger_{m\mathbb{l}} a_{n\mathbb{k}} b^\dagger_{i,-\mathbb{q}}$ and $a^\dagger_{m\mathbb{l}} a_{n\mathbb{k}} b_{i,\mathbb{q}}$. The dynamics of these quantities can again be found by evaluating the corresponding Heisenberg equations of motion (2.4):

$$\begin{aligned}
i\hbar \frac{d}{dt} (a^\dagger_{m\mathbb{l}} a_{m'\mathbb{l}'} b^\dagger_{i,-\mathbb{q}}) &= [a^\dagger_{m\mathbb{l}} a_{m'\mathbb{l}'} b^\dagger_{i,-\mathbb{q}}, H] \\
&= (E_{m\mathbb{l}} - E_{m'\mathbb{l}'} + \hbar\omega_{i\mathbb{q}}) a^\dagger_{m\mathbb{l}} a_{m'\mathbb{l}'} b^\dagger_{i,-\mathbb{q}} + \mathbf{A}(t) \sum_{n\mathbb{k}} \left(\mathbf{p}^{n\mathbb{k}}_{m\mathbb{l}} a^\dagger_{n\mathbb{k}} a_{m\mathbb{l}} b^\dagger_{i,-\mathbb{q}} - \mathbf{p}^{m'\mathbb{l}}_{n\mathbb{k}} a^\dagger_{m\mathbb{l}} a_{n\mathbb{k}} b^\dagger_{i,-\mathbb{q}} \right) \\
&\quad + \sum_{n\mathbb{k}} \sum_{i\mathbb{q}} \left(D^{m\mathbb{l}}_{\substack{n\mathbb{k}\\ i\mathbb{q}}} a^\dagger_{m'\mathbb{l}'} a_{n\mathbb{k}} (b^\dagger_{i,-\mathbb{q}} b^\dagger_{i,-\mathbb{q}} + b_{i\mathbb{q}} b^\dagger_{i,-\mathbb{q}}) - D^{m'\mathbb{l}'}_{\substack{n\mathbb{k}\\ i\mathbb{q}}} a^\dagger_{m\mathbb{l}} a_{n\mathbb{k}} (b^\dagger_{i,-\mathbb{q}} b^\dagger_{i,-\mathbb{q}} + b_{i\mathbb{q}} b^\dagger_{i,-\mathbb{q}}) \right) \\
&\quad + \sum_{n\mathbb{k}} \sum_{n'\mathbb{k}'} D^{n'\mathbb{k}'}_{\substack{n\mathbb{k}\\ i\mathbb{q}}} a^\dagger_{m\mathbb{l}} a_{m'\mathbb{l}'} a^\dagger_{n\mathbb{k}} a_{n'\mathbb{k}'}
\end{aligned} \tag{4.19a}$$

and

$$\begin{aligned}
i\hbar \frac{d}{dt} (a^\dagger_{m\mathbb{l}} a_{m'\mathbb{l}'} b_{i,\mathbb{q}}) &= [a^\dagger_{m\mathbb{l}} a_{m'\mathbb{l}'} b_{i,\mathbb{q}}, H] \\
&= (E_{m\mathbb{l}} - E_{m'\mathbb{l}'} - \hbar\omega_{i\mathbb{q}}) a^\dagger_{m\mathbb{l}} a_{m'\mathbb{l}'} b_{i,\mathbb{q}} + \mathbf{A}(t) \sum_{n\mathbb{k}} \left(\mathbf{p}^{n\mathbb{k}}_{m\mathbb{l}} a^\dagger_{n\mathbb{k}} a_{m\mathbb{l}} b_{i,\mathbb{q}} - \mathbf{p}^{m'\mathbb{l}}_{n\mathbb{k}} a^\dagger_{m\mathbb{l}} a_{n\mathbb{k}} b_{i,\mathbb{q}} \right) \\
&\quad + \sum_{n\mathbb{k}} \sum_{i\mathbb{q}} \left(D^{m\mathbb{l}}_{\substack{n\mathbb{k}\\ i\mathbb{q}}} a^\dagger_{m'\mathbb{l}'} a_{n\mathbb{k}} (b_{i,\mathbb{q}} b^\dagger_{i,-\mathbb{q}} + b_{i\mathbb{q}} b^\dagger_{i,-\mathbb{q}}) - D^{m'\mathbb{l}'}_{\substack{n\mathbb{k}\\ i\mathbb{q}}} a^\dagger_{m\mathbb{l}} a_{n\mathbb{k}} (b^\dagger_{i,-\mathbb{q}} b^\dagger_{i,-\mathbb{q}} + b_{i\mathbb{q}} b^\dagger_{i,-\mathbb{q}}) \right) \\
&\quad + \sum_{n\mathbb{k}} \sum_{n'\mathbb{k}'} D^{n'\mathbb{k}'}_{\substack{n\mathbb{k}\\ i\mathbb{q}}} a^\dagger_{m\mathbb{l}} a_{m'\mathbb{l}'} a^\dagger_{n\mathbb{k}} a_{n'\mathbb{k}'}.
\end{aligned} \tag{4.19b}$$

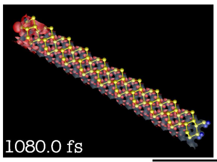

Here, again, we can see that the resulting system of equations is not closed and couples now to products of four operators. The dynamical equations for the four-order-terms would, themselves, couple to contributions containing even more-operators-terms. The only way to solve this hierarchy of equations is to introduce a method to truncate the series and to obtain a closed set of differential equations, which can possibly be solved. The order of truncation, however, has to be justified by the plausibility of the results.

4.2.2 Correlation expansion

A reasonable approach to an infinite-order problem is to use a mean-field method. The idea behind this is that usually, the higher an order gets, the smaller the effects of the dynamical evolution are. However, the expectation value of an N-operator product (called *N-order correlation*) is not independent from e.g. two-operator products, as generally, the N operators can be approximatively split into N expectation values (one operator is thus in the *mean-field* of the others). Similarly, also products of more operators which are contained in the original set of N operators can make a contribution, and basically every possible combination of operators has to be considered.

A general scheme to expand an N-order correlation into all possible sub-correlations is illustrated by the following equations [AS94, Fri96]: for a set of operators O_i, the first 3 orders can be separated according to

$$\begin{aligned}
\langle O_1\rangle &= \langle O_1\rangle^c \\
\langle O_1 O_2\rangle &= \langle O_1 O_2\rangle^c + \langle O_1\rangle^c\langle O_2\rangle^c \\
\langle O_1 O_2 O_3\rangle &= \langle O_1 O_2 O_3\rangle^c + \mathrm{sig}(\mathscr{P}_1)\langle O_1 O_2\rangle^c\langle O_3\rangle^c \\
&\quad + \mathrm{sig}(\mathscr{P}_2)\langle O_1 O_3\rangle^c\langle O_2\rangle^c + \mathrm{sig}(\mathscr{P}_3)\langle O_2 O_3\rangle^c\langle O_1\rangle^c + \langle O_1\rangle^c\langle O_2\rangle^c\langle O_3\rangle^c.
\end{aligned} \tag{4.20}$$

The sig-operator depends on the nature of the particles (fermions or bosons) and on the number of permutations $\mathscr{P}$ using appropriate commutation relations (which, in fact, determine the sign); for bosons, sig equals always one, for fermions, sig is given by $(-1)^{\mathscr{P}_i}$. Following the prescriptions indicated in Eqs. (4.20), the correlation expansion can be performed to any order. For the correlations $\langle\rangle^c$ on the rhs of Eq. (4.20), we can now assume that their contribution to the dynamical evolution is reduced by increasing order, so it is reasonable to neglect higher order correlations starting from a certain order.

In the case of a system with electronic and phononic operators, all contributions up to second order can be calculated explicitly. For electrons, as long as particle conservation is expected, only pair of creators and annihilators are non-vanishing, for phonons, corresponding assumptions can not be made at this level, but will be based on further assumptions in Sec. 4.2.3. The correlations mentioned in Eqs. (4.18) and (4.19) are:

$$\begin{aligned}
\langle a^\dagger_{n\mathbb{k}} a_{n'\mathbb{k}'}\rangle &= \langle a^\dagger_{n\mathbb{k}} a_{n'\mathbb{k}'}\rangle^c \\
\langle b^\dagger_{i\mathbb{q}}\rangle &= \langle b^\dagger_{i\mathbb{q}}\rangle^c \\
\langle b^\dagger_{i\mathbb{q}} b_{i'\mathbb{q}'}\rangle &= \langle b^\dagger_{i\mathbb{q}} b_{i'\mathbb{q}'}\rangle^c + \langle b^\dagger_{i\mathbb{q}}\rangle^c\langle b_{i'\mathbb{q}'}\rangle^c \\
\langle a^\dagger_{n\mathbb{k}} a_{n'\mathbb{k}'} b^\dagger_{i\mathbb{q}}\rangle &= \langle a^\dagger_{n\mathbb{k}} a_{n'\mathbb{k}'} b^\dagger_{i\mathbb{q}}\rangle^c + \langle a^\dagger_{n\mathbb{k}} a_{n'\mathbb{k}'}\rangle^c\langle b^\dagger_{i\mathbb{q}}\rangle^c \\
\langle a^\dagger_{n\mathbb{k}} a_{n'\mathbb{k}'} b^\dagger_{i\mathbb{q}} b_{i'\mathbb{q}'}\rangle &= \langle a^\dagger_{n\mathbb{k}} a_{n'\mathbb{k}'} b^\dagger_{i\mathbb{q}} b_{i'\mathbb{q}'}\rangle^c + \langle a^\dagger_{n\mathbb{k}} a_{n'\mathbb{k}'}\rangle^c\langle b^\dagger_{i\mathbb{q}} b_{i'\mathbb{q}'}\rangle^c + \langle a^\dagger_{n\mathbb{k}} a_{n'\mathbb{k}'} b^\dagger_{i\mathbb{q}}\rangle^c\langle b_{i'\mathbb{q}'}\rangle^c \\
&\quad + \langle a^\dagger_{n\mathbb{k}} a_{n'\mathbb{k}'} b_{i'\mathbb{q}'}\rangle^c\langle b_{i\mathbb{q}}\rangle^c + \langle a^\dagger_{n\mathbb{k}} a_{n'\mathbb{k}'}\rangle^c\langle b^\dagger_{i\mathbb{q}}\rangle^c\langle b_{i'\mathbb{q}'}\rangle^c
\end{aligned} \tag{4.21}$$

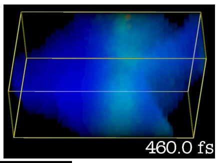

$$\langle a^\dagger_{n\mathbb{k}} a^\dagger_{m\mathbb{l}} a_{n'\mathbb{k}'} a_{m'\mathbb{l}'}\rangle = \langle a^\dagger_{n\mathbb{k}} a^\dagger_{m\mathbb{l}} a_{n'\mathbb{k}'} a_{n'\mathbb{k}'}\rangle^c + \langle a^\dagger_{n\mathbb{k}} a_{n'\mathbb{k}'}\rangle^c \langle a^\dagger_{m\mathbb{l}} a_{n'\mathbb{k}'}\rangle^c - \langle a^\dagger_{n\mathbb{k}} a_{n'\mathbb{k}'}\rangle^c \langle a^\dagger_{m\mathbb{l}} a_{m'\mathbb{l}'}\rangle^c.$$

These prescriptions can now be used inside Eqs. (4.18) and (4.19). All contributions with more than three operators are then neglected, so a new and closed set of differential equations for the correlation terms is obtained.

4.2.3 Bath hypothesis

While a complete evaluation of the phonon dynamics is involved, it is usually a good approximation for systems with weak excitation and weak coupling under thermal conditions to describe the phonons by a thermal distribution function. The assumption of thermal phonons is valid for most calculations in nanostructured materials [Bin92, But07], although the quality of the approximation can generally not be shown in detail. In silicon, the bath hypothesis should at least lead to a good description for the bulk phonon modes. A consequence of applying this approximation is that the phonon operators are not considered as dynamical variables and are not calculated in the differential equations. As a result of the assumption of equilibrium, all expectation values besides the phonon occupation

$$n_{i\mathbb{q}} = \langle b^\dagger_{i\mathbb{q}} b_{i\mathbb{q}}\rangle \tag{4.22}$$

vanish, as the phonons remain in a pure state. This applies especially for the expectation values of single phonon operators like $\langle b^\dagger_{i\mathbb{q}}\rangle$, which appear numerously in Eq. (4.21). The distribution function used is, due to the bosonic nature of the phonons, the *Bose-distribution*

$$n_{i\mathbb{q}}(T) = \frac{1}{e^{\frac{\hbar\omega_{i\mathbb{q}}}{k_B T}} - 1} \tag{4.23}$$

where T is the temperature of the system, k_B the *Boltzmann constant* and $\hbar\omega_{i\mathbb{q}}$ the phonon energy.

By applying now the correlation expansion and the bath hypothesis in the expectation values of the dynamical equations (4.18) and (4.19) and inserting (4.17), we obtain a simplified system of differential equations, where

$$\begin{aligned} i\hbar\frac{d}{dt} p^{m'\mathbb{l}'}_{m\mathbb{l}} = {} & \big(E_{m\mathbb{l}} - E_{m'\mathbb{l}'}\big) p^{m'\mathbb{l}'}_{m\mathbb{l}} + \mathbf{A}(t) \sum_{n\mathbb{k}} \Big(\mathbf{p}^{n\mathbb{k}}_{m\mathbb{l}} p^{m'\mathbb{l}'}_{n\mathbb{k}} - \mathbf{p}^{m'\mathbb{l}'}_{n\mathbb{k}} p^{n\mathbb{k}}_{m\mathbb{l}}\Big) \\ & + \sum_{n\mathbb{k}} \sum_{i'\mathbb{q}'} \Big(D^{m\mathbb{l}}_{\substack{n\mathbb{k}\\ i\mathbb{q}}} \langle a^\dagger_{m'\mathbb{l}'} a_{n\mathbb{k}} b^\dagger_{i',-\mathbb{q}'}\rangle + D^{m\mathbb{l}}_{\substack{n\mathbb{k}\\ i'\mathbb{q}'}} \langle a^\dagger_{m'\mathbb{l}'} a_{n\mathbb{k}} b_{i'\mathbb{q}'}\rangle - D^{m'\mathbb{l}'}_{\substack{n\mathbb{k}\\ i'\mathbb{q}'}} \langle a^\dagger_{m\mathbb{l}} a_{n\mathbb{k}} b^\dagger_{i',-\mathbb{q}'}\rangle - D^{m'\mathbb{l}'}_{\substack{n\mathbb{k}\\ i'\mathbb{q}'}} \langle a^\dagger_{m\mathbb{l}} a_{n\mathbb{k}} b_{i'\mathbb{q}'}\rangle\Big) \end{aligned} \tag{4.24}$$

yields for the polarization densities and

$$\begin{aligned} i\hbar\frac{d}{dt} \langle a^\dagger_{m\mathbb{l}} a_{m'\mathbb{l}'} b^\dagger_{i,-\mathbb{q}}\rangle = {} & \big(E_{m\mathbb{l}} - E_{m'\mathbb{l}'} + \hbar\omega_{i\mathbb{q}}\big) \langle a^\dagger_{m\mathbb{l}} a_{m'\mathbb{l}'} b^\dagger_{i,-\mathbb{q}}\rangle \\ & + \mathbf{A}(t) \sum_{n\mathbb{k}} \Big(\mathbf{p}^{n\mathbb{k}}_{m\mathbb{l}} \langle a^\dagger_{n\mathbb{k}} a_{m'\mathbb{l}'} b^\dagger_{i,-\mathbb{q}}\rangle - \mathbf{p}^{m'\mathbb{l}'}_{n\mathbb{k}} \langle a^\dagger_{m\mathbb{l}} a_{n\mathbb{k}} b^\dagger_{i,-\mathbb{q}}\rangle\Big) \\ & + \sum_{n\mathbb{k}} \sum_{i'\mathbb{q}'} \Big(D^{m\mathbb{l}}_{\substack{n\mathbb{k}\\ i'\mathbb{q}'}} p^{n\mathbb{k}}_{m'\mathbb{l}'} n_{i\mathbb{q}}(T) - D^{m'\mathbb{l}'}_{\substack{n\mathbb{k}\\ i'\mathbb{q}'}} p^{n\mathbb{k}}_{m\mathbb{l}} \big(n_{i\mathbb{q}}(T) + 1\big)\Big) \\ & + \sum_{n\mathbb{k}} \sum_{n'\mathbb{k}'} D^{n'\mathbb{k}'}_{\substack{n\mathbb{k}\\ i\mathbb{q}}} p^{n'\mathbb{k}'}_{m\mathbb{l}} p^{m'\mathbf{l}'}_{n\mathbb{k}} - \sum_{n\mathbb{k}} \sum_{n'\mathbb{k}'} D^{n'\mathbb{k}'}_{\substack{n\mathbb{k}\\ i\mathbb{q}}} p^{m'\mathbf{l}'}_{m\mathbb{l}} p^{n'\mathbb{k}'}_{n\mathbb{k}} \end{aligned} \tag{4.25a}$$

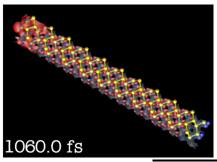

and

$$
\begin{aligned}
i\hbar\frac{d}{dt}\langle a^{\dagger}_{m\mathbb{l}}a_{m'\mathbb{l}'}b_{i,\mathbb{q}}\rangle =& \big(E_{m\mathbb{l}}-E_{m'\mathbb{l}'}-\hbar\omega_{i\mathbb{q}}\big)\langle a^{\dagger}_{m\mathbb{l}}a_{m'\mathbb{l}'}b_{i,\mathbb{q}}\rangle \\
&+\mathbf{A}(t)\sum_{n\mathbb{k}}\Big(\mathbf{p}^{n\mathbb{k}}_{m\mathbb{l}}\langle a^{\dagger}_{n\mathbb{k}}a_{m'\mathbb{l}'}b_{i,\mathbb{q}}\rangle-\mathbf{p}^{m'\mathbb{l}'}_{n\mathbb{k}}\langle a^{\dagger}_{m\mathbb{l}}a_{n\mathbb{k}}b_{i,\mathbb{q}}\rangle\Big) \\
&+\sum_{n\mathbb{k}}\sum_{i'\mathbb{q}'}\Big(D^{m\mathbb{l}}_{\substack{n\mathbb{k}\\ i'\mathbb{q}'}}p^{n\mathbb{k}}_{m'\mathbb{l}'}\big(n_{i\mathbb{q}}(T)+1\big)-D^{m'\mathbb{l}'}_{\substack{n\mathbb{k}\\ i'\mathbb{q}'}}p^{n\mathbb{k}}_{m\mathbb{l}}n_{i\mathbb{q}}(T)\Big) \\
&+\sum_{n\mathbb{k}}\sum_{n'\mathbb{k}'}D^{n'\mathbb{k}'}_{\substack{n\mathbb{k}\\ i\mathbb{q}}}p^{n'\mathbb{k}'}_{m\mathbb{l}}p^{m'\mathbf{l}'}_{n\mathbb{k}}-\sum_{n\mathbb{k}}\sum_{n'\mathbb{k}'}D^{n'\mathbb{k}'}_{\substack{n\mathbb{k}\\ i\mathbb{q}}}p^{m'\mathbf{l}'}_{m\mathbb{l}}p^{n'\mathbb{k}'}_{n\mathbb{k}}
\end{aligned}
\tag{4.25b}
$$

for the expectation values for the phonon assisted density matrices. The very last terms in (4.25a) and (4.25b) can be neglected, as the non-diagonal polarizations that occur inside these are always zero. With these equations, all requirements are made for a solvable problem. Nevertheless, a huge quantity of variables is contained in these differential equations: in addition to the densities $f_{n\mathbb{k}}$ and polarizations $p^{n'\mathbb{k}'}_{n\mathbb{k}}$, all phonon assisted quantities have to be evolved dynamically. In a system of N bands and K $\mathbb{k}$-points, the numerical effort scales with a factor of about N^2K^2. This is usually too cumbersome for a *personal computer* in a system with $N \approx 10$ and $K \geq 100$, as it is required for a surface slab.

4.2.4 Markov Approximation

It is well known that the effect of the phonon assisted density matrices is of minor importance in systems with many scattering channels and weak phononic coupling. This property can be can be exploited in the so called *Markov approximation* [SKM94, But07]. The idea behind this approximation is that the "memory" of the phonon-assisted quantities, e. g. their dependency on the dynamics of past, is negligible. The first assumption for this approach is that in the Eqs. (4.25), the influence of the light coupling is of minor importance an can be neglected (as it is, for the polarization equations (4.24), of second order in $\mathbf{A}(t)$). With it and by choosing an initial condition of $\langle a^{\dagger}_{m\mathbb{l}}a_{m'\mathbb{l}'}b^{\dagger}_{i,-\mathbb{q}}\rangle| = 0$ at $t = -\infty$, which can be justified by the fact that a $t = -\infty$, no deviation from the equilibrium occurs and consequently also no phonon-assisted density matrices, we can integrate Eqs. (4.25) formally:

$$
\begin{aligned}
\langle a^{\dagger}_{m\mathbb{l}}a_{m'\mathbb{l}'}b^{\dagger}_{i,-\mathbb{q}}\rangle =& \frac{i}{\hbar}\int_0^{\infty}\mathrm{d}t' e^{\frac{i}{\hbar}(E_{m\mathbb{l}}-E_{m'\mathbb{l}'}-\hbar\omega_{i\mathbb{q}})t'}\Bigg(\sum_{n\mathbb{k}}\sum_{i\mathbb{q}}D^{m\mathbb{l}}_{\substack{n\mathbb{k}\\ i\mathbb{q}}}n_{i\mathbb{q}}(T)p^{n\mathbb{k}}_{m'\mathbb{l}'}(t-t') \\
&-\sum_{n\mathbb{k}}\sum_{i\mathbb{q}}D^{m'\mathbb{l}'}_{\substack{n\mathbb{k}\\ i\mathbb{q}}}\big(n_{i\mathbb{q}}(T)+1\big)p^{n\mathbb{k}}_{m\mathbb{l}}(t-t')+\sum_{n\mathbb{k}}\sum_{n'\mathbb{k}'}D^{n'\mathbb{k}'}_{\substack{n\mathbb{k}\\ i\mathbb{q}}}p^{n'\mathbb{k}'}_{m\mathbb{l}}(t-t')p^{m'\mathbb{l}'}_{n\mathbb{k}}(t-t')\Bigg)
\end{aligned}
\tag{4.26a}
$$

$$
\begin{aligned}
\langle a^{\dagger}_{m\mathbb{l}}a_{m'\mathbb{l}'}b_{i,\mathbb{q}}\rangle =& \frac{i}{\hbar}\int_0^{\infty}\mathrm{d}t' e^{\frac{i}{\hbar}(E_{m\mathbb{l}}-E_{m'\mathbb{l}'}+\hbar\omega_{i\mathbb{q}})t'}\Bigg(\sum_{n\mathbb{k}}\sum_{i\mathbb{q}}D^{m\mathbb{l}}_{\substack{n\mathbb{k}\\ i\mathbb{q}}}\big(n_{i\mathbb{q}}(T)+1\big)p^{n\mathbb{k}}_{m'\mathbb{l}'}(t-t') \\
&-\sum_{n\mathbb{k}}\sum_{i\mathbb{q}}D^{m'\mathbb{l}'}_{\substack{n\mathbb{k}\\ i\mathbb{q}}}n_{i\mathbb{q}}(T)p^{n\mathbb{k}}_{m\mathbb{l}}(t-t')+\sum_{n\mathbb{k}}\sum_{n'\mathbb{k}'}D^{n'\mathbb{k}'}_{\substack{n\mathbb{k}\\ i\mathbb{q}}}p^{n'\mathbb{k}'}_{m\mathbb{l}}(t-t')p^{m'\mathbb{l}'}_{n\mathbb{k}}(t-t')\Bigg).
\end{aligned}
\tag{4.26b}
$$

The "memory" of those equations is now carried by the dynamics of the polarizations $p^{n'\mathbb{k}'}_{n\mathbb{k}}$. Therefore, the next step is to neglect the dynamical effects of the interactions inside the polarizations in Eqs. (4.26). This is achieved by setting all interaction terms in Eq. (4.24) to zero ($\mathbf{p}^{n'\mathbb{k}'}_{n\mathbb{k}} = 0$, $D^{n'\mathbb{k}'}_{n\mathbb{k};i,\mathbb{q}} = 0$) and perform a "free" integration of the polarization dynamics, which

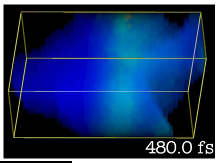

gives us a description of the unperturbed evolution of the polarization during t' of the "real" polarization $p^{m'\mathbb{l}'}_{m\mathbb{l}}(t)$:

$$p^{m'\mathbb{l}'}_{m\mathbb{l}}\Big|_{\text{free}}(t-t') = e^{-i(E_{m\mathbb{l}}-E_{m'\mathbb{l}'})t'}\, p^{m'\mathbb{l}'}_{m\mathbb{l}}(t). \tag{4.27}$$

If these relations are reinserted into the phonon-assisted dynamical equations (4.26), the temporal integration can be carried out, giving an analytical form of the dynamics, where only an explicit dependency on the equal-time polarizations $p^{m'\mathbb{l}'}_{m\mathbb{l}}(t)$ occurs. Now, the so-found equations are again inserted into the polarization dynamics (4.24) to totally eliminate the phonon-assisted quantities. The result is a system of differential equations depending purely on the polarizations:

$$\begin{aligned}
i\hbar\frac{d}{dt}p^{m'\mathbb{l}'}_{m\mathbb{l}} &= \left(E_{m\mathbb{l}}-E_{m'\mathbb{l}'}\right)p^{m'\mathbb{l}'}_{m\mathbb{l}} + \mathbf{A}(t)\sum_{n\mathbb{k}}\left(\mathbf{p}^{n\mathbb{k}}_{m\mathbb{l}}\,p^{m'\mathbb{l}'}_{n\mathbb{k}} - \mathbf{p}^{m'\mathbb{l}'}_{n\mathbb{k}}\,p^{n\mathbb{k}}_{m\mathbb{l}}\right) \\
&\quad -\frac{i}{\hbar}\sum_{n\mathbb{k}}\sum_{n'\mathbb{k}'}\sum_{n''\mathbb{k}''}\sum_{i\mathbb{q}} D^{n''\mathbb{k}''}_{\substack{m'\mathbb{l}'\\ i\mathbb{q}}}\,\overline{D}^{n\mathbb{k}}_{\substack{n'\mathbb{k}'\\ i\mathbb{q}}}\Bigg(\\
&\qquad \Delta(E_{n'\mathbb{k}'}-E_{n\mathbb{k}}-\hbar\omega_{i\mathbb{q}})\Big((n_{i\mathbb{q}}+1)\,p^{n'\mathbb{k}'}_{m\mathbb{l}}\left(\delta_{n,n''}\delta_{\mathbb{k},\mathbb{k}''}-p^{n''\mathbb{k}''}_{n\mathbb{k}}\right) - n_{i\mathbb{q}}\left(\delta_{m,n'}\delta_{\mathbb{l},\mathbb{k}'}-p^{n'\mathbb{k}'}_{m\mathbb{l}}\right)p^{n''\mathbb{k}''}_{n\mathbb{k}}\Big) \\
&\quad +\Delta(E_{n'\mathbb{k}'}-E_{n\mathbb{k}}+\hbar\omega_{i\mathbb{q}})\Big(n_{i\mathbb{q}}\,p^{n'\mathbb{k}'}_{m\mathbb{l}}\left(\delta_{n,n''}\delta_{\mathbb{k},\mathbb{k}''}-p^{n''\mathbb{k}''}_{n\mathbb{k}}\right) - (n_{i\mathbb{q}}+1)\left(\delta_{m,n'}\delta_{\mathbb{l},\mathbb{k}'}-p^{n'\mathbb{k}'}_{m\mathbb{l}}\right)p^{n''\mathbb{k}''}_{n\mathbb{k}}\Big)\Bigg) \\
&\quad -\frac{i}{\hbar}\sum_{n\mathbb{k}}\sum_{n'\mathbb{k}'}\sum_{n''\mathbb{k}''}\sum_{i\mathbb{q}} \overline{D}^{n''\mathbb{k}''}_{\substack{m\mathbb{l}\\ i\mathbb{q}}}\,D^{n\mathbb{k}}_{\substack{n'\mathbb{k}'\\ i\mathbb{q}}}\Bigg(\\
&\qquad \Delta(E_{n'\mathbb{k}'}-E_{n\mathbb{k}}-\hbar\omega_{i\mathbb{q}})\Big((n_{i\mathbb{q}}+1)\,p^{n'\mathbb{k}'}_{m'\mathbb{l}'}\left(\delta_{n'',n}\delta_{\mathbb{k}'',\mathbb{k}}-p^{n\mathbb{k}}_{n''\mathbb{k}''}\right) - n_{i\mathbb{q}}\left(\delta_{m',n'}\delta_{\mathbb{l}',\mathbb{k}'}-p^{n'\mathbb{k}'}_{m'\mathbb{l}'}\right)p^{n\mathbb{k}}_{n''\mathbb{k}''}\Big) \\
&\quad +\overline{\Delta}(E_{n'\mathbb{k}'}-E_{n\mathbb{k}}+\hbar\omega_{i\mathbb{q}})\Big(n_{i\mathbb{q}}\,p^{m'\mathbb{l}'}_{n'\mathbb{k}'}\left(\delta_{n'',n}\delta_{\mathbb{k}'',\mathbb{k}}-p^{n\mathbb{k}}_{n''\mathbb{k}''}\right) - (n_{i\mathbb{q}}+1)\left(\delta_{n',m'}\delta_{\mathbb{k}',\mathbb{l}'}-p^{m'\mathbb{l}'}_{n'\mathbb{k}'}\right)p^{n\mathbb{k}}_{n''\mathbb{k}''}\Big)\Bigg).
\end{aligned} \tag{4.28}$$

The integral $\Delta(\omega)$, stemming from the previous integration, can be expressed in terms of a *Cauchy principle value* $\mathscr{P}$:

$$\Delta(\omega) = \int_0^\infty \mathrm{d}t e^{i\omega t} = \lim_{\alpha\to 0}\frac{i\alpha}{\alpha^2+\omega^2} + \lim_{\alpha\to 0}\frac{i\omega}{\alpha^2+\omega^2} = \pi\delta(\omega) + i\mathscr{P}(\omega). \tag{4.29}$$

The principle value part of this equation makes only a complex-valued contribution to $\Delta(\omega)$. The effect of this in view of equation (4.28) is, contrarily to the other parts of the phonon coupling, a shift of the energies with respect to the free system, as it can be seen in line with the other energies $E_{m\mathbb{l}}$. For quantum heterostructures this *polaron shift* is usually expected to be small and therefore neglected [But04]. For the silicon (001) surface, the effect is generally non-negligible. However, in the present formulation of the theory, polaronic effects are not discussed. Whence, the imaginary part of Eq. (4.29) is neglected, and we assume $\Delta(\omega) = \overline{\Delta}(\omega) = \pi\delta(\omega)$.

Moreover, in Eq. (4.28), we notice that the dynamics depends on non-diagonal polarizations in quadratic order. Usually, these contributions are also expected to be very small, as the order of magnitude for non-diagonal polarizations is below that of the diagonal densities. Hence, we neglect all quadratic polarization terms by setting in Eq. (4.28)

$$\begin{aligned} m &= n' & n &= n'' \\ \mathbb{l} &= \mathbb{k}' & \mathbb{k} &= \mathbb{k}''. \end{aligned} \tag{4.30}$$

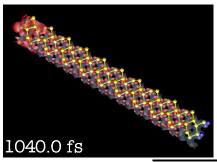

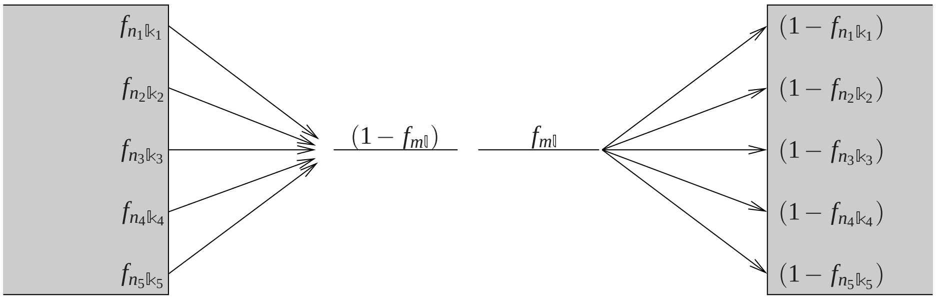

Figure 4.2: *The possible scattering channels of Eq.* (4.32).

The result of these additional approximations is a much simplified set of equations, where especially the number of summations is drastically reduced. For the non-diagonal polarizations ($m \neq m'$ and $\mathbb{l} \neq \mathbb{l}'$), the insertion into Eq. (4.28) yields:

$$\begin{aligned}\frac{d}{dt}p^{m'\mathbb{l}'}_{m\mathbb{l}} =& \frac{1}{i\hbar}\left(E_{m\mathbb{l}}-E_{m'\mathbb{l}'}\right)p^{m'\mathbb{l}'}_{m\mathbb{l}} + \frac{1}{i\hbar}\mathbf{A}(t)\sum_{n\mathbb{k}}\left(\mathbf{p}^{n\mathbb{k}}_{m\mathbb{l}}p^{m'\mathbb{l}'}_{n\mathbb{k}} - \mathbf{p}^{m'\mathbb{l}'}_{n\mathbb{k}}p^{n\mathbb{k}}_{m\mathbb{l}}\right)\\ &-\left(\Gamma^{\text{in}}_{m\mathbb{l}}+\Gamma^{\text{out}}_{m\mathbb{l}}+\Gamma^{\text{in}}_{m'\mathbb{l}'}+\Gamma^{\text{out}}_{m'\mathbb{l}'}\right)p^{m'\mathbb{l}'}_{m\mathbb{l}}.\end{aligned} \tag{4.31}$$

For the diagonal parts of the polarizations (densities), the corresponding equations are even simpler:

$$\frac{d}{dt}f_{m\mathbb{l}} = \frac{2}{\hbar}\mathbf{A}(t)\sum_{n\mathbb{k}}\Im\left(\mathbf{p}^{n\mathbb{k}}_{m\mathbb{l}}p^{m\mathbb{l}}_{n\mathbb{k}}\right) + 2\Gamma^{\text{in}}_{m\mathbb{l}}\left(1-f_{m\mathbb{l}}\right) - 2\Gamma^{\text{out}}_{m\mathbb{l}}f_{m\mathbb{l}}. \tag{4.32}$$

In these equations, new symbols $\Gamma^{\text{in/out}}_{m\mathbb{l}}$ have been introduced. These quantities denote the *scattering rates*, which give evidence of the scattering into and out of a state $|m\mathbb{l}\rangle$. They are given by

$$\begin{aligned}\Gamma^{\text{in}}_{m\mathbb{l}} =& \sum_{n\mathbb{k}}\sum_{i\mathbb{q}}\left|D^{n\mathbb{k}}_{m\mathbb{l}\atop i\mathbb{q}}\right|^2\Big(\delta(E_{m\mathbb{l}}-E_{n\mathbb{k}}-\hbar\omega_{i\mathbb{q}})\left(n_{i\mathbb{q}}+1\right)+\delta(E_{m\mathbb{l}}-E_{n\mathbb{k}}+\hbar\omega_{i\mathbb{q}})n_{i\mathbb{q}}\Big)f_{n\mathbb{k}}\\ =:& \sum_{n\mathbb{k}}\overleftarrow{\Lambda}^{n\mathbb{k}}_{m\mathbb{l}}f_{n\mathbb{k}}\end{aligned} \tag{4.33a}$$

and

$$\begin{aligned}\Gamma^{\text{out}}_{m\mathbb{l}} =& \sum_{n\mathbb{k}}\sum_{i\mathbb{q}}\left|D^{n\mathbb{k}}_{m\mathbb{l}\atop i\mathbb{q}}\right|^2\Big(\delta(E_{m\mathbb{l}}-E_{n\mathbb{k}}+\hbar\omega_{i\mathbb{q}})n_{i\mathbb{q}}+\delta(E_{m\mathbb{l}}-E_{n\mathbb{k}}-\hbar\omega_{i\mathbb{q}})\left(n_{i\mathbb{q}}+1\right)\Big)\left(1-f_{n\mathbb{k}}\right)\\ =:& \sum_{n\mathbb{k}}-\overrightarrow{\Lambda}^{n\mathbb{k}}_{m\mathbb{l}}\left(1-f_{n\mathbb{k}}\right).\end{aligned} \tag{4.33b}$$

The scattering matrices are entirely expressed in terms of the densities $f_{n\mathbb{k}}$ without the non-diagonal polarizations. The physical explanation of the non-diagonal equations (4.32) is obvious. Scattering in this equation relies on the two contributions containing Γ at the end of the rhs. The scatter-in part (with Γ^{in}) depends on $(1-f_{n\mathbb{k}})$, the more this state is populated, the less it is possible to scatter into it. The scatter-out part, depending on $f_{n\mathbb{k}}$, on the contrary,

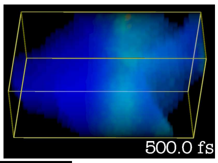

behaves in the opposite way: the more it is populated, the more electrons scatter out again. Furthermore, scattering depends on temperature through the phonon-distribution in the scattering matrices, and, due to the $n_{i\mathbb{q}}+1$-terms (which are related to spontaneous phonon emission), it is always more probable to scatter to a state of lower energy than to a state of higher energy. The scattering events are always energy-conserving, as is implied by the delta-distributions in Eqs. (4.33): the energy difference $E_{m\mathbb{l}}$ and $E_{n\mathbb{k}}$ of the two electronic states $|m\mathbb{l}\rangle$ and $|n\mathbb{k}\rangle$ must match the phonon energy $\hbar\omega_{i\mathbb{q}}$.

The dynamics of the polarizations (Eq. (4.31)) is mainly influenced by the optical excitation. The scatter matrices (4.33) (which are positive definite) occur only as damping terms. Without light field, the polarizations cannot be augmented and fade out.

4.2.5 Fundamental symmetries

The most obvious symmetry in the equations is contained in the matrix elements $p^{n'\mathbb{k}'}_{n\mathbb{k}}$ and $D^{n'\mathbb{k}'}_{n\mathbb{k};i\mathbb{q}}$. Due to construction, the following relations hold:

$$p^{n'\mathbb{k}'}_{n\mathbb{k}} = \overline{p}^{n\mathbb{k}}_{n'\mathbb{k}'} \tag{4.34a}$$

$$D^{n'\mathbb{k}'}_{\substack{n\mathbb{k}\\ i\mathbb{q}}} = \overline{D}^{n\mathbb{k}}_{\substack{n'\mathbb{k}'\\ i,-\mathbb{q}}} \tag{4.34b}$$

In the framework of an electronic many-particle system, particle conservation is required. For the dynamic of the electronic densities (Eq. (4.32)), this implies implicitly, that the sum over all densities must equal zero at all times, or its temporal derivation must vanish:

$$\frac{d}{dt}\sum_{m\mathbb{l}} f_{m\mathbb{l}} = \sum_{m\mathbb{l}} \frac{d}{dt} f_{m\mathbb{l}} = 0. \tag{4.35}$$

Eq. (4.32) can now be inserted with the scattering matrices $\overrightarrow{\Lambda}^{n\mathbb{k}}_{m\mathbb{l}}$ and $\overleftarrow{\Lambda}^{n\mathbb{k}}_{m\mathbb{l}}$ (cmp. Eqs. (4.33)), effecting a direct condition for the involved variables:

$$0 = \frac{1}{i\hbar}\mathbf{A}(t)\sum_{m\mathbb{l}}\sum_{n\mathbb{k}}\left(\mathbf{p}^{n\mathbb{k}}_{m\mathbb{l}} p^{m\mathbb{l}}_{n\mathbb{k}} - \mathbf{p}^{m\mathbb{l}}_{n\mathbb{k}} p^{n\mathbb{k}}_{m\mathbb{l}}\right) + \sum_{m\mathbb{l}}\sum_{n\mathbb{k}}\left(\overrightarrow{\Lambda}^{n\mathbb{k}}_{m\mathbb{l}}(1-f_{n\mathbb{k}})f_{m\mathbb{l}} + \overleftarrow{\Lambda}^{n\mathbb{k}}_{m\mathbb{l}} f_{n\mathbb{k}}(1-f_{m\mathbb{l}})\right). \tag{4.36}$$

The first term (proportional to $\mathbf{A}(t)$ is obviously zero, as the two negated contributions to the sum are the same. From the second term, a condition for the scatter matrices can be derived, as Eq. (4.36) must hold independent of the densities $f_{n\mathbb{k}}$:

$$\overrightarrow{\Lambda}^{n\mathbb{k}}_{m\mathbb{l}} + \overleftarrow{\Lambda}^{m\mathbb{l}}_{n\mathbb{k}} = 0. \tag{4.37}$$

This result complies with a direct comparison of the explicit scattering rates (4.33). Nevertheless, it has a significance a numerical compution of the scattering rates, where, if the rates can only be calculated approximatively, a symmetrization can be sensible to ensure a density-conserving relaxation.

4.2.6 Slow relaxation approximation

As it can be seen by comparing Eqs. (4.31) and (4.32), the polarizations $p^{n'\mathbb{k}'}_{n\mathbb{k}}$ are exclusively coupled to the dynamics of the densities $f_{n\mathbb{k}}$ in Eq. (4.32) through the vector potential $\mathbf{A}(t)$[1].

---

[1] We note that important light polarization effects can occur at the surface. While diffraction and reflection (*Fresnel laws*) are not important for a perpendicularly incident light ray, the field strength of the vector potential

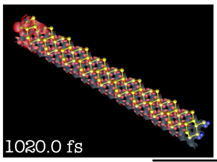

Under experimental conditions where relaxation behaviour is investigated, the system is usually excited by a very short laser pulse (≈ 100 fs). If the subsequent relaxation time can now be estimated significantly longer (≈ 1 ps), it is possible to separate the excitation dynamics through the light field $\mathbf{A}(t)$ from the relaxation dynamics: A short pulse is only non-vanishing during the pulse length τ and therefore zero for most of the time when relaxation occurs[2]. Consequently, the polarizations are only coupled for a very short time to the densities in the relaxation equation (4.32) at the beginning of the relaxation. On the other hand, the relaxation influences the polarization dynamics (Eq. (4.31)) only by damping through $\Gamma^{\text{in}}_{m\mathbb{k}}$ and $\Gamma^{\text{out}}_{m\mathbb{k}}$. For the duration of the light pulse, this damping can be neglected. As a result of these considerations, the dynamical equations can be formulated for two limiting cases:

1. The optical excitation is determined for an undamped system using both Eq. (4.31) and (4.32) without damping $\Gamma^{\text{in/out}} = 0$. These equations are valid during the pulse. It is convenient to set the pulse immediately before $t = 0$ (but it must be assured that at $t = 0$, the pulse has sufficiently vanished). Then, through the pulse, a distribution of densities $f_{n\mathbb{k}}$ is provided.
2. The relaxation process is totally independent of the polarizations $p^{n'\mathbb{k}'}_{n\mathbb{k}}$, and therefore described by Eq. (4.32) with $\mathbf{A}(t) = 0$. The optical excitation is introduced by taking the resulting density distribution of 1) as initial condition for the relaxation.

By utilizing the band gap property of the semiconductor band structure, the optical excitation can be integrated analytically.

4.2.6.1 Optical excitation

In a semiconductor, the bandgap separates the valence bands from the conduction bands. The population distribution is given by the *Fermi-Dirac-distribution*. At zero temperature ($T = 0$K), this behaviour can be formulated by introducing a distribution function according to

$$f_{n\mathbb{k}} = \theta(E_F - E_{n\mathbb{k}}), \tag{4.38}$$

where E_F denotes the Fermi-level (in the band gap) and $\theta(\omega)$ the unit-step function. This distribution is still a good approximation at room temperature for the real distribution. We assume a weak excitation with low intensities, so the population is always close to one or zero. If we neglect the temporal evolution of the densities and the polarizations, and insert Eq. (4.38), we obtain:

$$i\hbar\frac{d}{dt}p^{m\mathbb{k}}_{m'\mathbb{k}'} = (E_{m\mathbb{k}} - E_{m'\mathbb{k}'})p^{m\mathbb{k}}_{m'\mathbb{k}'} + \mathbf{A}(t)\left(\mathbf{p}^{m\mathbb{k}}_{m'\mathbb{k}'}\theta(E_0 - E_{m\mathbb{k}}) - \overline{\mathbf{p}}^{m\mathbb{k}}_{m'\mathbb{k}'}\theta(E_0 - E_{m'\mathbb{k}'})\right) \tag{4.39}$$

This equation can be integrated formally:

$$p^{m\mathbb{k}}_{m'\mathbb{k}'} = \int_{-\infty}^{t} dt'\mathbf{A}(t')\left(\mathbf{p}^{m\mathbb{k}}_{m'\mathbb{k}'}\theta(E_0 - E_{m\mathbb{k}}) - \overline{\mathbf{p}}^{m\mathbb{k}}_{m'\mathbb{k}'}\theta(E_0 - E_{m'})\right)e^{-\frac{i}{\hbar}(E_{m\mathbb{k}} - E_{m'\mathbb{k}'})(t-t')} \tag{4.40}$$

$\mathbf{A}(t)$ can be modified by a significant factor due to the different refraction indices of the silicon material and the vacuum. Due to the example character of this discussion, such effects are neglected.

[2] It should be noted that in $\mathbf{A}(t)\mathbf{p}$-coupling, we cannot assume that the vector potential $\mathbf{A}$ is vanishes for both limits $t \to -\infty$ and $t \to \infty$. It can be stated, however, that $\mathbf{A}(t)$ tends to a constant at $t = \pm\infty$ (at the other boundary, it can be set to zero), an this effect is eliminated in Eqs. 4.31 and (4.32). Still, the equivalence in (2.48) holds.

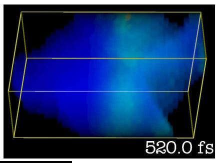

For the densities (Eq. (4.32)), the equation of motion under these circumstances is given by

$$i\hbar\frac{d}{dt}f_{m\mathbb{k}} = \mathbf{A}(t)\sum_{m'\mathbb{k}'}\Big(\mathbf{p}^{m\mathbb{k}}_{m\mathbb{k}}p^{m\mathbb{k}}_{m'\mathbb{k}'} - \overline{\mathbf{p}}^{m'\mathbb{k}'}_{m\mathbb{k}}\overline{p}^{m\mathbb{k}}_{m'\mathbb{k}'}\Big) = 2i\mathbf{A}(t)\sum_{m'\mathbb{k}'}\Im(\mathbf{p}^{m\mathbb{k}}_{m'\mathbb{k}'}p^{m'\mathbb{k}'}_{m\mathbb{k}}). \tag{4.41}$$

Here, the formal integration yields, after expanding the imaginary operators:

$$f_{m\mathbb{k}} = \frac{2}{\hbar}\int_{-\infty}^{t}dt'\mathbf{A}(t')\sum_{m'\mathbb{k}'}\Big(\Im(\mathbf{p}^{m'\mathbb{k}'}_{m\mathbb{k}})\Re(p^{m'\mathbb{k}'}_{m\mathbb{k}}) + \Re(\mathbf{p}^{m'\mathbb{k}'}_{m\mathbb{k}})\Im(p^{m'\mathbb{k}'}_{m\mathbb{k}})\Big)$$

Now, the formal solution Eq. (4.40) can be reinserted:

$$\begin{aligned}
=&\frac{2}{\hbar^2}\int_{-\infty}^{t}dt'\sum_{m'\mathbb{k}'}\Bigg(\Im(\mathbf{p}^{m'\mathbb{k}'}_{m\mathbb{k}})\Bigg(\qquad (4.42)\\
&\Big(\Im(\mathbf{p}^{m'\mathbb{k}'}_{m\mathbb{k}})\theta(E_F - E_{m'\mathbb{k}'}) + \Im(\mathbf{p}^{m'\mathbb{k}'}_{m\mathbb{k}})\theta(E_F - E_{m\mathbb{k}})\Big)\Re\Big(\int_{-\infty}^{t'}dt''\mathbf{A}(t'')e^{\frac{i}{\hbar}(E_{m'\mathbb{k}'}-E_{m\mathbb{k}})(t'-t'')}\Big)\\
&-\Big(\Re(\mathbf{p}^{m'\mathbb{k}'}_{m\mathbb{k}})\theta(E_F - E_{m'\mathbb{k}'}) - \Re(\overline{\mathbf{p}}^{m'\mathbb{k}'}_{m\mathbb{k}})\theta(E_F - E_{m\mathbb{k}})\Big)\Im\Big(\int_{-\infty}^{t'}dt''\mathbf{A}(t'')e^{\frac{i}{\hbar}(E_{m'\mathbb{k}'}-E_{m\mathbb{k}})(t'-t'')}\Big)\Bigg)\\
&+\Re(\mathbf{p}^{m'\mathbb{k}'}_{n})\Bigg(\\
&\quad\Big(\Im(\mathbf{p}^{m'\mathbb{k}'}_{n})\theta(E_F - E_{m'\mathbb{k}'}) + \Im(\mathbf{p}^{m'\mathbb{k}'}_{n})\theta(E_F - E_{m\mathbb{k}})\Big)\Im\Big(\int_{-\infty}^{t'}dt''\mathbf{A}(t'')e^{\frac{i}{\hbar}(E_{m'\mathbb{k}'}-E_{n})(t'-t'')}\Big)\\
&+\Big(\Re(\mathbf{p}^{m'\mathbb{k}'}_{m\mathbb{k}})\theta(E_F - E_{m'\mathbb{k}'}) + \Re(\mathbf{p}^{m'\mathbb{k}'}_{m\mathbb{k}})\theta(E_F - E_{m\mathbb{k}})\Big)\Re\Big(\int_{-\infty}^{t'}dt''\mathbf{A}(t'')e^{\frac{i}{\hbar}(E_{m'\mathbb{k}'}-E_{m\mathbb{k}})(t'-t'')}\Big)\Bigg)\Bigg).
\end{aligned}$$

The essential investigations of this thesis are about relaxation processes in the conduction band of a semiconductor. Therefore, we focus on the bands for which $E_{n\mathbb{k}} > E_F$ holds. After joining the complex exponentials to a cos-function, the distribution function for these excited states reads:

$$f_{m\mathbb{k}}\Big|_{E_{m\mathbb{k}}>E_F} = \frac{2}{\hbar^2}\sum_{m'\mathbb{k}'}\int_{-\infty}^{t}dt'\mathbf{A}(t')|\mathbf{p}^{m'\mathbb{k}'}_{m\mathbb{k}}|^2\int_{-\infty}^{t'}dt''\mathbf{A}(t'')\cos\Big(\frac{1}{\hbar}(E_{m'\mathbb{k}'} - E_{m\mathbb{k}})(t'-t'')\Big)$$

For a pair function, where $f(x) = f(-x)$, it is now possible to transform the two entangled integrals into two independent integrals. After subsequently reexpanding the cos, this yields:

$$\begin{aligned}
=&\frac{1}{\hbar^2}\sum_i|\mathbf{p}^i_n|^2\Big(\int_{-\infty}^{t}dt'\mathbf{A}(t')e^{\frac{i}{\hbar}(E_i-E_n)t'}\int_{-\infty}^{t}dt''\mathbf{A}(t'')e^{-\frac{i}{\hbar}(E_i-E_n)t''}\\
&+\int_{-\infty}^{t}dt'\mathbf{A}(t')e^{-\frac{i}{\hbar}(E_i-E_n)t'}\int_{-\infty}^{t}dt''\mathbf{A}(t'')e^{\frac{i}{\hbar}(E_i-E_n)t''}\Big)
\end{aligned}$$

which is finally equivalent to

$$=\frac{1}{\hbar^2}\sum_{m'\mathbb{k}'}|\mathbf{p}^i_{m\mathbb{k}}|^2\Big|\int_{-\infty}^{t}dt'\mathbf{A}(t')e^{\frac{i}{\hbar}(E_{m'\mathbb{k}'}-E_{m\mathbb{k}})t'}\Big|^2. \tag{4.43}$$

Hence, after the pulse, the distribution of the population in the conduction band is given by

$$f_{m\mathbb{k}}\Big|_{E_{m\mathbb{k}}>E_F} = \frac{1}{\hbar^2}\sum_{m'\mathbb{k}'}|\mathbf{p}^{m'\mathbb{k}'}_{m\mathbb{k}}|^2\Big|\widetilde{\mathbf{A}}\Big(\frac{E_{m'\mathbb{k}'} - E_{m\mathbb{k}}}{\hbar}\Big)\Big|^2 \tag{4.44}$$

where $\widetilde{\mathbf{A}}(\omega)$ is the temporal Fourier transform of the vector potential.

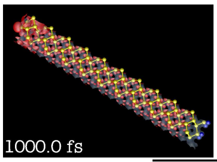

4.2.6.2 Phonon relaxation

Without considering the electron-light coupling dynamically, the relaxation equations (4.32) are independent of the polarizations:

$$\frac{d}{dt} f_{m\mathbb{l}} = 2\Gamma^{\text{in}}_{m\mathbb{l}}\left(1 - f_{m\mathbb{l}}\right) - 2\Gamma^{\text{out}}_{m\mathbb{l}} f_{m\mathbb{l}}. \tag{4.45}$$

This equation can not be solved by an analytical integration step, so a numerical *initial-value-problem* solving algorithm (like a *Runge-Kutta-method*) has to be used. With Eq. (4.45), it is however not necessary to perform the calculation of the polarizations $p^{n'\mathbb{k}'}_{n\mathbb{k}}$. This is a great reduction of computational hardware requirements, as the polarizations $p^{n'\mathbb{k}'}_{n\mathbb{k}}$ are defined for every pair of bands and are thus much more numerous than the densities $f_{n\mathbb{k}}$.

The initial conditions for the temporal evolution have to be chosen reasonable, e.g. by using Eq. (4.44).

4.3 Coupling matrix elements

The derived equations are generally valid for a two-dimensional multiband system. The specialization of the dynamical equations (4.44) and (4.45) to a specific material system is achieved by the definition of the matrix elements $p^{n'\mathbb{k}'}_{n\mathbb{k}}$ for the optical excitation and $D^{n'\mathbb{k}'}_{n\mathbb{k};i\mathbb{q}}$ for the phonon relaxation (cmp. Eq. (4.10)). Into these matrix elements, the system properties enter through the single particle wave functions $|\phi_{n\mathbb{k}}\rangle$, which appear as solutions of the ground state Hamiltonian (2.50) and which are calculated in Chapter 5, and through the phonon modes (2.33). In this section, the final link between the two methods *density-functional theory* for the ground states and *density-matrix theory* for the dynamical evolution is drawn.

4.3.1 Electron-phonon coupling matrix elements

The electron phonon coupling is described in Eq. (4.10) by the the coupling matrix element for a two-dimensional system

$$D^{n'\mathbb{k}'}_{\substack{n\mathbb{k}\\ i\mathbb{q}}} = \int \mathrm{d}^3 r \Big(\mathbf{D}^0_i(\mathbf{r})\mathbf{s}^i_{\mathbb{q}}(\mathbf{r}) + \mathbf{D}^0_i \nabla \mathbf{s}^i_{\mathbb{q}}(\mathbf{r})\overline{\phi}_{n\mathbb{k}}(\mathbf{r})\phi_{n'\mathbb{k}'}(\mathbf{r}). \tag{4.46}$$

The electron-phonon Potential $\mathbf{D}^{0/1}_i(\mathbf{r})$ can be derived as in Eq. (2.38). A general property (which holds, due to the supercell approach, for all directions) is that it is lattice periodic, so $\mathbf{D}^i(\mathbf{r}) = \mathbf{D}^i(\mathbf{r}+\mathbf{R})$ for a lattice vector $\mathbf{R}$. Thus, a convenient way to express the potential is in terms of a Fourier series (cmp. sec 2.3):

$$\mathbf{D}^{0/1}_i(\mathbf{r}) = \sum_{\mathbf{G}} \mathbf{D}^{0/1}_i(\mathbf{G}) e^{i\mathbf{G}\mathbf{r}}. \tag{4.47}$$

The phonon modes are influenced by the slab symmetry, so the functional form is given by $\mathbf{s}^i_{\mathbb{q}}(\mathbf{r}) = \mathbf{s}^i(z)e^{i\mathbb{q}\mathbf{r}} = \sum_{G_z} \mathbf{s}^i(G_z)e^{i(\mathbb{q}\mathbf{r}+G_z z)}$. Inserting this, the Bloch wave representation Eq. (2.26) and Eqs. (4.47) into Eq. (4.46), we get

$$D^{n'\mathbb{k}'}_{\substack{n\mathbb{k}\\ i\mathbb{q}}} = \sum_{\mathbf{G}}\sum_{\mathbf{G}'}\sum_{\mathbf{G}''}\sum_{G_z} \overline{u}_{n\mathbb{k}}(\mathbf{G})u_{n'\mathbb{k}'}(\mathbf{G}')\Big(\mathbf{D}^0_i(\mathbf{G}'') + \mathbf{D}^1_i(\mathbf{G}'')(\mathbb{q}, G_z)\Big)\mathbf{s}^i(G_z)) \tag{4.48}$$

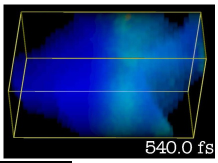

$$\underbrace{\int \mathrm{d}^3 r e^{i\left(-(\mathbf{G}+\mathbb{k})\mathbf{r}+(\mathbf{G}'+\mathbb{k}')\mathbf{r}+\mathbf{G}''\mathbf{r}+\mathbb{q}\mathbf{r}+G_z z\right)}}_{\delta_{\mathbf{G}'+\mathbf{G}''+G_z+\mathbb{k}'+\mathbb{q},\mathbf{G}+\mathbb{k}}}.$$

The spatial dependency of the electron-phonon potential, however, is difficult to investigate, as an explicit calculation of the spatially dependent electron-phonon potential is laborious. In principle, an electron phonon interaction is mainly determined by either the dependency on the phonon mode $\mathbf{s}^i(\mathbf{r},t)$ or, if the latter vanishes, by the dependence on the first derivative of the modes $\nabla\mathbf{s}^i(\mathbf{r},t)$. In our case, we only consider the direct dependency on the derivative of the mode ($\mathbf{D}_i^1$) as this is expected in a non-polar material and a purely longitudinal phonon mode, consequently, $\mathbf{D}_i 1(\mathbf{r})$ is non-vectorial. For *Fröhlich-coupling*, the other case would hold.

Furtheron, we assume that the spatial variation of the electron-phonon potential is not too important and neglect the spatial dependency of $\mathbf{D}_i^1(\mathbf{r})$. This drastical assumption that can not be justified by the material properties. With these declarations, the delta-condition in the matrix element (4.48) can be expressed much simpler, as $\mathbf{G}''$ vanishes:

$$D^{n'\mathbb{k}'}_{\substack{n\mathbb{k}\\ i\mathbb{q}}} = \sum_{\mathbf{G}}\sum_{\mathbf{G}'}\sum_{G_z} \overline{u}_{n\mathbb{k}}(\mathbf{G}) u_{n'\mathbb{k}'}(\mathbf{G}') D_i^1(\mathbb{q},G_z)\cdot\mathbf{s}^i(G_z)\,\delta_{\mathbf{G}'+G_z+\mathbb{k}'+\mathbb{q},\mathbf{G}+\mathbb{k}}. \tag{4.49}$$

The evaluation of the Kronecker-delta reveals a momentum conservation condition for the $\mathbb{k}$-vectors. Nevertheless, there are two different cases that have to be discussed. First, if the sum $\mathbb{k}'+\mathbb{q}$ remains inside the first Brillouin zone (2.20), the scattering is truly momentum conserving, and the conditions

$$\begin{aligned} \mathbb{k}'+\mathbb{q} &= \mathbb{k} \qquad (4.50a)\\ \mathbf{G}'+G_z &= \mathbf{G} \end{aligned}$$

hold. By this, only the sums over $\mathbf{G}$ and G_z are left over in Eq. (4.49).

If $\mathbb{k}'+\mathbb{q}$ points outside the first Brillouin zone, the determination of the matrix elements is more complicated. In this case, the vector is at most as long as one of the first **G**-vectors (which are composed as a sum of the lattice vectors b_i and a factor of $\{-1,0,1\}$). However it interferes in the Kronecker delta with the other **G**-vectors, so, if $\mathbb{k}'+\mathbb{q}-\mathbb{G}_0$ is again in the first Brillouin zone, the following conditions can be extracted from the delta:

$$\begin{aligned} \mathbb{k}'+\mathbb{q} &= \mathbb{k}+\mathbb{G}_0 \qquad (4.50b)\\ \mathbf{G}'+G_z &= \mathbf{G}+\mathbb{G}_0. \end{aligned}$$

This means for these *umklapp-processes* that for all possible $\mathbb{G}_0$-vectors, special matrix elements have to be provided. For a two-dimensional $\mathbb{G}_0$, as it is discussed in this thesis, there are basically eight different possible umklapp vectors.

While it is possible to calculate a set of realistic phonon modes (e.g. by evaluating the atomic forces as in Sec. 3.4) and also the phonon-electron coupling constants D_1^i, the computational requirements to calculate all matrix elements with a mode dependency as in Eq. (4.49) are still very high. A further simplification for the matrix elements can be achieved by replacing the explicit dependency on the slab modes by an approximated dependency on bulk modes. The main issue on this approach is that the special surface properties of the phonons are not included. The bulk modes can be transferred to the supercell by cutting the vacuum space at both sides and applying an adequate coordinate transformation. A single mode in the bulk will

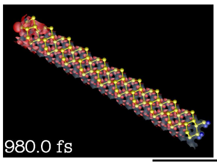

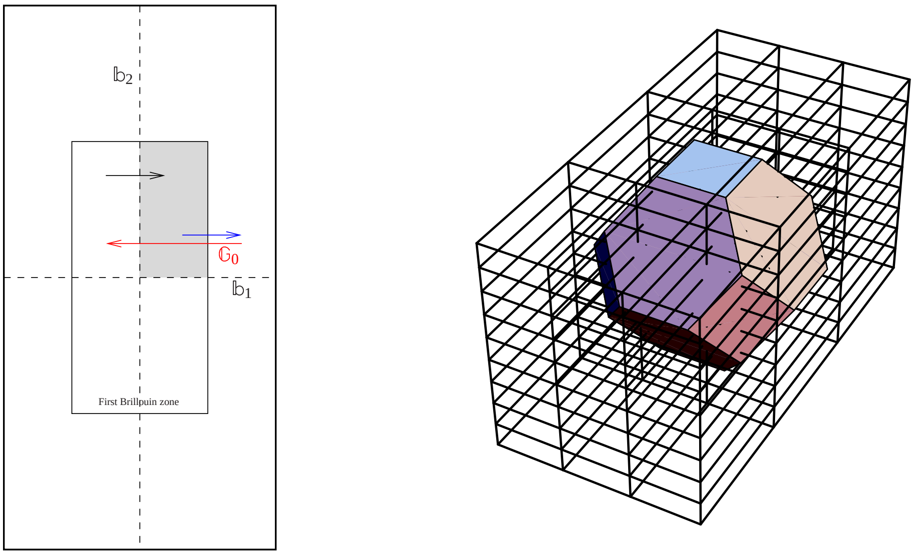

Figure 4.3: ***lhs:*** *Illustration of the possible scattering processes: within the Brillouin zone (black) or over the zone boundary (blue) with an umklapp vector $\mathbb{G}_0$ (red). The reduced zone is shaded in grey.* ***rhs:*** *Illustration of the bulk approximation. The Brillouin zone of the bulk (colored tetrahedron) is entirely covered by repeated Brillouin zones of the slab (brick mesh), such that all* **k***-points of bulk modes can be represented by a slab mode.*

be mapped to several modes with different $\omega_{i\mathbb{q}} = \omega^{\text{bulk}}_{i_{\text{bulk}}\mathbf{q}_{\text{bulk}}}$, where a new pair of $(i,\mathbb{q})$ is assigned from the bulk mode by the transformation in the slab because the Brillouin zone of the bulk is always bigger. By using the bulk mode expansion (2.34), Eq. (4.49) can be expressed by

$$D^{n'\mathbb{k}'}_{\substack{n\mathbb{k}\\ i\mathbb{q}}} = \sqrt{\frac{\hbar}{2M\omega_{i\mathbb{q}}}} \sum_{\mathbf{G}} \sum_{\mathbf{G}'} \overline{u}_{n\mathbb{k}}(\mathbf{G}) u_{n'\mathbb{k}'}(\mathbf{G}') D^{i}_{11}(\mathbb{q}) \cdot \mathbf{e}^{i}_{0} \delta_{\mathbf{G}'+\mathbb{k}'+\mathbb{q},\mathbf{G}+\mathbb{k}}. \tag{4.51}$$

This form of the coupling element corresponds to a macroscopical definition in terms of

$$D_{i\mathbb{q}} e^{i\mathbb{q}\mathbb{r}} = \sqrt{\frac{\hbar}{2\rho V \omega_{i\mathbb{q}}}} \underbrace{V \frac{\partial E_{\text{Ground}}}{\partial V}}_{D^{i}_{\text{DefPot}}} \frac{\Delta V}{V} \bigg|_{i\mathbb{q}}. \tag{4.52}$$

In this representation, the energy D^{i}_{DefPot} describes the relative change of the ground state energy by deformation through volume change $\Delta V/V$. This is the reason why this approach is often denoted as *Deformation potential representation*. Parameters for D^{i}_{DefPot} can in principle be calculated by ab-initio approaches, but are also accessible to experimental investigation [LB87].

4.3.2 Optical matrix elements

The electron light coupling in Eq. (4.10) depends mainly on the momentum matrix element $\mathbf{p}^{n'\mathbb{k}'}_{n\mathbb{k}}$. This matrix element can be calculated by

$$\mathbf{p}^{n'\mathbb{k}'}_{n\mathbb{k}} = \int \mathrm{d}^3 r \overline{\phi}_{n\mathbb{k}}(\mathbf{r}) \frac{\hbar}{i} \nabla \phi_{n'\mathbb{k}'}(\mathbf{r}). \tag{4.53}$$

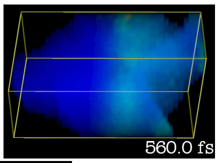

By inserting Eq. (2.26), this simplifies according to

$$\begin{aligned}\mathbf{p}_{n\mathbb{k}}^{n'\mathbb{k}'} &= \frac{1}{2\pi}\sum_{\mathbf{G},\mathbf{G}'}\overline{u}_{n\mathbb{k}}(\mathbf{G})u_{n'\mathbb{k}'}(\mathbf{G}')\int \mathrm{d}^3 r e^{-i(\mathbf{k}+\mathbf{G})\mathbf{r}}\frac{\hbar}{i}\nabla e^{i(\mathbf{k}'+\mathbf{G}')\mathbf{r}}\\ &= \frac{\hbar}{2\pi i}\sum_{\mathbf{G}}\overline{u}_{n\mathbb{k}}(\mathbf{G})\big(\mathbf{G}+\mathbf{k}\big)u_{n'\mathbb{k}}(\mathbf{G}), \end{aligned} \tag{4.54}$$

as the integral evaluates to a Kronecker-delta which assures $\mathbf{G}=\mathbf{G}'$ and $\mathbf{k}=\mathbf{k}'$. Consequently, only diagonal excitations with momentum conservation can be induced by this interaction (This is, besides the classical nature of this interaction, also a consequence of the dipole approximation, where the $\mathbf{A}(t)$-field is interpreted as spatially homogenous). Furtheron, the transitions to the equal state ($n=n'$) cancel out in the dynamical equations (4.31) and (4.32), so due to the orthogonality relation (2.28), the matrix elements are given by

$$\mathbf{p}_{n\mathbb{k}}^{n'\mathbb{k}} = \frac{\hbar}{2\pi i}\sum_{\mathbf{G}}\mathbf{G}\,\overline{u}_{n\mathbb{k}}(\mathbf{G})u_{n'\mathbb{k}}(\mathbf{G}). \tag{4.55}$$

4.4 Evaluation of the scatter matrices

In the scattering equations (4.45), the scatter matrices $\overleftarrow{\Lambda}_{m\mathbb{l}}^{n\mathbb{k}}$ and $\overrightarrow{\Lambda}_{m\mathbb{l}}^{n\mathbb{k}}$ are independent of the dynamics, but determine the relaxation process. The scattering conditions (4.50) are exploited by the elimination of the phonon wave vector sum and the dependent wave vector $\mathbb{q}_{\mathbb{G}_0}=\mathbb{k}-\mathbb{l}+\mathbb{G}_0$, where $\mathbb{G}_0$ can now also equal $\mathbb{0}$. According to Eqs. (4.33), the matrices are determined by the following equations:

$$\begin{aligned}\overleftarrow{\Lambda}_{m\mathbb{l}}^{n\mathbb{k}} &= \sum_i \left|D_{m\mathbb{l}\atop i\mathbb{q}_{\mathbb{G}_0}}^{n\mathbb{k}}\right|^2\Big(\delta(E_{m\mathbb{l}}-E_{n\mathbb{k}}-\hbar\omega_{i\mathbb{q}_{\mathbb{G}_0}})\big(n_{i\mathbb{q}_{\mathbb{G}_0}}+1\big)+\delta(E_{m\mathbb{l}}-E_{n\mathbb{k}}+\hbar\omega_{i\mathbb{q}_{\mathbb{G}_0}})n_{i\mathbb{q}_{\mathbb{G}_0}}\Big)\\ \overrightarrow{\Lambda}_{m\mathbb{l}}^{n\mathbb{k}} &= \sum_i -\left|D_{m\mathbb{l}\atop i\mathbb{q}_{\mathbb{G}_0}}^{n\mathbb{k}}\right|^2\Big(\delta(E_{m\mathbb{l}}-E_{n\mathbb{k}}-\hbar\omega_{i\mathbb{q}_{\mathbb{G}_0}})n_{i\mathbb{q}_{\mathbb{G}_0}}+\delta(E_{m\mathbb{l}}-E_{n\mathbb{k}}+\hbar\omega_{i\mathbb{q}_{\mathbb{G}_0}})\big(n_{i\mathbb{q}_{\mathbb{G}_0}}+1\big)\Big)\end{aligned} \tag{4.56}$$

These equations clarify that the scattering matrices have a lot of vanishing entries. Only those entries, where now the energy-δ-conditions are fulfilled, contribute to the scattering. The energy-variables in the δ-function can be transformed from a to a $\mathbb{l}$-dependency by inverting the kernel of the delta function

$$\mathbb{l}(m,n,\mathbb{k}) = \Big[E_{m\mathbb{l}}-E_{n\mathbb{k}}\pm\hbar\omega_{i\mathbb{q}_{\mathbb{G}_0}}\Big]^{-1} \tag{4.57}$$

and replacing the energy-δ by a condition for $\mathbb{l}$:

$$\delta(E_{m\mathbb{l}}-E_{n\mathbb{k}}\pm\hbar\omega_{i\mathbb{q}_{\mathbb{G}_0}}) = \sum_j \frac{1}{|\nabla_{\mathbb{l}}\big(E_{m\mathbb{l}}\pm\hbar\omega_{i\mathbb{q}_{\mathbb{G}_0}}\big)|}\delta(\mathbb{l}-\mathbb{l}_j). \tag{4.58}$$

The $\mathbb{l}_j$ are the zeros obtained by condition (4.57). The evaluation of these zeros is, of course, non-trivial, and has to be performed numerically on a discrete mesh of $\mathbb{l}$. Still, $\mathbb{l}_j$ is a two-dimensional vector, and the condition for $\mathbb{l}$ can be interpreted as a one-dimensional curve (or a set of curves) $\mathbb{C}^{\pm}_{mn\mathbb{k}i}(s)$ in the Brillouin zone, which depends on all free parameters of the

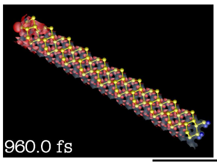

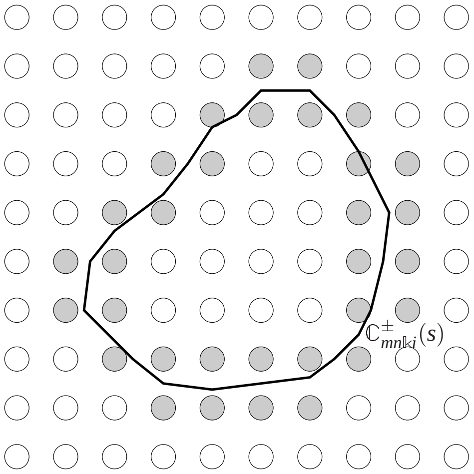

Figure 4.4: *Illustration of the interpolation process for the evaluation of the energy-delta-condition by Eq.* (4.57). *The black curve signifies the path on which the zeros are located, the circles are the mesh of the discretization. Scattering processes are attributed to all mesh points with a grey shading according to the distance of the zero-point on an edge of the mesh.*

equation, including the sign (±) of the phonon energy. The summation over $\mathbb{l}$ in Eq. (4.33) is therewith expressed by an integration over the curve:

$$\sum_{\mathbb{l}} \longrightarrow \int \frac{d\mathbb{C}^{\pm}_{mn\mathbb{k}i}}{ds} \mathrm{d}s \tag{4.59}$$

For given m, n, $\mathbb{k}$, i and $\pm$, the vectors $\mathbb{l}(s)$ pointing to the non-vanishing elements of the scattering matrices $\overleftarrow{\Lambda}^{n\mathbb{k}}_{m\mathbb{l}}$ and $\overrightarrow{\Lambda}^{n\mathbb{k}}_{m\mathbb{l}}$ are given by

$$\mathbb{l}(s) = \mathbb{C}^{\pm}_{mn\mathbb{k}i}(s), \tag{4.60}$$

while their magnitude is set according to

$$\overleftarrow{\Lambda}^{n\mathbb{k}}_{m\mathbb{l}(s)} = \sum_i \left| D^{n\mathbb{k}}_{\substack{m\mathbb{l}(s)\\ i\mathbb{q}_{\mathbb{G}_0}}} \right|^2 \left(G^{-}_{mn\mathbb{k}i}(s) \left(n_{i\mathbb{q}_{\mathbb{G}_0}} + 1 \right) + G^{+}_{mn\mathbb{k}i}(s) n_{i\mathbb{q}_{\mathbb{G}_0}} \right) \tag{4.61a}$$

$$\overrightarrow{\Lambda}^{n\mathbb{k}}_{m\mathbb{l}} = \sum_i - \left| D^{n\mathbb{k}}_{\substack{m\mathbb{l}\\ i\mathbb{q}_{\mathbb{G}_0}}} \right|^2 \left(G^{-}_{mn\mathbb{k}i}(s) n_{i\mathbb{q}_{\mathbb{G}_0}} + G^{+}_{mn\mathbb{k}i}(s) \left(n_{i\mathbb{q}_{\mathbb{G}_0}} + 1 \right) \right) \tag{4.61b}$$

with the size parameters

$$G^{+}_{mn\mathbb{k}i}(s) = \frac{1}{\left| \nabla_{\mathbb{l}} \left(E_{m\mathbb{l}(s)} + \hbar\omega_{i\mathbb{q}_{\mathbb{G}_0}} \right) \right|} \frac{d\mathbb{C}^{+}_{mn\mathbb{k}i}}{ds} \mathrm{d}s \tag{4.62a}$$

$$G^{-}_{mn\mathbb{k}i}(s) = \frac{1}{\left| \nabla_{\mathbb{l}} \left(E_{m\mathbb{l}(s)} - \hbar\omega_{i\mathbb{q}_{\mathbb{G}_0}} \right) \right|} \frac{d\mathbb{C}^{-}_{mn\mathbb{k}i}}{ds} \mathrm{d}s \tag{4.62b}$$

The mapping of the curve to the discrete supporting points of the underlying mesh of $\mathbb{l}$ in Eq. (4.60) must be done using a method of interpolation (cmp. Fig. 4.4). Although the calculation of the mapping and the interpolation is quite costly, it is only required once for a dynamical calculation run, while the multiplication of the matrix is done in every dynamical time step. Thus, due to the high number of vanishing entries in the matrix, it is also a big advantage to implement a method to perform the summations in Eq. (4.45) exclusively on the non-vanishing entries.

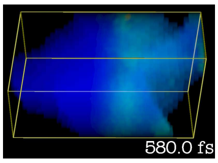

Part II

Computational Implementation and Investigation of Electron Relaxation at Silicon (001)

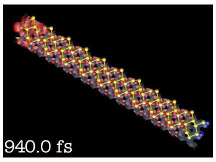
940.0 fs

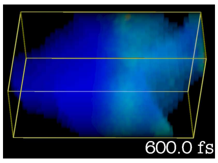

Chapter 5

Density-Functional Calculations at the Silicon (100) 2×1 surface

After presenting the basics of theory, we now proceed to the application of the methods introduced in Part I. As first step, we thus perform density-functional calculations for a specific surface system. As surface system, the silicon (001) surface is chosen for investigation (cmp. Sec. 1.2). At this surface, various locally identical reconstructions appear, and according to the size of the reconstruction unit cell, a number of additional surface bands occurs in the band structure. For temperatures of about 90 K, the predominant reconstruction is the 4×2 reconstruction. In our simulations, we will use the asymmetric 2×1 reconstruction, which is energetically close to the 4×2 reconstruction and already contains most features.

The first step in calculating a surface structure, however, is to investigate the corresponding bulk structure. For silicon, this is a diamond lattice with a two-atom basis in a tetrahedral unit cell. The main purpose of these investigations is, besides the adjustment of parameters for the applied computer program, the derivation of a theoretical bulk lattice constant. A good agreement of the experimental and the theoretical lattice constants is a prerequisite for a trustworthy calculation.

The DFT calculations have been carried out with the program package `fhi98md` [BKNS97], which has a long reputation for structure calculations. It has been programmed in *Fortran 90* and is particularly adapted for the use in solid state supercell computation.

5.1 Calculations on bulk silicon

For the band structure calculation with the `fhi98md` package, several steps are necessary. The first step consists of the calculation of the pseudopotentials (cmp. Sec. 3.5) using the program `fhipp`. In the atomistic nomenclature, the silicon nucleus has 14 protons and has thus an atomistic charge of $14e_0$. The first ten electrons are the core electrons, they are described by the s^1, s^2 and p^2 orbitals. The pseudopotential is build up on a calculation of these ten core electrons. Then, with the pseudopotentials, the ground state calculation can be started, where the *Kohn-Sham-states* for the electrons are determined for the ground state. As a further step, a band structure can be evaluated by using the electron density from the ground state calculation (Sec. 5.1.2).

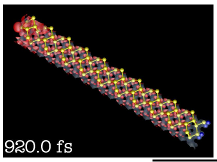

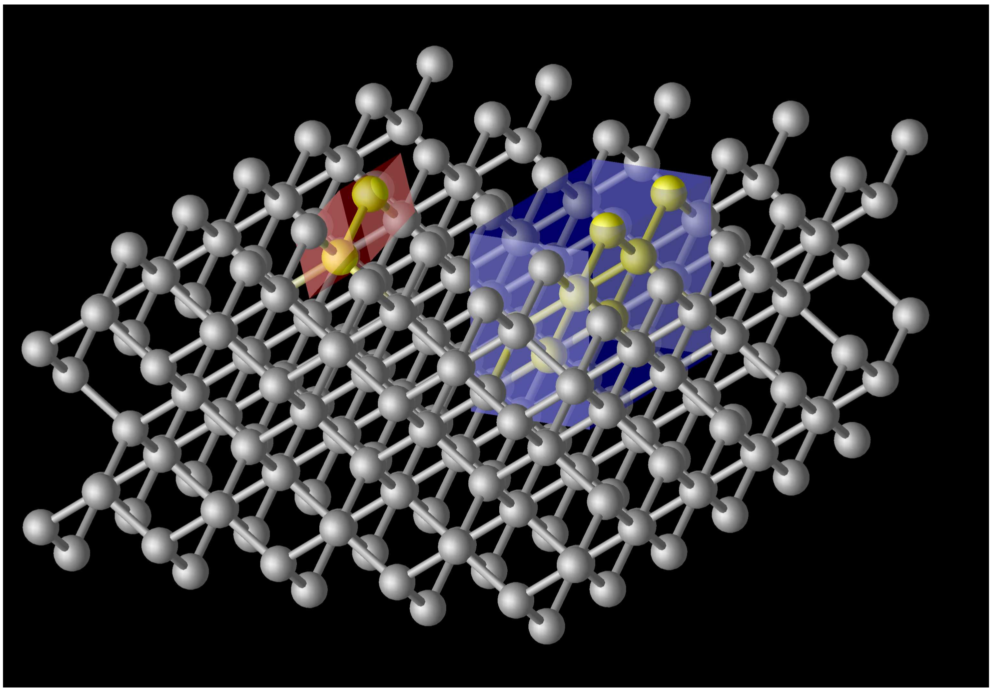

Figure 5.1: *The silicon diamond lattice structure. The top plane represents a (100) cut of the structure. The bulk unit cells for the diamond structure (red) and an orthorhombic (2×1) cell (blue) are indicated.*

5.1.1 Ground state calculation

The calculation of the bulk structure is then achieved using a plane wave basis defined by the cutoff radius (Eq. (3.22)), the lattice basis (Eq. (2.17)) and its reciprocal counterpart (Eq. (2.19)). The lattice basis in diamond geometry is influenced by the bulk lattice constant a, which can be understood as a isotropic stretch factor (although it is oriented at the underlying cubic supercell, rhs. of Fig. 5.2). For the ground-state calculation, a regular mesh (*Monkhurst-Pack-mesh*) of **k**-points on the first Brillouin-zone is chosen in order to sufficiently describe the different features of the wave functions at different **k**-points. The number of **k**-points is also a parameter to these calculations. Due to the high symmetry of the diamond lattice, only a fraction of the mesh points have to be included in the calculation, as many of them are geometrically equivalent and the others can be mapped by symmetry operations. The Kohn-Sham-equations (Sec. (3.2)) for this reduced **k**-point set are then evaluated using the iterative approach described in Fig. 3.1. The algorithm continues looping until the ground state energy has reached a total minimum, which can be investigated by looking at the variation of the energy per time step. For the diagonalization of the Hamiltonian in the single particle Schrödinger equation (3.8), an iterative approach (*Williams-Soler* or *damped Joannopoulos*) is used which is possible for a self-adjoint Hamiltonian. In spite of the disadvantages of such an algorithm (dependency on parameters for solving algorithm, required orthogonalization of eigenvectors after each iteration step), the numerical effort compared to a polynomial solving scales with a more favorable dependency on the size of the structure. The choice of good parameters for the algorithm decides about the number of iterations required for convergence (or, in the worst case, about the divergence),

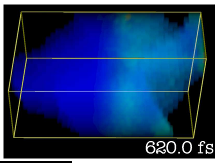

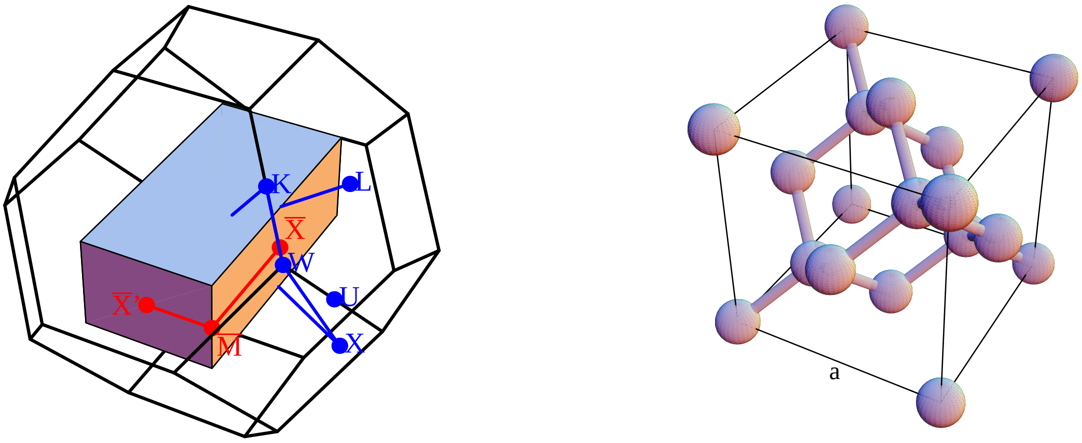

Figure 5.2: ***lhs:*** *Brillouin zone of the diamond lattice structure (black lines) and of the orthorhombic 2×1 bulk structure (colored brick) in the same geometry. The zone boundaries fulfill condition* (2.20)*.* ***rhs:*** *Illustration of the diamond structure inside a cubic lattice. The edge of the cubic superstructure (a) is used as lattice constant for the diamond structure.*

these parameters depend mainly on the particular lattice structure.

Additionally to the diamond-lattice bulk calculations, the silicon bulk is calculated within another superstructure. With regard to the future 2×1-surface-structure calculations, it is useful for comparison to perform a computation in the same surface geometry. To this end, a single orthorhombic (001) 2×1 cell (containing eight atoms) is investigated. A silicon bulk structure, the diamond unit cell (red) and the orthorhombic unit cell (blue) are presented in Fig. 5.1. The corresponding first Brillouin zones for the **k**-vectors, given by condition Eq. (2.20), are shown for those two geometries in Fig. (5.2). The orthorhombic cell, which is bigger in real space (Fig. 5.1), supplies a smaller Brillouin zone in the reciprocal space (lhs of Fig. (5.2)). Some high symmetry points and lines are indicated in the two Brillouin zones.

The check on the dependency of the diamond bulk calculation on certain computational parameters is summarized in Figs. 5.3 and 5.4. The course of action to investigate the bulk lattice minima and the total energy minima with respect to the density of the **k**-point mesh and the cutoff energy (Eq. (3.22)) is as follows: first, sampling values are chosen for the lattice constant and the cutoff energy around the estimated minimum value. For the mesh, only a few choices are possible for the discretization (like $4 \times 4 \times 4$ or $8 \times 8 \times 8$). Calculations are then performed for all combinations of the values for lattice minimum, the cutoff energy and the mesh, allowing to extract ground state energy values from these. The most evident conclusion from these calculations if Fig. 5.3 is that a mesh of $4 \times 4 \times 4$ is sufficient for this bulk description, as there is no apparent difference to the higher discretized computations. The second conclusion from this Figure is that the energy minimum is still influenced by the cutoff energy, though the energy change is small (≈ 0.05 Ry between 8 Ry and 20 Ry cutoff). A convergence is however seen for the highest cutoff energies. In Fig. 5.4, the lattice minima and corresponding ground state energies of Fig. 5.3 are plotted. These minima are found by fitting the previously calculated lattice-energy curves with a thermodynamical state equation (*Murnaghan equation*), from which the minimum can be derived analytically. This is achieved using the program `murn`, which is also a part of the `fhimd` package. Both ground state energy

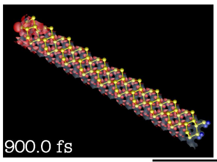

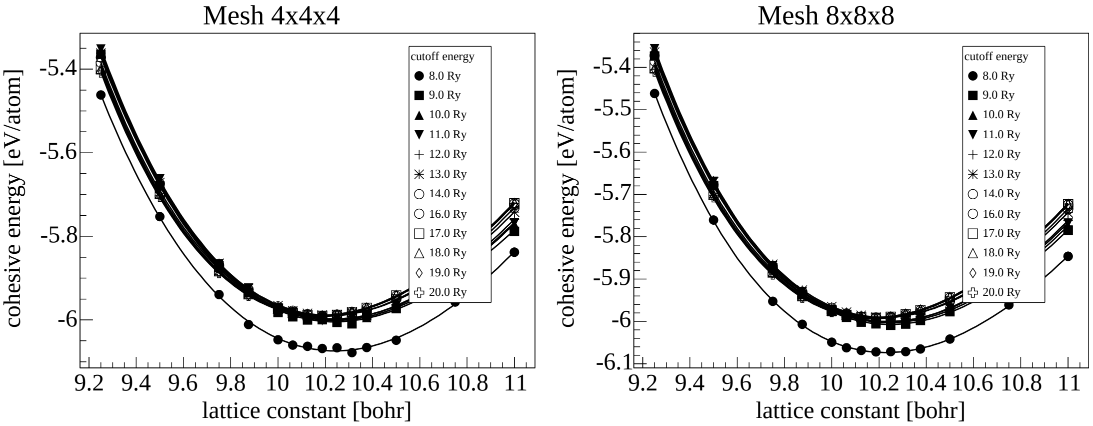

Figure 5.3: *Determination of the lattice constant minimum with respect to the cohesive energy per atom and investigation of someconvergence criteria for the diamond bulk lattice. The different markers signify a difference of the cutoff energies. On the lhs, the calculations are performed with a mesh of* $4 \times 4 \times 4$*, on the rhs, for* $8 \times 8 \times 8$*. No significant changes are found between the two pictures*

and lattice constant finally converge at a cutoff radius of 20 H, while the ground state energy shrinks monotonously, the lattice constant has a non-continuous behaviour. In contrast to the variational principles used to derive the Kohn-Sham-equations, no equivalent approach holds for the **k**-point sets, so a global minimum can not be found in any case by increasing the density of the mesh.

5.1.2 Band structure calculation

The band structure of the two bulk geometries can be then calculated using a second run of the `fhimd` program. A band structure run typically needs only points on some symmetry lines with a relatively high discretization with respect to the discretization needed to perform a converging ground state calculation. The execution of a ground state calculation on a mesh containing all necessary points for the band structure is therefore a waste of computer resource requirements. An easy way to avoid this relatively high discretization is to insert an electron density from another calculation with low discretization (but high enough to assure a proper convergence) into a *band structure calculation*, where only the **k**-points which are to be shown in the band structure are included. The electron density in this run is not changed during the iterations, so the only task of the program is to diagonalize the Hamiltonian at the chosen **k**-points, without any self-consistent iterations. A justification of this procedure is that the results for the electron density for a converged calculation is not significantly changed by applying a denser mesh with more **k**-points. This technique is particularly useful if conduction band states are calculated, as these are irrelevant for the electron density and the ground state energy. Another advantage is the fact that there are no restrictions about the **k**-points chosen in the second run. Consequently, it is possible to calculate a numerous subsets of **k**-points in parallel within totally independent calculations. This feature will be used extensively in Chapter 6.

The band structures for the two bulk geometries are shown in Fig. 5.5. For the diamond lattice (lhs), a true three-dimensional path through the Brillouin zone is taken. The nature of silicon as semiconductor is pointed out by the bandgap between the valence bands ($\widehat{=}$ the lowest

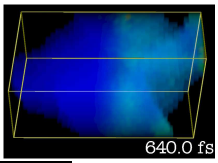

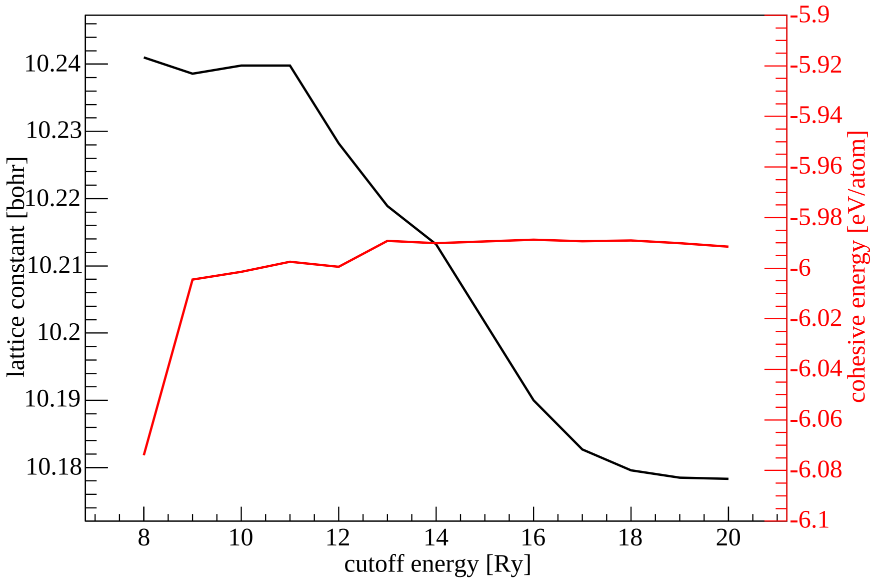

Figure 5.4: *Convergence test for the cutoff energy. The minimum bulk lattice constant (black) and the associated cohesive energy per atom (red) are gained from a fit with a murnaghan state equation, as shown in Fig. 5.3.*

four bands) and the conduction bands (the higher bands). At low temperatures, only the valence bands are populated. It is clearly visible that the band gap is only indirect, the maximum of the highest valence band is located at another **k**-point as the minimum of the lowest conduction band. Consequently, for an optical excitation with band gap energy ($\approx$ 1.1 eV), a scattering of the photon via an auxiliary phonon is necessary. A direct excitation, as it is described by the optical Hamiltonian (2.45) or (2.47), is only possible for much higher energies ($\approx$ 2.5 eV).

For the orthorhombic bulk structure (rhs of Fig. 5.5), the path is oriented at the surface geometry. To this end, only the k_x and k_y parts of the vector are non-zero. In this two-dimensional cut of the Brillouin-zone, the indirect band gap of the diamond lattice is not visible any more. The selection rules on the participating electron states, however, still forbid optical transitions by these channels[1]. Furthermore, the number of bands has increased according to the augmentation of the number of atoms in the unit cell, while, on the other hand, the bands in the band structure are related by a folding at the symmetry lines. This is clearly an effect of the reduced Brillouin zone with respect to the diamond lattice. Note that no new physical effects can be expected by just augmenting the bulk unit cell. A comparison to surface structures can be achieved by also varying the k_z-coordinate of the orthorhombic bulk cell. This allows to evaluate a range of possible energies for a specific **k**-point and band in the surface geometry, on which the surface band structure can be mapped lateron. An application of this technique is shown in Figs. 5.6-5.11.

---

[1] This can be seen by reminding that the wave functions of the states are not changed by switching only the geometry. Thus, a wave function $e^{i\mathbf{kr}}u_{n\mathbf{k}}(\mathbf{r})$ in the diamond structure is replaced by a wave function $e^{i\tilde{\mathbf{k}}\mathbf{r}}e^{i\mathbf{k}_0\mathbf{r}}u_{n(\tilde{\mathbf{k}}+\mathbf{k}_0)}(\mathbf{r})$ in orthorhombical symmetry, where $\tilde{\mathbf{k}}_0$ is the constant lattice vector difference originating from the reducing of the zone and, while nonzero, constitutes a new band. While calculating momentum matrix elements (Sec. 4.3.2), $\tilde{\mathbf{k}}_0$ annihilates all matrix elements which are not non-zero before in the diamond lattice.

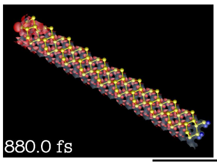

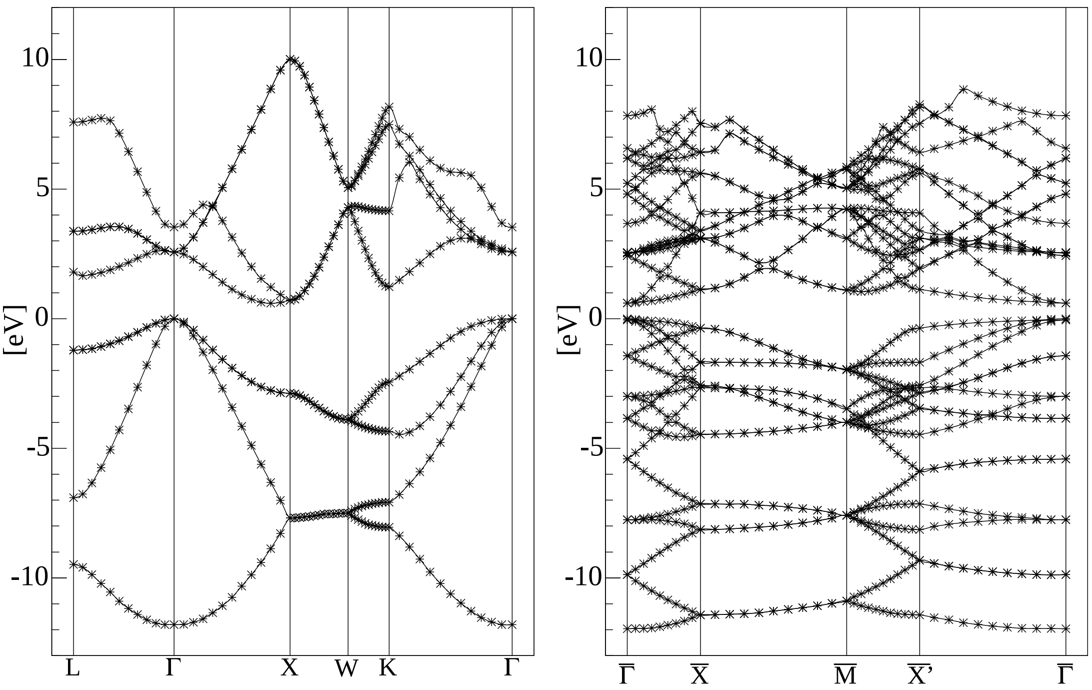

Figure 5.5: *Bulk band structure for the ground states and the lowest conduction states for silicon. On the lhs, the band structure along the high symmetry lines of the diamond unit cell is shown. On the rhs, the bandstructure along a 2×1 (100) unit cell (for $k_z = 0$) is depicted. The indirect band gap in the lhs picture is no more visible in the rhs.*

5.2 Supercell calculations for the 2×1 surface

After discussing the bulk structure, we will now investigate the 2×1 reconstruction of a silicon (100) surface by the supercell approach. In contrast to the atomic positions of the bulk cells, which are determined by the underlying symmetry group (which only leaves the lattice constant as an open parameter), the geometrical structure of a surface reconstruction is given in a orthorhombical cell with a two-dimensional symmetry. The atomic positions are not precisely known beforehand, and at surface, huge deviations from the corresponding bulk positions can be expected. The atomic positions are however determined by the interatomic forces on the ions, which can be calculated using the method introduced in Sec. 3.4. Nevertheless, the use of this technique is numerically much costlier than the pure bulk calculations, as not only the lattice structure is much bigger for a reasonable slab system (which increases both the number of bands by the number of atoms and the number of plane waves (**G**-vectors) by the energy condition (3.22) in the discretization), but also an additional loop over the ground state minimization has to be implemented (cmp. Fig 3.1). In this second loop, the atomic positions can be modified and slowly converge to the equilibrium position (see Sec. 3.4). While this method is applicable by a physical point of view to find the positions of all atoms of the structure, the algorithm is often numerically instable if the number of degrees of freedom is too high, and also the need of CPU time is highly influenced by that fact. Consequently, it is usually required to constrict the motion of atoms to those which are close to the reconstructed surface and are

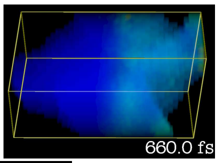

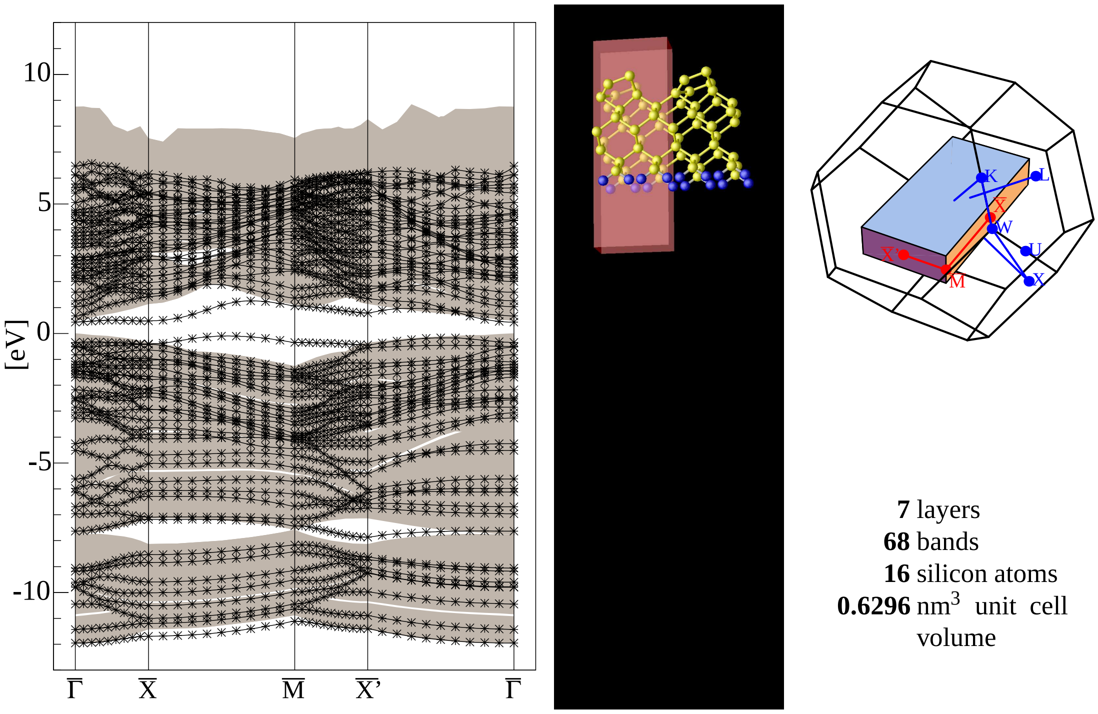

7 layers
68 bands
16 silicon atoms
0.6296 nm^3 unit cell volume

Figure 5.6: *Band structure, atomic structure and Brillouin zone of a* ***7 layer supercell****.*

therefore subjected to perform big changes. The decision of how many atoms should be moved, is based on the calculation and analysis of the force constants for all atoms and can be assisted by test calculations.

In the case of a silicon (100) 2×1 surface, the most important effect of surface reconstruction is the formation of a *tilted dimer*. It is obvious that this requires a huge deformation of the first atomic layers with respect to the bulk. In our calculations, the three first layers are allowed to move. One measure for the quality of the Density Functional calculation in this context is the comparison of the experimental to the calculated dimer angle. In silicon, the *p*-orbitals of the dimer atoms cause the appearance of the new surface bands , which partly reach energetically into the band gap. A consequence of this is that the position of the atoms is not only influenced by known program parameters (cutoff energy), but is also highly dependent on the occupation of the surface states, which is, due to the reduced band gap, much more sensitive to temperature changes than the bulk material. The *fhimd* code allows a temperature dependent population of the conduction band states.

5.2.1 Ground state calculation

The procedure to calculate the electronic band structure has, as in the case of the bulk, two steps: First, the energy is minimized, the electron density is calculated and supplementally the structure is optimized by moving some atoms, all this at a relatively low discretization of the **k**-point mesh. The initial electron density is generated from atomic orbitals of the valence electrons, these are stronger bound to the core atoms and accelerate the convergence of the *Kohn-Sham* wave functions towards the ground state, including the states in the surface bands. A structure optimization step can be applied after convergence of the ground state energy for

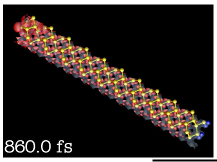

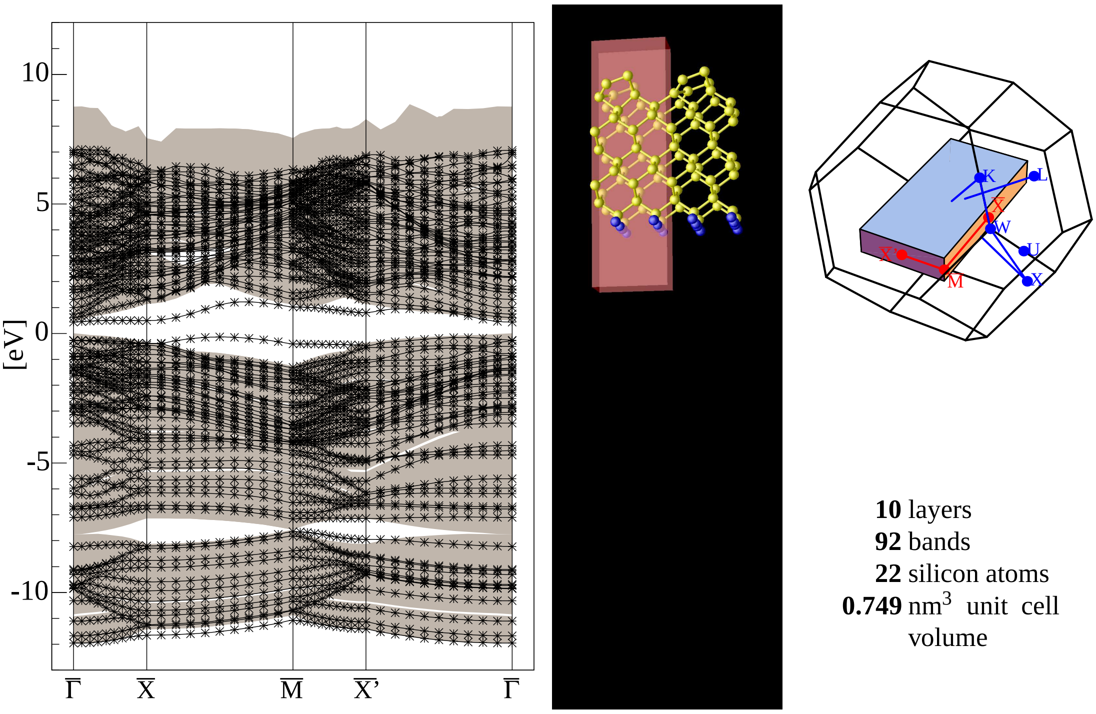

10 layers
92 bands
22 silicon atoms
0.749 nm^3 unit cell volume

Figure 5.7: *Band structure, atomic structure and Brillouin zone of a **10 layer supercell**.*

given atomic positions, whereby a damped dynamical force equation (*damped verlet algorithm*) is exploited. After the moving, the formerly gained electron density is reused and taken as an initial condition for the new ground state energy minimization. The parameters governing the atomic move (the "mass", the "damping" and the "timestep") have to be adapted in order to assure find the global minimum. All in all, the density-functional calculations for the supercell with structure relaxation are much more elaborate than for the bulk and the convergence depends on numerous parameters, however, the convergence calculations for the bulk give hints about the cutoff energy and the lattice constant to use.

Ground state calculations have been realized for different cutoff energies ranging from 8 Ry

		no. of layers					
	[°]	**7**	**10**	**15**	**22**	**30**	**40**
cutoff energy [Ry]	**8.0**	18.369	17.092	17.071	*	17.071	18.175
	10.0	18.369	18.184	18.156	18.150	18.160	18.143
	12.0	18.369	18.231	18.218	*	18.192	18.187
	14.0	18.369	18.123	18.212	*	18.100	18.095
	16.0	18.369	18.096	18.212	*	18.071	18.069
	18.0	18.369	18.110	18.212	*	18.086	*
	20.0	18.369	18.124	18.212	*	18.098	18.096

Table 5.1: *The dimer tilting angle in dependency of the number of layers and cutoff energy. For the starred table entries, data is incomplete.*

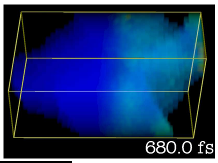

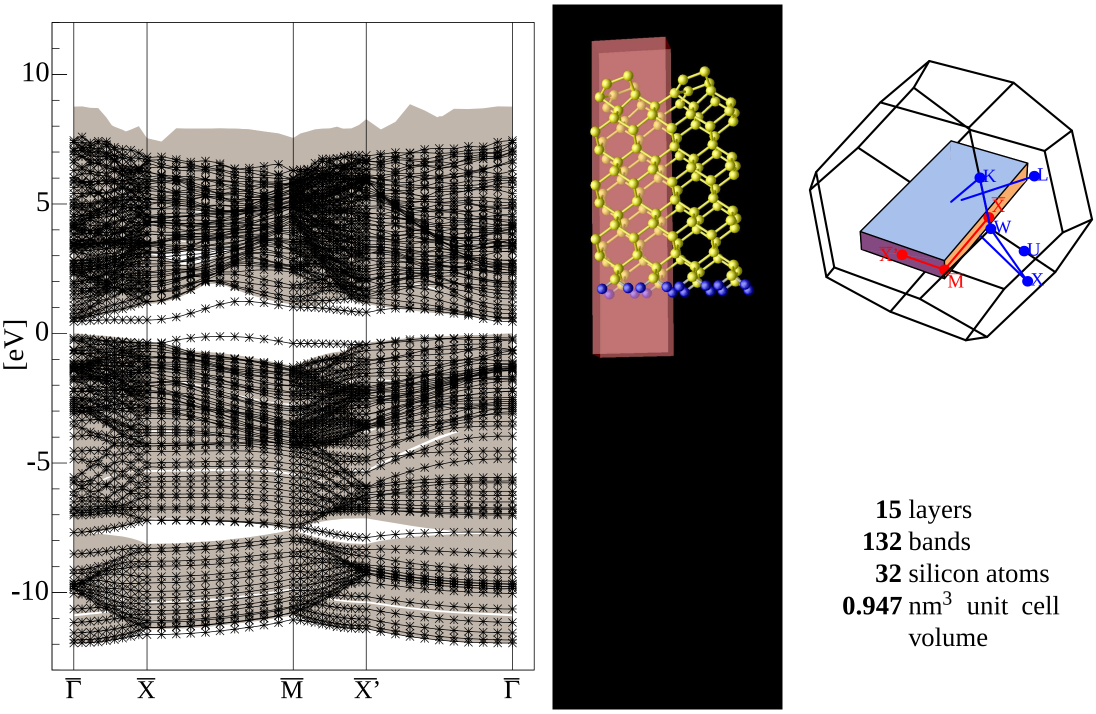

15 layers
132 bands
32 silicon atoms
0.947 nm^3 unit cell volume

Figure 5.8: *Band structure, atomic structure and Brillouin zone of a* ***15 layer supercell****.*

to 20 Ry and for a different number of layers ranging from 7 to 40. The temperature for the occupation of the states has been fixed at 300 K, and four conduction bands is included into this calculation, which is necessary to allow a statistical distribution for this temperature. In Figs. 5.6-5.11, the resulting structures of these calculations for a cutoff energy of 10 Ry are depicted in the middle. The extension of the unit cell, including the vacuum of the supercell, is indicated by the red brick, the yellow spheres represent the silicon ions, whereas the blue spheres symbolize the passivating hydrogen atoms at the backside of the slab (bottom). The tilted dimer and the reconstruction of the first layers is clearly observable on top of the structures. The corresponding Brillouin zones in reciprocal space and their size with respect to the

		no. of layers					
	[eV]	**7**	**10**	**15**	**22**	**30**	**40**
cutoff energy [Ry]	**8.0**	-64.999	-88.629	-127.866	*	-246.168	-324.935
	10.0	-65.265	-88.982	-128.509	-183.845	-247.087	-326.141
	12.0	-65.434	-89.203	-128.671	*	-247.654	-326.879
	14.0	-65.531	-89.328	-128.842	*	-247.965	-327.283
	16.0	-65.581	-89.391	-128.926	*	-248.110	-327.470
	18.0	-65.605	-89.419	-128.962	*	-248.169	-327.544
	20.0	-65.618	-89.434	-128.978	*	-248.195	-327.575

Table 5.2: *The ground state energy in dependency of the number of layers and cutoff energy. For the starred table entries, data is incomplete.*

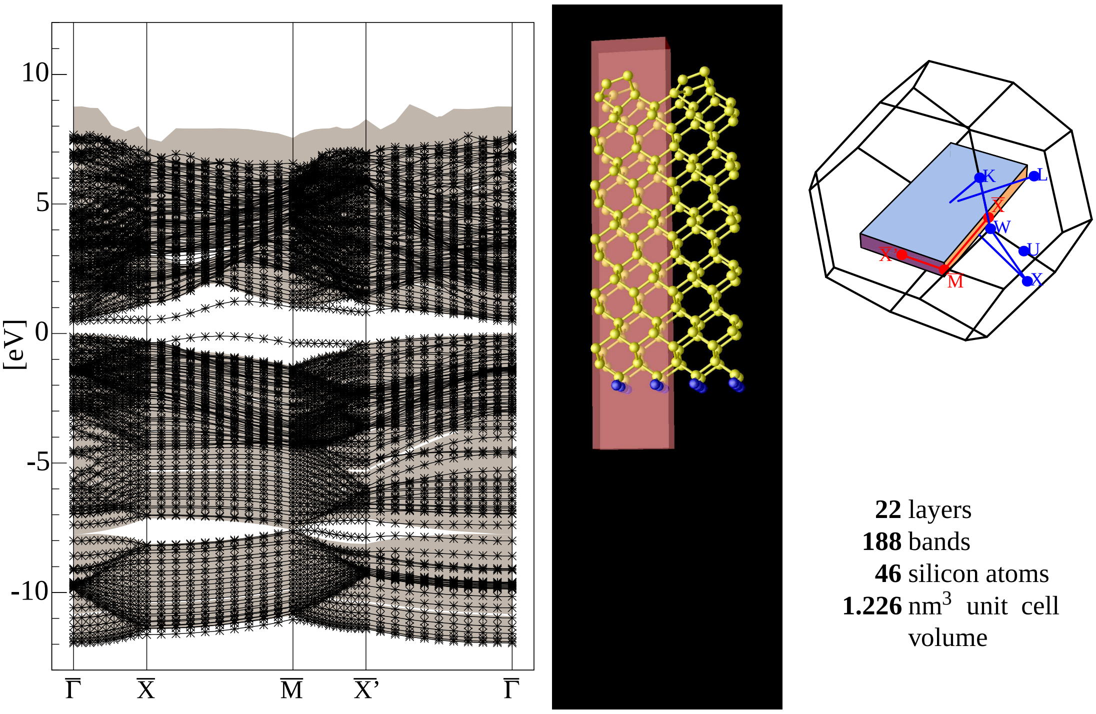

Figure 5.9: *Band structure, atomic structure and Brillouin zone of a* ***22 layer supercell****.*

bulk Brillouin zone are shown on the rhs of the pictures. The relation between the dimer tilting angle and the cutoff energy and the number of layers is shown in table 5.1. Obviously, the changes with respect to the cutoff energy are quite insignificant, whereas the variation depending on the layer number has slightly more effect. As a matter of fact, both the need of CPU time and of hard disk space for the storage of the electronic wave functions (which are not problematic for single band structure runs) for a big number of $\mathbb{k}$-points (up to 1089, cmp. Chapter 6), which will be needed in later steps of our calculation, are increasing fast with the cutoff energy (as the number of **G**-vectors is increased approximately by a factor $\sim E_{\mathrm{cutoff}}^{3/2}$, cmp Eq. (3.23)). We conclude therefore that for the given resources, it is a minor limitation to the surface properties to use a cutoff energy of 10 Ry, where the dimer angle has yet the right magnitude, but the other parameters are not fully converged. In table 5.2, the ground state energies for the different cutoff energies and number of layers are indicated. Although only each row of the table can be compared, it can be seen that the overall difference is below one percent of the total value of a row. This error seems tolerable in view of the increase in CPU efficiency. A final decision about the cutoff energy, however, could only be investigated by performing parallelly all subsequent steps of calculation for different cutoff energies, which requires storing most intermediate data from density-functional calculation runs. The storage system is therefore the limiting factor of the entire calculations, and at the time the simulations where started, only a single calculation could be established on the hard disk.

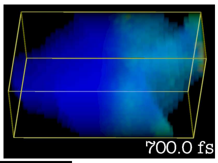

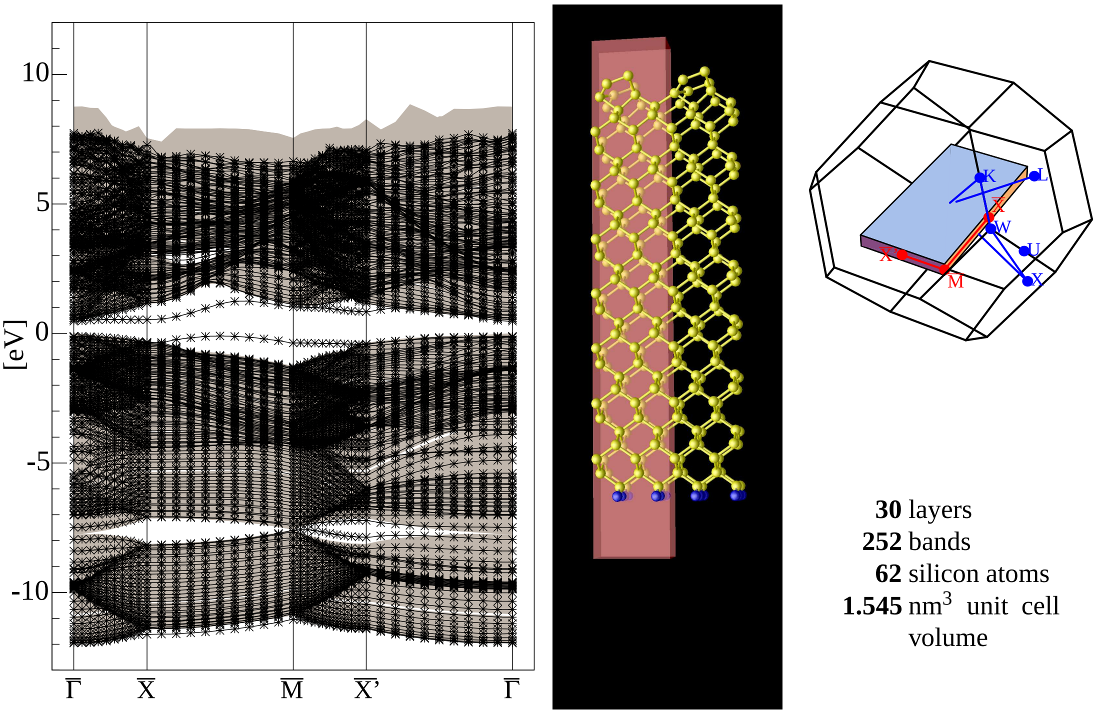

Figure 5.10: *Band structure, atomic structure and Brillouin zone of a* ***30 layer supercell****.*

5.2.2 Band structure calculation

In contrast to the time consuming structure relaxation iterations for the ground state, the band structure calculations for a supercell structure are not more complex than the band structure calculations for the bulk. However, as we intend to describe a great portion of the conduction bands where phononic relaxation processes take place, the same number of conduction bands as of valence bands is calculated in the band structure run. As in the bulk case, the electron density is not updated and inserted from a beforehand accomplished ground state calculation. Of course, in addition to this, the modified atomic positions from the structure relaxation have to be considered in place of the idealized starting positions, as the electron density is now oriented at the new, more realistic positions. Due to the supercell approach (and in contrast to the rhs pictures in Figs. 5.6-5.11, where the volume of the reciprocal lattice vectors is shown), the Brillouin zone is now truly two dimensional (cmp. Sec. 3.7), as the third dimension does not imply a new continuous quantum number. The path in the Brillouin zone (which is the same as introduced for the 2×1 orthorhombic bulk cell in Sec. 5.1) is oriented at the border of the irreducible part of the surface Brillouin zone. The irreducible part of the zone is in principle half of the whole zone (e.g. $k_y > 0$), this is related to the inversion symmetry along the $x-z$-plane. From the time reversal invariance of the Schrödinger equation, an additional inversion symmetry at the $\overline{\Gamma}$-point can be extracted, which holds at least for the energy eigenvalues (whereas the wave functions are complex conjugated – this is however no limitation to the later steps of our calculation)[2]. Consequently, the irreducible part of the Brillouin zone is

---

[2] The main reason for this property is the fact that the potentials in the Schrödinger equation are real and thus, the energies are not influenced by complex conjugation of the equation – but the $\mathbb{k}$-vectors are transformed to $-\mathbb{k}$.

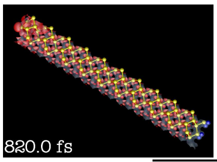

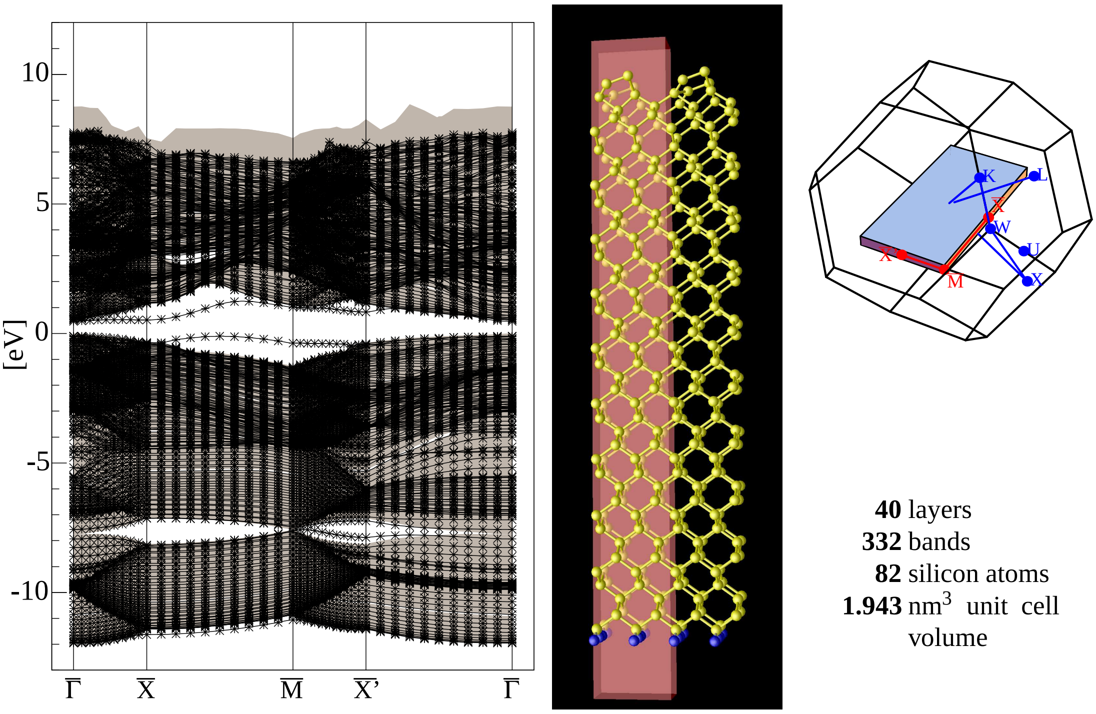

Figure 5.11: *Band structure, atomic structure and Brillouin zone of a **40 layer supercell**.*

represented by only a quarter of the original zone, like the part of Ω where $k_x \geq 0$ and $k_y \geq 0$ (as indicated in Fig. 4.3). The symmetry path in the Brillouin zone is indicated by the red points and lines in the rhs pictures of Figs. 5.6-5.11.

The band structures of calculations for structures with 7, 10, 15, 22, 30 and 40 layers are shown on the lhs of Figs. 5.6-5.11. In the background of these pictures, the projection of the bulk states obtained from the orthorhombical bulk band structure (Fig. 5.5) by varying the k_z component (cmp. Sec. 5.1) is drawn. By this, a direct comparison of the bands in the surface structure to the bulk bands is possible. It is clearly observable how the size of the structure influences the number of resulting bands in the calculation. By increasing the number of layers, the continuous k_z-dispersion in the bulk is replaced by discrete energy eigenvalues of the particular bands. While for seven layers in Fig. 5.6, the 68 single bands are clearly separated and there exists a wide energy spacing between the energy values, as it is similarly the case in a nano-confined system (like a quantum well structure), and also big areas of the bulk bands are not covered by the slab bands, the situation is quite different for 40 layers. Here, in Fig. 5.11, the slab bands are a fairly good approximation of the bulk, all regions of the bulk band structure are represented in the slab band structure, and at some places, the slab bands are even sufficiently dense to prevent a clear distinction of the separate bands. At the same time the number of bands has increased to 332. The process of transition from a "*confined*" system to a "*bulk like system*" is illustrated in the intermediate figures 5.7, 5.8, 5.9 and 5.10. Of course, a clear classification is impossible, as it depends much on the actual problem which surface properties are outstanding and most important, but the later dynamical investigations in Chapter 7 show that bulk properties are much better approximated by slabs of 30 layers and more than with less than 20 layers.

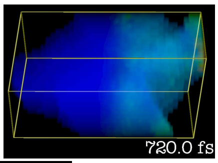

In all of the figures, however, the main difference to the bulk bands is concordantly given by two additional bands which reach into the band gap between valence and conduction bands (at 0 eV). These bands are related to the dimer surface reconstruction of the slabs, so it is evident that no corresponding feature can be contained in a pure bulk description of the band structure. These two bands are classified as D^{up} and D^{down} surface bands, which are related to the dangling bonds of the p-orbitals of the dimer atoms at the surface. While the D^{up} band is a valence band and reaches deeply into the zones where the bulk bands exist (it is only clearly inside the band gap between $\overline{X}-\overline{M}-\overline{X}'$), the D^{down} band is a conduction band and only touches the bulk at $\overline{M}-\overline{X}'$. These bands are found in any of the calculations, the position is only slightly changed throughout the augmentation of the layer number. A certain difficulty lies in the fact that for the calculations with lower layer number (7-15 layers), the trend of the surface bands is definitely distinguishable from the bulk bands in the regions where they overlap. This, however, is an artificial feature due to the limited number of bulk bands in those calculations and is therefore not visible in the higher layer calculations (22-40 layers). A non-ambiguous assignment of the calculated eigenvalues to the bands is only possible by geometrical investigation of the symmetry of the associated electron state, e. g. by projection on the surface orbitals [Egg05]. This part of the study has not been accomplished in this thesis: the dynamical investigations in Chapter 7 are uniquely extended on the conduction bands, and the involved D^{down} surface band is much better separatable from the bulk bands than the D^{up}.

In Fig. 5.12, the location and extension of the D^{up} and D^{down} surface states is exemplarily shown for a $\mathbb{k}$-point on the $\overline{X}-\overline{M}$-line, where the surface bands are well defined and separated from the bulk bands. The square modulus $|\phi_{n\mathbb{k}}(\mathbf{r})|^2$ of the wave functions is shown for any of the slab calculations with different slab layers. For any of the two wave functions show, two isosurfaces are plotted: one at an electron density of $2\cdot10^{-4}$ (solid fill), whereas the maximum is at $3\cdot10^{-4}$, and the other at an electron density of $2\cdot10^{-5}$ (hollow fill). By the solid filled isosurfaces, it can be seen that the orientation of the wave functions is still influenced by the p-orbitals of the dimer atoms; the D^{up} band is built up from the highest level dimer atoms (red), while the D^{down} band is related to the lower level dimer atoms (green). The major part of the wave functions is located in the first three layers of the slabs. Furthermore, the optical appearance of the surface wave functions is fairly similar for all different calculations with different layers, even at the seven layer calculation, the main features of the electron distribution are reproduced. Nevertheless, in the seven layer calculation, the a certain electron density of the surface states still reaches the backside atoms of the slab, yet at ten layers, the decrease of the surface state leads to a total vanishing of the state at the sixth layer.

We can conclude from these considerations that seven layers are in fact sufficient to investigate principle features which stem from the surface reconstruction (like the surface reconstruction, dimer tilting angle, dispersion of the surface bands or the extension of the surface states) and also most properties of the bulk. If however an accurate description of the band structure with a dense discretization of the bands on the energy scale is required for subsequent calculations, the slab has to be expanded to at least 20 to 30 layers. In this case, we can also expect that the bulk band structure and the interplay of bulk and surface states is mapped sufficiently precise by the supercell band structure. These observations, which are purely empiric at this level of examination, will be confirmed be the dynamical calculations in Chapter 7, where the interaction of bulk and surface is a part of the discussion.

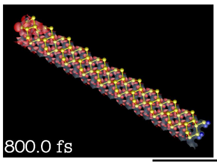

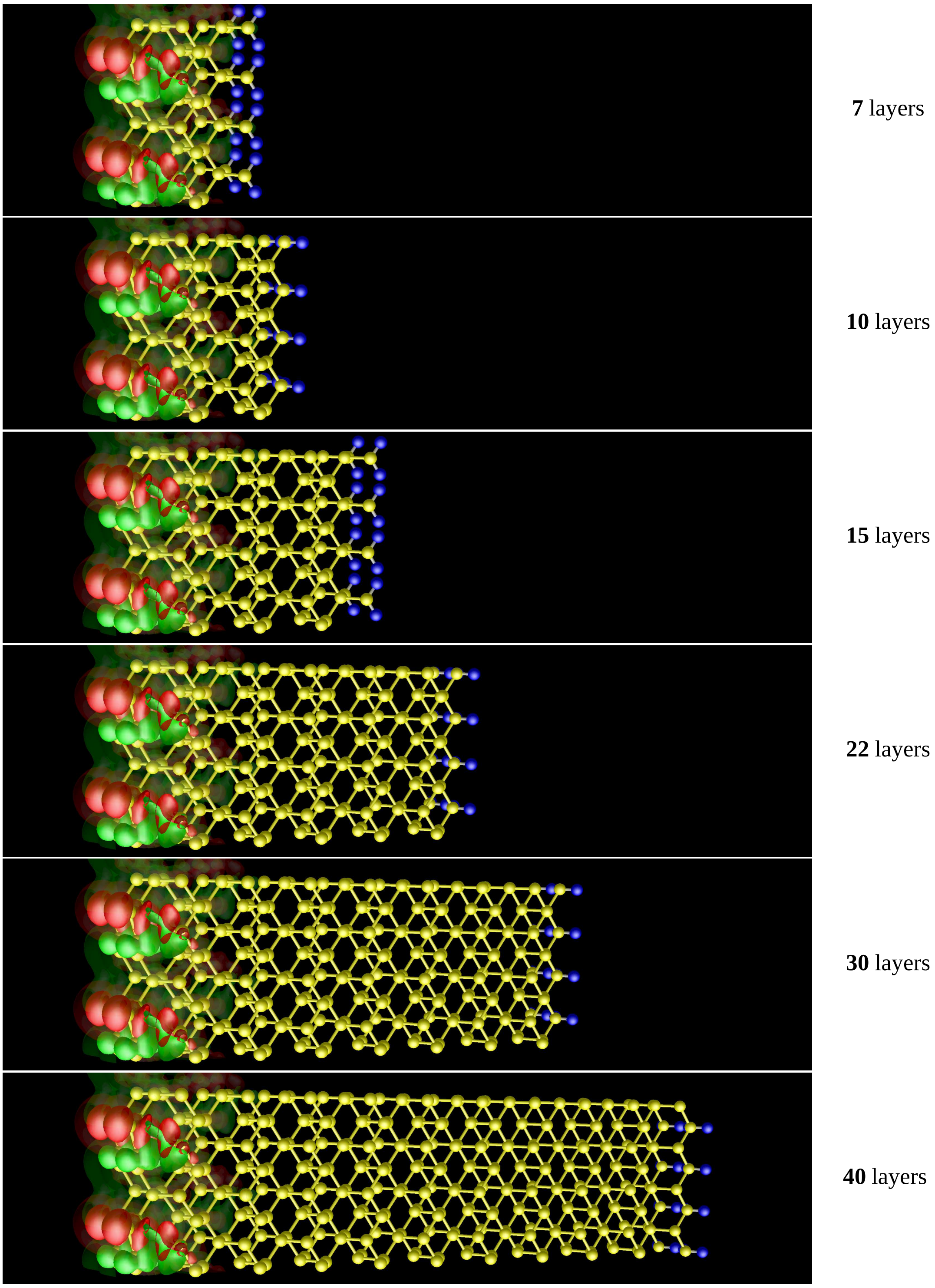

Figure 5.12: *Location of the* D^{up} *(red) and* D^{down} *(green) surface states at* $\Bbbk = (8.20\,\mathrm{nm}^{-1}, 8.20\,\mathrm{nm}^{-1})$. *At this point on the* $\overline{X} - \overline{M}$*-line, the surface bands are clearly separated from the bulk bands (see band structures in Figs 5.6-5.11). The isosurfaces are plotted at an electron density of* $2 \cdot 10^{-4}$ *(solid) and at* $2 \cdot 10^{-5}$ *(hollow). The p-orbital shape of the surface states is obvious. No significant difference is visible for the extension of the surface states in the slabs (7 – 40 layers)*

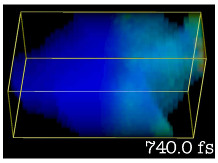

Chapter 6

Calculation of Matrix elements

After solving the quantum mechanical ground state problem the silicon (100) 2×1 surface problem, we will now proceed to the dynamical properties of the phonon induced relaxation processes of the conduction band. The link between the two theories (DFT and DMT, Chapter 4) is essentially based on the implementation of the band structure and the matrix elements (4.49) and (4.53) which enter in the scattering equations (4.45).

In this chapter, the numerical requirements and the proceeding to calculate these matrix elements from the density-functional theoretical results of Chapter 5 is presented. For the evaluation of dynamical equations like Eq. (4.45), the band structure and matrix elements must be present on a mesh covering the irreducible part of the Brillouin zone, as it is important for a realistic dynamical calculation that principally all features of the band structure enter the equations. For the evaluation of the phonon scattering processes (to fulfill the scattering conditions in Eqs. (4.33)), it is moreover required to have a regular, equidistant mesh in both k_x and k_y directions. The calculation of matrix elements is achieved in two steps: first, the mesh is set up and the band structure is calculated on that mesh (this mesh contains generally much more points than in a simple band structure calculation on a symmetry path as in Sec. 5.2.2). In a second step, all energy eigenvalues and wave function of this band structure are collected together, and the matrix elements (4.49) and (4.53) are computed from these wave functions. The matrix element values and the merged energy eigenvalues are then stored in a separate file, so the evaluation of the dynamical equations can then be executed totally independent of the previous calculations by reading from this file. Though the flexibility of this approach is very high, as it also allows many dynamical calculations with different initial conditions at the same time, the main disadvantage is the huge amount of hard disk storage space (up to 100 GB for the calculations in this work) which has to be kept accessible to file operations (and as the matrix elements can not be considered as intermediate results, but are quite costly to calculate (for the thickest slab in the highest discretization the accumulated CPU time amounts to 14,000 hours), they should be even stored on a file system with a backup utility). Whence, the need of disk space is momentaneously the primary limiting factor of the whole approach.

6.1 Band structure calculations for matrix elements

The main issue in performing band structure calculations in the supercell approach on a regular and relatively dense mesh (up to $\approx$ 1000 points in the reduced part of the Brillouin zone) is

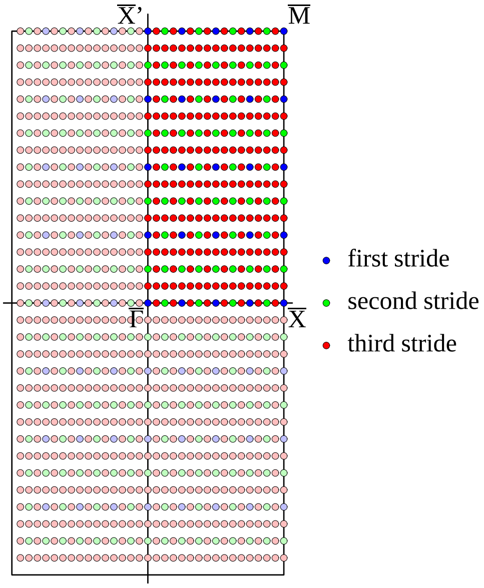

Figure 6.1: *Selection of the mesh for the* $\mathbb{k}$*-point sampling of the Brillouin zone. Only the points in the irreducible part of the Brillouin zone of silicon (001)* 2×1 *(bright colors) is computed, while the rest of the sampling points is geometrically equivalent (pale colors). The different strides (red, green and blue points) refer to several levels of approximation from* 5×5 *effective points to* 17×17 *effective points. The lower discretized meshes are a part of the higher discretized meshes.*

that the memory requirements of these mesh points and the slab usually not allow a calculation within a single run (where all mesh points are computed in the same time). Although it is conceptually no problem to split the calculations into several runs (as in the band structure mode, the different **k**-points are considered as totally independent on each other – cmp. Sec. 5.1), the special requirements of our problem for the choice and initialization of the $\mathbb{k}$-points exceed the capabilities of the tools included in the the `fhimd` program package, and consequently, extensions are needed at this point.

As a consequence, all program parts from this point of investigation on have to be developed from scratch. It is obvious that for debugging and lateron convergence tests very different discretizations for the Brillouin zone mesh are needed, especially because the scaling relation of CPU-time requirements to the number of **k**-points is of at least $O(N(\mathbf{k})^2)$. By choosing a well factorizable mesh discretization, it is possible to use mesh points of lower discretization density also in a mesh of higher discretization: if, for example, the discretization is chosen according to powers of two, the points of a eight-times-discretization are all contained in a 16-times-discretization and those are contained in a 32-times-discretization. The Brillouin zone can be entirely described by its irreducible part, but it should be assured that high symmetry points and -lines are represented in the discretization points, as they might play a crucial role in relaxation processes. In Fig. 6.1, a discretization for the silicon 2×1 unit cell which fulfills these requirements is shown: the $\overline{\Gamma}$, $\overline{X}$, $\overline{M}$ and $\overline{X}'$ points are all mesh points. The discretization in this plot is 32×32, but by symmetry, the irreducible part of the first Brillouin zone is covered by a discretization of 17×17. Lower discretizations with 5×5 (8×8) and 9×9

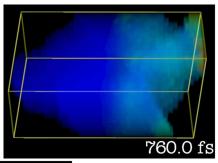

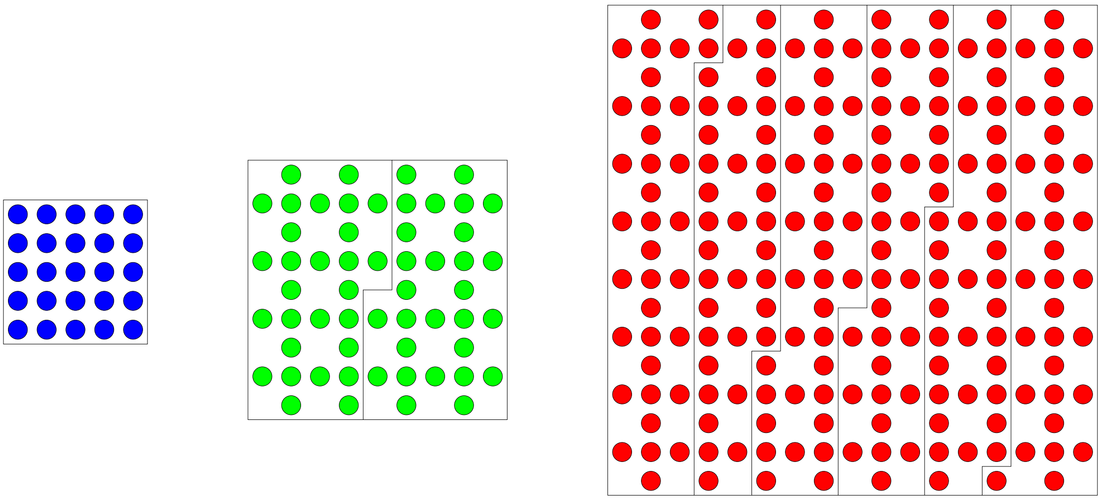

Figure 6.2: *Distribution of the different strides (Fig. 6.1) on multiple band structure calculation runs. While the first stride (lhs, the 25 red* $\mathbb{k}$*-points in Fig. 6.1) usually can be achieved in a single run, the subsequent strides are split as indicated by the black edges (middle and rhs, green and red points). By this selection of points, the runs for the lower discretizations are independent from the higher discretized runs.*

(16×16) points are also comprised: in the picture, we have the blue points (5×5), the green points (9×9) and the red points (17×17).

Another gain in flexibility can be reached by intelligently distributing the mesh points to the particular band structure runs. The total number of runs necessary is limited by the available memory, however, the relation between number of **k**-points and memory consumption is non-trivial. In addition, as the computation speeds up for runs with less **k**-points, it can make sense to take more runs, if a lot of machines are accessible at the same time. In the current implementation, the number of **k**-points is estimated by the number of **k**-points in the previous band structure run, which is usually 40[1]. The easiest way to share the **k**-points on the particular runs would be to just count the points along the rows and columns and put an equal number of them in each run parameter file. This, on the other hand, has a great disadvantage: every discretization level of the matrix elements would depend – in the worst case – on all band structure runs, as the points can appear anywhere in the run file setup. Not only this is quite unflexible (at least as long the debugging phase of new code persists), but also, it would require that the highest discretization is known in advance (it can be necessary to enhance the density of points due to numerical instabilities), and, at last, the extraction of matrix elements will be a much costlier process, as, even if only one **k**-point of a whole run is needed, the whole wave-function information of the run will have to be read in. As a consequence, another method comes to exercise in this context: all **k**-points of a specific discretization level are grouped together in subsequent runs, called *strides*. In Fig. 6.1, the lowest level is symbolized by the blue points. In Fig. 6.2, these 25 points form the first run on the lhs. The next stride, the green points of Fig. 6.1, then consists of 56 points. In Fig. 6.2 (middle), this is indicated, where the "missing" points are the 25 **k**-points from the first stride. The 56 points are distributed on two

---

[1] In the 40-layer calculation, however, this exceeds the computer's capacity, yet the band structure run has to be split in two runs of 20 points.

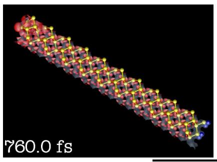

runs of 28, which is signified by the black edges. The complete set of points of the second stride is then obtained by combining the points from the first and the second stride. For the third stride, the procedure is similar, now, the first and the second stride are missing in the corresponding picture (rhs of Fig. 6.2), and 208 points are now shared by 6 runs (34 or 35 per run). In the calculations there is also a final discretization level of 64×64, or 33×33 in the reduced Brillouin zone, which owns then a total of 800 points and distributes them on 20 runs of 40 points.

The major task of this application is thus to the control of the approved `fhimd` program – no interference with the intrinsic band structure calculations is required. This functionality can be satisfied by modifying the parameter files for the `fhimd` run and starting the several runs. As this comprises basically copying of directories and altering text files, the natural choice of the programming environment for this part of the project is a script oriented language, which also brings along the big advantage of being very flexible in application. In our case, this is achieved by using the interpreter language `python` [vR06], which has also wide spread abilities in numerical computation (which are of use for the setup of atomic coordinates and **k**-points). The setup of a calculation is then accomplished in two steps: by a first script, the standard parameters are read in from a sample band structure calculation (as the calculation on a symmetry path in Sec. 5.2.2). The several strides are made up in the script, whereas the discretization level is provided as an input parameter. Then a control file is written for each stride (which is used lateron for the matrix element calculation), in this file, besides some information on the discretization level, the several runs of the stride and eventually the lower discretized strides which have to be included for the complete set of matrix elements are referenced. Finally a run directory is created for every run, in which the standard parameter files from the standard run are inserted and the **k**-point set for the run is adapted. A second script then allows to start the runs belonging to a specific stride selectively by reading the corresponding control file and inserting the specific runs into the queueing system. All runs are then executed totally independent from the others in their run directory. It is in principle also possible to augment the discretization level after the runs of the lower levels are initialized, as in the hierarchy of the control files, the files for the lower discretizations do not contain any information about the higher levels (so each stride is "self consistent"), but of course the higher discretizations need to know about their predecessor, as they depend on some points of the lower discretized strides (Fig. 6.2).

6.2 Aspects of the matrix element calculations

By here, the raw wave functions $\phi_{n\mathbb{k}}(\mathbf{r})$ and the electron dispersion $E_{n\mathbb{k}}$ have been computed on a regular mesh in a predefined discretization (cmp. Sec. 6.1). In this section, the principles of calculation of the electron-optical matrix elements $\mathbf{p}_{n\mathbb{k}}^{n'\mathbb{k}}$ (4.53) and electron-phonon matrix elements $D_{n\mathbb{k},i\mathbb{q}}^{n',\mathbb{k}+\mathbb{q}+\mathbb{G}_0}$ (4.49) are elucidated. It is obvious from the definitions that the computation of electron-optical matrix elements is a lot less costly than the electron-phonon matrix elements: although the former depend on a pair of bands n and n', they are based on only one $\mathbb{k}$-vector, while the latter also comprise a dependency on a second $\mathbb{k}$-vector (cmp. Sec. 4.3.2 and Sec. 4.3.1). While the eigenvalues belonging to different bands at the same $\mathbb{k}$-point are always contained in the same bandstructure run (as this is an intrinsic feature of the plane wave density functional algorithm, Sec. 3.6), the different $\mathbb{k}$-points belonging to a band, according to

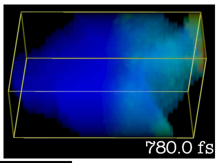

Sec. 6.1, are not necessarily. Although is is possible to create an algorithm where subsequently all combinations of pairs of the different wave function files are read in and thus a complete covering of all matrix elements is reached in the end, such an algorithm is difficult to handle (as it has also to account for the different strides) and the file access is normally a very slow process, especially for data on storage systems. It is more convenient to pursue a slightly more elaborate technique by using the computer system's scratch directory (or temporary storage directory). Such an explicit scratch directory is available on most computing clusters and is generally optimized for access speed by a fast network connection. This scratch directory can at this point be used to rearrange the wave function data of all runs of a stride and save them in direct access mode, which allows to access all entries in the file independently of each other by an index[2]. Through this direct access, this intermediate storage file can be used like a classical array in the RAM memory, and allows therefore a much more flexible handling of the wave functions.

A further difficulty in the evaluation of $\mathbb{k}$-$\mathbb{k}'$ matrix elements is the fact that through the cutoff of the underlying **G**-vectors by the cutoff energy (Eq. (3.22)), the variety of the **G**-vectors differs for the $\mathbb{k}$-points. As a consequence, he order of the **G**-vectors in the plane-wave implementation of `fhimd` is also different for each $\mathbb{k}$-point. As for the electron-phonon matrix elements, also umklapp processes are considered (Eq. (4.48)), it can not be avoided to map the condensed set of **G**-vectors which is saved in the wave functions file to an expanded set, where the **G**-vectors are ordered by their location along the three dimensions of reciprocal space to enable the direct access to a specificly oriented wave vector (while all vectors not represented in the condensed set are set to zero). When performing a matrix element calculation, it suffices to do this expansion for only one of the to wave functions, as the other one can be multiplied in situ. For umklapp processes in the form of (4.48), the **G**-vectors of one of the two wave functions has to be increased or decreased by reciprocal lattice vector $\mathbb{G}_0$ in the umklapp-direction. Due to the expanded wave vectors, this is nothing more than the increasing or decreasing the index for a specific dimension in the **G**-vector table for the wave function.

While the calculation momentum matrix element for the electron optical coupling can be implemented without further complications, as all necessary parameters (as reciprocal lattice vectors) are contained in the wave function file, the situation for the electron-phonon matrix elements is more complex. In the simplified form of the matrix elements which will be used here, matrix elements $D^{n'\mathbb{k}'}_{n\mathbb{k};i\mathbb{q}}$ as in Eq. (4.51) consist of two parts: first a phonon mode dependent part $\sqrt{\frac{\hbar}{2M\omega_{i\mathbb{q}}}}D^i_1\mathbb{q}\cdot\mathbf{e}^i_0$ and the principally phonon independent electron matrix element part $\sum_{\mathbf{G}}\sum_{\mathbf{G}'}\overline{u}_{n\mathbb{k}}(\mathbf{G})u_{n'\mathbb{k}'}(\mathbf{G}')\delta_{\mathbf{G}'+\mathbb{k}'+\mathbb{q},\mathbf{G}+\mathbb{k}}$. In the current implementation, only the second part is actually done in the matrix element calculation. Besides the fact, that the parameters D^i_1 and $\omega_{i\mathbb{q}}$ are not extracted from calculations, but by heuristical parameters, the pure matrix elements in bulk approximation can be used be multiple phonon modes, as nothing mode specific enters the calculation. It is in principle feasible to perform phonon mode calculations for the given silicon structure, in this case, a more general z-dependency of the modes as in (4.49) would be necessary, and hence, the matrix elements would have to be calculated with an additional explicit z-dependency of the modes $\sum_{\mathbf{G}}\sum_{\mathbf{G}'}\sum_{G_z}\overline{u}_{n\mathbb{k}}(\mathbf{G})u_{n'\mathbb{k}'}(\mathbf{G}')\cdot\mathbf{s}^i(G_z)\delta_{\mathbf{G}'+G_z+\mathbb{k}'+\mathbb{q},\mathbf{G}+\mathbb{k}}$. It should however be noted that both the CPU time and the hard disk requirements for this enhanced matrix element calculation are momentaneously exceeding the possibilities.

---

[2] Yet, as the employed computer system in based on an 32-bit-architecture, it is necessary to use multiple direct access files, as the total size of all wave functions exceeds 2^{32} bytes for some configurations.

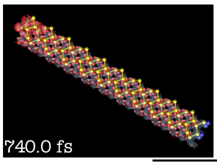

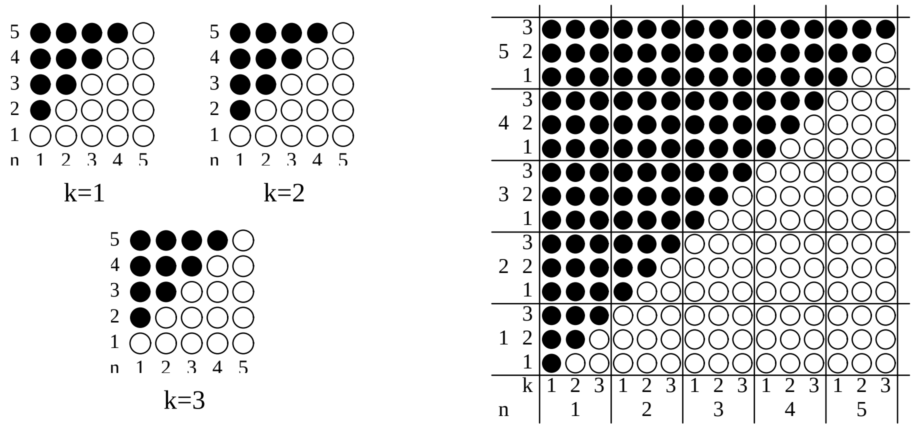

Figure 6.3: *Calculation of optical (lhs) and phonon-electron matrix elements (rhs). Due to symmetry relations (Eqs.* (4.34)*), only the black-filled circles do actually have to be computed. While the optical matrix elements are only defined for different* n *and* n'*, the phonon-electron matrix elements have to be calculated for all pairs of* $n, \mathbb{k}$ *and* $n', \mathbb{k}'$*. It is obvious from this sketch that the number of electron-phonon matrix elements can get very huge.*

As the wave function output from the `fhimd` package is only available in the intrinsic *Fortran 90* file format and there is no standard representation of this format in alternative programming languages, the most convenient way is to implement the matrix element calculation program in the same Fortran 90 dialect as the `fhimd` code. The calculation is achieved in two phases: first, after parsing the stride control files for the different discretization strides (where the control file for the highest discretization is given as a run-time parameter and the lower discretization control files are then read recursively from the former as a link in the control file), the necessary band structure matrix element files are read in and immediately reordered and rewritten into the direct access scratch file. The energy eigenvalues are also reordered, but can be kept in memory. In the second phase, all combinations of wave functions are iterated by two nested loops, the momentum matrix elements are calculated for every combination of two bands using Eq. (4.55) and the electron-phonon matrix elements also for every combination of $\mathbb{k}$-points. Due to the symmetry relations (4.34), basically only a half of the elements has to be computed, for the momentum matrix elements, this can be implemented by only considering matrix elements with $n > n'$, for the electron-phonon matrix elements, this is slightly more complicated, but can be achieved by computing the elements for all $\mathbb{k}$ and $\mathbb{k}'$ if $n > n'$, but only the $\mathbb{k} >= \mathbb{k}'$ for $n = n'$. This technique is illustrated in Fig. 6.3. While for the momentum matrix elements, all bands can be considered because the computational effort is relatively limited, it is crucial for the electron-phonon matrix elements to preselect a subrange of the available bands, because, again, both time and disk space would be exceeded otherwise. With regard to the relaxation processes in the conduction bands which are the topic of this thesis, the usual selection are a few bands at the conduction band bottom (including the D^{down} band) which cover the energy range sensitive to optical excitation at a given laser frequency (cmp. Sec 7.4). Hence their number depends on the number of layers in the slab, as this influences the number and the energetical spacing of the bands (cmp. Chapter 5).

During the looping, the matrix elements are immediately written into the output file. To allow a further investigation of the results in a platform- and programming environmental in-

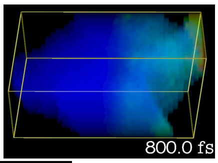

dependent way, the output file is used in the `netcdf` format [Uni36], which is accessible in numerous programming languages and can be used independent of the system architecture. Not only the matrix elements and the total band structure is saved in the file, but basically all information that is important for the future handling in the dynamical evaluation, as lattice vectors, symmetry operations or $\Bbbk$-point positions. By this, only one file will be necessary lateron to accomplish the dynamical evaluation.

6.3 Investigation of optical and electron phonon matrix elements

Having accomplished the numerical calculation of the matrix elements, we now proceed to the examination of the results. Although a general investigation of all matrix elements is, due to their generally huge number, impossible, some exemplary and cumulative comparisons can be however accomplished. The purpose of this analysis is, at first, to check the influence of the discretization and the number of layers in the band structure calculations. It is obvious that this is only one aspect of the convergence behaviour of the matrix elements, a final study has to include the characteristics of the dynamical relaxation, which is induced by the matrix elements. A side effect is that the optical matrix elements can be related to macroscopical quantities like the optical absorption coefficient. Thus, the results can in principle be compared to experimental findings, this is however inhibited by the fact that excitonic interactions are very significant for optical absorption, and cannot be neglected in the spectra, as it is the case in our theory (which has the focus not on the optical spectra). Whence, the comparison has to appear on a qualitative level.

6.3.1 Dipole matrix elements

While our theory is on the evaluation of $\mathbf{A}\cdot\mathbf{p}$-coupling (Sec. 2.3.5), the equivalent formulation in terms of $\mathbf{d}\cdot\mathbf{E}$-coupling (Eq. (2.48)), better adapted to macroscopical analysis of data. The dipole matrix elements $\mathbf{d}$ are investigated in two ways. The linear macroscopic absorption coefficient $\alpha(\omega)$ can be related to the macroscopical polarization (4.13) and the incident electrical field by

$$\alpha(\omega) = c_\alpha \,\Im\left(\frac{\mathbf{P}(\omega)}{\mathbf{E}(\omega)}\right). \tag{6.1}$$

Here c_α is a constant. The Fourier transform of the macroscopical polarization can be derived by solving Eq. (4.39) for the microscopical polarizations in Fourier space, whereby a spectral distribution function with Lorentzian shape is found, when a heuristical damping factor γ is introduced into the differential equation (4.39):

$$\alpha(\omega) = c_\alpha \sum_{n\Bbbk}\sum_{n'\Bbbk'} \left|\mathbf{d}^{n'\Bbbk}_{n\Bbbk}\mathbf{e}_P\right|^2 \left(\frac{\gamma}{\gamma^2+(\frac{E_{n\Bbbk}-E_{n'\Bbbk}}{\hbar}-\omega)^2}+\frac{\gamma}{\gamma^2+(\frac{E_{n\Bbbk}-E_{n'\Bbbk}}{\hbar}+\omega)^2}\right), \tag{6.2}$$

where $\mathbf{e}_P$ is the polarization vector of the light field $\mathbf{E}(\mathbf{t})$. ω can be interpreted as the variable frequency of the incident light. The second term in the parenthesis can be neglected, as it is only relevant for negative frequencies (which correspond to induced emission). The linear absorption spectrum based on this elementary electron-optical interaction is therefore a superposition of Lorentzian peaks with a weight according to the transition matrix elements. However, for a realistic spectrum, more effects have to be considered in the equations: Apart

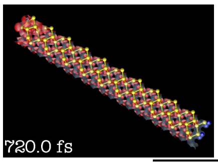

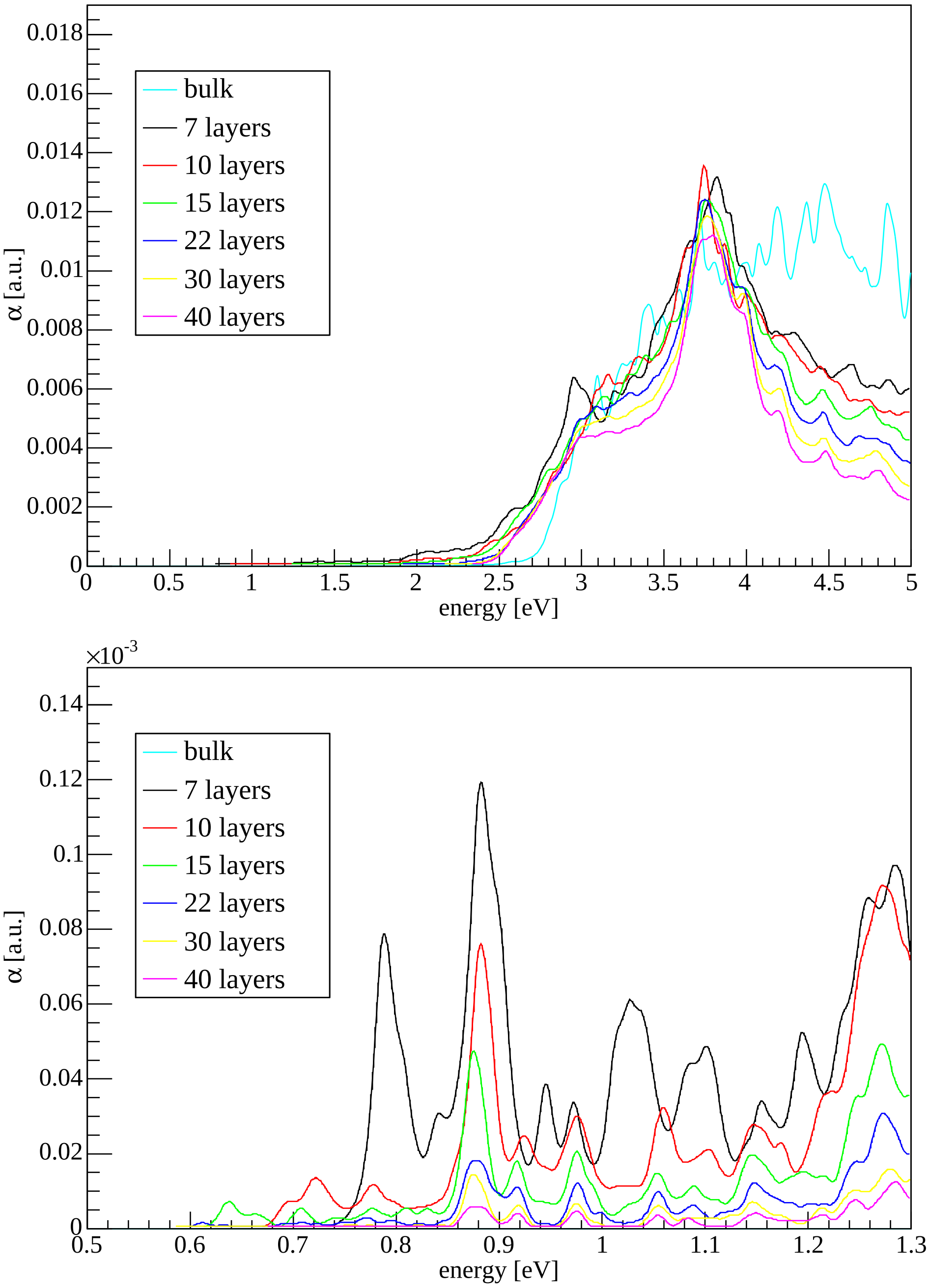

Figure 6.4: *DFT-LDA Absorption spectra plot for a polarization of the incident field along the x-direction for silicon (001)* 2×1*-supercell calculations of various numbers of layers for a discretization of* 32×32 *points in the Brillouin zone and for Silicon bulk (diamond) structure. The normalization is according to the size of the unit cell. In the top level figure, the spectra are shown for the range 0-5 eV. For energies greater than ca. 4 eV, the spectra are not reliable for the slab data, as the number of points depends on the number of considered bands in the band structures (cmp. Figs. 5.6-5.11). At the bottom, a cutout for 0.5-1.3 eV is shown. The peaks represent the energetical positions of* $\Bbbk$*-points to allow a comparison of the transitions for different slab calculations. In this part of the spectrum, only transitions from the valence bands to the* D^{down}*-band are present, thus the intensity of the spectrum decreases with increasing layer number.*

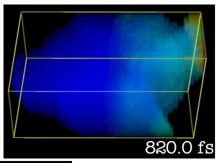

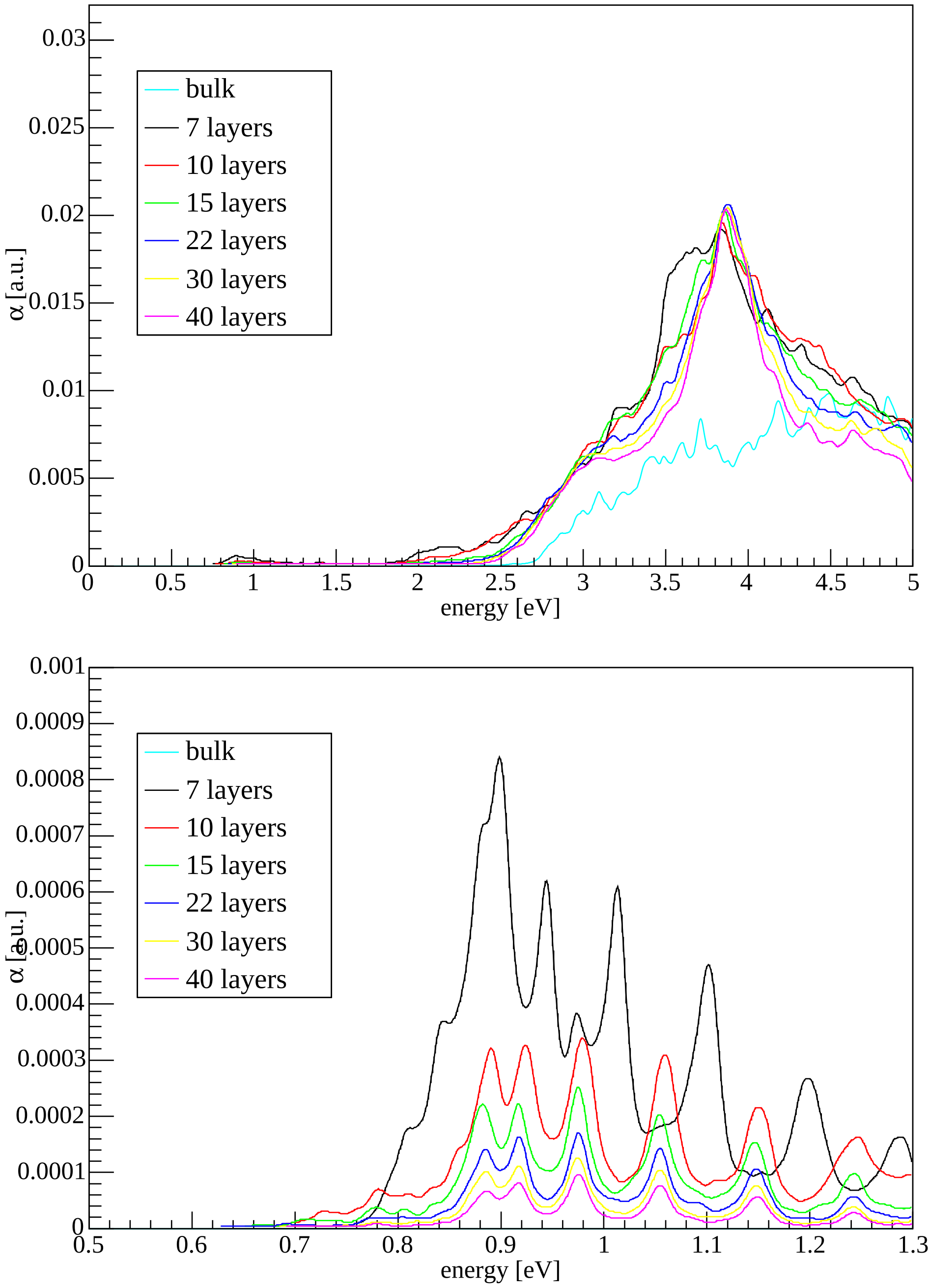

Figure 6.5: *Analogous DFT-LDA absorption spectra (as in Fig. 6.4) for a polarization of the incident field along the y-direction. While the shape of the spectra is similar to Fig. 6.4, the different extension of the unit cell in y-direction results in a different normalization of the spectra with respect to the bulk spectrum. In the detailed plots (bottom), bigger differences occur.*

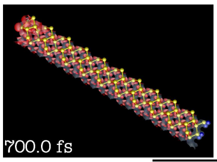

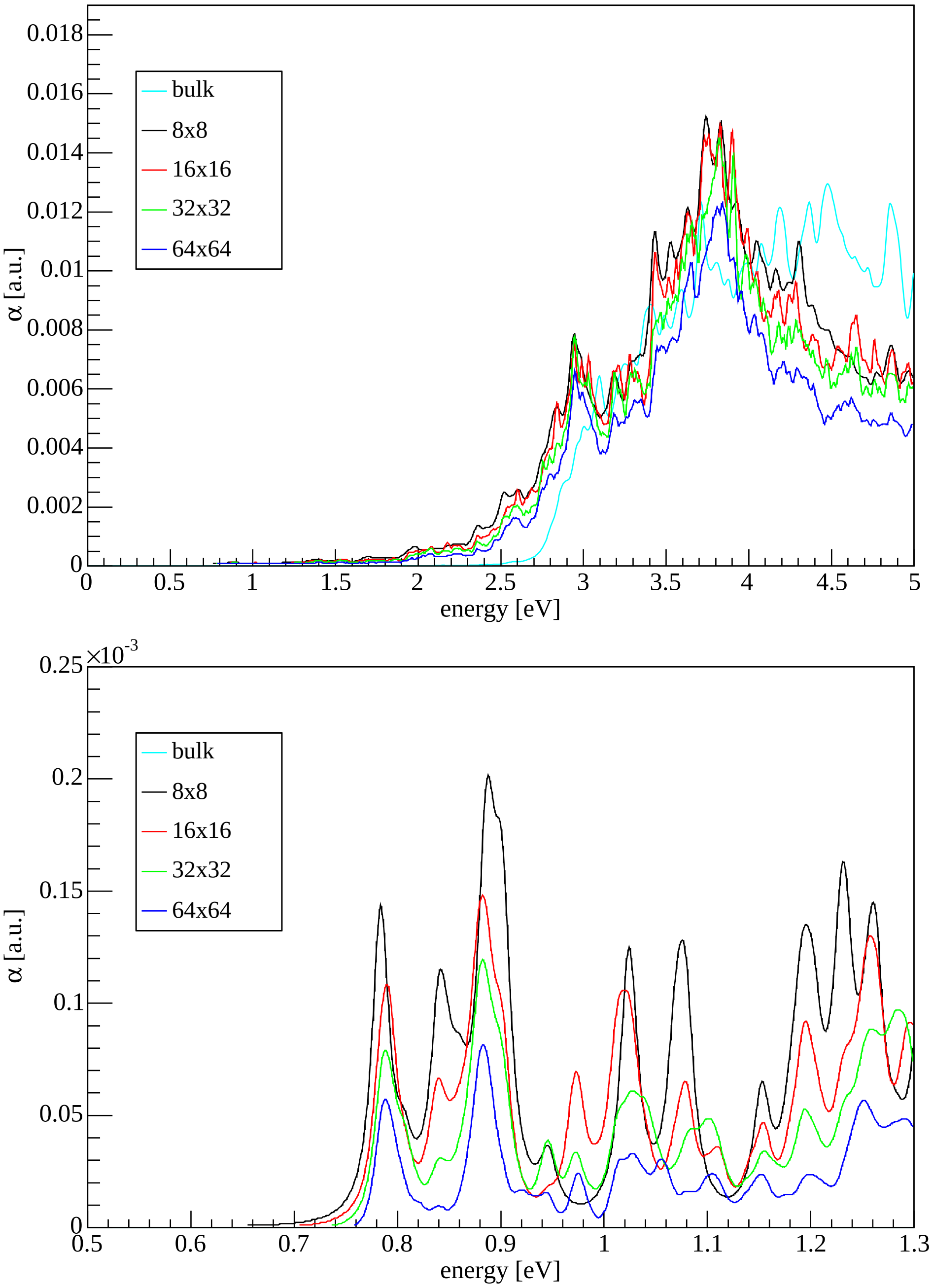

Figure 6.6: *DFT-LDA absorption spectra plot for a polarization of the incident field along the x-direction for silicon (001)* 2×1*-supercell calculations of various discretizations of the Brillouin zone for a layer number of 7 and for silicon bulk (diamond) structure. The normalzation is according to the size of the unit cell. Only slight differences appear between the different plots, also the position of the peaks for the transitions into the surface band (cmp. Fig. 6.4) are more or less invariant.*

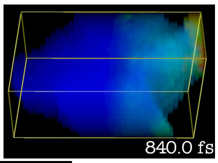

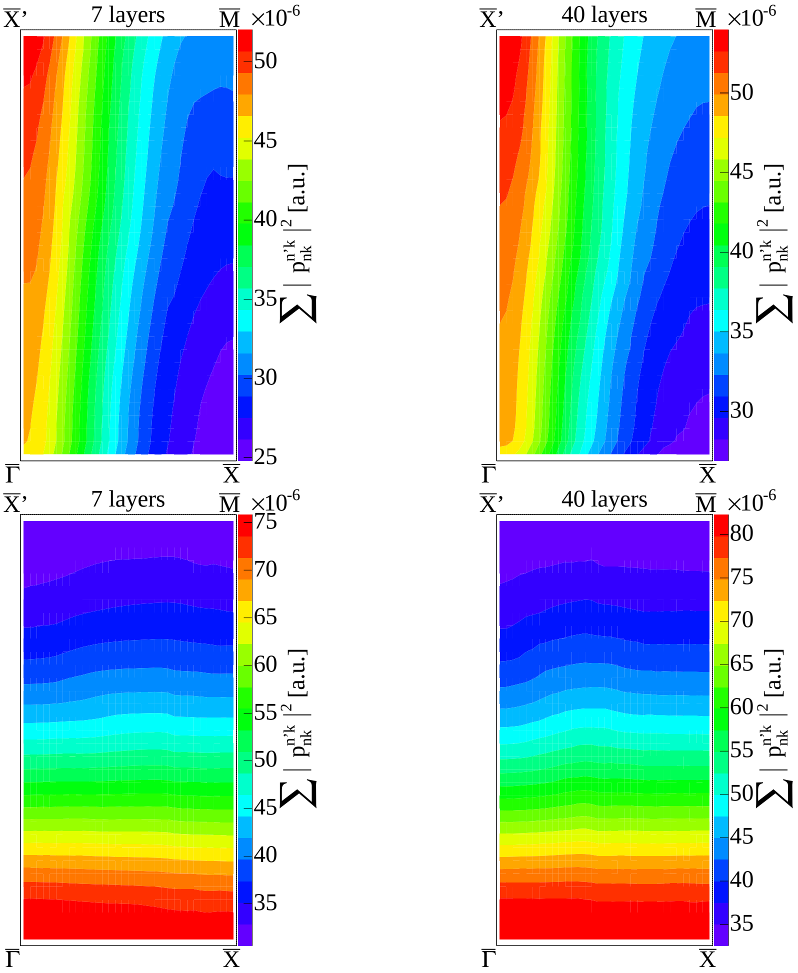

Figure 6.7: *Distribution of the optical absorption over the Brillouin zone. The sum of all relevant transition dipole matrix elements (all transition from valence to bulk bands) are shown for a polarization of the incident light in x-direction (top) and in y-direction (bottom) for a supercell of 7 layers (left) and 40 layers (right) are shown. No significant differences occur between the 7 and 40 layer plots.*

from a homogenous *scissors shift* of the band gap in the band structure (cmp. Sec. 1.4.1), also the appearance of additional excitonic peaks (as a result of the formation of excitons at the band edge) is expected. In this presented spectra, the quasiparticle and excitonic effects are not discussed at all, thus the energies in the spectra cannot be compared directly to measured data. Nevertheless, some effects of the silicon dimer surface reconstruction on the spectra can be discussed at this level.

In Fig. 6.4 and Fig. 6.5, the absorption spectra are plotted for incident light polarized along the x and the y-direction, respectively, for calculations with a different number of slab layers for a $\mathbb{k}$-point discretization mesh of 8×8 (5×5 in the reduced zone). The bulk spectrum is indicated as a reference by the light-blue lines. In the top level pictures of Fig. 6.4 and Fig. 6.5, an overall spectrum up to 5 eV is shown. Only slight differences are obvious for the spectra with a higher number of layers (the blue, yellow and magenta lines for the 22, 30 and 40 layer calculations), so a convergence of the spectra is achieved for a layer number of above 22. For

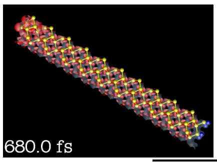

lower layer number, however, the differences are more obvious, and some of the peaks which also appear in the other calculations are shifted to higher or lower energies, so we can conclude that below 22 layers, the calculations are not inspiring confidence. This convergence with respect to the layer number is found independently for the *x*- and *y*-polarized light. Although the spectra are similar for the two polarizations, the strength of the excitation is on average about 2 times larger in the *y*-direction. In the bottom pictures, a cutout of this spectrum is shown for an energy range of 0.5 - 1.3 eV. In this range, there are no contributions in the bulk spectrum, as the direct optical transitions which are discussed here only appear above 1.6 eV. The effects in these pictures are consequently uniquely induced by the surface reconstruction, in the first order, the transitions from valence band bulk states to the D^{down} surface band are the cause. An obvious fact is that the relative strength of those surface band transitions is reduced with increasing layer number. This is a consequence of the growing number of bulk bands with respect to the surface bands D^{up} and D^{down}, or, in other words, by increasing the structure into the bulk (cmp. Figs. 5.6-5.12), the influence of the surface is decreased. As in the case of the full spectrum, it appears that the number of considered $\mathbb{k}$-points is sufficiently high and thus the positions of the peaks are quite stable above a layer number of 22, while big differences are visible for the lower layer calculations. However, with increasing layer number, still particular additional $\mathbb{k}$-points and the related peaks are occuring in the spectra, their contribution to the shape of the curves is limited.

In Fig. 6.6, the absorption spectra of calculations with an equal layer number of 7, but different discretizations ranging from 8×8 to 64×64 are shown. While in the 8×8 (or 5×5 in the reduced Brillouin zone, cmp. to Fig. 6.1) plot, the curve is highly influenced by singular peaks (top, black lines), the curve is much more smooth for the higher discretizations. Nevertheless, the shape of the curve is not changed by a higher discretization. This behaviour is also visible in the cutout range picture at the bottom of Fig. 6.6: the total size of the single peaks decreases by increasing the discretization size, but the shape of the curve remains unchanged. In conclusion we state that obviously, all important features of the optical absorption within our approximations are reproduced by a relatively low discretization, whereas the number of layers in the supercell influences the shape of the spectrum and the position of the peaks much more. A qualitative comparison to the bulk spectra also reveals a high accordance to the higher layer calculations, with exception of the low energy transitions (< 2.5 eV), where the surface bands come to play.

A different form of investigation is illustrated by Fig. 6.7. Now, the plotted matrix elements are not chosen by the energetical selection through the frequency of the incident light, but by the location inside the first Brillouin zone. For each point of the discretization (where the highest available discretization of 64×64 is selected), the square modulus of all dipole matrix elements $\mathbf{d}_{n\mathbb{k}}^{n'\mathbb{k}}$ going from valence to bulk (e.g. n is a valence band and n' is a conduction band or vice versa), in the light polarization direction, is summed. Although no specific conclusions about the excitation of particular electron states in the band structure can be made by this construction, the main destination of the transitions of an white-light excitation can be read out from these images. Two parameters are varied inside these plots: First, the number of layers in the supercell structure which is the origin of the dipole matrix elements is changed, and second, the polarization direction is selected in x and y-directions. While only slight changes are visible by the variation of the layer number in the pictures (left and right row of Fig. 6.7), the orientation of the absorption maxima in the Brillouin zone is completely altered by the change of orientation of the polarization vector: while for x-polarized light, absorption is mainly found

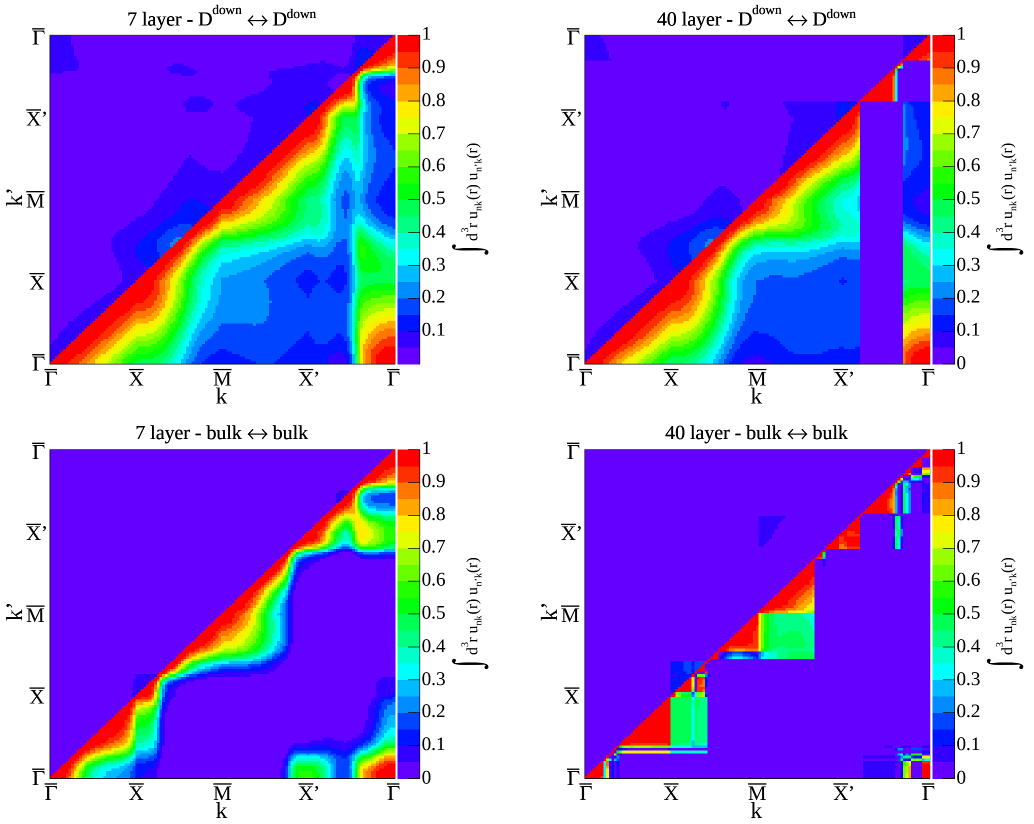

Figure 6.8: *Size of the matrix element of electronic Bloch wave functions* $\int d^3r \bar{u}_{n\Bbbk}(\mathbf{r}) u_{n'\Bbbk'}(\mathbf{r})$ *for intraband transitions on the symmetry path* $\overline{\Gamma}-\overline{X}-\overline{M}-\overline{X}'-\overline{\Gamma}$ *(cmp. Fig. 5.2, 5.6-5.11) from a state* $\Bbbk$ *to a state* $\Bbbk'$ *inside the* D^{down} *surface band (top) and inside the lowest bulk-like band (bottom) for a seven layer slab (lhs) and a forty layer slab (rhs). At the upper left side of the plots, the matrix elements of umklapp processes are shown. The block-like structures in the 40 layer slab picture for the surface band can be identified as the zones in the band structure where the surface band enters into the bulk (Fig. 5.11) and cannot be clearly identified. Similarly, the the first bulk band for the 40 layer slab is obviously build up from several states of different symmetry.*

along the k_y-direction, it is found along the x-direction for k_y-polarized light. Obviously, most features of the spatial distribution are yet contained in the dipole matrix elements of the supercell calculations with low number of layers (7), but in all cases, the matrix elements are highly inhomogeneous with respect to the polarization direction.

6.3.2 Phonon matrix elements

In contrast to the optical transition matrix elements, no direct link to a macroscopical quantity exists for the electron-phonon coupling. Furthermore, the number of electron-phonon matrix elements is not diagonal with respect to the $\Bbbk$ point (Fig. 6.3). Consequently, the high number of parameters (n, n', $\Bbbk$, $\Bbbk'$, i) makes it impossible to draw the relations between the parameters in a simple graphical representation. Thus, only some exemplary transitions will be discussed here. As the electron-phonon coupling is represented by two parts (Sec. 6.2), where only

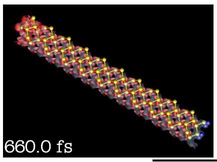

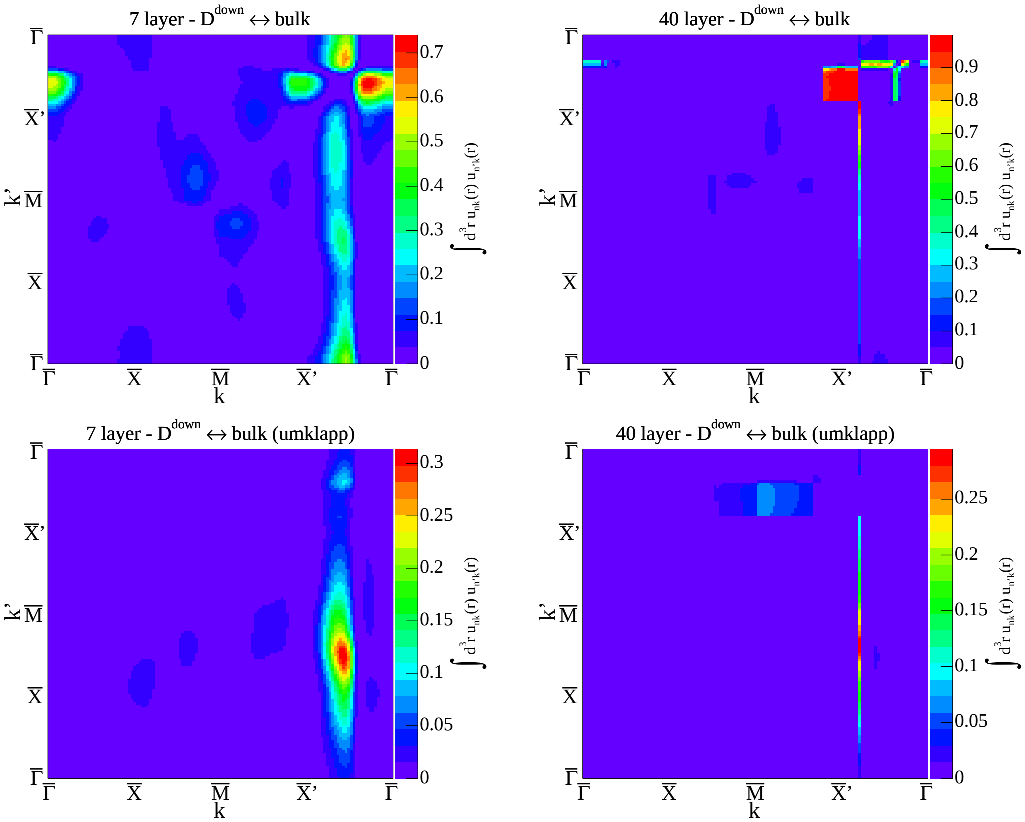

Figure 6.9: *Size of the matrix element of electronic Bloch wave functions* $\int d^3r\bar{u}_{n\Bbbk}(\mathbf{r})u_{n'\Bbbk'}(\mathbf{r})$ *for interband transitions on the symmetry path* $\overline{\Gamma}-\overline{X}-\overline{M}-\overline{X}'-\overline{\Gamma}$ *(cmp. Fig. 5.2, 5.6-5.11) from a state* $\Bbbk$ *of the surface band to a state* $\Bbbk'$ *of the lowest bulk-like band (top) for a seven layer slab (lhs) and a forty layer slab (rhs) and the corresponding umklapp processes (bottom). As in the case of intraband scattering (Fig. 6.8), the attribution of states to the bands is not definite for the 40 layer calculation, thus a block structure occurs in the pictures.*

the second part is gained from the electronic wave functions in the current implementation, the discussion will be limited to the matrix element of the electronic Bloch wave functions $\int d^3r\bar{u}_{n\Bbbk}(\mathbf{r})u_{n'\Bbbk'}(\mathbf{r})$ (Eq. (4.51)). Those matrix elements have to be treated differently for the direct scattering and the different umklapp processes (Eq. (4.50)). Yet, the full discussion of two two-dimensional wave vectors $\Bbbk$ and $\Bbbk'$ already exceeds the possibilities of commonly used graphical representions in printed form (as still another coordinate is needed to represent the dependency), we simplify this by discussing only the $\Bbbk$ and $\Bbbk'$ points on the symmetry path introduced in Sec. 5.2 (Fig. 5.2).

Two bands and two situations are presented in Figs. 6.8 and 6.9. In Fig. 6.8, the square modulus of size of the matrix elements of the intraband transitions (where $n = n'$) for the surface band and for the first bulk band are shown. By evaluation of the matrix elements, a basic result for these intraband transitions is that for $\Bbbk = \Bbbk'$, the matrix elements must yield one, as in and out states are identical. Additionally, due to the symmetry of the matrix elements (Sec. 6.2), only one half of these matrix elements has to be calculated, as the other half can be mapped to the same points. Thus, the matrix elements for one of the eight occuring umklapp-processes

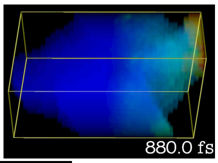

with $\mathbb{G}_0 = \mathbb{b}_1$ are plotted in the upper-left half of these intraband pictures[3]. The matrix elements are plotted for the calculation with a seven layer slab and for the calculation with the 40 layer slab. In Fig. 6.8, for the seven layer slab, the matrix elements express a smooth dependency with a well defined maximum of one at the diagonal both for the surface band and for the bulk band, as it is expected from the analytical evaluation. In a certain range of $|\mathbb{k} - \mathbb{k}'|$ of about 20% of $\overline{\Gamma} - \overline{X}$, depending on the location of $\mathbb{k}$, around the diagonal, the matrix elements are still above 0.9. This complies with estimations which have been done for quantum dots [Ahn06]. For the 40 layer calculation, however, the plots are not coherent: for transitions originating from a $\mathbb{k}$ point between the $\overline{X}'$ and $\overline{\Gamma}$ points, a block-like hole inside the plot occurs, where the size of the matrix elements is not smoothly connected to the rest of the plot. This hole can however be understood by looking at the band structure in Fig. 5.11: At the $\mathbb{k}$-points where the hole occurs, the surface band enters the region of the bulk bands and can not be distinguished any more by energetical comparison. Although it could however be possible to identify the surface states by projection on the surface atom orbitals, this has not been implemented in the current calculations (as the affiliation to specific bands has no significance to the later dynamical calculations), and thus the states represented in the top-rhs picture of Fig. 6.8 are not all states with a surface geometry as in Fig. 5.12, but with a bulk geometry. Consequently, the matrix elements for those wrongly identified states, if not on the diagonal, appear much smaller. For the first bulk band (bottom-rhs picture), this behaviour is even more pronounced, here, inside the bulk bands, the affiliation of the states to different bands is purely arbitrary, so the significance of this picture is quite reduced – a sensible comparison can only be done at or near the diagonal inside one block. As a consequence, this kind of investigation of particular bands is only sensible if the states in the bands can be clearly identified and affiliated – as it is the case for the seven layer calculation. Another result of these analysis is that for the intraband scattering, the umklapp processes are negligible, as their size is at least an order of magnitude below the corresponding normal scattering processes.

In the top of Fig. 6.9, a similar discussion is led for the interband scattering between the surface band and the first bulk band. Now, the upper left half of the matrix transitions is important, the bands are not diagonal ($n \neq n'$), and the evaluation for the umklapp processes is shown at bottom of Fig. 6.9. Both integral and maximum size for the normal scattering processes is smaller than in the intraband case (0.7 maximum cmp. to 1.0 maximum), furthermore, the scattering at the diagonal is not prioritized, but occurs between selected points on the symmetry lines. The umklapp processes, however, are much more significant with respect to intraband scattering and in relation to normal scattering. For the matrix elements of the 40 layer slab, the same limitations as in the intraband-case apply, the occuring of a linear structure in the scattering pattern leads to the assumption that the wave function at a single $\mathbb{k}$-point is out of the common symmetry of the other $\mathbb{k}$-points. Again, the investigation is more or less useless for the 40 layer slab, as a coherent comparison of the scattering is impossible.

However, we should note that the matrix elements analyzed here are only one component of the real scattering treated in the dynamical equations (4.45). The energy conditions (4.57) which are contained in the scattering matrices (4.33), but also the $\mathbb{q}$-dependent form factor of the electron-phonon coupling (4.51), can have a great effect on the strength of the scattering. Especially for the intraband processes, scattering is highly improbable for small $\mathbb{q}$, as either

---

[3] It should be noted that the classification of in and out states is purely academic, as this only influences the phase of the matrix elements and is therefore irrelevant for the square modulus of the matrix elements in the relaxation equations. For the umklapp processes, the correct assignment would be $(n\mathbb{k})$ as out state and $(n'\mathbb{k}')$ as in state.

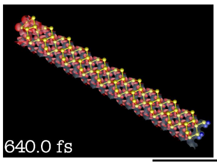

the form factor vanishes at $\mathbb{q} = 0$ (acoustical phonons), or the energy condition makes scattering impossible (optical phonons: $\omega_{i,\mathbb{q}=0} \neq 0$). At those points, on the other hand, the matrix elements are close to one (Fig. 6.8).

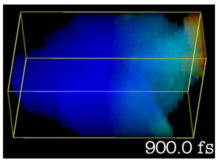

Chapter 7

Relaxation dynamics at the Silicon 2×1 (100) surface

After the presentation of the numerical implementation and the results of the calculations of the interaction matrix elements and the band structures, we now move on to the discussion of the final step in our calculations: the supercell structure has to be integrated into the dynamical equations (4.45) by embedding the matrix elements, the band structure and the phonon dispersion into the equations of motion, with the final goal to simulate the relaxation processes in the conduction band. First, we will give and idea of some aspects of the involved programming methods. The main task, the calculation of the band structure and the matrix elements has been completed in Chapter 6, so the remaining open questions are about the implementation of the scatter matrices (Sec. 4.4) and the subsequent dynamical evaluation. Then, some results of a testing procedure using an isotropic standard system with one parabolic band and constant matrix elements, without externally considering a structure, are realized. The main purpose of this step is to check the homogeneity of the relaxation process, as the proposed approach from Sec. 4.4 is a great source of errors. Finally we present the results of the relaxation in the silicon 2×1 (100) surface supercell for different initial conditions: the general relaxation behaviour for a high-frequency excitation is simulated by a Gaussian energy distribution of the initial population at the upper limits of the investigated band structure, and, finally, a realistic scattering process is computed by implementing experimental optical excitation conditions. The relaxation timescales from this process are then finally compared to the experimental values.

7.1 Implementation of the dynamical evaluation

As indicated in Sec. 4.4, a big gain in efficiency can be obtained by evaluating the delta conditions of the energy conditions (4.57) before the start of the dynamical relaxation loop. It is therefore consequent to organize the program code in two parts: first, the initialization is performed, where mainly the scattering matrices are built up, but also the initial conditions are set up. The second step comprises then the computation of the population dynamics up to a predefined time step. The initialization procedure accomplishes several tasks: first, some parameters are read in from a separate file. Parameters are for example the system bath temperature, the maximum timestep and the timestep discretization, filenames for the matrix element

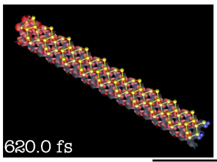

file and output file, information for the initial distribution, and, due to the reduced bulk mode model (cmp. Sec. 4.3.1), also the bulk phonon mode dispersion (in the form of sonic speed and optical phonon frequency) and deformation potentials are referred to in the parameter file. Then, the band structure of the system is read in, whereby all information related to the actual structure (including the discretization level) is extracted from the matrix element file. Now, from this band structure information, we can proceed to the construction of the scattering matrices: first, the inversion of the energy dispersion by the mapping (4.60) is exploited, this is achieved by basically evaluating the energy condition (4.57), with the bulk phonon energies $\omega_i(\mathbb{q})$ at $\mathbb{q} = \mathbb{k} - \mathbb{k}' + \mathbb{G}_0$, for all combinations of n, $\mathbb{k}$ and n', $\mathbb{k}'$. Due to the various scattering processes, the whole Brillouin zone of the system has to be considered at this point, it doesn't suffice to use the reduced part. Therefore, an zone unfolding has to be performed for the band structure. The zeros of the mapping $\mathbb{I}(s)$ are identified by a sign change of the corner points of the involved mesh, and also the path length ds is evaluated from the actual zero points between the mesh points (but on the mesh edges) by using a linear interpolation of the corner point differences (cmp Fig. 4.4). For every combination of n, $\mathbb{k}$ and n', $\mathbb{k}'$, the zeros, path lengths and strength factors $G^{\pm}_{mn\mathbb{k}i}(s)$ (Eq. (4.62a)) for all different umklapp processes, phonon modes and for all identical points in the unfolded Brillouin zone (thus, the zone is refolded at this point) are added cumulatively for the $+\omega_{i\mathbb{q}}$ and the $-\omega_{i\mathbb{q}}$ branch separately. Finally, for the meshes of the underlying mesh discretization where zeros occur, the matrix elements are read in from the matrix element file (it is, however, not possible to read the whole matrix element file at one time due to the limitations of computer memory, and also not all matrix elements are finally needed), and the scattering equations can be assembled according to Eq. (4.61a) from the different contributions of the Bose distribution $n_{i\mathbb{q}}(T)$ and the size parameters.

As only a small fraction of the elements of the scattering matrix are non-vanishing, a specially dedicated matrix structure can help to reduce the numerical effort by preventing the multiplication of all zero elements in the evaluation of the scattering equations (4.45). The special requirement of the matrix is that the non-zero elements can be distributed totally randomly on all elements. An obvious choice to meet this requirement is a so called *index-oriented matrix representation*: Only the non-zero matrix elements are stored, and each of them with its own column index. An additional row index references the starts of each row in the column index list. A matrix multiplication with a vector can then be performed by adding all components of the vector referenced by elements of the column index list for each row separately. The results of each addition row are then composed to the resulting vector. This approach is surely faster as full multiplication of all matrix elements, as long as the rate of non-zero elements to total elements is low, and it surely consumes a lot less memory (the quantification of the memory consumption is highly influenced by the employed computer system, as additionally to the size of the floating point numbers for matrix elements, the size of the index variables play a crucial role). The main issue of this technique should however also come to mention: While it is possible (by the row index) to directly access a specific row, it is very costly to find a particular element of the matrix, as in the worst case, all column indices in a specific row have to be checked for equality with the required column, especially if the element is zero and no column index exists. Thus, the effort to read out a specific element is of the order of the number of columns in the matrix (and the order to randomly read out all elements is about (number of rows)×(number of columns)^2). Furthermore, elements can only be added row-by-row, it is extremely costly to add elements later, after all rows have been completed, as basically all indices have to be recalculated and the later entries have to be copied. As a consequence, a

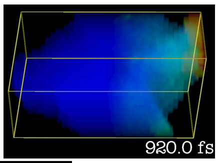

symmetrization step according to Eq. (4.37), which has proven to highly improve the numerical stability of the calculation, is quite costly and only possible by completely rebuilding new, symmetrized matrices. Although the computation of the scattering matrices is a singular step, it can take a considerable portion of the whole computation time of the dynamics – so, if only a few timesteps have to be calculated, it can even take longer than the dynamical calculation. Nevertheless, it is inevitable for this kind of simulation, as otherwise, the scattering rates would have to be derived from the band structure in every time step, with basically the same effort that is applied once in our algorithm (and furthermore, the matrix element file would have to be reloaded after every time step). This is an elementary difference to the common application of these scattering equations (4.45) on spatially homogenous systems with parabolic band approximation, where the scattering rates can be simplified analytically and the resulting equations are sufficiently simple to evaluate them in every time step.

The initialization step is completed by the composition of the initial population. There are two principle modes implemented in the program: one possibility is to set the population from different features of the band structure, like the energy or the $\mathbb{k}$-vector. This can for example be done to test special features of dynamical relaxation explicitly, for example, all states above a certain energy can be populated or all states can be populated by a Gaussian distribution with the peak at a certain energy. The second mode is based on the principles of optical excitation discussed in Sec. 4.2.6.1. In this mode, the optical field is assumed as a harmonic wave of frequency ω with an amplitude modulated by a Gaussian shape of width τ[1], the total amplitude, the frequency and the pulse width of the Gaussian are defined in the input parameter file. Then, the states are populated by applying Eq. (4.44), where the Fourier transform of the field is again given by a Gaussian distribution function centered at the optical frequency, and the required momentum matrix elements are read from the matrix element file.

After initialization, the numerical computation of the dynamical evolution is performed. For the implementation of this initial value problem, a *Runge-Kutta method* of order four [SB00] is used with a constant timestep. Although no convergence check and variable timestep control can be easily included in this algorithm, the convergence order is generally sufficient for this kind of calculation. As all statical information is cumulated in the scattering matrices $\overleftarrow{\Lambda}$ and $\overrightarrow{\Lambda}$, the required steps to evaluate a timestep in the relaxation equation (4.45) are two matrix multiplications of the dynamical population vector with the scattering matrices in index-oriented representation, then two vector-vector additions and finally a vector-vector multiplication. These operations can be implemented highly efficiently on most computers and are often optimized versions can be found in special libraries.

The results of the dynamical evaluation are written into the output file in by copying predefined timesteps of the population. Additionally, the band structure information, the shape and symmetry of the Brillouin zone and other information is put into this file. By this, a direct interpretation of the results from the data in this single file is possible. For this part of the project, the programming language `C++` is used. The main advantage of this *object-oriented* framework is that, while excellent interfaces to the elementary system services exist on the one hand, a high level of abstraction can be used to define new data types (like the index-oriented scattering matrices) and polymorphal structures (like differently implemented initial condi-

---

[1] A realistic implementation would require a Gaussian shaped plane wave for the $\mathbf{E}(t)$ field and the integral of this expression for the vector potential $\mathbf{A}(t)$ (cmp. Sec. 2.3.5). However, this integral can be approximated by $\mathbf{A}(t) = -\frac{1}{i\omega}\mathbf{E}(t)$, if the length τ of the pulse is fairly bigger then $1/\omega$. Then, the shape of the vector potential is also Gaussian.

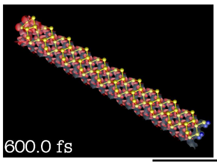

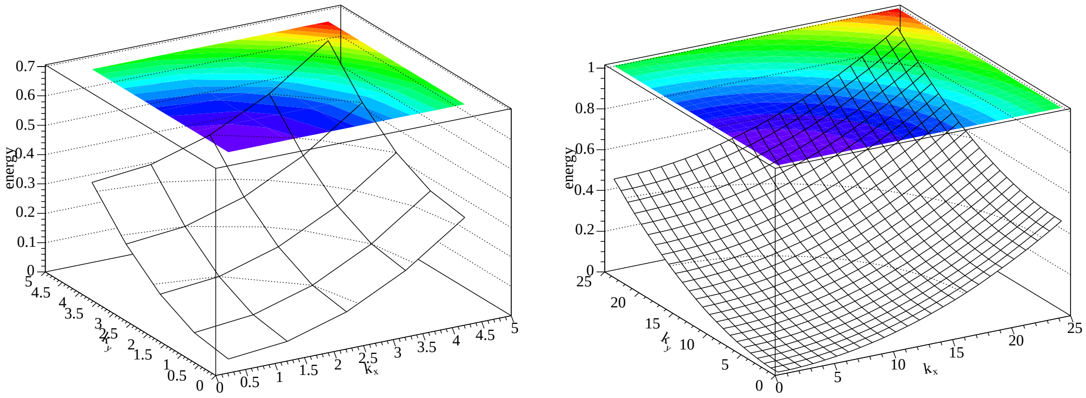

Figure 7.1: *Isotropic parabolic band structure of the test system for a discretization of* 5×5 *points (lhs) and* 25×25 *points (rhs). All dimensions are unitless, the energy and the extension of the “Brillouin zone” are normed to one at the boundary. Only a forth of the Brillouin zone is shown.*

tions). Furthermore, the language is highly standardized and there exist good `C++`-compilers for nearly any system architecture. For the output files, the `netcdf` format is used [Uni36], as it yet is the case for the matrix element file. Thus, in principle, the calculation of thematrix elements, the evaluation of the dynamics and the investigation of the results could be performed on different system architectures. This feature is however not used in the calculations of the present thesis.

7.2 Relaxation in a test system

Although the relaxation program collection has been designed for the use with externally obtained matrix elements from two dimensional structures, it is useful to implement a test routine for a highly simplified standard system to check the functionality of the relaxation mechanism. A convenient test system is an isotropic parabolic single band system (Fig. 7.1). A big advantage of this system is, apart from the simple applicability of a parabolic function, that a band minimum is genuinely contained and no discontinuity in the function or its derivatives has to be handled. Additionally, parabolic band structures are the most widely used model system in the world of semiconductor physics (although, of course, this model is not of use in the case of silicon), it can be applied, for example, in two-dimensional (multi-) quantum well structures [But07].

Within this test setup, no realistic physical units are attached to the variables, the Brillouin zone boundaries and the energy maximum are set to a value of one. The same applies to the electron-phonon coupling, where the coupling parameter D and the electron matrix elements are set to one (this is, at last, a quite unphysical assumption). A single optical phonon mode with an energy of $\hbar\omega = 0.15$ governs the relaxation. With respect to the Silicon (100) 2×1 structure, the same geometrical arrangement is used, to this end, only a quarter of the total Brillouin zone is sampled, while the rest of the Brillouin zone is mapped on this reduced part by the x, y and inversion symmetries, which naturally exist in an isotropic radial symmetric system. It should be mentioned that these symmetries are not exhaustive for this system, as for the description, a single radial coordinate would suffice. Nevertheless, the discussion of

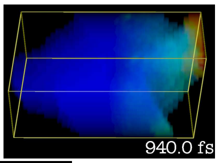

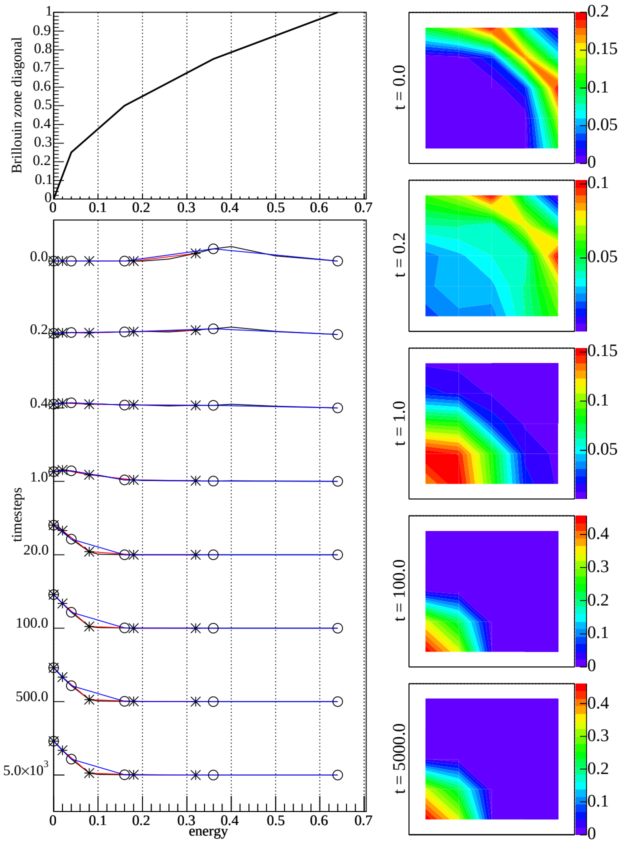

Figure 7.2: *Relaxation in the test system for an isotropic initial condition and a discretization of* 5×5 *points. At the lhs, the relaxation is shown for all states (black), the states with* $k_y=0$ *(red, black crosses) and the states with* $k_x=k_y$ *(blue, black circles). The derivations from the isotropic distribution (all curves are congruent) is only due to discretization, and not to the dynamics.*

the isotropic system in a Cartesian system enables us to discuss anisotropic initial conditions (although cylindrical coordinates might be more appropriate for this kind of discussion). By these test conditions, however, we can check some of the features of the relaxation program which are relevant for the later realistic relaxations under physical conditions. To illustrate the convergence of the program, two different parameters are discussed within this test investigation: the Brillouin zone discretization is chosen at different levels of 5×5 and 25×25 points, and two initial conditions are arranged: first an isotropic distribution which is located with a Gaussian shape around an energy of 0.4 is relaxed to check the isotropicity of the relaxation mechanism, and second, an anisotropic distribution around $\mathbb{k}=(0.75,0.75)$ is chosen to illustrate the relaxation into an isotropic final state.

7.2.1 Isotropic relaxation

The relaxation behaviour for a relaxation with isotropic initial condition is shown in Figs. 7.2 and 7.3. Though the discretization is very low in Fig. 7.2, the isotropicity is quite well maintained throughout the whole relaxation process – both at the energy scale (lhs), where devia-

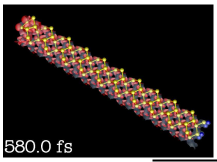

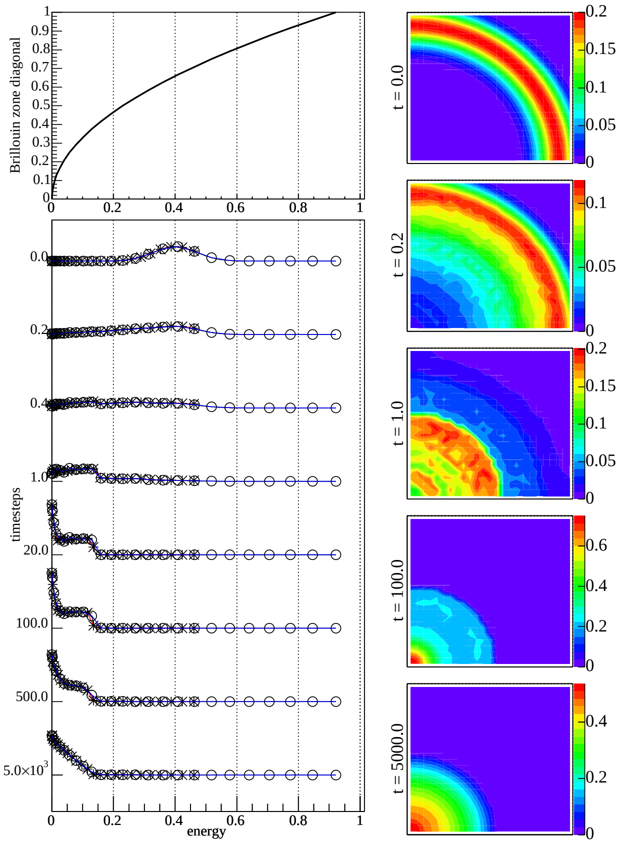

Figure 7.3: *Relaxation in the test system for an isotropic initial condition and a discretization of* 25×25 *points. While no anisotropic behaviour is found on the energy scale (lhs), weak phonon replica peaks can be observed in the Brillouin zone plot (rhs).*

tions are visible in the different cut direction for the data points (where the red curve is related to points in k_x-direction and the blue curve for points on diagonal, while the black curve contains all points), but these are related to the discretization, and on the Brillouin-zone distribution (rhs), where single points are pronounced due to the matching of the discretization of energy. Nevertheless, the discretization in Fig. 7.2 is too low to accurately describe all features of the relaxation process, as can be seen by comparing to Fig. 7.3: while in the 5×5-discretization, the relaxation is mostly terminated already at $t = 30.0$, significant changes are still visible for later timesteps in the 25×25-discretization. In Fig. 7.3, the isotropicity is even clearer pronounced. It can be observed that the relaxation of a particular state takes place in several steps, which are separated by the energy of the optical phonon. This behaviour is expressed in the occurrence of concentrical distribution peaks is the Brillouin zone picture (rhs), usually referred to as *phonon replica*. In the present Figure 7.3, those rings are only weakly pronounced at $\mathbb{k} = (0.5, 0.5)$ and $\mathbb{k} = (0.25, 0.25)$. At $t = 1.0$, a step has formed in the population distribution at an energy of a phonon energy. This is a typical behaviour in a relaxation by purely optical phonons in Markovian (energy conserving) scattering environment: below the phonon energy, the electron states can no more relax, as the minimum relaxation jump is in steps of the phonon energy $\hbar\omega$. Only through the slight weakening of the energy conservation condition

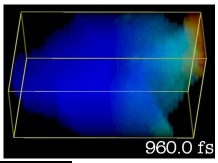

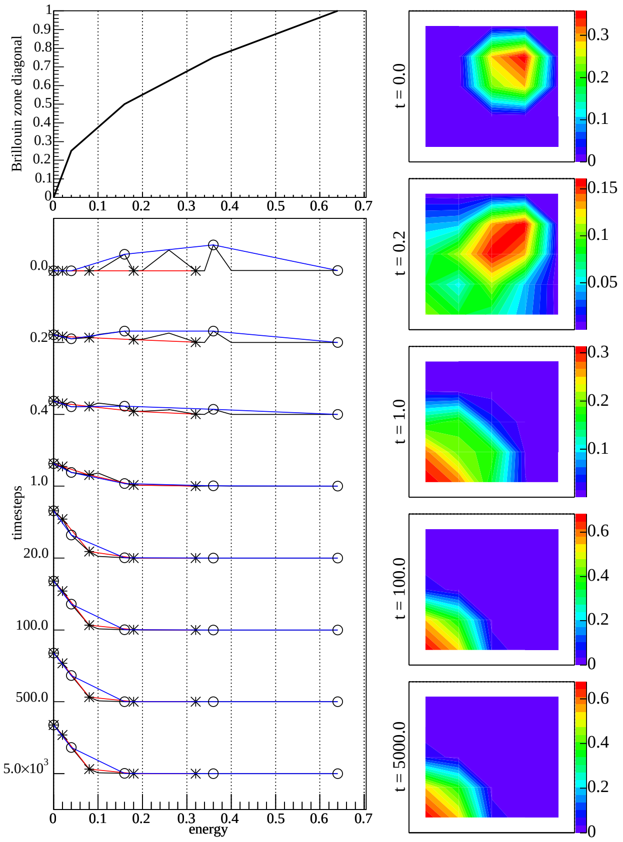

Figure 7.4: *Relaxation in the test system for an anisotropic initial condition and a discretization of* 5×5 *points.*

(Eq. (4.57)) due to discretization and the non-zero temperature, the scattering to lower states by intermediate scattering into an higher energy state is possible at $t = 5000$. This is a good illustration of the limits of the Markovian approximation (cmp. Sec. 4.2.4), as this is clearly a consequence of the energy conservation, which originates from (4.29). The timescales for the relaxation are not reliable in this case. For our investigation of silicon (001) however, these considerations are not relevant, as scattering also involves acoustical phonons which do not allow for a similar bottleneck-behaviour.

7.2.2 Anisotropic relaxation

While the stability of the implementation with respect to isotropical relaxation was investigated in Sec. 7.2.1, we now address the case of a highly anisotropic initial condition. As the entire system is isotropic, also the final state after relaxation should show no signs of anisotropicity. The initial condition distribution is chosen as a bi-Gaussian function in $\mathbb{k}$-space, the initial peak is located at $\mathbb{k} = (0.75, 0.75)$. In Figs. 7.4 and 7.5, the relaxations of those distributions is shown for discretizations of 5×5 and 25×25. For both discretizations, a mostly isotropic distribution after a relaxation time of 1.0, and in both cases, the later step are very similar to the steps of the isotropic relaxation (Figs. 7.2 and 7.3). This allows us to draw two conclusions

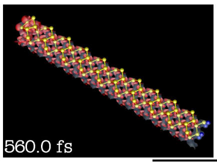

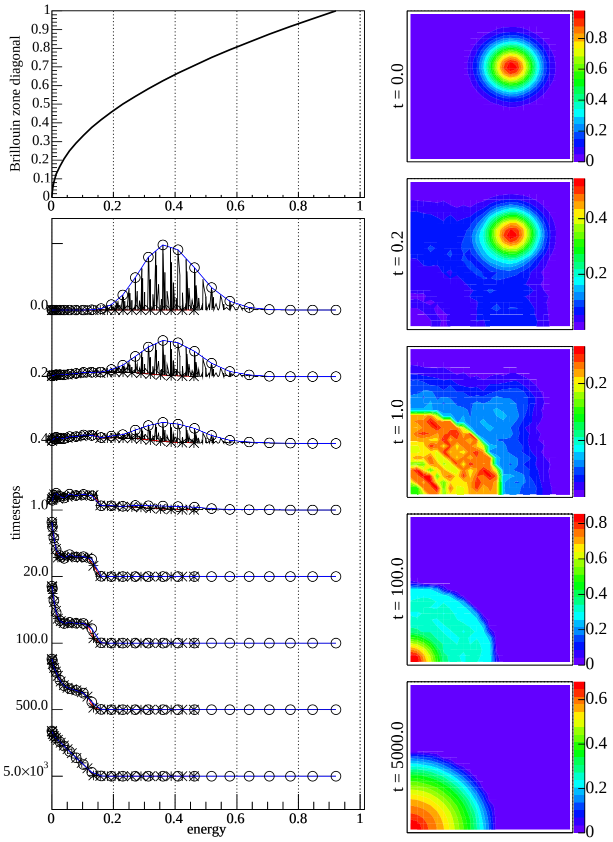

Figure 7.5: *Relaxation in the test system for an isotropic initial condition and a discretization of* 25×25 *points.*

from these simulations: first, the relaxation implementation allows the calculation of a relaxation process who is insensitive to the initial condition (not taking into account, of course, the overall electron density, which depends from the initial condition), and second, in contrast to the timescales (Sec. 7.2.1), the restitution of the isotropicity is independent from discretization in the given range. However, while at the 5×5-discretization, the resolution of the distribution function is too low to feature all details of the relaxation, much more can be seen in the 25×25 case. The phonon replica, which show up as concentrical circles in Sec. 7.2.1, are now expected to be more concentrated around the initial peak. Indeed, at a timestep of 1.0 at the rhs of Fig. 7.5, two single peak-formed phonon replica can be observed outside the concentrical isotropic distribution. The process of establishing the isotropicity can be understood by assuming that while the initial distribution can be quite anisotropic, the system will tend to a more isotropic state by every timestep. On the energy scale (lhs of Fig. 7.4 and 7.5), the anisotropicity is indicated by the very different distributions in k_x-direction (blue) and diagonal ($k_x = k_y$) direction (red), and the discontinuity of the total distribution (black). The "new" states at lower energy, which are increasingly populated, however, are all isotropic – no difference occurs from the three curves. In other words, for the given initial condition, we can state that isotropicity is accomplished when the initial distribution states are without significant population.

The isotropic relaxation after $t = 1.0$ comprises basically the same features as discussed in

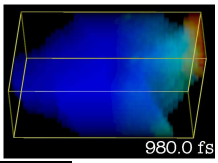

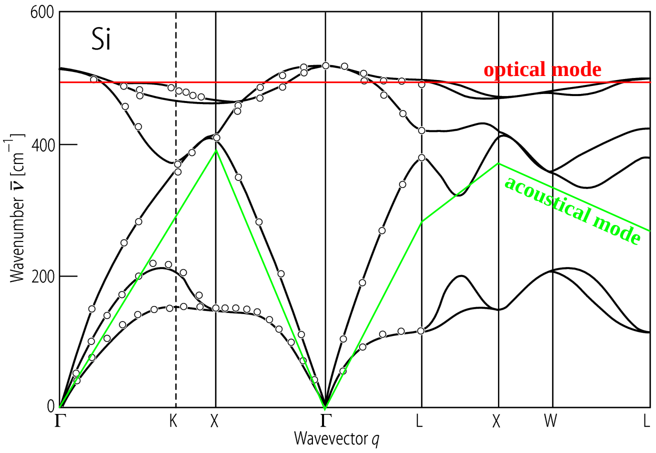

Figure 7.6: *Illustration of the effective two-mode-model: the total bulk phonon spectrum is approximated by two isotropic linear modes with acoustical (green) and optical (red) signature. From [LB87].*

Sec. 7.2.1. This means that especially the *optical-phonon bottleneck* is also formed.

7.3 Relaxation in silicon for a Gaussian initial condition

After investigating the principle applicability of the relaxation equations under simplified conditions, we can now proceed to the simulation of a distribution under realistic conditions in the silicon (001) surface system. The most realistic situtation that can be investigated by our program is, of course, the simulation using initial conditions of optical excitation (Eq. (4.44)). Nevertheless, the optical initial condition has only a very limited range of population at selected points of the band structure, which makes the investigation of relaxation quite difficult. Thus, as first approach, we choose a different initial condition by an energetical “gauss-pulse” (as in the test system in Sec. 7.2.1), while we will discuss the optical excitation in Sec. 7.4.

The matrix elements and the band structures that have been calculated in Chapter 6 are read into the dynamic file, whereby only the electron-phonon matrix elements are relevant for the relaxation. For the phonons, a simplified two-mode-model is used (cmp. Sec. 4.3.1) which comprises one acoustical and one optical mode (Fig. 7.6). The modes are chosen in order to interpolate the phonon spectrum from literature [NN72, PV81, GdGPB91, LB87] with heuristical parameters. The dependency on the bulk-k_z-coordinate is neglected. The acoustical mode is approximated by a linear dispersion with a sonic speed c:

$$\omega_{\mathbf{q}}^{\mathrm{ac}} = c|\mathbf{q}|, \tag{7.1}$$

whereas the optical mode has a constant dispersion:

$$\omega_{\mathbf{q}}^{\mathrm{opt}} = \omega_0. \tag{7.2}$$

Parameters for the corresponding deformation potentials can also be found in literature [MCFF78, BPC84, vdW89, LB87]. The functional form of this dependency is however quite complex. For the acoustical mode, the electron-phonon coupling in Eq. (4.51) $D_1^i(\mathbb{q})$ is expressed in terms of a longitudinal mode:

$$D_1^i(\mathbb{q}) = D^i \mathbb{q}. \tag{7.3}$$

This is justified by the fact that in bulk semiconductors, the coupling to the longitudinal modes is much stronger than to all other modes [YC96, SW02]. If this and the dispersion (7.1) is

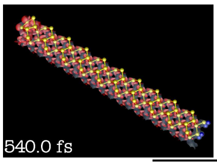

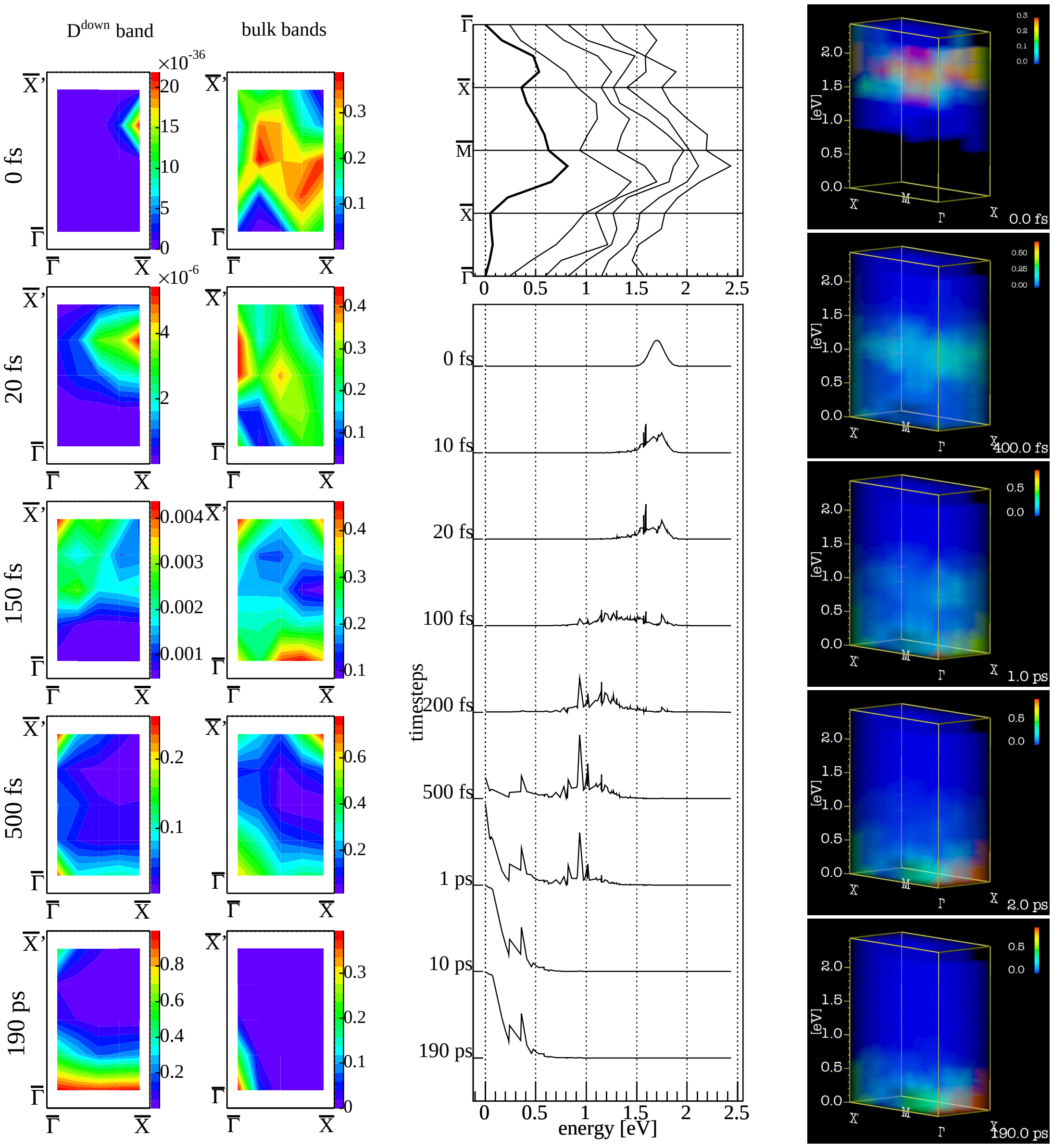

Figure 7.7: *Relaxation dynamics of a supercell with 7 layers and a discretization of 8x8 points in the complete Brillouin zone for an initial condition with a Gaussian peak a* 1.7 *eV above conduction band minimum.*

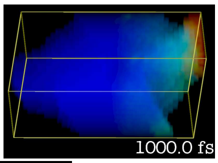

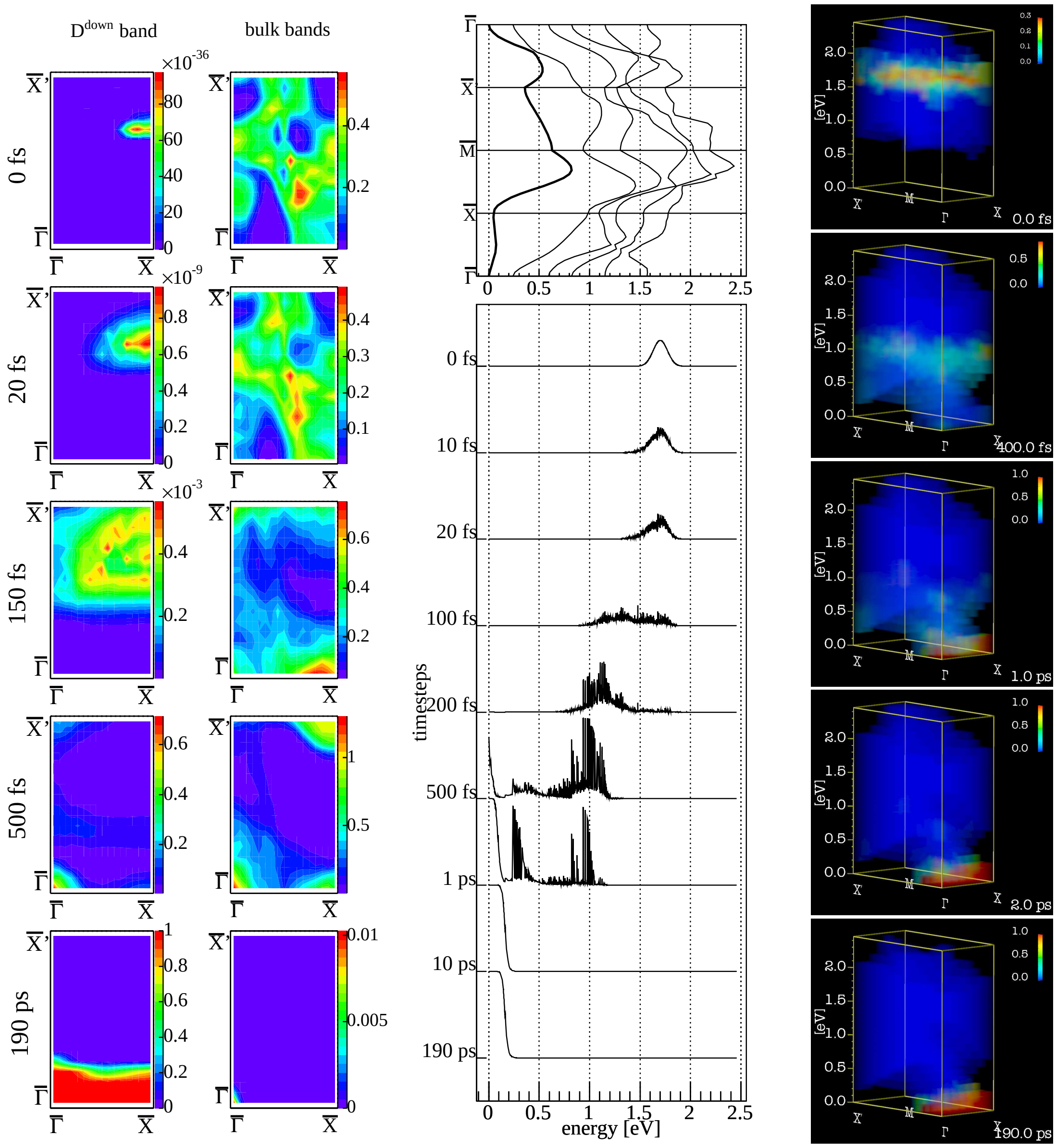

Figure 7.8: *Relaxation dynamics of a supercell with 7 layers and a discretization of* 32×32 *points in the complete Brillouin zone for an initial condition with a Gaussian peak a* 1.7 *eV above conduction band minimum.*

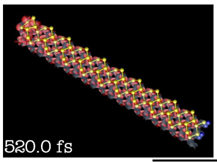

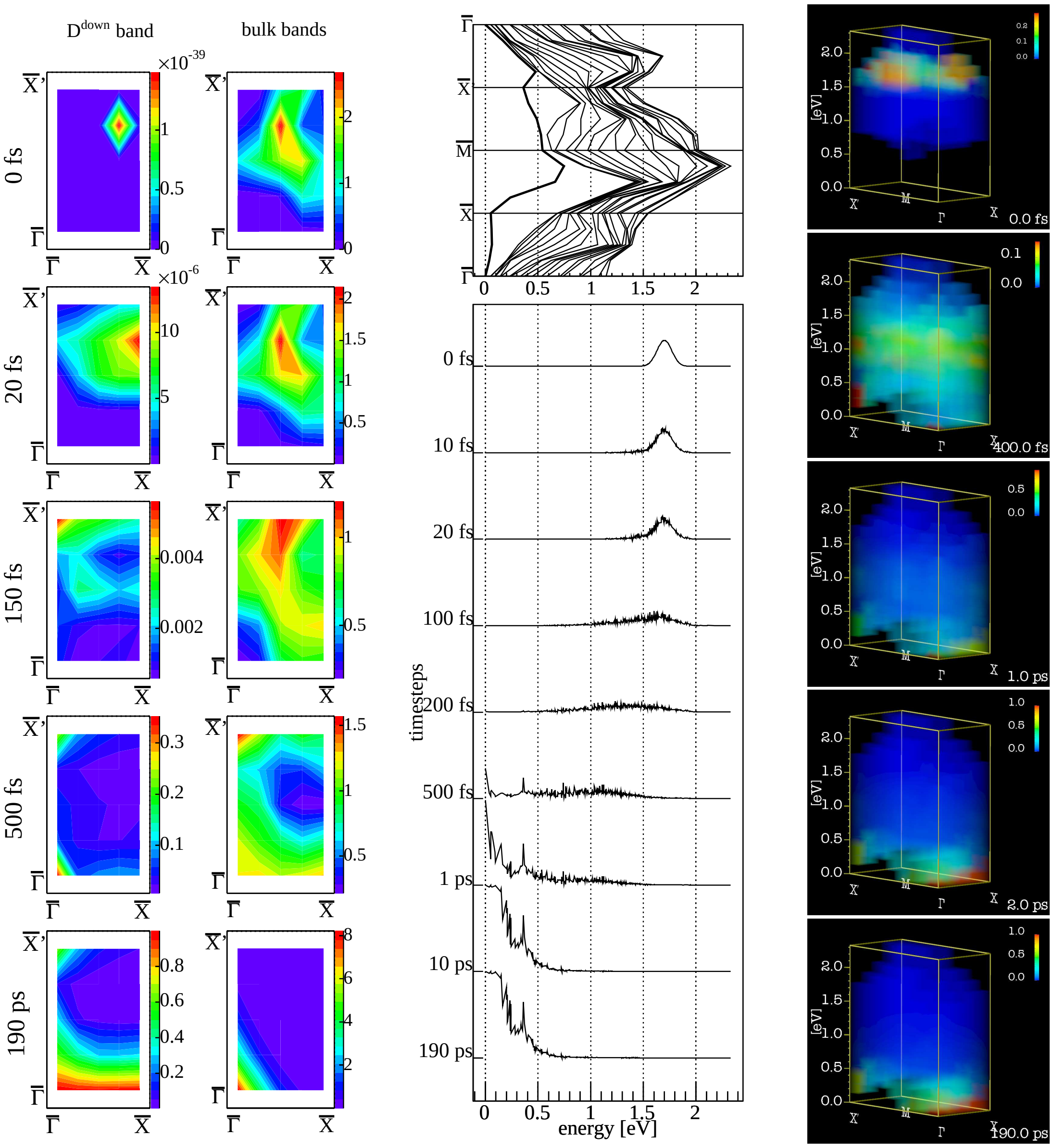

Figure 7.9: *Relaxation dynamics of a supercell with 40 layers and a discretization of* 8×8 *points in the complete Brillouin zone for an initial condition with a Gaussian peak a* 1.7 *eV above conduction band minimum.*

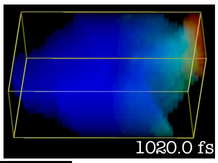

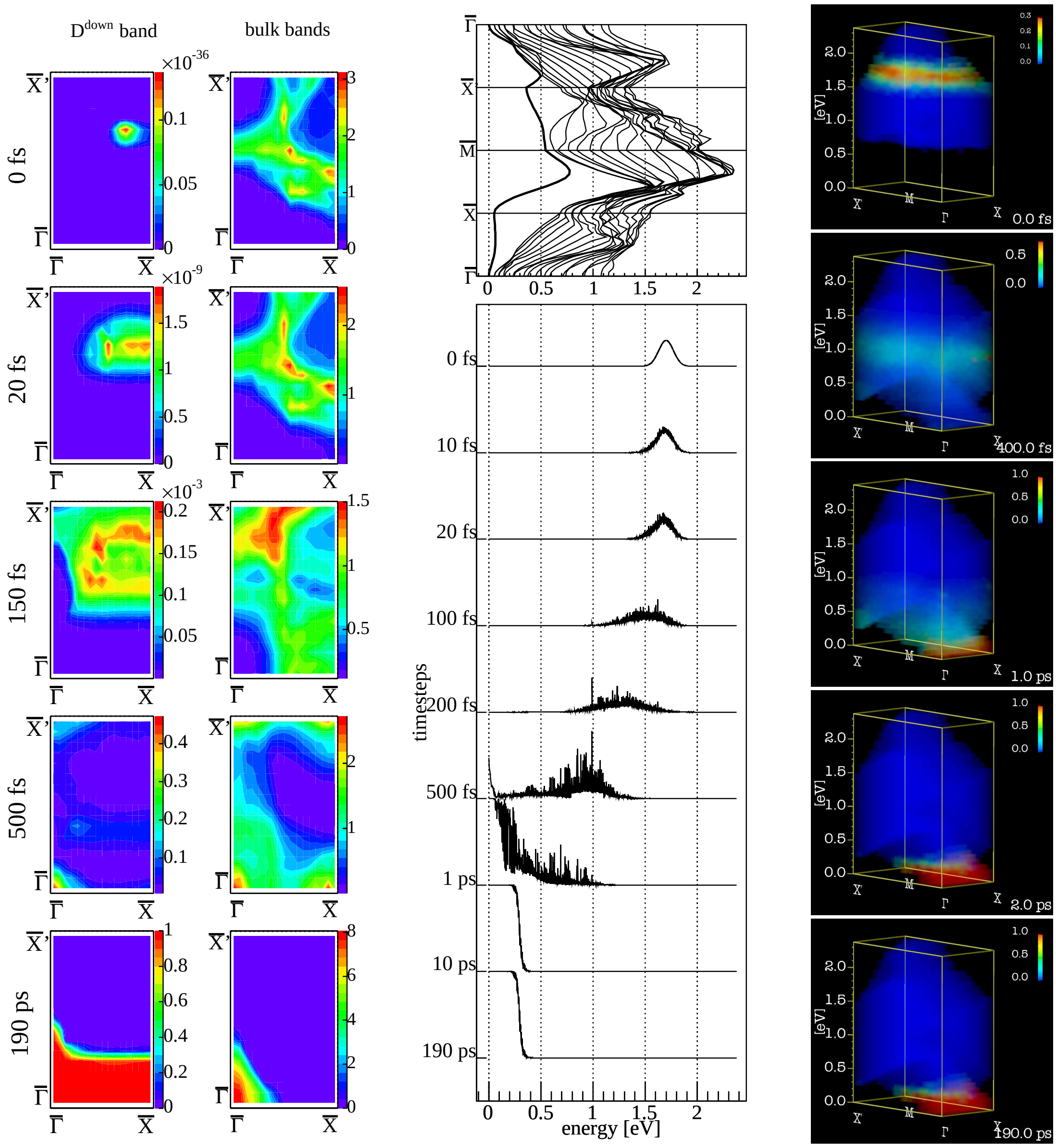

Figure 7.10: *Relaxation dynamics of a supercell with 40 layers and a discretization of* 32 × 32 *points in the complete Brillouin zone for an initial condition with a Gaussian peak a* 1.7 *eV above conduction band minimum.*

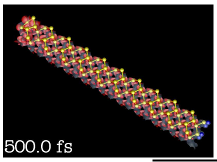

reinserted into Eq. (4.51), we find an overall dependency of $\sim \sqrt{|\mathbb{q}|}$ for the overall matrix element $D^{n'\mathbb{k}'}_{n\mathbb{k};i\mathbb{q}}$ [YC96]. For the optical mode, however, the coupling constant $D^{i}_{11}(\mathbb{q})$ can not be approximated in a similar manner, as an optical mode also includes an oscillation inside the unit cell. Apart from the fact that the coupling to this kind of oscillation is much stronger, the only possible and reasonable approximation is a constant, $\mathbb{q}$-independent coupling, as the difference of elongation of the single atom coordinates in the unit cell (which, at last, determines the coupling strength at this level of approximation) is quite unchanging throughout the whole Brillouin zone. As also the phonon energy (7.2) is independent of $\mathbb{q}$, the matrix element $D^{n'\mathbb{k}'}_{n\mathbb{k};i\mathbb{q}}$ for the optical mode from Eq. (4.51) is completely constant on the Brillouin zone in this approximation. The employed values are taken from [LB87] and [LB87] and yield a sonic speed of 6.1 meV/nm and a total deformation matrix element $D^{n'\mathbb{k}'}_{n\mathbb{k};i\mathbb{q}} = D^{\text{acou}} \cdot \sqrt{|\mathbb{q}|}$ with a D^{acou} of 7.37 eVnm$^{1/2}$ for the acoustical phonons and a phonon energy of 0.057 eV with a deformation matrix element of $D^{n'\mathbb{k}'}_{n\mathbb{k};i\mathbb{q}} = D^{\text{opt}} = 40.0$ eV for the optical phonons.

With these parameters for the phonons, we can now investigate the dynamical evolution of the system. The initial condition is defined by a Gaussian pulse at an energy of 1.7 eV above the conduction band minimum. In Figs. 7.7-7.10, the dynamics of this initialization is illustrated for slabs of 7 and 40 layers and for $\mathbb{k}$-discretizations of 8×8 and 32×32 for selected timesteps, including the initial population. At the lhs, the population distribution over the Brillouin zone is depicted for the D^{down} band, while in the middle, the population is resolved on the energy scale, with the corresponding band structures of the relevant regions of the conduction bands plotted at the top level. On the rhs, finally, the populations are shown energy and time resolved, basically, this corresponds to a combination of the other pictures in this figure.

The choice of the initial condition as a Gaussian peak at this energy makes it possible to discuss the relaxation process in different phases, as the peak energy and the width of the gauss-pulse are selected in order to assure a practically exclusive excitation of bulk states, because the maximum energy of the D^{down} surface state is located energetically below. In all Figs. 7.7-7.10, this is visible from the fact that the initial population on the Brillouin zone is negligible low in the surface band ($\sim 10^{-36}$, left hand row of the lhs pictures) and the extension of the Gaussian can be regarded in the energy resolved plot (middle row). The temperature for the phonon bath (cmp. Sec. 4.2.3) is fixed at 90 K.

The classification of the relaxation process into phases is done in the following way: in the first phase which lasts until ca. 200 fs, the relaxation only touches bulk bands. Nevertheless, the relaxation is not homogenous, the initial peak is dispersed to a much wider (approx. 5×) distribution below the initial peak energy, but still above the surface band maximum. The extension of this first-phase distribution varies only slightly within the different figures, and seems to be mostly independent from slab thickness and discretization. Although obviously the relaxation timescales are very sensitive to the different possible channels (and the emergence of peaks implies that some channels are more probable than others), this bulk-related relaxation is in average on a time scale of ~ 100 fs.

After 200 fs, the second phase of the relaxation begins. Now, the D^{down} band is also involved in the process. At 500 fs, the relaxation clearly splits into two distinct timescales: On the one hand, the relaxation inside the bulk slows down with respect to the first phase and merges with a relaxation from bulk to surface band. On the other hand, a relaxation inside the surface band evolves. This surface-bound relaxation is on a much faster timescale: at 1.0 ps, the surface band minimum is already entirely relaxed to a Fermi-like distribution function. This behaviour is at best visible in Fig. 7.8 (middle row), where the range of overlap of surface and bulk bands

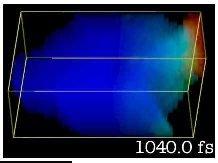

is limited to higher energies. In Figs. 7.7 and 7.9, however, it can now be clearly stated that the discretization is insufficient: the final state of the relaxation has no shape as in the equilibrium (*Fermi-distribution*, Eq. (B.1)). In Fig. 7.10, the Fermi-shape is shadowed by the populations of the bulk-like bands, which reach down to 0.05 eV above the surface band minimum. The effect of the two-timescale relaxation is at most pronounced in Fig. 7.8 at 1.0 ps: at the minimum of the lowest bulk band (0.3 eV), additionally to the peak at the surface minimum, a second peak has formed with a Fermi-like shape (while other peaks remain at higher energies). Here, we can definitely conclude that the relaxation from bulk band minimum to surface is much slower than parts of the relaxation inside the bulk: apart from a small fraction which is transferred from bulk to surface band at a higher energy, relaxations inside bulk and surface are quasily independent and thus form their separated local distribution functions. The relaxation down to the “total” equilibrium state acts then on the slower timescale (which is obviously of the same order as the slowest processes in bulk relaxation), such that at 10.0 ps, relaxation is more or less completed. In Fig. 7.10, this process is not clearly visible: Here, the final population of electrons in the surface band reaches energetically up to the bulk bands, especially the bulk band minimum is completely populated (1.0) at 1.0 ps, so no further interaction between the bands is necessary for the relaxation at the bulk band minimum, and no separated distributions form. As we will see in Sec. 7.4, this so called *Pauli-blocking* has not only visible effects as in this case, but also influences the relaxation behaviour at the surface band minimum.

Within the Brillouin zone, the relaxation does not happen in a homogenous manner. In Figs. 7.8 and 7.10 on the lhs, it can be seen that while the population is initially more or less concentrated at the center of the reduced Brillouin zone (the shape of the distribution reflects the band structure at the energy of initial excitation), it shifts to the edges (500 fs) and finally proceeds to the $\overline{\Gamma}$-point (or the $\overline{\Gamma}$-$\overline{X}$-line, respectively). The surface band is not significantly populated until 500 fs, but is then strongly populated in the final state. While this principal evidence is yet visible in Figs. 7.7 and 7.9, the resolution at this discretization is too low to allow an accurate interpretation. However, the pictures from the first timesteps in Figs. 7.8 and 7.10 differ significantly. Hence, we can conclude that number of bands in the seven layer slab is insufficient to sample the bulk band structure in the required resolution, while a convergence with respect to this sampling is achieved with a higher layer number (see Appendix C.2 for a summary of all calculations). A second effect of a thicker slab is a volume-surface effect with respect to the final population of the surface band: as the relation of the number of states in the surface band decreases with respect to the total number of states in the bulk bands and also more states are populated initially due to the higher number of bands in the bulk, a higher fraction of the surface band is populated in the final state. This can be extracted from the fact that the extension of the population (red zone) is much bigger in Fig. 7.10 (lhs) than in Fig. 7.8, and also the “*pseudo-Fermi energy*”, which is defined as the energy at which the Fermi-like distribution function of the final population of the conduction bands is at 0.5 shifts from 0.15 eV in Fig. 7.8 (middle row) to 0.3 eV in Fig. 7.10. This effect is only partly physical, it should be expected that in a realistic materical, the absorption limits the depth of penetration into the bulk and consequently the population of the bulk bands also decreases with increasing slab thickness. The modelling of light absorption [Mah90, HSC$^+$93, LSS$^+$97, MP00] is, however, beyond the scope of this thesis, especially as the usual penetration depth of light in silicon ($\sim$ 1 pm) is of a much bigger order as the depth of our calculated supercells ($\sim$ 10.0 nm).

An overview of the relaxation process including all so far discussed features can be observed on the rhs pictures of Figs. 7.7-7.10. While at 0 fs, the narrow energetical range of the

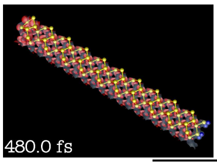

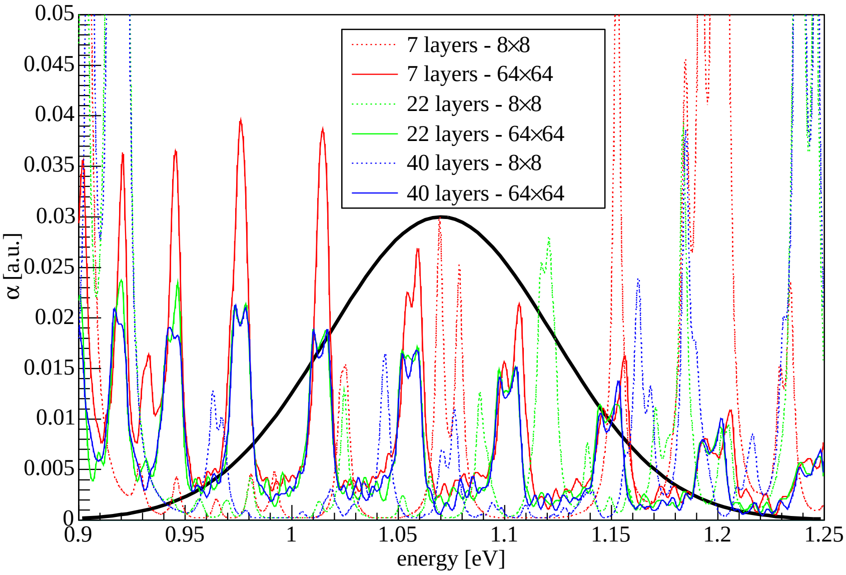

Figure 7.11: *Momentum matrix transitions in the range 0.9-1.25 eV for different slabs and* $\mathbb{k}$*-discretizations. The black curve indicates the shape of the frequency distribution (the Fourier transform) of the optical pulse. While for the transition of the low discretized* (8×8) *calculations only a few single peaks within the range of the pulse appear, the transitions quasily form a continuum in the high discretized* (64×64) *calculations. Note that in contrast to Figs. 6.4-6.6, the spectra are only normed on the* $\mathbb{k}$*-point number in order to avoid the surface-volume effect which applies to transitions to the surface band.*

initial population around the excitation energy of 1.7 eV is visible, the population is spread over a wider range at 200 fs, and then populates the $\overline{\Gamma}$-$\overline{X}$-line relatively fast from 500 fs on. Later, the populations of the higher states all relax to the minimum.

7.4 Relaxation after optical excitation

In this section, we will now finally examine a relaxation at the silicon (001) 2×1 surface with initial conditions from optical excitation determined using Eq. (4.44). Following the experimental boundary conditions described in [WKFR04], the frequency of the optical excitation is chosen as 1.69 eV with an amplitude of Gaussian shape of a duration of 50 fs. Due to the known deficiencies of the DFT-LDA-bandstructure, which is known to underestimate the bandgap energy, a so called scissors-shift is applied to the excitation frequency by decreasing the frequency by a certain value (cmp. Sec 1.4.1). The justification for this scissors shift is the known fact that in silicon, the bandgap energy of the DFT-LDA calculation is reduced for all **k**-points by the same value with respect to a real band structure, which can be investigated by experiments or calculations with quasi-particle corrections (for example the GW method) [Egg05]. The value of this necessary shift is fixed to 0.62 eV by comparison of the calculated indirect bulk bandgap energy from Sec. 5.1 to the experimental indirect bandgap value.

In a realistic system, mechanisms exist to depopulate the conduction band states, e. g. by recombination with valence band holes. In [WKFR04], a scattering process via excitonic states

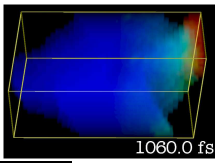

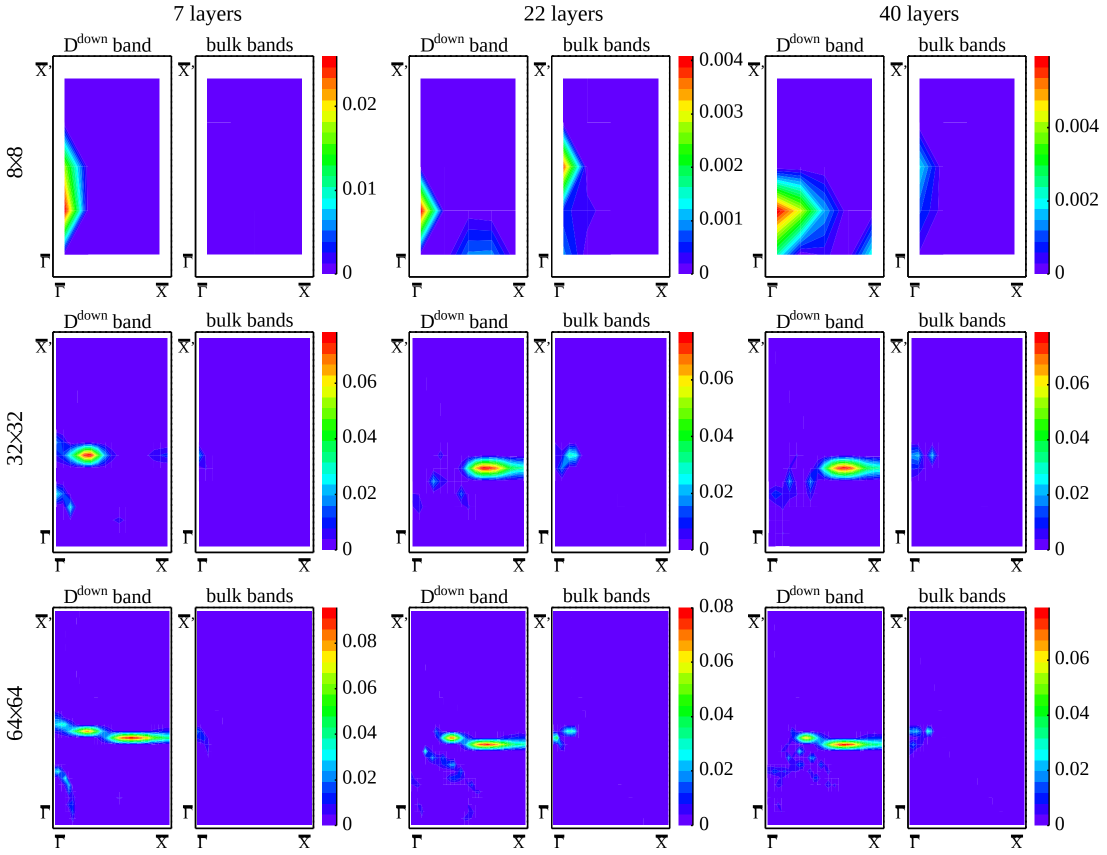

Figure 7.12: *Initial distribution within the Brillouin zone for 7, 22 and 40 layer slabs and for discretizations of* 8×8, 32×32 *and* 64×64. *While the* 8×8 *discretization is obviously insufficient to describe the distribution, good agreements are found for all slabs with the higher discretizations. Nevertheless, an accurate accordance is only found for* 64×64 $\mathbb{k}$*-points.*

in the bandgap is assumed, which acts on a slower, but for phonon scattering relevant timescale. In our relaxation model, no electron hole recombination is considered, the electrons initially inserted in the conduction bands have to relax to the conduction band minimum. On the other hand we have seen in Sec. 7.3 how a *Pauli-blocking* mechanism can exclude some states at the conduction band minimum from taking part in the relaxation dynamics. In order to investigate the *phonon-induced* timescales involving the states at the conduction band minimum, we have to guarantee that the population at the minimum remains low. This can be achieved by limiting the total conduction band population through applying a sufficiently weak optical pulse, which is also an implicit requirement of the *slow relaxation approximation* (Sec. 4.2.6) within linear optics in order to neglect the polarization dynamics.

The initial distribution after optical excitation is highly sensitive to the discretization and the slab thickness of the underlying calculation. In order to cover the different aspects of the optical excitation in x-direction (Fig. 6.4) and in y-direction (Fig. 6.5), the polarization of the incident light is chosen along the diagonal ($x = y$). In Fig. 7.11, a cutout of the spectrum around the light frequency is shown. The Fourier transform of the initial pulse, which can, due to its form as plane wave with a Gaussian envelope function, be cast into a Gaussian in energy space with a variance of 0.075 eV, is symbolized by the black curve. To allow a consistent

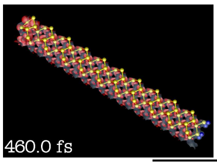

comparison, the different spectra of slabs with 7 (red), 22 (green) and 40 (blue) layers and discretizations with 8×8 (dashed) and 64×64 (solid) are now only normed on the number of $\Bbbk$-points, in contrast to the figures in Sec. 6.3.1. The reason for this is that excitation with a pulse of that energy always ends in the surface band, as no direct bulk transition exists in silicon below the direct bandgap of 2.4 eV. The weight of the surface band with respect to the bulk bands, however, falls with increasing total number of bands (cmp. 6.3.1), as the surface band remains a single band in all calculations. Consequently, the number of transitions should be independent of the number of layers in the slab calculation.

While the form and the position of the peaks for the 64×64 layer calculations is very similar for the 22 and 40 layer calculation, the differences to the 8×8-discretized calculations are significant. Here, the peaks appears really as singular structures, while in the 64×64 discretization, the peaks are at reproduceable positions and emerge from a continuum. Again, we conclude that the 8×8 discretization is insufficient to describe the system in the required accuracy. Also layer number is however an important parameters for the convergence of the spectrum structure, as in the 7 layer calculation, the height of the peaks differs from the 22 and 40 layer calculations even at the 64×64 discretization. On the other hand, for 64×64 points, all peaks are principally found in the 7 layer slab calculation, which is not the case in lower discretizations. In Fig. 7.12, the distribution of the initial population within the Brillouin zone is shown. At a discretization of 8×8, the differences of the distributions are obvious, especially as their size differs by an order of magnitude. At 32×32, similar peaks are found for the 22 and 40 layer calculations, while the 7-layer calculation has a completely different peak structure. At 64×64 $\Bbbk$-points, the distributions look quite similar for all slabs: a high discretization is obviously required for an adequate resolution of the excitation process.

After initialization by the optical excitation, the relaxation calculations are performed for two different bath temperatures (cmp. Sec. 4.2.3) of the system. The experimental investigation in [WKFR04] is effected at a temperature of 90 K. A similar experiment has been performed at room temperature [TT03]. Our simulations are thus performed at temperatures of 90 K and 300 K, and a few examples of the numerous calculations for different layer numbers and discretizations are presented on the following pages.

7.4.1 Relaxation for optical excitation at 90 K

The relaxation for different slabs of the optical initial conditions are shown in Figs. 7.13-7.15. The frequency of the light after the application of the scissors shift is at 1.07 eV, whereas the unadjusted bandgap extracted from the band structure calculations (Sec. 5.2) is at 0.56. A pronounced peak at 0.45 eV is visible for all slabs, this peak corresponds to an optical excitation from the valence band top to the D^{down} surface band. Single additional peaks exist for all calculations. While the surface band (the leftmost band in the top picture of the middle row) is very similar for all slabs, the bulk is represented by a varying number of bands: At the seven layer slab, only a single bulk band covers the energy range in which excitation occurs. At the 22 layer slab, the number of relevant bulk bands increases to 7, and at the 40 layer slab, about 15 bands can be found between 0.0 and 0.6 eV above conduction band minimum. Consequently, the average spacing between the bands ranges from 0.6 eV for the 7 layers to 0.04 eV for the 40 layer slab. This value has a significance for the relaxation process, as a bulk-like relaxation can be expected when the average energy difference between two $\Bbbk$-points of two neighboring bands is of the same order as the average energy difference of two $\Bbbk$-points of

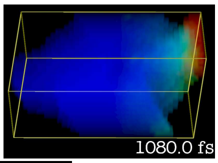

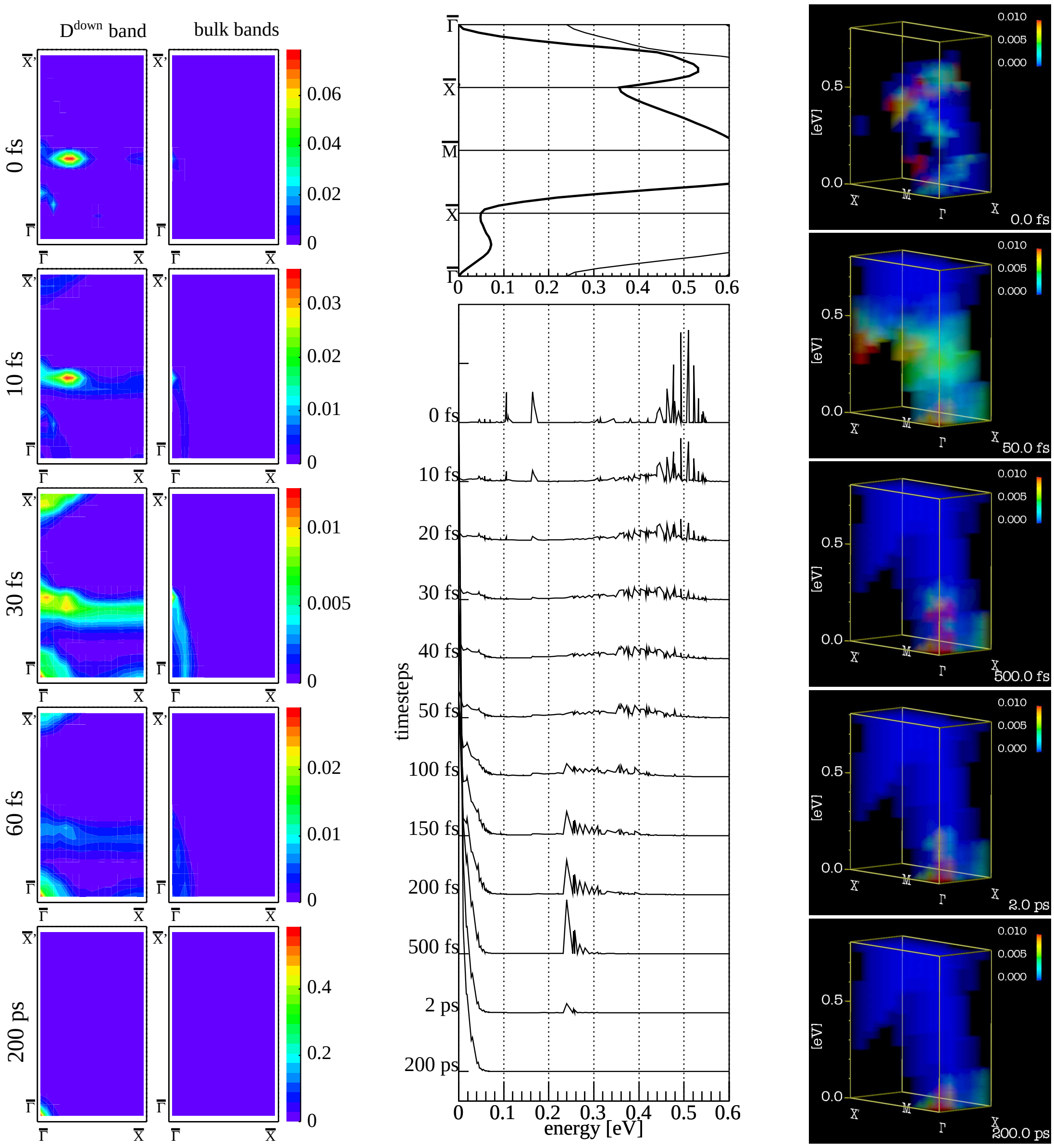

Figure 7.13: *Relaxation dynamics for a slab of 7 layers at a discretization of* 32×32 *points in the complete Brillouin zone and for a temperature of 90 K after an excitation with a optical 1.69 eV pulse. Only two bands reach into the considered energy region (middle row, top level). The energy resolved population (middle row) is increased by a factor of 25 with respect to Figs. 7.7-7.10. The bottleneck formation at the bulk band minimum (0.25 eV) can be clearly observed.*

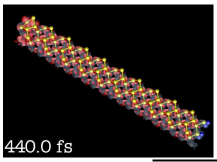

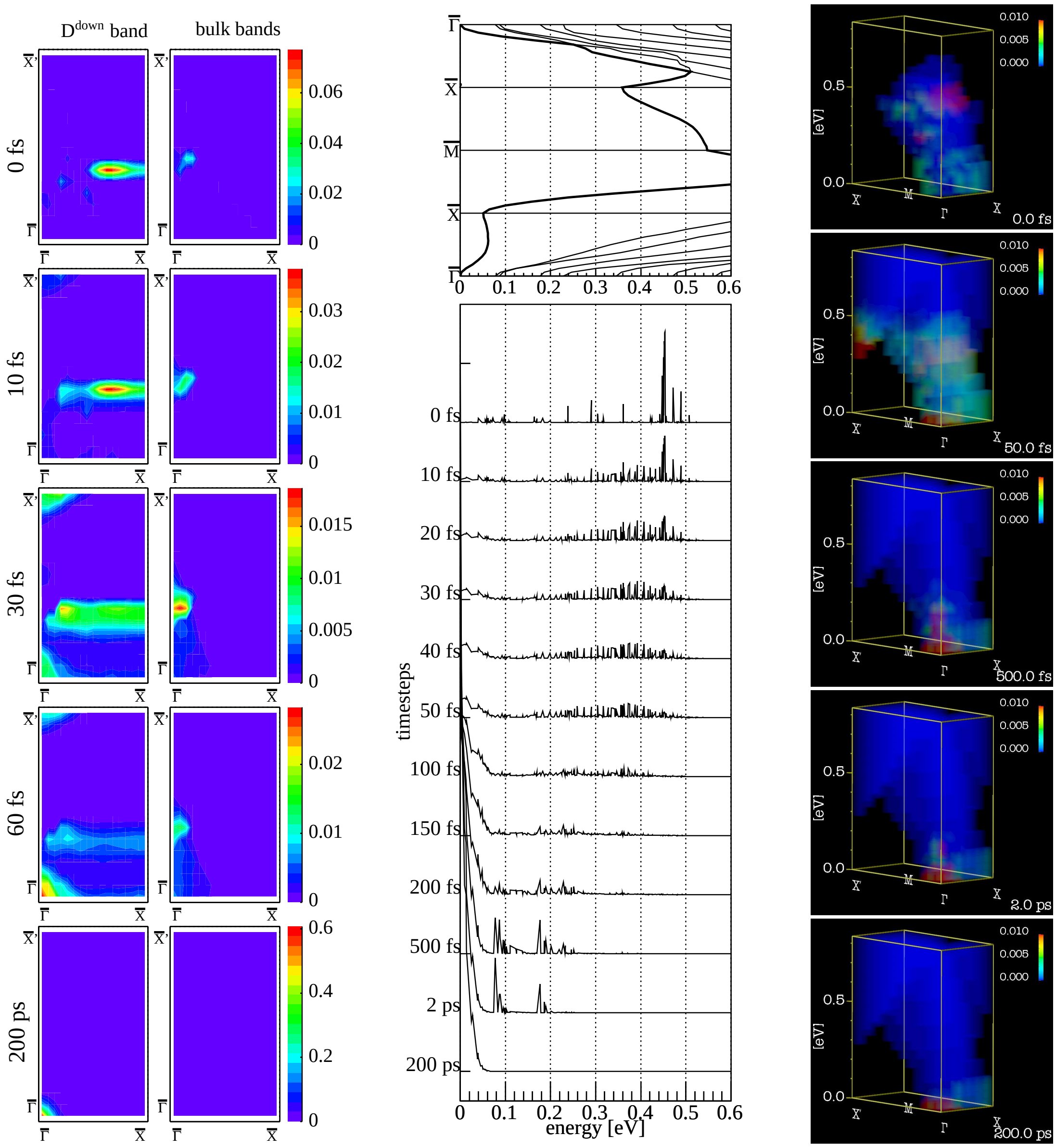

Figure 7.14: *Relaxation dynamics for a slab of 22 layers at a discretization of* 32×32 *points in the complete Brillouin zone and for a temperature of 90 K after an optical excitation with a 1.69 eV pulse. The energy resolved population (middle row) is increased by a factor of 25 with respect to Figs. 7.7-7.10. Now, a few bands are present in the required region. The bottleneck and the bulk band minimum shift towards a lower energy (0.8 eV).*

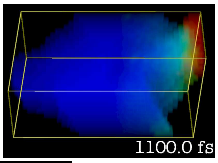

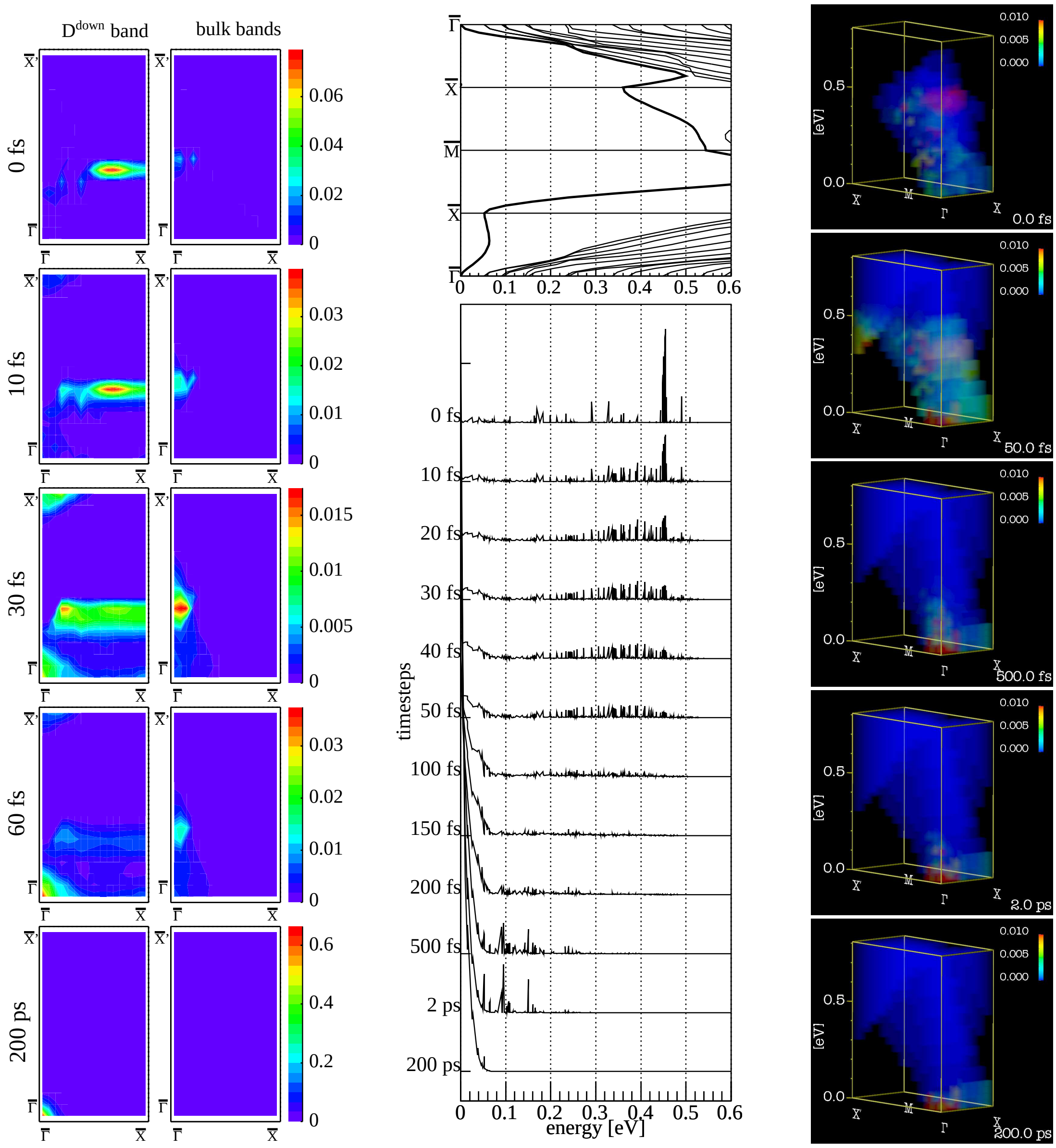

Figure 7.15: *Relaxation dynamics for a slab of 40 layers at a discretization of* 32×32 *points in the complete Brillouin zone and for a temperature of 90 K after an optical excitation with a 1.69 eV pulse. The energy resolved population (middle row) is increased by a factor of 25 with respect to Figs. 7.7-7.10. The bands are now in an average distance of ca. 0.05 eV. The bulk band minimum with the bottleneck has shifted to 0.05 eV.*

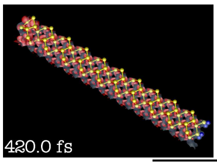

the same band. Otherwise, intraband relaxation inside a single band might be privileged with respect to interband relaxation. Furthermore, the interplay of optical and acoustical phonons is dependent on the energies of the states, if the states are energetically close, a scattering by optical phonons might be impossible, while scattering via acoustical phonons occurs – on a slower time scale.

After the optical pulse, a structure with pronounced peaks is left. While in Fig. 7.13, a Gaussian envelope function which limits the single peaks, resembling to the optical envelope function, around the maximum at 0.45 eV is observable, the distribution is more focused on a single, narrow peak at 0.45 eV in the thicker slabs (Figs. 7.14 and 7.15). The strong transition at 0.45 eV is obviously not accurately described in the seven layer slab calculation, as it extends on multiple states with different energy. Furthermore, the location of the initial peak within the Brillouin zone (lhs of Fig. 7.13) differs significantly from the positions of peaks of the other slabs.

In consecution of the initial excitation, the relaxation starts. As in the case of relaxation of a Gaussian initial condition, the distribution is broadened in a first phase. Nevertheless, a clear decoupling of bulk- and surface relaxation cannot be observed: due to excitation into the surface band (cmp. Fig. 7.12), the bulk band(s) are populated after the surface band, and a fraction of the population directly relaxes inside the surface band to the surface band minimum. Thus, a peak forms at the minimum quasi immediately (20-30 fs after excitation). During relaxation, the shape of the distribution remains a peak-like structure, consequently, only some of the states at a given energy are involved in the relaxation. This is plausible, as scattering depends on the $\Bbbk$-vectors and the matrix element between the in and out states. At 150 fs (7 layer calculation, Fig. 7.13) - 500 fs (40 layer calculation, Fig. 7.15), a peak forms at the particular bulk band minimum of the band structure – in contrast to the calculations in Sec. 7.3, these peaks do not interfere with the final equilibrium distribution for the calculations with a thicker slab. This is a consequence of the very low excitation distribution.

Inside the Brillouin zone, the initial distribution relaxes not immediately to the surface band minimum, but by a sequence of processes. Initially, the peak lies on a line parallel to the $\overline{\Gamma}-\overline{X}$-direction, at the seven layer slab (Fig. 7.13, lhs), the maximum is close to the left edge ($\overline{\Gamma}-\overline{X}'$-line), while at the 22 and 40 layer slabs (Figs. 7.14 and 7.15, lhs), the peak is found at the right edge. In the first steps of relaxation (0 fs-30 fs), to effects can be observed: On one hand, the population extends parallel to the $\overline{\Gamma}-\overline{X}$, on the other hand, a part of the population is transferred to the bulk bands, where, for energetical reasons (as the gap between bulk and surface band shrinks), the population is very low for the 7 layer slab and temporarily even higher than in the surface band for the 40 layer slab (at 30 fs). Additionally, at 30 fs, a part of the population is trapped in a local minimum of the band structure at the $\overline{X}'$-point. At the later steps of the relaxation, these local peaks of population are now transfered to the surface band minimum without the occurrence of new local minima patterns in the plots.

7.4.2 Relaxation for optical excitation at 300 K

The beginning of the relaxation at a temperature of 300 K, illustrated in Figs. 7.16-7.18 cannot be distinguished from the beginning of the 90 K-relaxation (Sec. 7.4.1. However, as soon as the distribution reaches the surface band minimum and forms a Fermi-like shape, the effect of the higher temperature becomes obvious by the existence of a much longer tail of the population distribution, which reaches up to 0.15 eV. For the seven-layer calculation (Fig. 7.16, middle

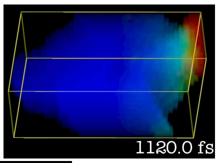

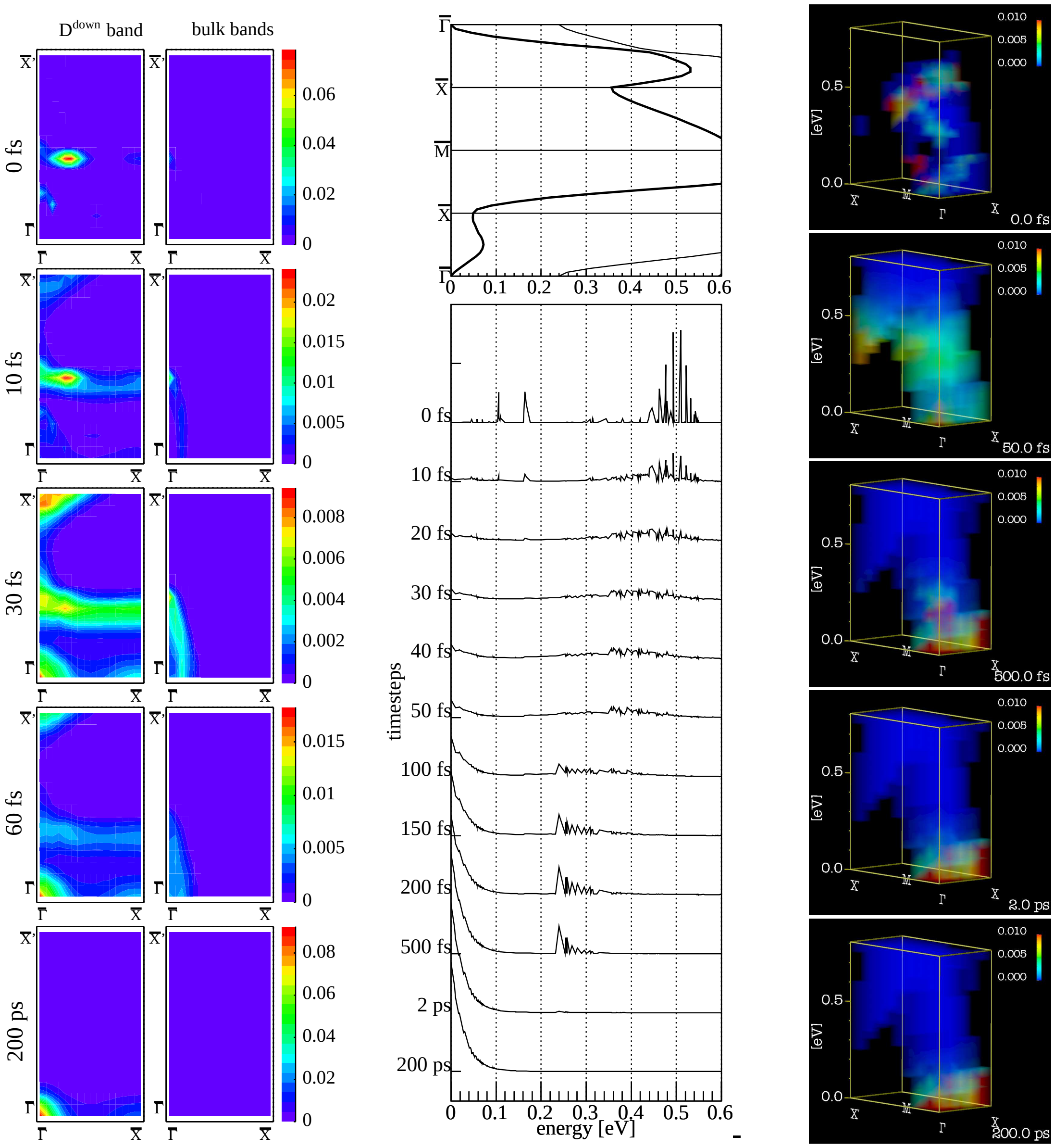

Figure 7.16: *Relaxation dynamics for a slab of 7 layers at a discretization of* 32×32 *points in the complete Brillouin zone and for a temperature of 300 K after an optical excitation with a 1.69 eV pulse. Only two bands reach into the considered energy region (middle row, top level). The energy resolved population (middle row) is increased by a factor of 25 with respect to Figs. 7.7-7.10. The bottleneck formation at the bulk band minimum (0.25 eV) can be clearly observed.*

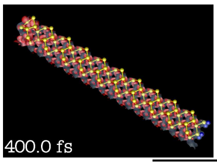

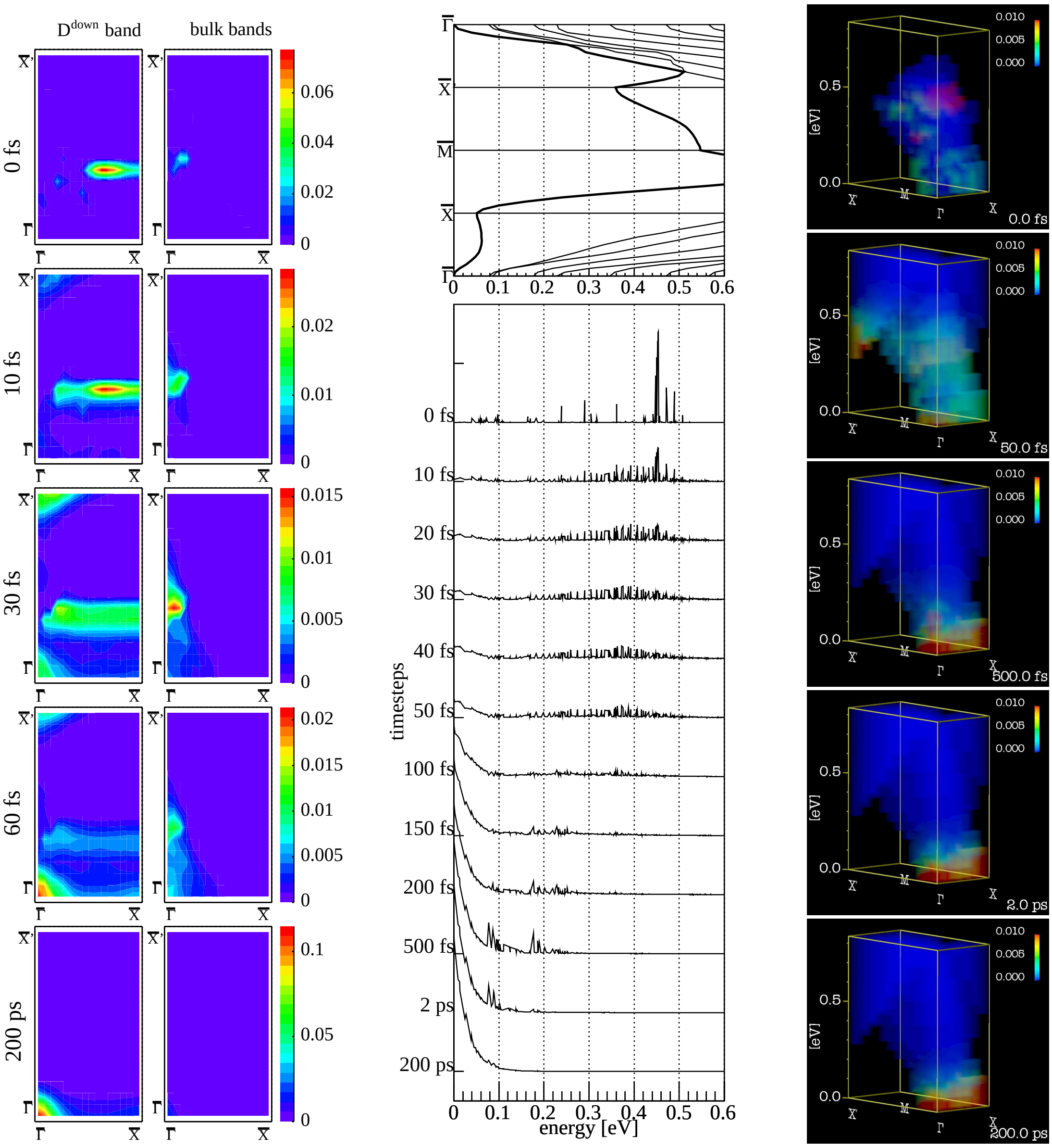

Figure 7.17: *Relaxation dynamics for a slab of 22 layers at a discretization of* 32×32 *points in the complete Brillouin zone and for a temperature of 300 K after an optical excitation with a 1.69 eV pulse. The energy resolved population (middle row) is increased by a factor of 25 with respect to Figs. 7.7-7.10. Now, a few bands are present in the required region. The bottleneck and the bulk band minimum shift towards a lower energy (0.8 eV).*

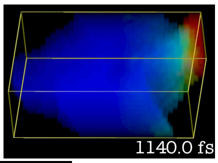

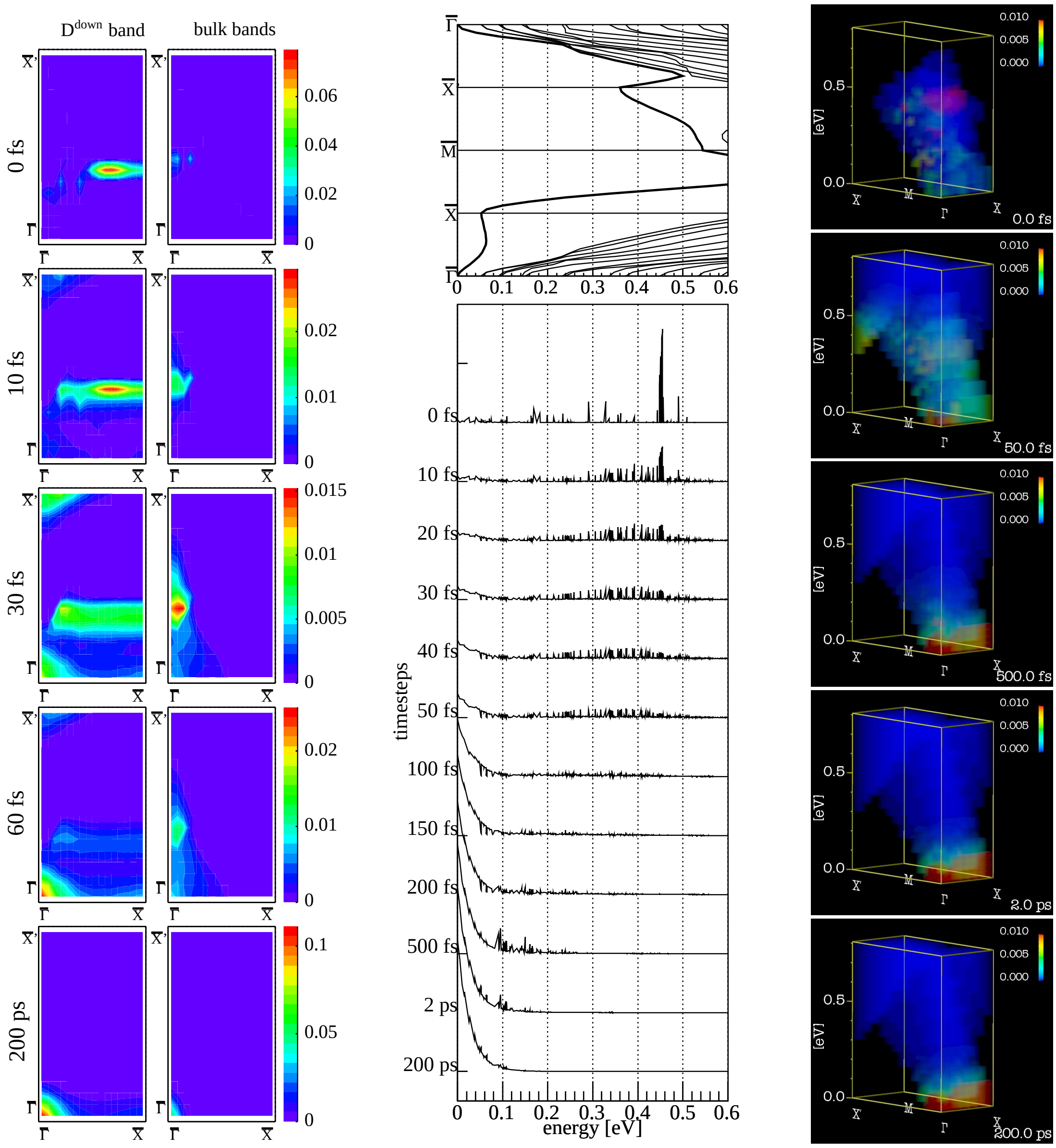

Figure 7.18: *Relaxation dynamics for a slab of 40 layers at a discretization of* 32×32 *points in the complete Brillouin zone and for a temperature of 300 K after an optical excitation with a 1.69 eV pulse. The energy resolved population (middle row) is increased by a factor of 25 with respect to Figs. 7.7-7.10. The bands are now in an average distance of ca. 0.05 eV. The bulk band minimum with the bottleneck has shifted to 0.05 eV.*

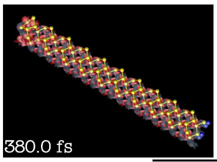

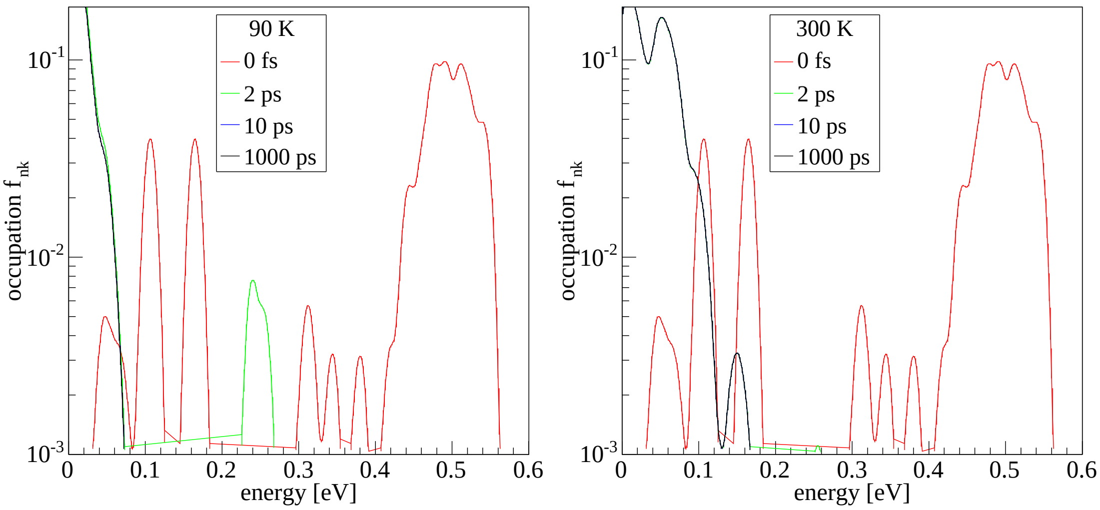

Figure 7.19: *Integrated logarithmic plot of the integrated population over the energy scale for 7 layers at 90 K and 300 K.*

column), also the later steps of relaxation are fairly similar to the 90 K calculation apart from this obvious deviation and a faster relaxation timescale (this is an expected effect at a higher relaxation temperature), especially the population at the bulk band minimum (at 1 ps) is still significant. For the 40 layer calculation (Fig. 7.18), however, the bulk band minimum is populated by the final distribution, as it was the case in the Gaussian initial condition (Sec. 7.3), and, as a consequence, no distinguishable population forms at the minimum. The effect of this behaviour on the timescales in contrast to the 90 K case will be discussed in Sec. 7.4.4. In the Brillouin zone distribution (lhs of Fig. 7.18), it is clarified that also the bulk band minimum is finally populated at the $\overline{\Gamma}$ point, while at the 7 and 22 layer calculations (lhs of Figs. 7.16 and 7.17), only a broadening of the population at the surface band minimum is visible. All in all, the relaxation at 300 K occurs on a significant faster timescale.

7.4.3 Phonon relaxation bottleneck

The formation of a particular non-equilibrium distribution at the specific bulk band minima in the calculations for the different slabs in Sec. 7.4.1 lead to a bottleneck effect, as a part of the population is formally trapped in the bulk band minimum state (cmp. Sec. 7.3) and can only leave it on a much longer timescale. While the fast timescale for the relaxation to the surface band minimum appears very similar for all slabs (cmp. Sec. 7.4.4), the timescale related to the bottleneck depends on the thickness of the slab. Due to the peaky form of the distribution (middle column of Figs 7.13 and 7.15) and the high number of involved states, a definite comparison of the populations is not possible. To facilitate the comparison, an alternative presentation is now chosen for the distributions: In Figs. 7.19-7.21, the energy-integrated population distribution for selected timesteps are shown on a logarithmic scale for 7, 22 and 40 layer slabs and for temperatures of 90 K and 300 K, respectively. The integration is performed by energetically broadening the discrete states with a Gaussian of 0.01 eV variance and subsequently summing all obtained peaks, this corresponds approximatively to considering the density of states $g(E)$

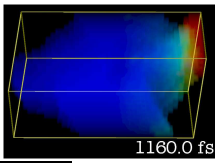

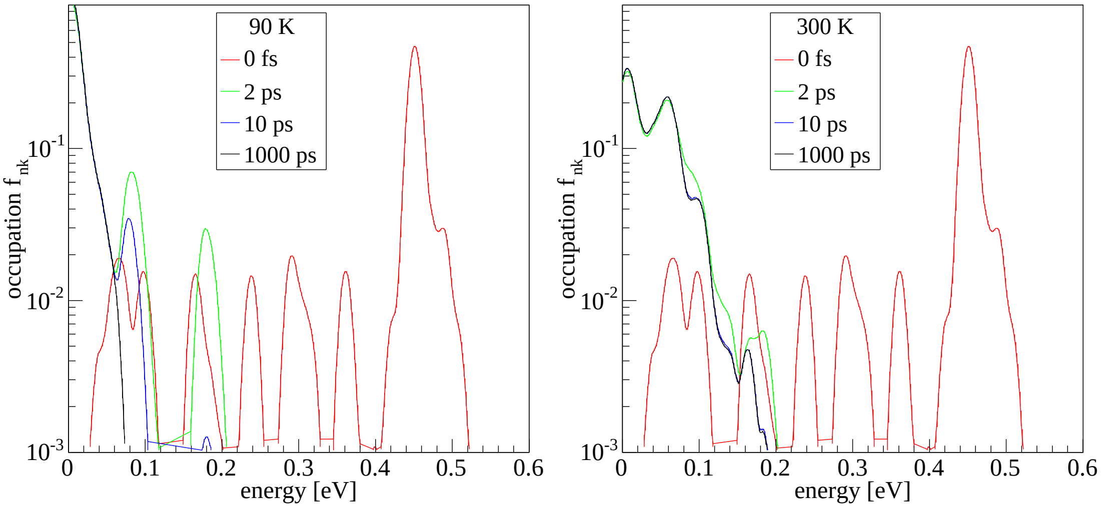

Figure 7.20: *Integrated logarithmic plot of the integrated population over the energy scale for 22 layers at 90 K and 300 K.*

in the distribution function:

$$f_{\text{integrated}}(E) = \int \mathrm{d}E\, g(E_{n_{\mathbb{k}}})\, f(E) = \sum_{n\mathbb{k}} f_{n\mathbb{k}}\, \delta(E - E_{n\mathbb{k}}). \tag{7.4}$$

In principle, the shape of the integrated distributions for the different slabs can be described in the same manner as it was done for the Figs. 7.13-7.18 : the initial distribution (red curves) relaxes through some intermediate states (at 2 ps, green curves) into the equilibrium distribution and the additional bottleneck states (10 ps, blue curves) until finally, only the equilibrium distribution is left over. However, the number, form and strength of the different states differs significantly: While at the seven layer slab (Fig. 7.19), no bottleneck states appears at 10 ps and the relaxation is quasily equilibrated at this timestep, we observe two (22 layers, Fig. 7.20) or three (40 layers, Fig. 7.21) distinguishable bottleneck states at the other slabs. In all cases, the bottleneck states have evolved from the intermediate states of the 2 ps-timesteps. Corresponding to the decrease of the gap between surface and bulk band minima with increasing slab thickness, the bottleneck states are shifted very close to the surface band minimum (0 eV) for the 40 layer slab, such that a small final population remains in the lowest bottleneck state. An explication of this strong layer dependency of bottleneck formation and breakup is the interplay of acoustical and optical phonons within the relaxation process: While at seven layers (Fig. 7.19), the energy gap of the intermediate state at the bulk band minimum (ca. 0.25 eV) at 2 ps (green curve) and the surface band minimum is still a multiple of the optical phonon energy (0.057 eV), this is not the case at the 22 and 40 layer calculations[2]. Consequently, for the thicker slabs, a growing fraction of the population has to relax by acoustical phonon coupling (by which also very small energy differences can be overborn) using a smaller coupling deformation potential (cmp. Sec. 7.3), which accumulates with the higher number of scattering steps to overcome an energy distance in contrast to optical phonon scattering to a much slower

---

[2] Relaxation cannot occur directly from the bulk band minimum to surface band minimum for several reasons: On the one hand, the matrix element of two Bloch-states is vanishes for different bands at the same $\mathbb{k}$-points (cmp. sec 6.3.2), on the other hand, at least acoustical phonon coupling is zero for a vanishing $\mathbb{q}$.

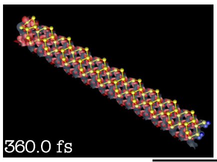

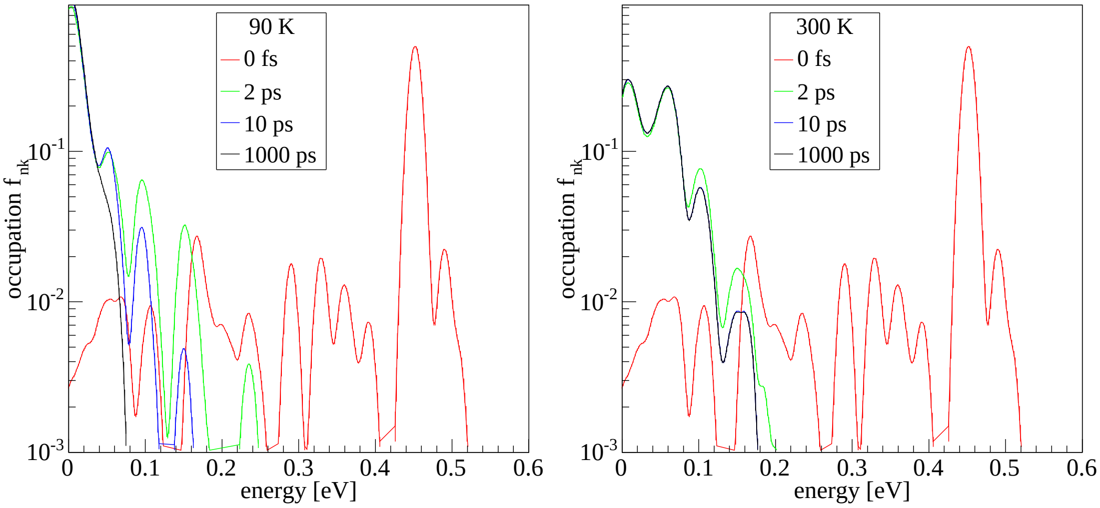

Figure 7.21: *Integrated logarithmic plot of the integrated population over the energy scale for 40 layers at 90 K and 300 K.*

relaxation timescale. A discussion of the resulting timescales will be elaborated in Sec. 7.4.4. Although the employed phonon model is partly heuristic and highly simplified (cmp. Sec. 7.3), the main bulk features are doubtlessly included in form of the limiting cases for high-energy optical phonons and low energy acoustical phonons. One open question, which is unfortunately beyond the possibilities of the `code` presented in this thesis, is the influence of surface-bound phonon modes, in special the so-called dimer-tilting-mode, which are also suspected to induce a polaronic effect at high excitation and induce a dynamic energy renormalization on the band structure (Sec. 1.2).

The relaxations at 300 K (lhs of Figs. 7.19-7.21) exhibit some significant differences to the 90 K-pictures: The final state extends to a much higher energy (ca. 0.18 eV)[3], and the relaxation is much faster. At 7 layers, (Fig. 7.19), the final state is already almost reached at 2 ps, at the other slabs, the 10 ps curve is indistinguishable from the equilibrium distribution. All bottleneck states of the 90 K distributions interfere with the equilibrium distribution at 300 K, and the quite low final population of the surface band minimum states together with the broadness of the distribution obviously inhibit an efficient formation of bottleneck states. Additionally, the higher temperature usually enables other, faster relaxation channels, as high-energy phonon modes are more probable through the Fermi-distribution (cmp. Sec. 4.2.3).

7.4.4 Time constants

In this section, we will discuss the timescales that can be found from the calculations in Sec. 7.4. The extraction of time constants in a quantitative manner is not a clearly defined procedure, as, as we have seen within the discussion of the relaxation processes in Secs. 7.3, 7.4.1 and 7.4.2, the time of relaxation depends on numerous factors, especially the initial condition has a crucial importance. In experiments, usually only the decay rate of a signal can be analyzed, and normally, in the Two-color-two-photon-photoemission-experiments as in

---

[3] Note that in this integrated representation, the shape of the final state needs not to correspond to a Fermi-distribution on the energy scale.

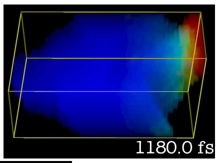

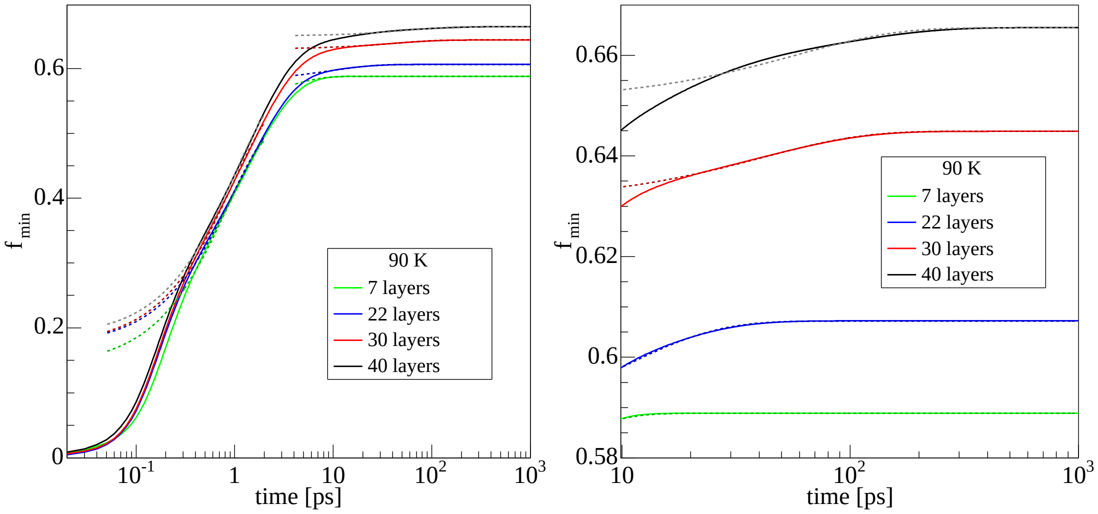

Figure 7.22: *Population of the D^{down} surface band minimum for slabs of 7, 22, 30 and 40 layers for a bath temperature of 90 K. The time axis is logarithmic. The numerically extracted timescales are indicated by the dashed lines.*

[TT03, WKFR04], the signal corresponds to a specific electron state, as here, the minimum of the D^{down}-band. Consequently, to allow a comparison to the experiments, the population of the minimum surface band state is a convenient choice as a data input for the determination of the relaxation timescale. It is not possible to extract the specific reasons for an accelerated or delayed relaxation from such a single-scale investigation. For this kind of examination, particular processes and selected states involved in the specific relaxation would have to be investigated. With the given representation, an interpretation is only possible in an overall approach.

In Figs. 7.22 and 7.23, the temporal evolution of the D^{down} minimum state is drawn for a temperature of 90 K and 300 K. Due to a logarithmic time axis, it is possible to investigate the relaxation on several decades of picoseconds. At the calculations at 90 K, the relaxation is still not completely equilibrated at 1000 ps (for a forty layer slab), while at 300 K, the final state is reached after 10 ps of relaxation. The big dependency on the slab thickness that

[ps]		No of layers						exp. value
		7	**10**	**15**	**22**	**30**	**40**	
90 K	long	2.47	6.91	2.37	9.62	41.73	58.47	220[a]
	short	0.83	0.78	0.98	0.93	0.94	1.00	1.5[ab]
300 K	long	0.47	0.16	0.23	1.52	1.83	1.70	190[c]
	short	0.094	0.096	0.12	0.097	0.094	0.086	5[c]

---

[a] [WKFR04]

[b] In [WKFR04], this is the overall relaxation time

[c] [TT03]

Table 7.1: *Numeric values for the relaxation timescales extracted from the calculations and comparison to experimental values.*

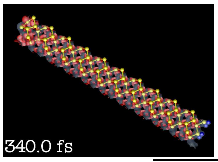

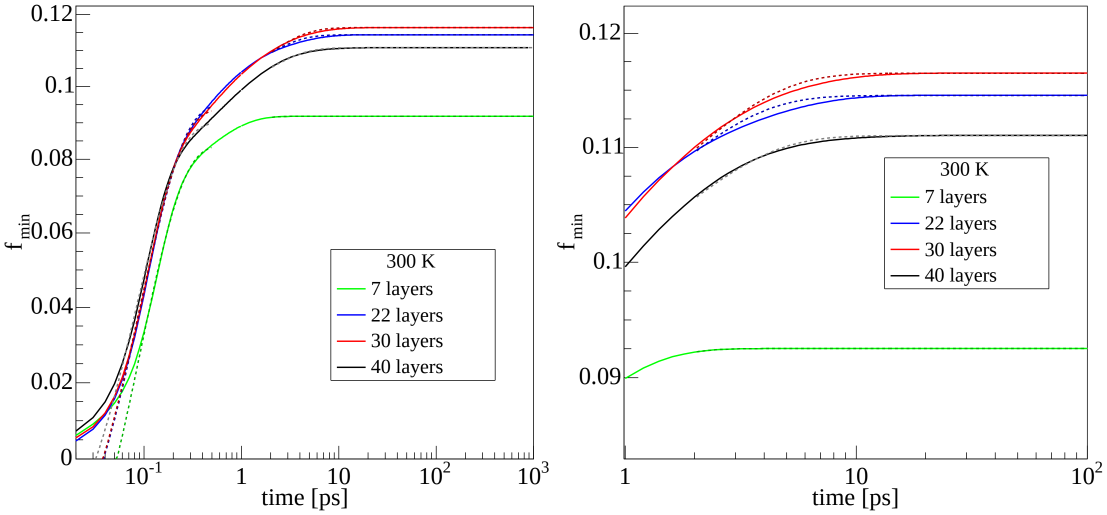

Figure 7.23: *Population of the D^{down} surface band minimum for slabs of 7, 22, 30 and 40 layers for a bath temperature of 300 K. The time axis is logarithmic. The numerically extracted timescales are indicated by the dashed lines.*

is expected as a consequence of the results found in Sec. 7.4.3 can now be quantified: At 90 K, for seven layers, the relaxation is finished at 10 ps, with increasing layer number, also the relaxation takes longer. Numerical values for the time constants are now extracted from these population evolution functions by fitting parts of the function with an exponential. It is obvious that especially for the fast short term time scale, this is a quite ambiguous task, as in the beginning of relaxation, the shape of the function is non-exponential. Therefore, to impose a certain clarity, the timescale is not fit at the beginning of relaxation, but after an initialization time, when the relaxation function has approximated to an exponential shape. The long-term timescale is much easier to find, as here, the asymptotic behaviour of the system towards the equilibrium state is investigated and the asymptotic evolution of a *Boltzmann*-like system at low population density always approaches to an exponential decay. In Fig. 7.22 and 7.23, the fitted timeconstants are indicated by the dashed lines. While for 90 K, there is an excellent agreement of the fit-exponentials to the population distribution at a certain specific range, the agreement is worse for the 300 K relaxation.

The resulting values of the relaxation are resumed in Table 7.1 and a logarithmic plot of these timescales is realized in Fig. 7.1 (lhs). The relevant results of the experiment [WKFR04] are shown on the (rhs) of the same figure. In this publication, three timescales have been found: a surface-surface scattering timescale of 1.5 ps, a bulk-surface scattering timescale of 220 ps, and an exciton formation timescale of 5 ps. While the first two are related to phononic processes and thus can be compared to our simulations, the third timescale involves processes neglected by our dynamical equations. From our data and the comparison to experiment, two conclusions can be drawn: First, while the qualitative classification of the relaxation processes is feasible, the quantitative interpretation is only reliable for the short-term timescale, as the strong dependency on the layer number with an monotone growing trend implies that the resolution of the band structure points in the energy space (the average distance between two bands) is still too low to resolve the phonon relaxation process in an accurate way. Due to the nature of the band structure and the location of the bottleneck-peaks (Sec. 7.4.3), it is likely that the short

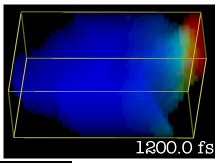

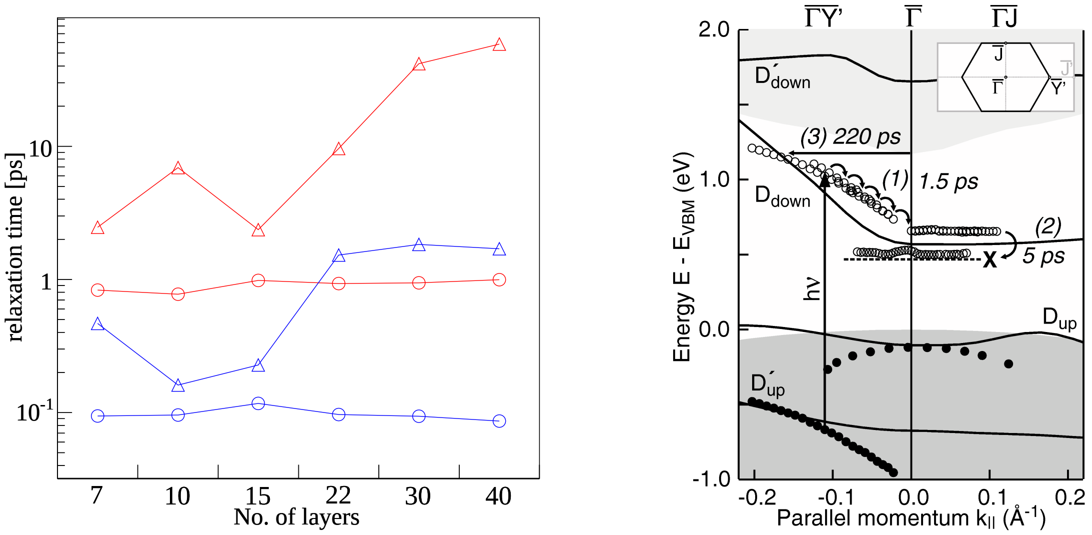

Figure 7.24: ***lhs:*** *Graphical representation of the relaxation timescales (Tab. 7.1). The triangles refer to the long term timescales, the circles to the short timescales, the red symbols are at a temperature of 90 K, while the blue symbols are for the calculations at 300 K* ***rhs:*** *the interpretation of experimentally observed results. From [WKFR04].*

time scale is associated to relaxation via optical phonons, while the long time scale is bound to acoustical phonon processes. The short timescale corresponds very well to the experimental findings (as the accuracy of the experimental resolution in [WKFR04] is also limited for this kind of timescale, and the number given from the experiment is rather the overall duration of the fast relaxation than the exponential growth factor). The long timescale differs still by a factor of 3.5 from the experiment. Other open questions about the phonon relaxation timescales are the effect of surface-related phonon processes, these are however expected to effectuate a rather fast relaxation and the influence of quasi-particle and polaronic effects on the optical and electron-phonon matrix elements, which are currently neglected, as well as the discussion of other, perhaps more realistic surface reconstructions.

The second conclusion concerns the calculations at 300 K. Here, the experimental results [TT03] imply a relaxation on two timescales of basically the same magnitude as in the 90 K-case, while we find in our simulations a much faster relaxation and practically no slow relaxation timescale. A possible explanation of this discrepancy is that at this temperature level, the approximations made for our model system are no longer valid. Especially the broadening of the distribution function with respect to the 90 K function has a significant effect on the relaxation dynamics of the bottleneck states, as, as it was discussed in Sec. 7.4.3, these states are neither particularly populated, nor do they play a special role in the relaxation process at 300 K: At room temperature, the lower bottleneck states are populated within 10 ps for statistical reasons, while the higher bottleneck states are obviously depopulated fast through new deexcitation channels. At last, this effect is a consequence of the focusing on the phonon relaxation inside the conduction band, which ends up in a more or less unphysical final distribution with a fixed number of electrons inside the conduction band. This could only be resolved by also considering recombination processes to allow a depopulation of the conduction band, e.g. by excitonic scattering, or by spontaneous emission of light. By such a depopulation, which is expected on a 5 ps timescale, the bottleneck states would gain importance as intermediate, slow

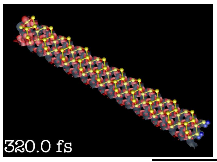

scattering states, and it is likely that the timescales could be reproduced. The extremely high numerical effort to calculate a dynamical excitonic interaction in a consistent way (using density matrix theory) makes it however actually very difficult to implement such a recombination interaction in the given system.

Nevertheless, as the 90 K calculation leads to a fairly good agreement of theoretical and experimental data, we can conclude that we have shown a successful application of the whole approach, although some of the approximations are quite drastic. The strength of this method of combining *Density Functional* and *Density Matrix Theory* is that other interactions (like excitons or optical recombination) can in principle be considered in the dynamical equations, and also some of the approximations have only been made to reach a high level of simplicity in this first-approach work. Therefore, it seems that the basics of the underlying processes are already understood and can be explained by the interplay of acoustical and optical bulk phonons, while a higher level of accuracy can only be reached by taking the electron-phonon interactions more precisely (e.g. by applying a surface-phonon spectrum from an integrated ab-initio calculation) and additional scattering mechanism into account.

7.4.5 Relaxation in real space

While the discussion of the relaxation process of the optical initial condition in Sec. 7.4 has been elaborated mostly on the distribution of the population on the $\mathbb{k}$ and energy space, the question about the initial and final distributions in real space has been left open so far. By performing a sum over the square modulus all conduction band electronic wave functions, weighted by their specific population factor from the relaxation dynamics calculation, a dynamical picture of the non-equilibrium electron distribution in the real space can be calculated.

In Figs. 7.25 and 7.26, the real space distribution of for temperatures of 90 K and 300 K is drawn for selected timesteps. As a basic result, the interpretation of the relaxation processes introduced in Sec. 7.4.1 and 7.4.2 is confirmed: Initially (0 fs), the electrons populate states that are complete inside the D^{down} band, and consequently, the electron distribution is entirely located in the within the first layers (on the lhs in Figs. 7.25 and 7.26). Then, when relaxation proceeds (50 fs-2 ps), a fraction of the population is transfered to bulk states and the electron population reaches down to deeper parts of the structure, touching the back-end atoms. The gravity of the population remains however centered at surface, as the biggest part of the population obviously scatters intraband. After 2 ps, the 90 K (Fig 7.25) and 300 K (Fig 7.26) pictures start to differ significantly: while at 90 K, the bulk is depopulated quasi entirely at 10 ps (there still remains a population, which is below the threshold of the isosurface) and the electron distribution shifts back to surface along with the population of the surface minimum state, a part of the population remains in bulk for the 300 K distribution. This is the effect of the broader Fermi-distribution at the higher temperature, which also leads to a population of the bulk band minimum in equilibrium. At 90 K, very small differences are still observable between 10 ps and 200 ps, here the slow relaxation timescale comes into play, while all other effects are rather determined by the faster relaxation.

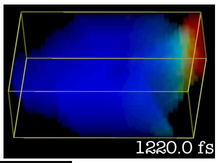

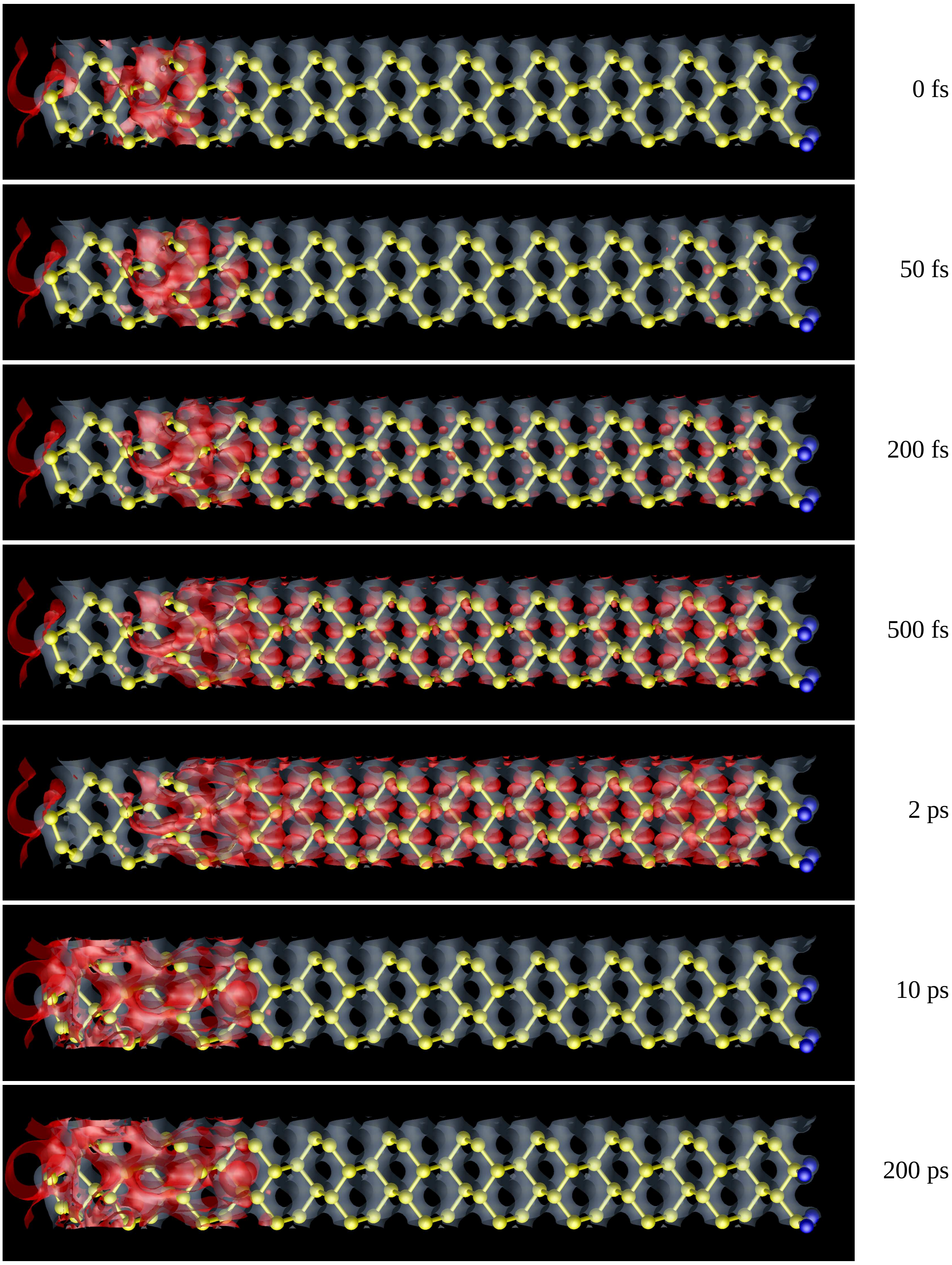

Figure 7.25: *Isosurface plot of the electron density distribution for the conduction band states for a relaxation process after optical excitation. The calculation is achieved for a slab with 40 layers at a discretization of* 32×32 *points at 90 K. The red isosurface corresponds to a density of* 10^{-6}*. In the background, the ground state population is shown by the grey isosurface.*

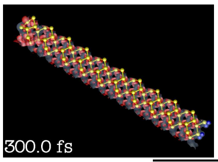

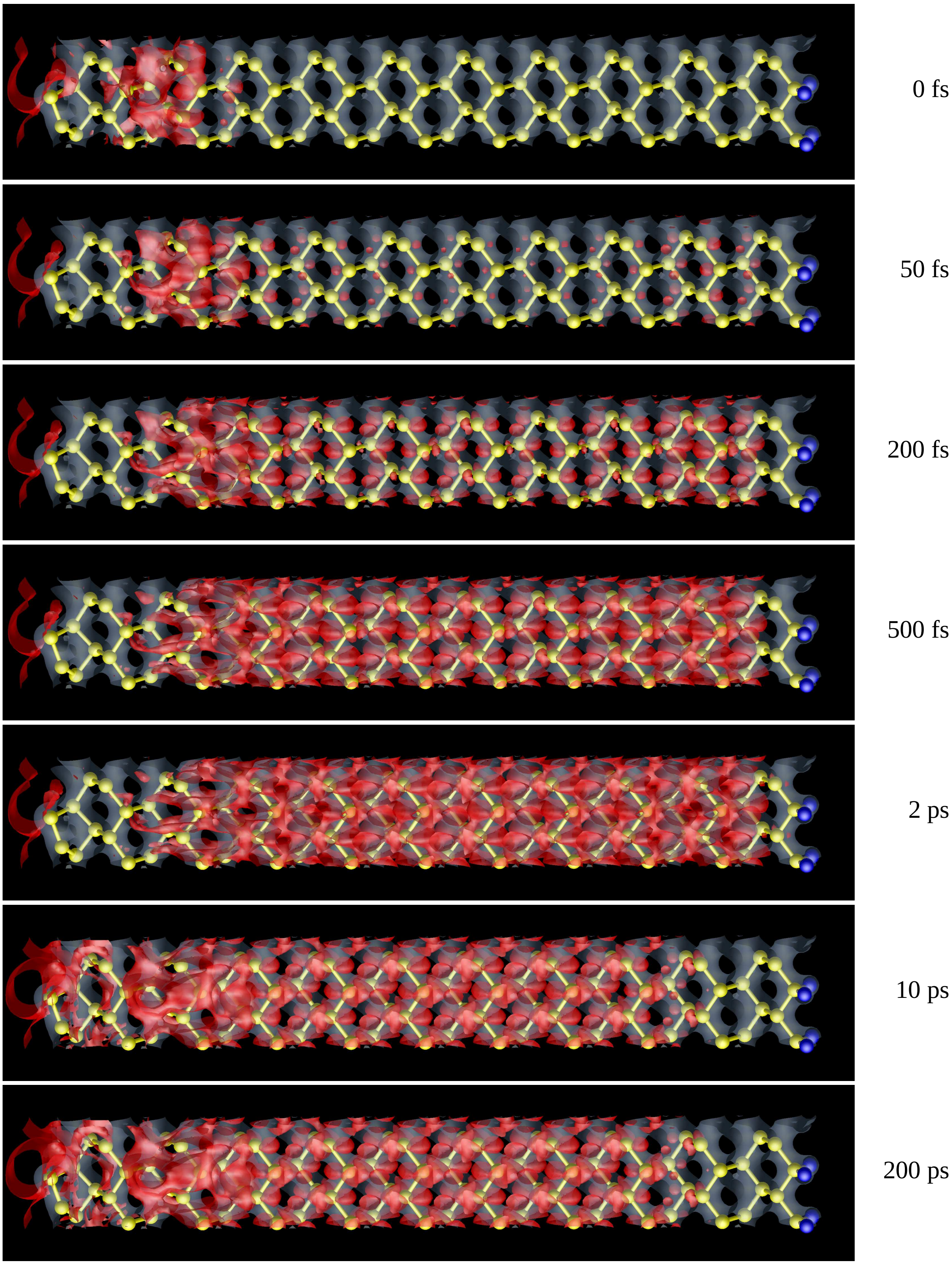

Figure 7.26: *Isosurface plot of the electron density distribution for the conduction band states for a relaxation process after optical excitation. The calculation is achieved for a slab with 40 layers at a discretization of* 32×32 *points at 300 K. The red isosurface corresponds to a density of* 10^{-6}*. In the background, the ground state population is shown by the grey isosurface.*

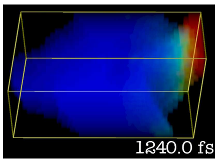

Chapter 8

Conclusion and outlook

From the application of the combined density-functional and density-matrix theory formalism, we have seen in Chapter 7 that a fairly good agreement of our theory to the experiment is obtained. Both the qualitative picture of the relaxation as a two-timescale process, where the relaxation is influenced by intraband surface scattering for the fast timescale and by bulk-surface scattering via acoustical phonons, and a good correspondence of the fast time-scale is found. The divergence of the longer timescale between theory and experiment needs not necessarily to be a principal problem of the theory, as the strong dependency of the number of layers implies that bulk effects are not sufficiently considered in the calculation and an even bigger slab structure is needed to obtain a converged and reliable long-term timescale. Under the given conditions (90 K), also the negligence of the surface phonon modes appears to be a constraint of secondary order, as the speed of the intra-surfaceband-scattering is quite similar to the experimental value.

For 300 K, the results are not so coherent. While no big difference is seen experimentally to the measurements at 90 K, all timescales are much faster in our simulation. While the provenience of the faster timescales in theory can be understood as an effect of the broader *Fermi-distribution* (which inhibits scattering to energetically low states) and the higher probability in the of the optical phonon due to the *Bose-distribution*, the discrepancy to experiment is probably based on the same effects: the formation of a *Fermi-distribution* distribution is a direct consequence of neglecting the recombination of conduction band electrons with the (in this thesis not investigated) holes in the valence band. In [WKFR04], a scattering channel via a surface exciton is described. While at 90 K, the recombination can be neglected due to the sharp Fermi-distribution, this cannot be expected at 300 K, and the complete dynamical picture would only be seen by depopulating the D^{down}-surface-minimum state. The simplified phonon spectrum can lead to similar effect in this context: while we approximated the total spectrum by two pure bulk modes, a detailed view might be important for the bulk-surface processes at room temperature, as many phonon modes of the slab are probably located between modes of our two-mode model and are then activated by the higher temperature.

All in all, the combination of density-functional and density-matrix theory is successful even with the given assumptions, as, in contrast to the older approaches (Sec. 1.3, [ZBFK05]) the results are physically reliable. A big advantage of the time- and energy resolved simulation is the big number of analyses that can be effected on the huge quantity of information that can be won from the timesteps, i.a. a time, energy and $\mathbb{k}$-resolved interpretation (cmp. e.g. Figs. 7.13-7.15) and even a retransformation to real space is possible. This allows especially a

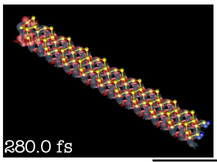

detailed investigation of the different phases of a scattering process from the initial to the final distribution.

In addition to the reapplication of an identical theory to another material or to a different surface reconstruction (e.g. a 4×2 reconstruction for the silicon (001) surface), there are several possible avenues that a potential enhancement of this theory can take:

- The implementation of a realistic surface phonon spectrum could be achieved by using the *frozen-phonon* calculation capabilities of the `fhimd`-code or other codes. In the same step, the calculation of corresponding deformation potentials could be done. While the technical implementation could be reached (the `dynamic` code has the ability to cope with numerous phonon modes and deformation potentials), the numerical effort is considerable for a structure of this size (40 layer slab).

- The consideration of quantum-correlation effects by dynamically evolving the polarizations (Eq. (4.15)). If this is understood to allow induced emission of light, it requires a complete dynamical treatment of the valence band (hole dynamics). The polarizations can also be coupled to higher order phonon relaxation processes. Unfortunately, the numerical effort is very high.

- The integration of electron-electron interaction in the dynamical part of the approach, at least for an excitonic interaction, would probably allow a deeper investigation of the final relaxation, as in the silicon (001) case, this is suspected to interact with phonon relaxation [WKFR04]. This is only useful in combination with an implementation of hole dynamics, but it would introduce a genuine relaxation mechanism from conduction to valence bands. However, the high number of summation indices in this interaction provokes an unbearable effort, such that this could be only performed cumulatively.

- Dynamical treatment of phonon modes (in contrast to the coupling to a bath) is in principle a possible extension to the dynamical equations. In the silicon (001) surface structure, the implementation of such a mechanism would probably give new insights, as the dimer surface phonon mode is suspected to perform a hot, non-equilibrium vibration at high optical excitations. Again, the high complexity of the resulting dynamical equations would require to focus on single modes (as the expected dimer tilting mode at silicon (001)). Another point of this technique is the unresolved thermalization behaviour (as the dynamical evolution of the modes is primarily energy conserving).

- One could also think of approaches with a electron-population-dependent phonon potential. The density-matrix formalism is capable to cope with a Hamiltonian depending on higher (> 1) order terms of the electronic polarizations, but the expected resulting equations are accordingly complex with multiple sums on the orders of the polarizations, such that it is not likely that a analogous system of equations can be successfully derived for a rather complex surface structure problem. Another open question is the deduction of the interaction term in the dynamical Hamiltonian (Eq. (2.51)), as currently, no theory exists to derive or model these interactions or at least to simulate them by structure investigation methods (e.g. density-functional theory).

- The phonon potential and the electron-phonon interaction could also be described by a non-linear interaction of the phonons (e.g. depending on higher orders of $b_{n\mathbb{k}}$). Of

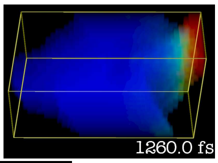

course, even if this is more question of principle about the applicability of the (linear) phonon mode theory, this could help to describe non-linear effects for the vibrations, which is especially of interest for highly excited phonon modes, e.g. for a dimer-tilting mode. While the parametrization of such a potential using a *frozen phonon* calculation seems possible, the resulting equations are probably, again, far too complex to be treated with an arguable resource consumption.

As a final conclusion, we hope that we have convinced the reader of the high potential lying in this combination of theories and yet in the presented results. To move on, however, it should be mentioned that, in addition to the time for implementation and testing, any of the points above requires at least a doubling of the computational power and of the disk space consumption, at the current state of the art, the accumulated time for a single run (of all steps) in the highest discretization amounts to ca. 6 months of CPU-time and requires more than 100 GB of always accessible disk space.

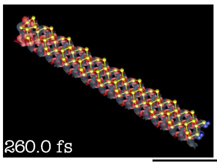
260.0 fs

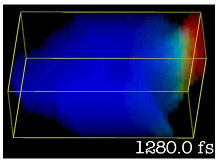

Appendix A

Summary of the employed physical constants and parameters

symbol	value	description
a	10.21 bohr	theoretical lattice constant
a	10.26 bohr	experimental lattice constant
E_{gap}	0.65 eV	DFT-LDA indirect bandgap energy of Si
E_{gap}	1.17 eV	experimental indirect bandgap energy of Si
	0.52 eV	scissors shift
E_{cut}	10 Ry	plane-wave cutoff energy
$\hbar\omega^{\text{opt}}$	57 meV	optical phonon energy (Si)
$\hbar c$	6.1 meV/nm	sonic speed (Si)
D^{opt}	40 eV	optical deformation potential (Si)
D^{acou}	$7.37\ \text{eV}/\sqrt{nm}$	acoustical deformation potential (Si)
$\hbar\omega_0$	1.69 eV	optical excitation frequency (experimental)
$\hbar\omega_0$	1.07 eV	optical excitation frequency (adjusted by scissors shift)
τ	50 fs	optical pulse duration
$\mathbb{v}$		two-dimensional vector
$\mathbf{v}$		three-dimensional vector
$\mathbf{R}_i$		real-space lattice vectors
$\mathbf{G}_i$		reciprocal space lattice vectors
$\Im$		imaginary part
$\mathscr{P}$		Cauchy principal value
$E_{n\mathbb{k}}$	[eV]	energy eigenvalue
$f_{n\mathbb{k}}$	[1/nm^3]	microscopical electron density
$p_{n\mathbb{k}}^{n'\mathbb{k}'}$	[1/nm^3]	microscopical polarization
$\mathbf{p}_{n\mathbb{k}}^{n'\mathbb{k}'}$	[kgm]	momentum matrix element
$\mathbf{d}_{n\mathbb{k}}^{n'\mathbb{k}'}$	[em]	dipole matrix element
$D_{n\mathbb{k};i\mathbb{q}}^{n'\mathbb{k}'}$	[eV]	electron-phonon coupling element
$\mathbf{A}(t)$	[Vs/nm]	electromagnetic vector potential (Coulomb gauge)
$\mathbf{E}(t)$	[V/nm]	electrical field (Coulomb gauge)
$\mathbf{P}(t)$	[V/nm]	macroscopical polarization
$\alpha(\omega)$	[ ]	optical absorption coefficient

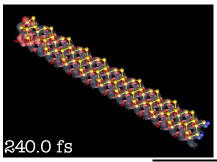
240.0 fs

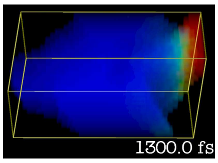

Appendix B

Tools for calculus

B.1 Equilibrium distributions

The equilibrium state of a quantum system is determined, according to the nature of the involved particles as *fermions* or *bosons*, by the *Fermi-Dirac-distribution* or the *Bose-Einstein-distribution*, resp. Examples for fermions are the electrons, the holes in a semiconductor and most elementary nuclear particles, while bosons are mostly interaction particles as photons, phonons and others. The two distributions are given by

$$f_i = \frac{1}{1 + e^{\frac{E_i - \mu}{k_B T}}} \qquad \text{Fermi-Dirac-distribution} \tag{B.1}$$

$$n_i = \frac{1}{1 - e^{\frac{E_i - \mu}{k_B T}}} \qquad \text{Bose-Einstein-distribution} \tag{B.2}$$

where E_i is the energy of the quantum state i, k_B the Boltzmann constant and T the temperature. The chemical potential is a normation constant determined by the total number of particles described by a distribution f_i or n_i for a given quantum system with the states $\{|i\rangle\}$ of energies E_i. It can be interpreted as the energy necessary to add another particle to the system, and thus, it only makes sense in systems where the particles have a mass.

B.2 Functional Derivative

The functional derivative is an extension to the derivatives with respect to variables. At the place of variables, its arguments are functions and it acts on functionals.

B.2.1 Definitions

The derivative $\delta/\delta\Xi(x)$ of a functional $F[\Xi(x)]$ is given by

$$\frac{\delta F[\Xi(y)]}{\delta \Xi(x)} = \lim_{\alpha \to 0} \frac{F[\Xi(y) + \alpha\delta(y-x)] - F[\Xi(y)]}{\alpha}. \tag{B.3}$$

For a functional of the form

$$F[\Xi(x)] = \int \mathrm{d}y \, f(\Xi(y)) \tag{B.4}$$

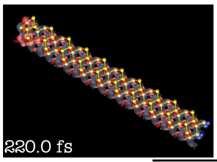

this expression can be simplified to

$$\begin{aligned}\frac{\delta}{\delta\Xi(x)}\int \mathrm{d}y f(\Xi(y)) &= \lim_{\alpha\to 0}\frac{\int \mathrm{d}y\big(f(\Xi(y))+\alpha\delta(y-x)\frac{\partial}{\partial\Xi}f(\Xi(y))+\mathcal{O}(\alpha^2)\big)-\int \mathrm{d}y f(\Xi(y))}{\alpha}\\ &= \frac{\partial f(\Xi(x))}{\partial\Xi(x)}.\end{aligned} \tag{B.5}$$

For a functional of the form

$$F[\Xi(x)] = \int \mathrm{d}y f(\Xi'(y)) \tag{B.6}$$

this yields

$$\begin{aligned}\frac{\delta}{\delta\Xi(x)}\int \mathrm{d}y f(\Xi'(y)) &= \lim_{\alpha\to 0}\frac{\int \mathrm{d}y\big(f(\Xi'(y))+\alpha\delta'(y-x)\frac{\partial}{\partial\Xi'}f(\Xi'(y))+\mathcal{O}(\alpha^2)\big)-\int \mathrm{d}y f(\Xi'(y))}{\alpha}\\ &= -\int \mathrm{d}y\delta(y-x)\frac{\partial}{\partial y}\frac{\partial}{\partial\Xi'}f(\Xi'(y)) + \text{boundary term}\\ &= -\frac{\partial}{\partial x}\frac{\partial f(\Xi'(x))}{\partial\Xi'(x)}.\end{aligned} \tag{B.7}$$

B.2.2 Series expansion of functionals

Similar to the *Taylor expansion series*, a functional $F[\Xi(y)]$ can be expanded into a series of the function $\Xi(x)$, if the $\Xi(x)$ is assumed to be small. The basic derivation is in line with the definition of the Taylor expansion:

$$F[\Xi(x)] = F\Big|_{\Xi=0} + \int \mathrm{d}x\Xi(x)\frac{\delta F}{\delta\Xi(x)}\Big|_{\Xi=0} + \frac{1}{2}\int \mathrm{d}x\Xi(x)\int \mathrm{d}x'\Xi(x')\frac{\delta^2 F}{\delta\Xi(x)\delta\Xi(x')}\Big|_{\Xi=0} + \ldots \tag{B.8}$$

For an expansion of a functional of form

$$F[\Xi(x),\Xi'(x)] = \int \mathrm{d}y f(\Xi(y),\Xi'(y)), \tag{B.9}$$

the expansion up to first order yields:

$$\int \mathrm{d}y f(\Xi(y),\Xi'(y)) = \int \mathrm{d}y f(\Xi(y),\Xi'(y))\Big|_{\substack{\Xi=0\\ \Xi'=0}} + \int \mathrm{d}x\Xi(x)\Big(\frac{\partial f}{\partial\Xi} - \frac{\partial}{\partial x}\frac{\partial f}{\partial\Xi'}\Big)\Big|_{\substack{\Xi=0\\ \Xi'=0}}. \tag{B.10}$$

By reintegration and negligence of the boundary term of the second term in the parentheses, we finally obtain:

$$= F\Big|_{\substack{\Xi=0\\ \Xi'=0}} + \int \mathrm{d}x\Xi(x)\frac{\partial f}{\partial\Xi}\Big|_{\substack{\Xi=0\\ \Xi'=0}} - \int \mathrm{d}x\Xi'(x)\frac{\partial f}{\partial\Xi'}\Big|_{\substack{\Xi=0\\ \Xi'=0}}. \tag{B.11}$$

The expressions for functionals of vectorial fields can be derived accordingly.

B.3 Lagrange Formalism for higher (infinite) order

The Lagrange equations for a field Ξ are derived by applying a variational principle to the integral of the Lagrange density $\mathscr{L}$ over a reference volume Ω, which is also denoted as the *action integral*:

$$0 = \delta\int_\Omega \mathrm{d}^4x\,\mathscr{L} = \int \mathrm{d}^4x\Big[\frac{\partial\mathscr{L}}{\partial\Xi}\delta\Xi + \sum_{i_1=1}^{4} \frac{\partial\mathscr{L}}{\partial\partial_{i_1}\Xi}\delta\partial_{i_1}\Xi + \sum_{i_1=1}^{4}\sum_{i_2=1}^{4} \frac{\partial\mathscr{L}}{\partial\partial_{i_1}\partial_{i_2}\Xi}\delta\partial_{i_1}\partial_{i_2}\Xi + \ldots + + \sum_{i_1=1}^{4}\sum_{i_2=1}^{4}\cdots\sum_{i_n=1}^{4}\frac{\partial\mathscr{L}}{\partial\partial_{i_1}\partial_{i_2}\cdots\partial_{i_n}\Xi}\delta\partial_{i_1}\partial_{i_2}\cdots\partial_{i_2}\Xi\Big]. \tag{B.12}$$

By performing some partial integrations (note that $\delta\partial_i\Xi = \partial_i\delta\Xi$), this can be evaluated to

$$= \int_\Omega \mathrm{d}^4x\Big[\frac{\partial\mathscr{L}}{\partial\Xi} - \sum_{i_1=1}^{4}\partial_{i_1}\frac{\partial\mathscr{L}}{\partial\partial_{i_1}\Xi} + \sum_{i_1=1}^{4}\sum_{i_2=1}^{4}\partial_{i_1}\partial_{i_2}\frac{\partial\mathscr{L}}{\partial\partial_{i_1}\partial_{i_2}\Xi} + \sum_{k=3}^{n}(-1)^k\sum_{i_1=1}^{4}\sum_{i_2=1}^{4}\cdots\sum_{i_k=1}^{4}\partial_{i_1}\partial_{i_2}\ldots\partial_{i_k}\frac{\partial\mathscr{L}}{\partial\partial_{i_1}\partial_{i_2}\cdots\partial_{i_k}\Xi}\Big]\delta\Xi \tag{B.13}$$

$$+ \int_\Omega \mathrm{d}^4x\Big[\sum_{i_1=1}^{4}\partial_{i_1}\big(\frac{\partial\mathscr{L}}{\partial\partial_{i_1}\Xi}\delta\Xi\big) + \sum_{i_1=1}^{4}\partial_{i_1}\big(\sum_{i_2=1}^{4}\frac{\partial\mathscr{L}}{\partial\partial_{i_1}\partial_{i_2}\Xi}\delta\partial_{i_2}\Xi\big) - \sum_{i_2=1}^{4}\partial_{i_2}\big(\sum_{i_1=1}^{4}\partial_{i_1}\frac{\partial\mathscr{L}}{\partial\partial_{i_1}}\delta\Xi\big) + \ldots\Big] \tag{B.14}$$

Although in Eq. (B.14) only the very first terms of the partial integration procedure are given, essentially all parts that do not figure in Eq. (B.13) can be brought into a "divergence-kind" form similar to the terms in Eq. (B.14). If we impose now that all variations of the field and its derivations derivations at least to order $n-1$ vanish on the boundary of the integrals ($\delta\partial_{i_1}\ldots\partial_{i_{n-1}}\Xi|_{\partial\Omega} = 0$), we can make use of *Gauß' law*, and (B.14) vanishes completely.

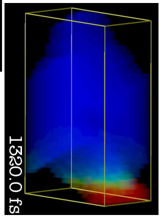

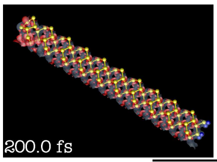

Eq. (B.13) must be valid independently for all $\delta\Xi$, consequently the *Lagrange equations* must hold:

$$0 = \frac{\partial \mathscr{L}}{\partial \Xi} - \sum_{i_1=1}^{4} \partial_{i_1} \frac{\partial \mathscr{L}}{\partial \partial_{i_1} \Xi} + \sum_{k=2}^{n} (-1)^k \sum_{i_1=1}^{4} \cdots \sum_{i_k=1}^{4} \partial_{i_1} \ldots \partial_{i_k} \frac{\partial \mathscr{L}}{\partial \partial_{i_1} \cdots \partial_{i_k} \Xi}. \tag{B.15}$$

For the usually used field equations, only the first two of the terms on the rhs of this equation are employed, as the corresponding Lagrange densities $\mathscr{L}$ do not contain field derivatives of a higher order than 1. Nevertheless, for our considerations (phonons in a periodic solid state material), higher derivatives are used.

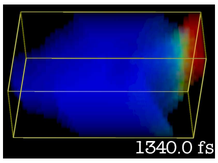

Appendix C

Summary of the computer programs and results from the dynamical calculation

C.1 Program structure

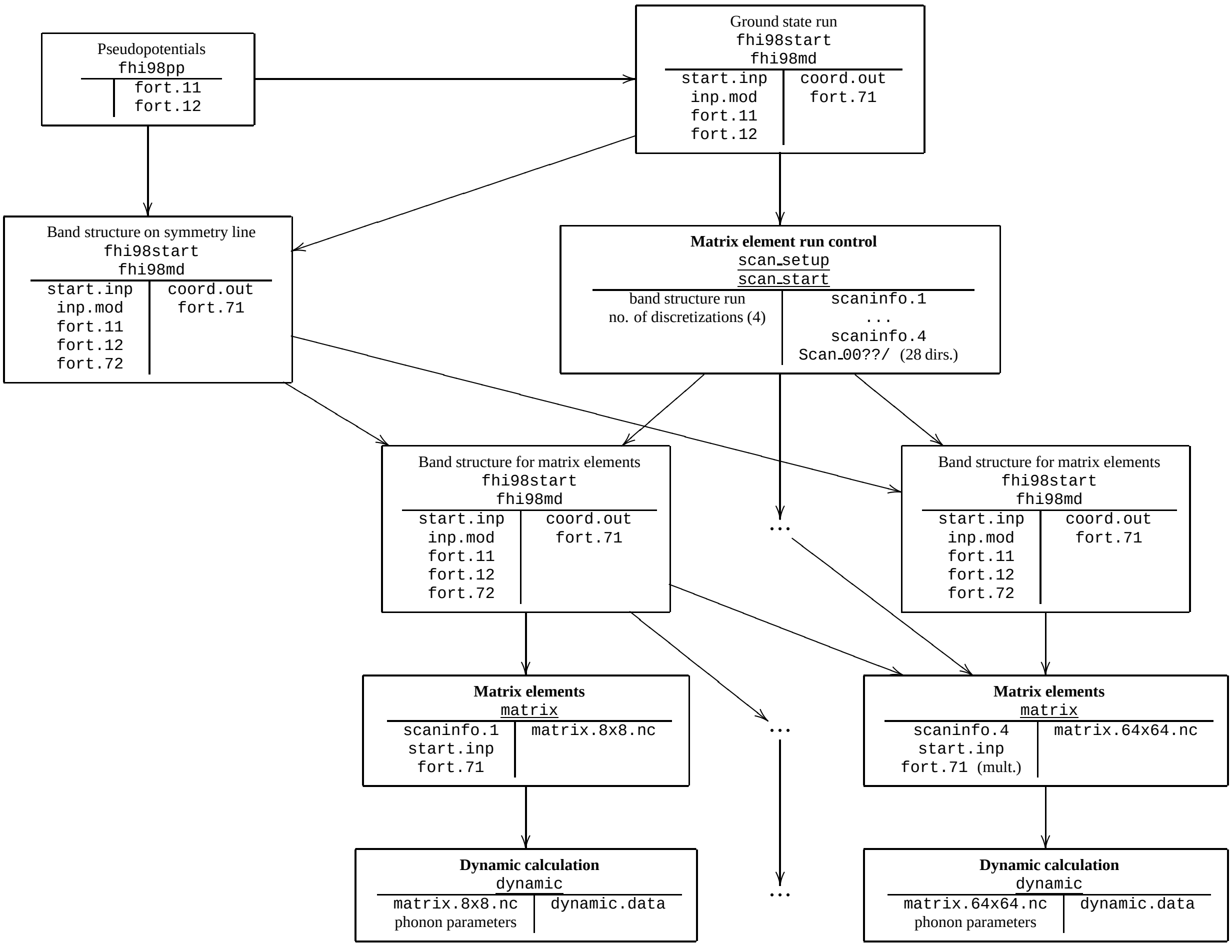

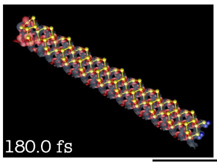

Description
`program name`
`input file(s)` | `output file(s)`
input parameters

On the previous page, the programs used for the entire implementation are illustrated with their dependency. For each program, an overview of the input and output files is given (see top). For the programs that have been developed from scratch within this thesis, the description tag is in boldface and the program name is underlined.

C.2 Summary of the computational results

On the following pages, an exhaustive collection of the results for the simulation of the relaxation processes from the optical initial conditions is shown. The plots are similar to Figs. 7.13-7.18 for temperatures of 90 K and 300 K.

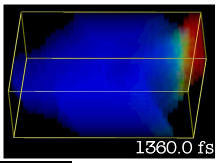

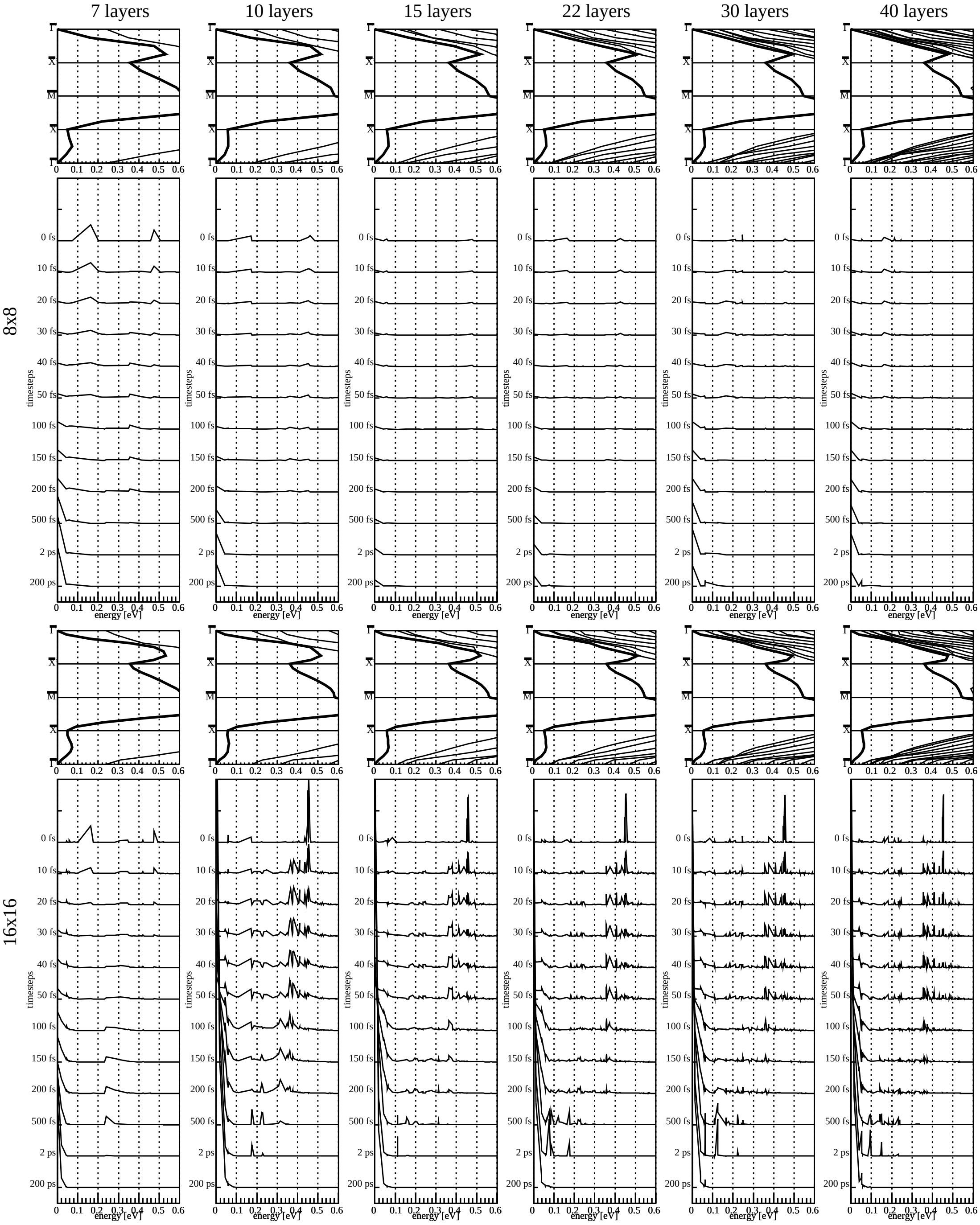

90 K, lower discretizations

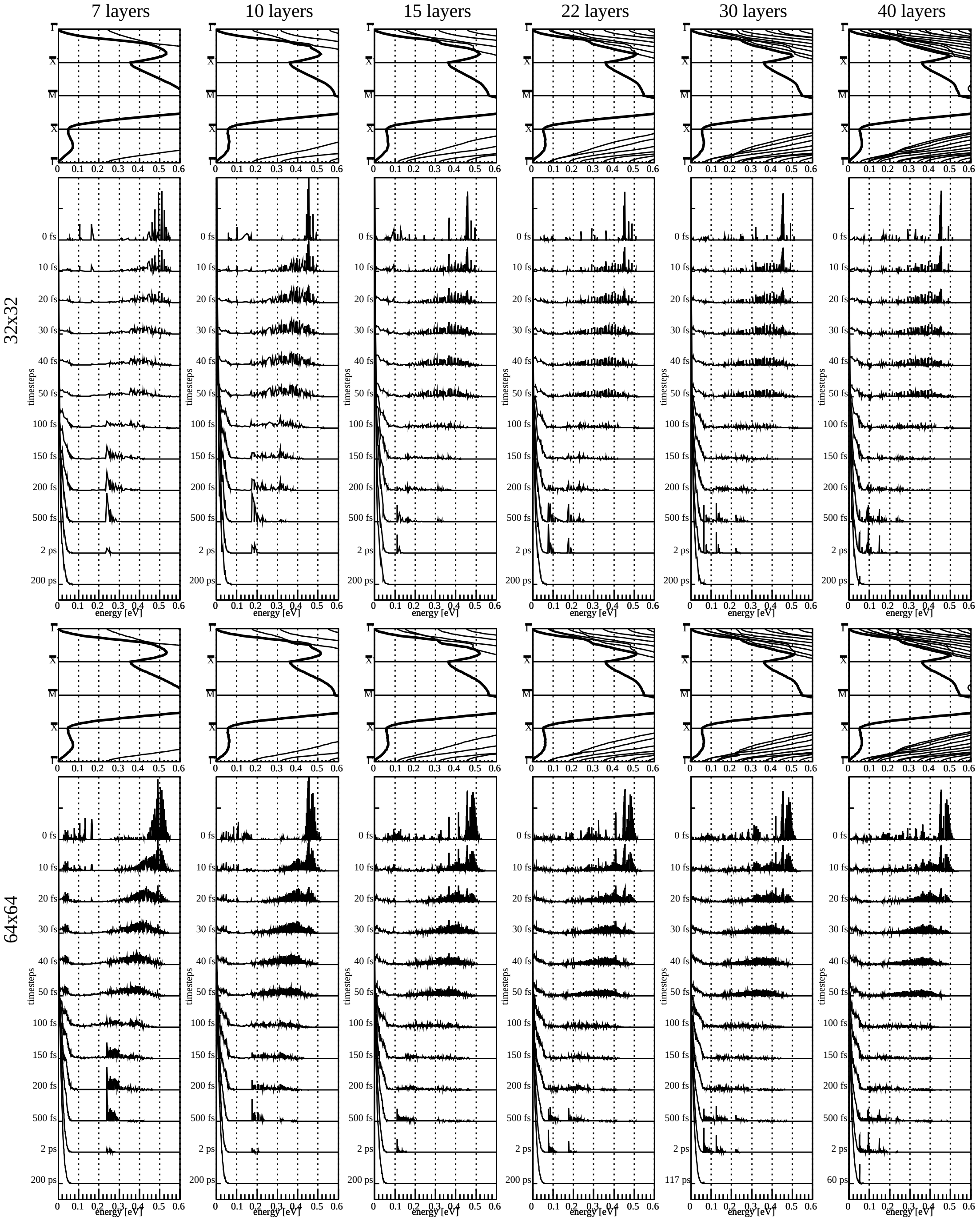

90 K, higher discretizations

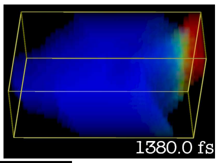

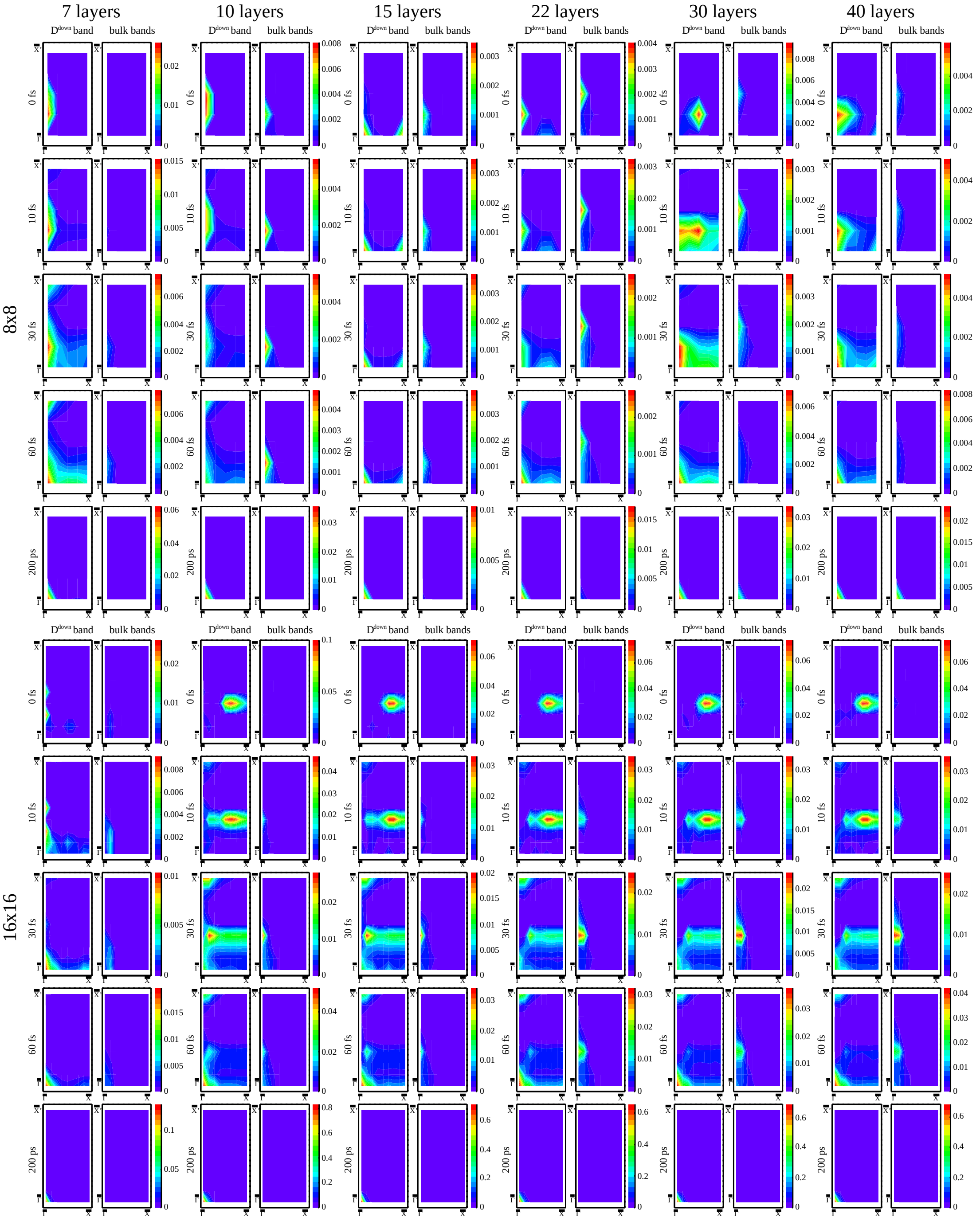

90 K, lower discretizations

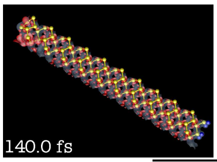

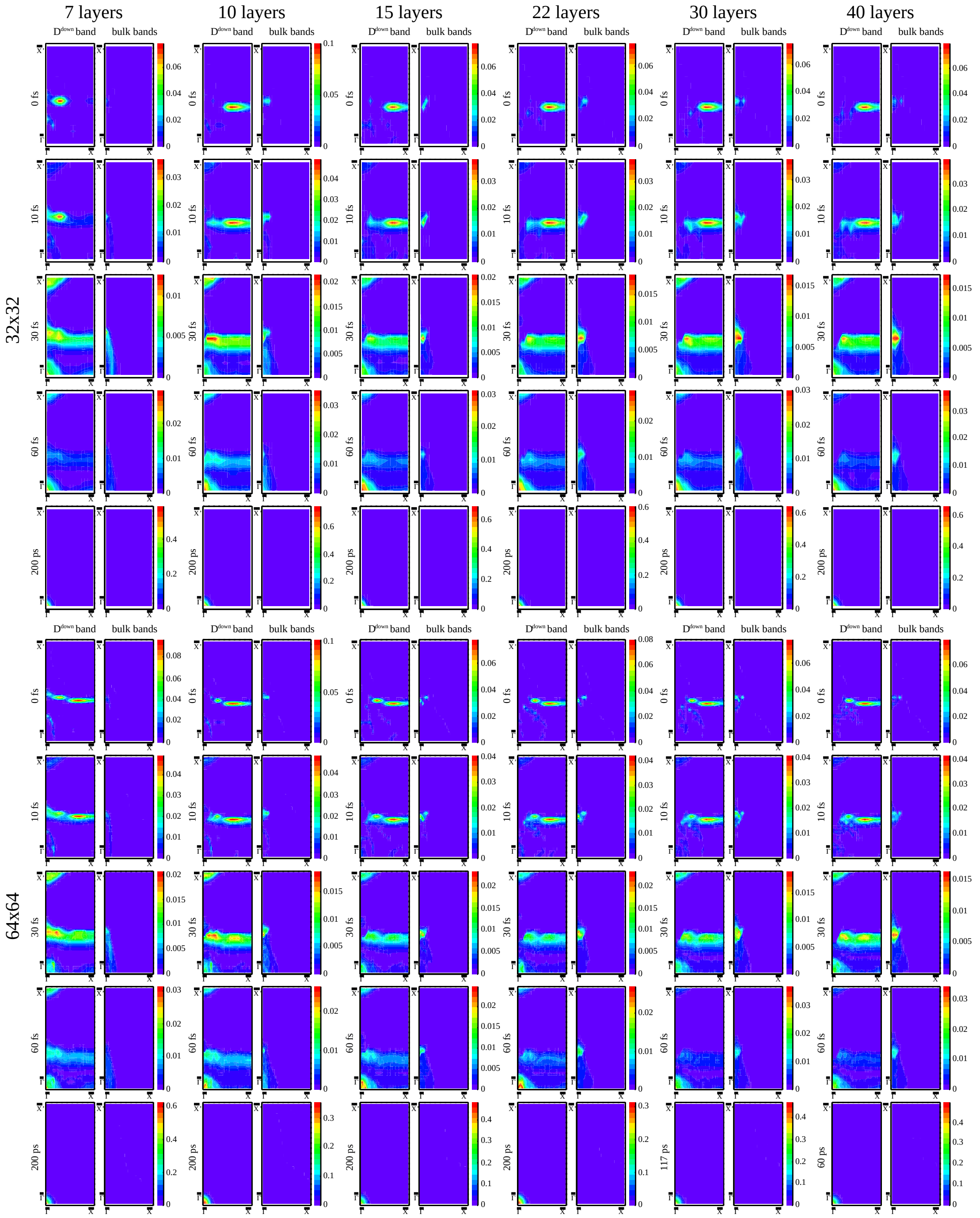

90 K, higher discretizations

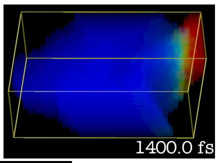

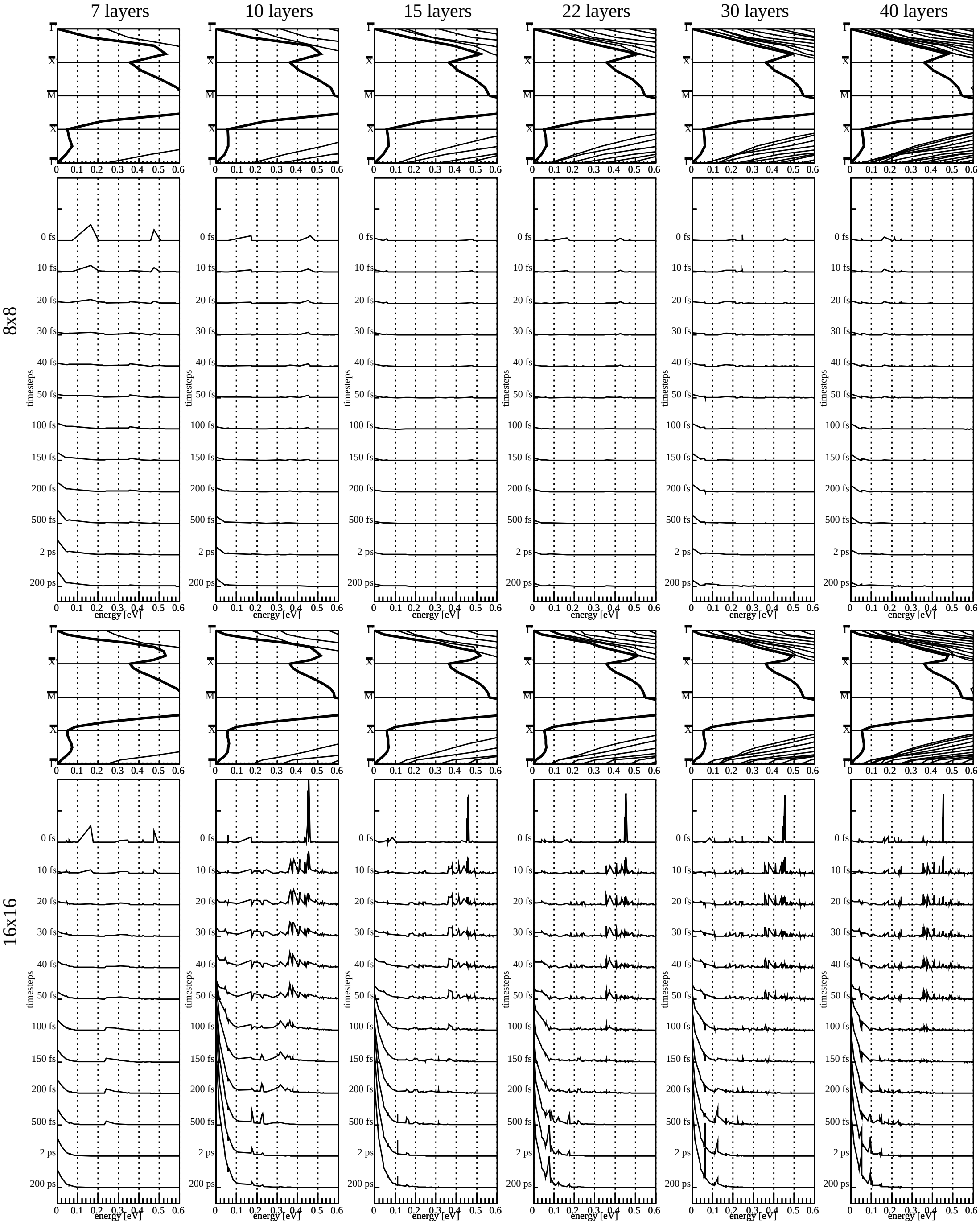

300 K, lower discretizations

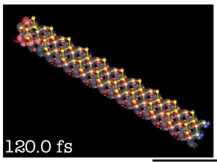

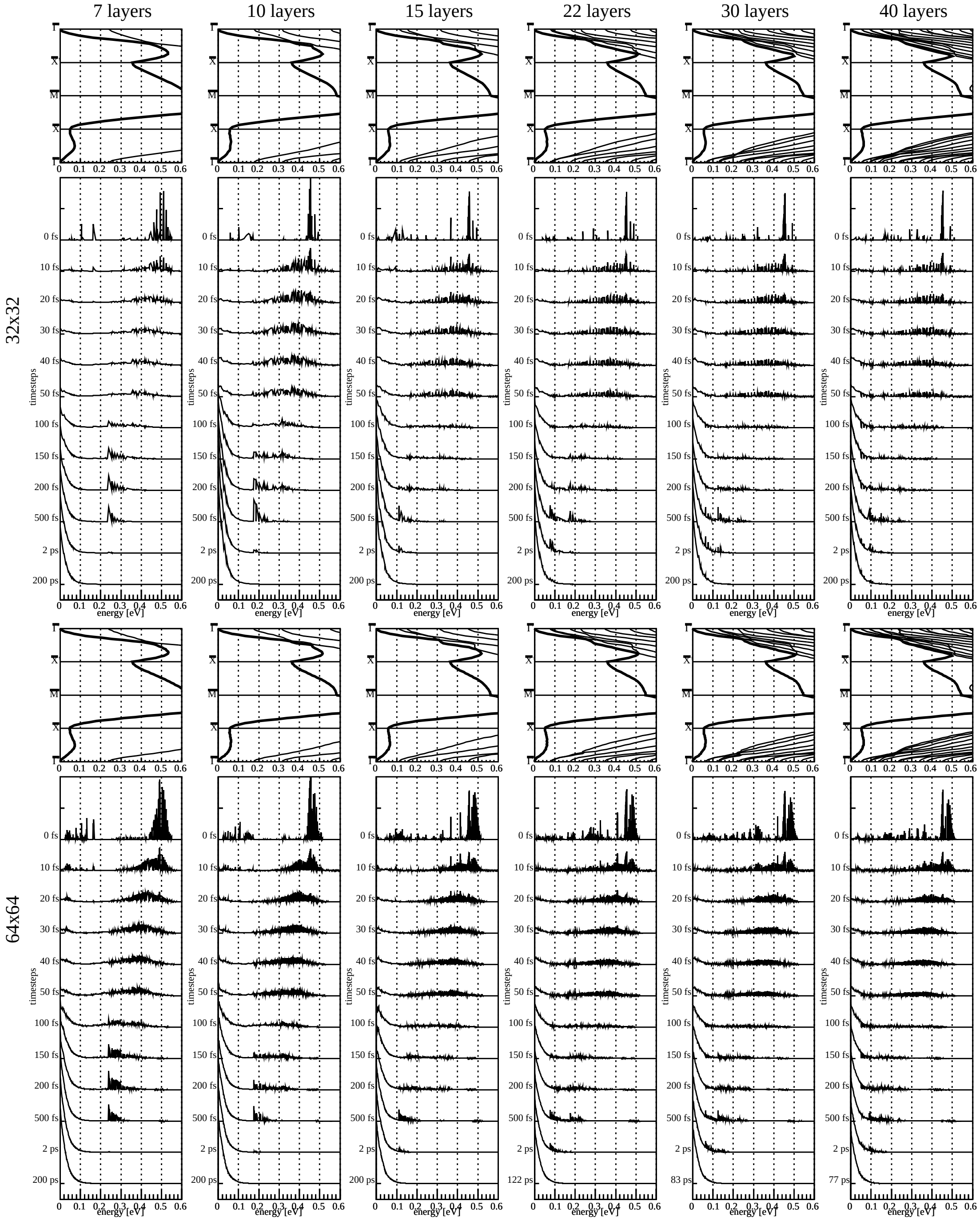

300 K, higher discretizations

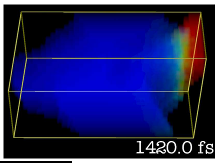

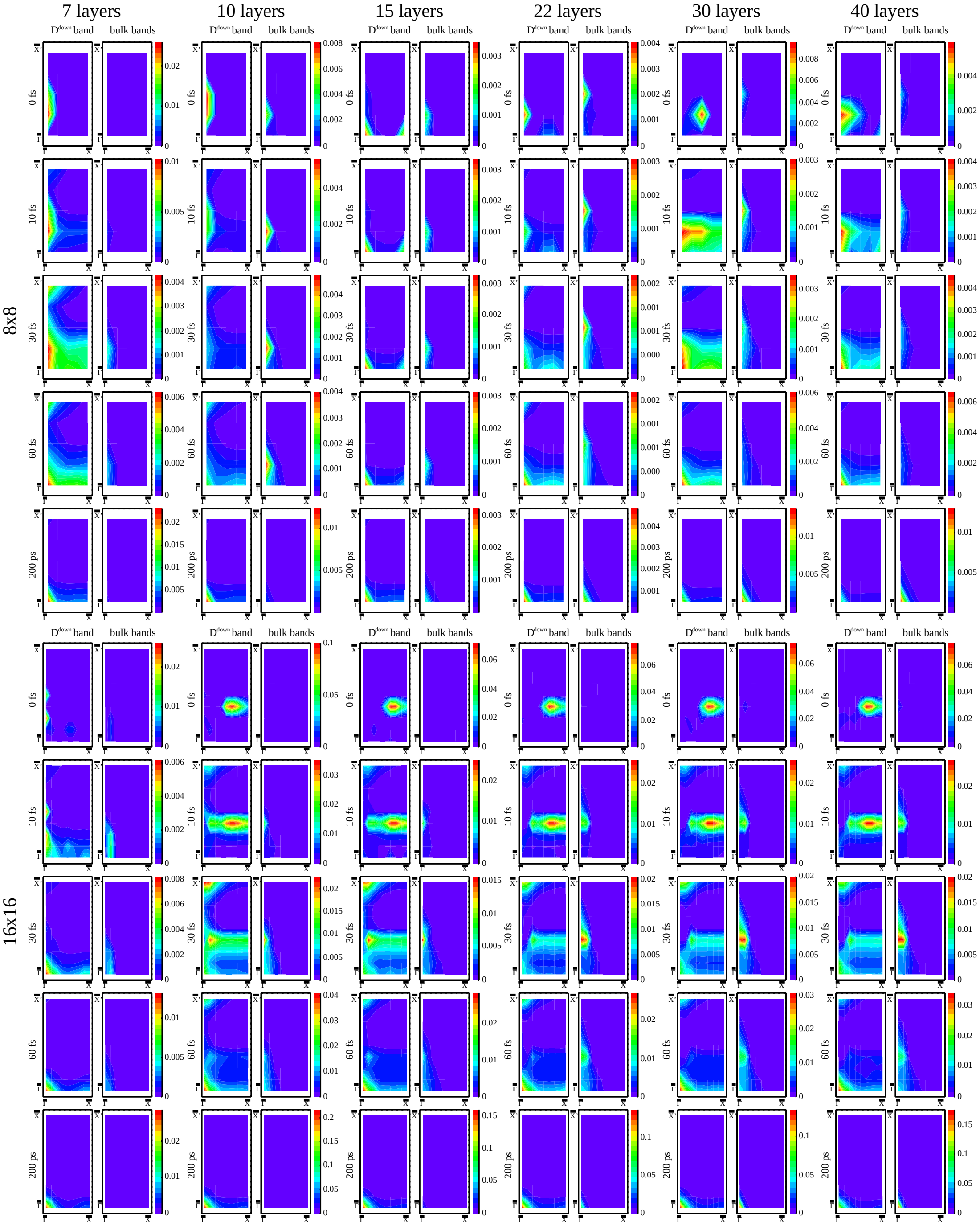

300 K, lower discretizations

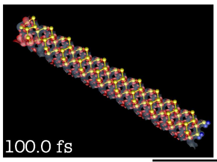

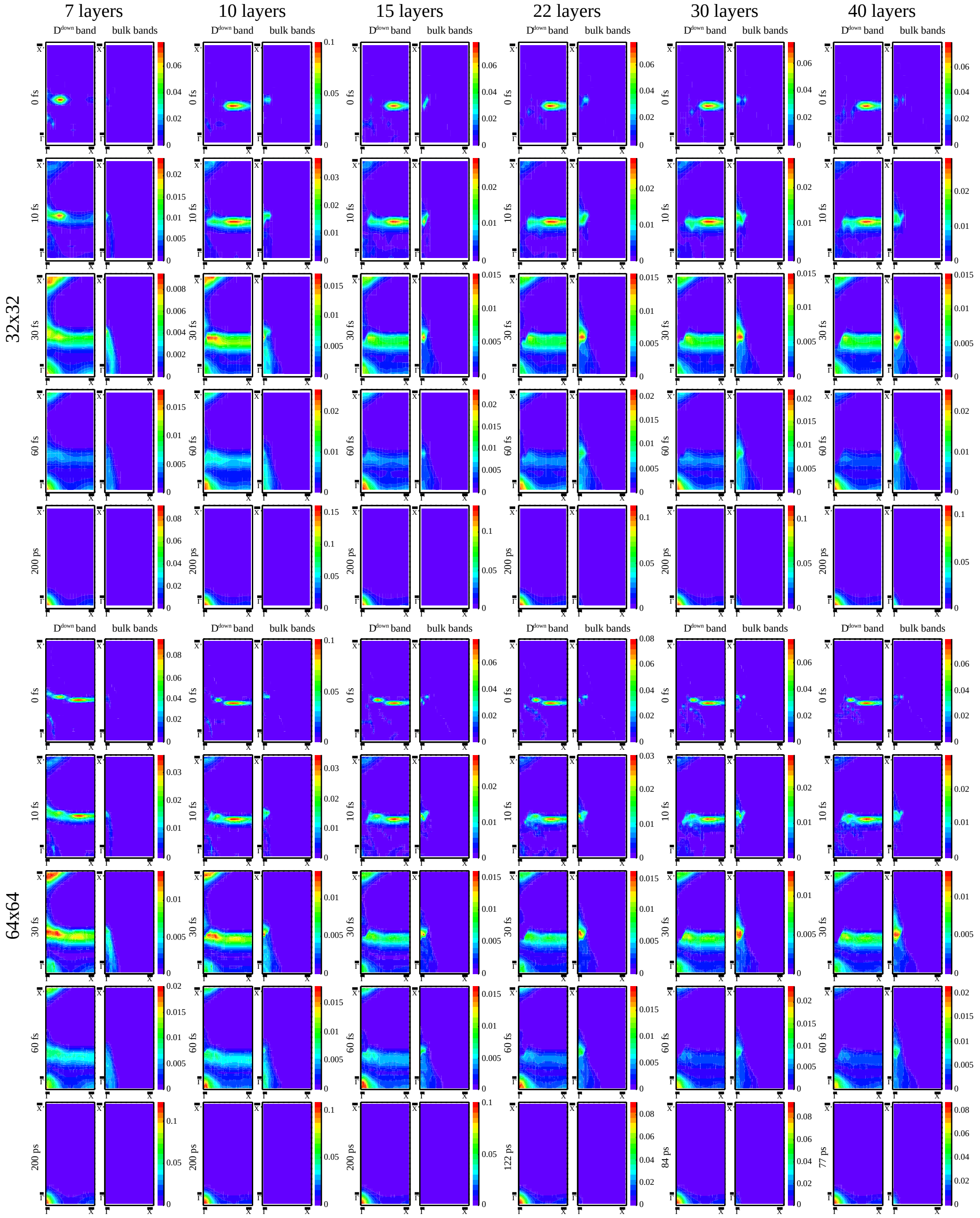

300 K, higher discretizations

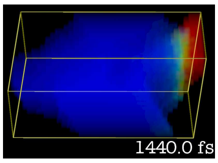

Bibliography

[AE75] L. Allen and J. H. Eberly. *Optical Resonance and Two-Level Atoms*. Dover, New York, 1975.

[Ahn06] K. J. Ahn. *Fully Quantum Mechanical Description of Ultrashort Time Dynamics of Semiconductor Quantum Dots*. PhD thesis, TU Berlin, 2006.

[AM81] N. W. Ashcroft and N. D. Mermin. *Solid State Physics*. Holt-Saunders International Editions, Tokyo, 1981.

[AM98] V. M. Axt and S. Mukamel. Nonlinear optics of semiconductor and molecular nanostructures: a common perspective. *Reviews of Modern Physics*, 70:145, 1998.

[ARSO98] S. Albrecht, L. Reining, R. Del Sole, and G. Onida. Ab initio calculation of excitonic effects in the optical spectra of semiconductors. *Physical Review Letters*, 80:4510, 1998.

[AS94] V. M. Axt and A. Stahl. A dynamics-controlled truncation scheme for the hierarchy of density-matrices in semiconductor optics. *Zeitschrift für Physik B*, 93:195, 1994.

[BD65] J. D. Bjorken and S. D. Drell. *Relativistic quantum fields*. McGraw Hill, New York, 1965.

[BE88] F. Bechstedt and R. Enderlein. *Semiconductor Surfaces and Interfaces*. Akademie-Verlag, Berlin, 1988.

[Bec03] F. Bechstedt. *Principles of surface science*. Springer, Berlin, 2003.

[Bin92] R. Binder. Carrier-carrier scattering and optical dephasing in highly excited semiconductors. *Physical Review B*, 45(3):1107, 1992.

[BKNS97] M. Bockstedte, A. Kley, J. Neugebauer, and M. Scheffler. Density-functional theory calculations for poly-atomic systems: electronic structure, static and elastic properties and ab initio molecular dynamics. *Computer Physics Communications*, 107:187, 1997.

[BKSK07a] N. Buecking, P. Kratzer, M. Scheffler, and A. Knorr. Linking density-functional and density-matrix theory: picosecond electron relaxation at the Si (100) surface. *submitted to Physical Review Letters*, 2007.

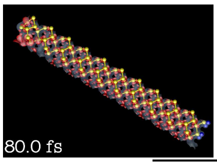

[BKSK07b] N. Buecking, P. Kratzer, M. Scheffler, and A. Knorr. Theory of optical excitation and relaxation phenomena at semiconductor surfaces: linking density functional and density matrix theory. *Applied Physics A*, 88:505, 2007.

[BPC84] A. Blacha, H. Presting, and M. Cardona. Deformation potentials of $\mathbf{k} = 0$ states of tetrahedral semiconductors. *Physica Status Solidi (b)*, 126:11, 1984.

[Büc04] N. Bücking. Konstruktionsprinzipien für Spin-Tensoren in Riemann-Cartan-Räumen. Master's thesis, TU Berlin, 2004.

[But04] S. Butscher. Theory of the non-markovian intersubband dynamics of semiconduction quantum wells. Master's thesis, TU Berlin, 2004.

[But07] S. Butscher. *Many Particle Effects in Two Dimensional Nanostructures Semiconductor Intersubband Transitions and Graphene*. PhD thesis, TU Berlin, 2007.

[CTDL07] C. Cohen-Tannoudji, B. Diu, and F. Laloë. *Quantenmechanik*, volume 1 and 2. de Gruyter, Berlin, 2007.

[Czy00] G. Czycholl. *Theoretische Festkörperphysik*. Vieweg, Braunschweig/Wiesbaden, 2000.

[DG93] R. DelSole and R. Girlanda. Optical properties of semiconductors within the independent-quasiparticle approximation. *Physical Review B*, 48:11789, 1993.

[DM00] J. Dabrowski and H.-J. Müssig. *Silicon Surfaces and Formation of Interfaces*. World Scientific, Singapore, 2000.

[DS92] J. Dabrowski and M. Scheffler. Self consistent study of the electronic and structural properties of the clean Si (001)(2x1) surface. *Applied Surface Science*, 56-58:15, 1992.

[DS96] M. C. Desjonquères and D. Spanjaard. *Concepts in Surface Physics*. Springer, Berlin, second edition, 1996.

[Egg05] P. Eggert. *Theoretische Untersuchung von Vielteilcheneffekten auf Silizium- Halbleiteroberflächen*. PhD thesis, FU Berlin, 2005.

[Fey39] R. P. Feynman. Forces in molecules. *Physical Review*, 56:340, 1939.

[FP95] J. Fritsch and P. Pavone. Ab initio calculation of the structure, electronic states, and the phonon dispersion of the Si (100) surface. *Surface Science*, 344:159, 1995.

[Fri96] J. Fricke. Transport equations including many-particle correlations for an arbitrary quantum system: A general formalism. *Annals of Physics*, 252:479, 1996.

[FSKK06] T. Feldtmann, L. Schneebeli, M. Kira, and S. W. Koch. Quantum theory of light emission from a semiconductor quantum dot. *Physical Review B*, 73:155319, 2006.

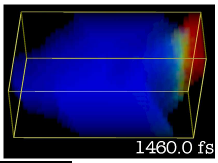

[FVV$^+$00] A. M. Frisch, P. Vogt, S. Visbeck, T. Hannappel, F. Willig, W. Braun, W. Richter, J. Bernholc, W. G. Schmidt, and N. Esser. Angle resolved photoemission spectroscopy of the InP (001) surface. *Applied Surface Science*, 166:224, 2000.

[FWDK03] J. Förstner, C. Weber, J. Danckwerts, and A. Knorr. Phonon-assisted damping of rabi oscillations in semiconductor quantum dots. *Physical Review Letters*, 91:127401, 2003.

[GdGPB91] P. Giannozzi, S. de Gironcoli, P. Pavone, and S. Baroni. Ab initio calculation of phonon dispersions in semiconductors. *Physical Review B*, 43:7231, 1991.

[GP94] J. R. Goldmann and J. A. Prybyla. Ultrafast dynamics of laser-excited electron distributions in silicon. *Physical Review Letters*, 72:1364, 1994.

[Hai95] R. Haight. Electron dynamics at surfaces. *Surface Science Report*, 21:275, 1995.

[Hak73] H. Haken. *Quantenfeldtheorie des Festkörpers*. B.G. Teubner, Stuttgart, 1973.

[Ham89] D. R. Hamann. Generalized norm-conserving pseudopotentials. *Physical Review B*, 40:2980, 1989.

[HBS$^+$86] R. Haight, J. Bokor, J. Stark, R. H. Storz, R. R. Freeman, and P. H. Bucksbaum. Picosecond time-resolved photoemission study of the InP (110) surface. *Physical Review Letters*, 54:1302, 1986.

[Hed65] L. Hedin. New method for calculating the one-particle green's function with application to the electron-gas problem. *Physical Review*, 139:A796, 1965.

[Hel37] H. Hellmann. *Einführung in die Quantenchemie*. Deuticke, Leipzig/Wien, 1937.

[HGB00a] K. Hannewald, S. Glutsch, and F. Bechstedt. Quantum-kinetic study of femtosecond pump-and-probe spectra of bulk GaAs. *Physical Review B*, 61:10792, 2000.

[HGB00b] K. Hannewald, S. Glutsch, and F. Bechstedt. Theory of photoluminescence in semiconductors. *Physical Review B*, 62:4519, 2000.

[HGB01] K. Hannewald, S. Glutsch, and F. Bechstedt. Quantum-kinetic theory of hot luminescence from pulse-excited semiconductors. *Physical Review Letters*, 86:2451, 2001.

[HGB03] K. Hannewald, S. Glutsch, and F. Bechstedt. Non-equilibrium photoluminescence excitation spectroscopy in GaAs: Bottleneck and memory effects. *Physical Review B*, 67:233202, 2003.

[HGL$^+$97] C. B. Harris, N. H. Ge, R. L. Lingle, J. D. McNeill, and C. M. Wong. Femtosecond dynamics of electrons on surfaces and at interfaces. *Annual Reviews of Physical Chemistry*, 48:711, 1997.

[HJ98] H. Haug and A.-P. Jauho. *Quantum Kinetics in Transport and Optics of Semiconductors*, volume 123 of *Springer Series in Solid-State Sciences*. Springer, Berlin, 1998.

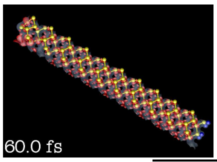

[HK64] P. Hohenberg and W. Kohn. Inhomogeneous electron gas. *Physical Review*, 136:B 864, 1964.

[HK90] H. Haug and S. W. Koch. *Quantum Theory of the Optical and Electronic Properties of Semiconductors*. World Scientific, Singapore, third edition, 1990.

[HKK03] W. Hoyer, M. Kira, and S. W. Koch. Influence of coulomb and phonon interaction on the exciton formation dynamics in semiconductor heterostructures. *Physical Review B*, 67:155113, 2003.

[HSC$^+$93] J. Henk, W. Schattke, H. Carstensen, R. Manzke, and M. Skibowski. Surface-barrier and polarization effects in the photoemission from GaAs (110). *Physical Review B*, 47:2251, 1993.

[HSK$^+$93] U. Hohenester, P. Supancic, P. Kocevar, X. Q. Zhou, W. Kütt, and H. Kurz. Subpicosecond thermalization and relaxation of highly photoexcited electrons and holes in intrinsic and p-type GaAs and InP. *Physical Review B*, 47:13233, 1993.

[Jac99] J. D. Jackson. *Classical Electrodynamics*. John Wiley & Sons, Inc., New York, third edition, 1999.

[JB99] S. Jeong and J. Bokor. Ultrafast carrier dynamics near the Si (100)(2×1) surface. *Physical Review B*, 59:4943, 1999.

[JRM01] S. Jorgensen, M. Ratner, and K.V. Mikkelsen. Time-resolved two-photon photoemission spectroscopy of image potential states: A phenomenological approach. *Journal of Chemical Physics*, 115:4314, 2001.

[KHSK96] A. Knorr, S. Hughes, T. Stroucken, and S. W. Koch. Theory of ultrafast spatio-temporal dynamics in semiconductor heterostructures. *Chemical Physics*, 210:27, 1996.

[Kit91] C. Kittel. *Einführung in die Festkörperphysik*. Oldenburg, München, 1991.

[KP95] P. Krüger and J. Pollmann. Dimer reconstruction of diamond (001), Si (001), and Ge (001) surfaces. *Physical Review Letters*, 74:1155, 1995.

[KS65] W. Kohn and L. J. Sham. Self-consistent equations including exchange and correlation effects. *Phys. Rev.*, 140:A 1133, 1965.

[KSM$^+$99] S. W. Koch, C. Sieh, T. Meier, F. Jahnke, A. Knorr, P. Brick, M. Hübner, C. Ell, J. Prineas, G. Khitrova, and H. M. Gibbs. Theory of coherent effects in semiconductors. *Journal of Luminescence*, 83:4, 1999.

[Kuh98] T. Kuhn. Density matrix theory of coherent ultrafast dynamics. In E. Schöll, editor, *Theory of Transport Properties of Semiconductor Nanostructures*, page 173. Chapman & Hall, London, 1998.

[LB87] H. H. Landolt and R. Börnstein. *Landolt-Börnstein*. Springer Berlin, 1987. `www.landolt-boernstein.de`.

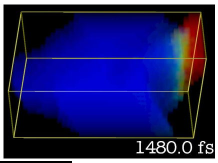

[LFL$^+$96] A. Leitenstorfer, C. Fürst, A. Laubereau, W. Kaiser, G. Tränkle, and G. Weimann. Femtosecond carrier dynamics in GaAs far from equilibrium. *Physical Review Letters*, 76:1545, 1996.

[LSS$^+$97] S. Lorenz, C. Solterbeck, W. Schattke, J. Burmeister, and W. Hackbusch. Electron-scattering states at solid surfaces calculated with realistic potentials. *Physical Review B*, 55:13432, 1997.

[Lüt93] H. Lüth. *Surfaces and Interfaces of Solids*. Springer, Berlin, 1993.

[Mah81] G. D. Mahan. *Many-Particle Physics*. Plenum Press, New York, 1981.

[Mah90] G. D. Mahan. Theory of photoemission. In M. Campagna and R. Rosei, editors, *Photoemission and Absorption Spectroscopy of Solids and Interfaces with Synchotron Radiation*, page 25. North Holland, Amsterdam, 1990.

[MCFF78] J. C. Merle, M. Capizzi, P. Fionini, and A. Frova. Uniaxially stressed silicon: Fine structure of the exciton and deformation potentials. *Physical Review B*, 17:4821, 1978.

[MP00] G. D. Mahan and E. W. Plummer. Many-body effects in photoemission. In K. Horn and M. Scheffler, editors, *Electronic Structure*, volume 2 of *Handbook of Surface Science*, pages 953–987. Elsevier, Amsterdam, 2000.

[NN72] G. Nilsson and G. Nelin. Study of the homology between silicon and germanium by thermal-neutron spectrometry. *Physical Review B*, 6:3777, 1972.

[ORR02] G. Onida, L. Reining, and A. Rubio. Electronic excitations: density-functional versus many-body green's-function approaches. *Review of Modern Physics*, 74:601, 2002.

[PV81] W. Pötz and P. Vogl. Theory of optical-phonon deformation potentials in tetrahedral semiconductors. *Physical Review B*, 24:2025, 1981.

[RBK95] A. Ramstad, G. Brocks, and P. J. Kelly. Theoretical study of the Si (100) surface reconstruction. *Physical Review B*, 51:14504, 1995.

[RG94] E. Runge and E. K. U. Gross. Density-functional theory for time-dependent systems. *Physical Review Letters*, 52:997, 1994.

[RK02] F. Rossi and T. Kuhn. Theory of ultrafast phenomena in photoexcited semiconductors. *Review of Modern Physics*, 74:895, 2002.

[RMKR03] M. Reichelt, T. Meier, S. W. Koch, and M. Rohlfing. Theory for the nonlinear optical response of semiconductor surfaces: Application to the optical stark effect and spectral oscillations of the Si (111)-(2×1) surface exciton. *Physical Review B*, 68:045330, 2003.

[RQN$^+$05] P. Rinke, A. Qteish, J. Neugebauer, C. Freysoldt, and M. Scheffler. Combining GW calculations with exact-exchange density-functional theory: an analysis of valence-band photoemission for compound semiconductors. *New Journal of Physics*, 7:126, 2005.

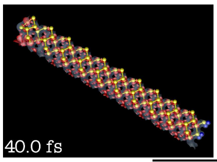

[RWK04a] S. Ramakrishna, F. Willig, and A. Knorr. Photoinduced bulk-surface dynamics: time resolved two photon photoemission signals at semiconductor surfaces. *Surface Science*, 558:159, 2004.

[RWK04b] S. Ramakrishna, F. Willig, and A. Knorr. Time-resolved two-photon photoemission spectroscopy of semiconductor bulk states. *Applied Physics A*, 78:247, 2004.

[SB98] W. G. Schmidt and F. Bechstedt. Geometry and electronic structure of InP (001)(2×4) reconstructions. *Surface Science*, 409:474, 1998.

[SB00] J. Stoer and R. Bulirsch. *Numerische Mathematik*, volume 2. Springer, Berlin, 2000.

[SBE^{+}98] W. G. Schmidt, F. Bechstedt, N. Esser, M. Pristovsek, C. Schultz, and W. Richter. Atomic structure of InP (001)-(2×4): A dimer reconstruction. *Physical Review B*, 57(14596), 1998.

[Sch02] F. Schwabl. *Quantenmechanik*. Springer, Berlin, 2002.

[Sch06] M. Schaarschmidt. *Theory of Light Propagation in Nano-Structured Materials and Semiconductors*. PhD thesis, TU Berlin, 2006.

[SEE^{+}00] W. G. Schmidt, N. Esser, N. Esser, A. M. Frisch, P. Vogt, J. Bernholc, F. Bechstedt, M. Zorn, Th. Hannappel, S. Visbeck, F. Willig, and W. Richter. Understanding reflectance anisotropy: Surface-state signatures and bulk-related features in the optical spectrum of InP (001)(2×4). *Physical Review B*, 61:R16335, 2000.

[Sha99] J. Shah. *Ultrafast Spectroscopy of Semiconductors and Semiconductor Nanostructures*. Springer, Berlin, 1999.

[SKM94] J. Schilp, T. Kuhn, and G. Mahler. Electron-phonon quantum kinetics in pulse-excited semiconductors: Memory and renormalization effects. *Physical Review B*, 50:5435, 1994.

[SKS^{+}96] F. Steininger, A. Knorr, T. Stroucken, P. Thomas, and S. W. Koch. Dynamic evolution of spatiotemporally localized electronic wave packets in semiconductor quantum wells. *Physical Review Letters*, 77:550, 1996.

[SMH^{+}96] C. A. Schmuttenmaer, C. C. Miller, J. W. Herman, J. Cao, D. A. Mantell, Y. Gao, and R. J. D. Miller. Femtosecond time-resolved photoemission study of hot electron relaxation at the GaAs (100) surface. *Chem. Phys.*, 205:91, 1996.

[SS06] W. G. Schmidt and K. Seino. Si (001) $c(4\times 2)-p(2\times 2)$ surface phase transitions induced by electric fields and doping. *Current Applied Physics*, 6:331, 2006.

[SSB04] K. Seino, W. G. Schmidt, and F. Bechstedt. Energetics of Si (001) surfaces exposed to electric fields and charge injection. *Physical Review Letters*, 93:036101, 2004.

[SW93] M. Schubert and G. Weber. *Quantentheorie: Grundlagen und Anwendungen*. Spektrum Akad. Verlag, Heidelberg, Berlin, 1993.

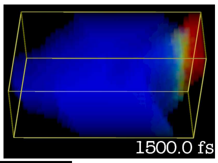

[SW02] W. Schäfer and M. Wegener. *Semiconductor Optics and Transport Phenomena*. Springer, Berlin, 2002.

[TGE$^+$05] L. Töben, L. Gundlach, R. Ernstorfer, R. Eichberger, T. Hannappel, F. Willig, A. Zeiser, J. Förstner, A. Knorr, P. H. Hahn, and W. G. Schmidt. Femtosecond transfer dynamics of photogenerated electrons at a surface resonance of reconstructed InP (100). *Physical Review Letters*, 94:067601, 2005.

[TGH$^+$04] L. Töben, L. Gundlach, T. Hannappel, R. Ernstorfer, R. Eichberger, and F. Willig. Dynamics of electron scattering between bulk states and the c-1 surface state of InP (100). *Applied Physics A*, 78:239, 2004.

[THE$^+$03] L. Töben, T. Hannappel, R. Eichberger, K. Möller, L. Gundlach, R. Ernstorfer, and F. Willig. Two-photon photoemission as a probe of unoccupied and occupied surface states of InP (100). *Journal of Crystal Growth*, 248C:206, 2003.

[TT03] S. Tanaka and K. Tanimura. Time-resolved two-photon photoelectron spectroscopy of the Si (001)-(2×1) surface. *Surface Science*, 529:251, 2003.

[Uni36] Unidata. Network Common Data Form, Version 3.6. current version and documentation available at `www.unidata.ucar.edu/software/netcdf/`.

[vdW89] C. G. van der Walle. Band lineups and deformation potentials in the model-solid theory. *Physical Review B*, 39:1871, 1989.

[vHLP05] J. van Heys, M. Lindenblatt, and E. Pehlke. Molecular-dynamics simulations of non-adiabatic processes at surfaces. *Phase Transitions*, 78:773, 2005.

[vR06] G. van Rossum. *An Introduction to Python - The Python Tutorial (version 2.5)*. Network Theory Ltd, 2006. current version and documentation available at `www.python.org`.

[WFK03] I. Waldmüller, J. Förstner, and A. Knorr. *Nonequilibrium Physics at Short Time Scales*, chapter Self-consistent Projector Operator Theory of Intersubband Absorbance in Semiconductor Quantum Wells. Springer, Berlin, 2003.

[WFL$^+$04] I. Waldmüller, J. Förstner, S.-C. Lee, A. Knorr, M. Woerner, K. Reimann, R. A. Kaindl, T. Elsaesser, R. Hey, and K. H. Ploog. Optical dephasing of coherent intersubband transitions in a quasi-two-dimensional electron gas. *Physical Review B*, 69:205307, 2004.

[WKFR04] M. Weinelt, M. Kutschera, T. Fauster, and M. Rohlfing. Dynamics of exciton formation at the Si (100) $c(4 \times 2)$ surface. *Physical Review Letters*, 92:126801, 2004.

[WRKP05] N.-P. Wang, M. Rohlfing, P. Krüger, and J. Pollmann. Femtosecond dynamics of excited states of CO adsorbed on MgO(001)-(1×1). *Phys. Rev. B*, 71:045407, 2005.

[YC96] P. Y. Yu and M. Cardona. *Fundamentals of Semiconductors*. Springer, Berlin, second edition, 1996.

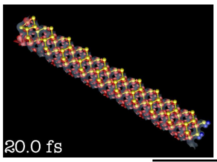

[ZBFK05] A. Zeiser, N. Bücking, J. Förstner, and A. Knorr. Microscopic theory of electron dynamics and time-resolved two-color two-photon photoemission at semiconductor surfaces. *Physical Review B*, 71:245309, 2005.

[ZBG$^+$04] A. Zeiser, N. Bücking, J. Götte, J. Förstner, P. Hahn, W. G. Schmidt, and A. Knorr. Dynamics of the phonon-induced electron transfer between semiconductor bulk and surface states. *Physica Status Solidi (b)*, 241:R60, 2004.

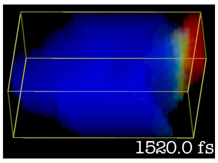

Index

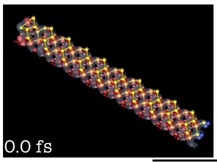
0.0 fs

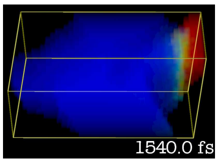

Danksagung

Für das Gelingen dieser Doktorarbeit waren viele Menschen maßgeblich, ist sie doch in einer Kooperation, d.h. virtuell am *Fritz-Haber-Institut* und physisch an der *TU Berlin* entstanden. Zunächst sind mein Doktorvater Andreas Knorr, der sich unermüdlich für die Fortentwicklung dieses Projektes eingesetzt hat, und mein "Zweit-Doktorvater" Matthias Scheffler, der die Infrastruktur zur Verfügung stellte und das know-how für die Dichte-Funktional-Theorie einbrachte, und außerdem das Zweitgutachten schrieb, die Adressaten meines Dankes. Zu ganz besonderem Dank bin ich in diesem Zusammenhang aber auch Peter Kratzer verpflichtet, der mir – zu seiner Zeit am FHI – unermüdlich Hilfestellungen leistete und auch später viel für das Vollenden der Publikationen beitrug.

An der TU war es vor allem die wunderbare Atmosphäre in der *Knorr-Gruppe*, die mir einen Ansporn gaben. Insbesondere sind dabei Martin Schaarschmidt, mit dem es nie langweilig wurde und dem ich für seine Hilfsbereitschaft danke, Stefan Butscher, mit dem man lange Diskussionen (natürlich nur über Physik) führen und viel Tee trinken kann, Carsten Weber, der nicht zuletzt mit Chaos die Gruppe neu ordnete, Marten Richter, mit dessen Hilfe alles irgendwann funktioniert, Peter Orlowski, ohne dessen Hilfe nichts funktioniert, Frank Milde und Matthias Hirtschulz als nächste und übernächste Nachbarn, Ermin Malic, und nicht zu vergessen Andreas Zeiser, der einige Grundlagen für diese Arbeit lieferte, zu erwähnen.

Diese Arbeit wäre dennoch nichts geworden ohne meine Familie. In erster Linie danke ich meiner Frau Ulrike, die meine Launen (besonders in der Endphase) wegsteckte, trotz daß sie sich selber in einer vergleichbaren Situation befand, und mich dennoch mit ihrer Wärme wiederaufrichtete, außerdem meinem Sohn Simon, der nun wahrscheinlich erst wieder lernen muß, was man mit einem Papa alles anstellen kann, meinen Schwiegereltern, die uns in dieser Zeit sehr entlastet haben, meinen Brüdern und meinen Eltern, die leider alle zu weit entfernt waren um an der Entwicklung dieser Arbeit teilzuhaben.